17th Numerical Towing Tank Symposium

28-30 September 2014
Marstrand, Sweden

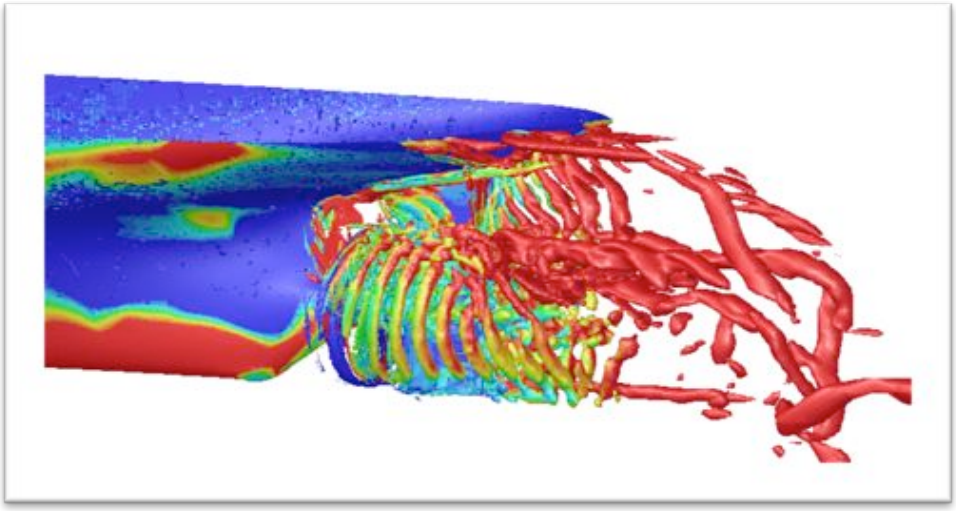

Rickard E Bensow (Ed.)

CHALMERS
UNIVERSITY OF TECHNOLOGY

Sponsored by

www.catpropulsion.com

www.cd-adapco.com

www.numeca.com

www.rolls-royce.com

Table of Contents

Study of influence of unsteady wake on the propeller performance using the hybrid RANS-LES methods
N. Abbas, N. Kornev

Shear Stress Effects in Cavitating Flows
A. Asnaghi, A. Feymark, R.E. Bensow

Ship wake field analysis using a coupled BEMt-RANS approach
C. Badoe, A. Phillips, S.R. Turnock

Developing tools for assessing bend-twist coupled foils
J. Banks, L.M. Giovannetti, S.R. Turnock, S.W. Boyd

Numerical Analysis of Propeller-induced Pressure Pulses in Wakes Modified by Improvement Devices
T. Bugalski, J.A. Szantyr

RANSE simulations for the effect of welds on ship resistance
C. Cosmin, V. Bertram

A fish shoal algorithm for global derivative-free simulation-based ship design optimization
M. Diez, A. Serani, U. Iemma, E.F. Campana

Simulation cases for verification of flow noise prediction in the parameter range of interest for naval applications
A. Feymark, M. Liefvendahl, R.E. Bensow

OpenFOAM investigations of a flushed water-jet inlet performance
A. Gattoronchieri, C. Cravero

Potential of Chaotic Iterative Solvers for CFD
J. Hawkes, G. Vaz, S.R. Turnock, S.J. Cox, A.B. Phillips

RANS simulations of cavitating propeller flows
T. Huuva, S. Törnros

A comparison of CFD and wind tunnel tests for exhaust gas dispersion analysis of an Aframax tanker
K. Kalaskar, S. Whitworth, D. Radosavljevic

Prediction of added resistance in waves using RANS-based analysis
Y.-C. Kim, K.-S. Kim, Y. Kim, J. Kim, S.-H. Van

Validation of a numerical experiment by using the non-intrusive measurement technique PIV
T. H. Knudsen

Simulation of Airflow Around Wing Sails Using BEM, Blender, and OpenCL
J.A. Kramer, S. Steen

Computations of wave loads on support structures of bottom-fixed offshore wind turbines
M. Kraskowski, D. Veić

Study of underwater noise signature from a tanker with a cavitating propeller
D.-Q. Li, J. Hallander, R. Karlsson

The influence of turbulence modelling techniques on the predicted cavitation behaviour on a NACA0009 foil
A.K. Lidtke, S.R. Turnock, V.F. Humphries

Implementing the Ffowcs Williams-Hawkings acoustic analogy into a viscous CFD solver
T.P. Lloyd, D. Rijpkema, E. Van Wijngaarden

Simulation of seakeeping tests using OpenFOAM
J. Löhrmann, A.C. Hochbaum

Numerical Prediction of Resistance and Squat for a Containership in Shallow Water
P. Mucha, B. El Moctar

Multi-objective extensions of the deterministic particle swarm algorithm for RBRDO in ship design: a parametric study
R. Pellegrini, A. Serani, M. Diez, U. Iemma, E.F. Campana

On the use of Hybrid Turbulence Models
F.S. Pereira, G. Vaz, L. Eça

Optimization of the STREAMLINE tanker using RANS/FS computations
A. van der Ploeg

Numerical Studies of Hydrodynamic Interactions of Two Bodies in Waves
W. Qiu, P. Wen, M. Liu, H. Peng

Development of URaNS Maneuvering Simulator and its Application to ESSO OSAKA
N. Sakamoto, K. Ohashi

Adjoint-Based Shape Optimisation Applied to the Bow of a Bulk Carrier
L.-U. Schrader

Extended dynamic controller for quick and accurate CFD calculations of self-propelled ships at imposed power
I. Schrooyen, K. Randle, L. Clous, B. Herry, B. Mallol

Cavitation simulation on Kappel propeller with a hull wake field
K.W. Shin

Numerical Simulation of Breaking Wave and Re-attachment Inside an Air Cavity
A. Shiri, R.E. Bensow, M. Leer-Andersen, J. Norrby

Comparison of LES and DNS for the flow past a circular cylinder with fairings
H. Strandenes, J.P. Gallardo, B. Pettersen , H.I. Andersson

Particle Swarm Optimisation - An Alternative in Marine Propeller Optimisation?
F. Vesting, R.E. Bensow

Study of a volume of fluid type methodology in computational hydrodynamics
V. Viitanen

Hessian-based grid refinement for the simulation of surface-piercing hydrofoils
J. Wackers, E. Guilmineau, A. Palmieri, P. Queutey

Numerical Simulation of Slamming Problems Based on a CIP Method Using MPI
P. Wen, W. Qiu

Self propulsion modelling of the KCS container ship using an open source framework
B. Windén, S.R. Turnock, D. Hudson

Study of influence of unsteady wake on the propeller performance using the hybrid RANS-LES methods

Nawar Abbas* and Nikolai Kornev
Chair for Modelling and Simulation,
University of Rostock, 18059 Rostock, Germany

Introduction

Determination of unsteady loadings on marine propeller is one of the important and challenging problems for the prediction of hull structure and propulsion shafting vibrations. Classical engineering methods of the marine propeller forces calculations assume the velocity field to be stationary, the so-called "frozen field". These methods allow one to predict the propeller forces fluctuations with dominating blade frequencies proportional to nZ, where Z is the number of blades and n is the frequency of the propeller. Such variations of forces and moments are referred to periodic rather than unsteady ones if the wake is considered as steady wake. The fact that the wake can be strongly unsteady has not been studied thoroughly because of limitations of available measurement techniques and traditional numerical approaches based on the Reynolds averaged Navier Stokes equations.

During the previous conference of NUTTS (NUTTS 2013) we showed, that the URANS (Unsteady Reynolds Averaged Navies Stokes) method, is capable of capturing steady effects and large scale unsteadiness, but is not capable of modeling unsteady vortices arising in the ship stern area flow. This technique (URANS) is not able to resolve small scale flow oscillations due to large diffusivity which is an unavoidable feature of URANS closure models. The grid resolution necessary for a pure LES is so huge, that this makes the direct application of LES impossible. A practical solution of this problem is the use of a hybrid URANS-LES approach, in which the near body flow region is treated using URANS and far flow regions are calculated with LES.

This paper presents the latest results of the development and validation of hybrid method undertaken at the Chair of Modelling and Simulation of the Rostock University (see [1] and [2]). In the previous work [2] we tested the applicability of the Prandt- Kolmogorov estimation for the integral length, which is used in our work to switch between LES and URANS, and found an appropriate value for the constant in this formula. A very critical question which remained open was the influence of the resolution on the velocity fluctuation field as well as on the forces acting on the propeller.

In our recent paper [3] the hybrid RANS-LES was validated using the planar diffuser flow for three resolutions ranging from 2.6×10^5 to 1.2×10^6. Results demonstrated convergence to reference data and measurement. In this paper we studied this problem for the benchmark test tanker KVLCC2. For the bare hull case the grid was gradually refined from $7 \cdot 10^6$ to $45 \cdot 10^6$ cells. The results show the convergence which is different at different points in the propeller plane. In the next step the ship with rotating propeller was calculated with $22.5 \cdot 10^6$ cells. Despite of relatively slow convergence of the velocity field the integral forces show faster convergence in time. Furthemore, the forces standard deviations show good agreement with estimations based on the Krylov Insitute method.

Description of methods for prediction of unsteady loadings on marine propellers

In this section we give a short overview of some methods utilized in this paper for computation of forces and moments on a propeller.

*nawar.abbas@uni-rostock.de

Engineering methods

The engineering methods described in this section use different kinds of simplifications and approximations of the available experimental data to estimate the desired quantities.

Scheme B is a very simple and at the same time a very efficient method proposed by experts of the Krylov Research Shipbuilding Institute [4]. The method is based on the hypothesis of quasi-stationarity and assumes that the thrust and the moment coefficients are known (K_T,K_Q). These coefficients are determined under the open water conditions as functions of the propeller advance ratio. The force and the moment are then distributed along the blade span using correlations taken from the lifting surface theory. From these distributions it is possible to estimate the local lift and drag coefficients corresponding to each blade profile at a certain radius along the span. At each time instant, the force and the moment arising on this profile are calculated using these coefficients, the local values of the incident velocity and the angle of attack. The total force and the moment are determined by integration of local loadings along the blade span. The nominal wake velocity field including tangential and axial components is represented via the Fourier series as a function of the rotation angle. This allows one to express forces and moments in terms of the Fourier coefficients. The influence of the propeller on the nominal wake is taken into account by the contraction of the propeller jet determined using the formula of the actuator disc theory.

The Veritec approximation is briefly discussed in the book of [5]. It is based on the approximation of results of theoretical investigation of the dynamic forces at blade and twice blade frequencies performed for twenty typical ships [6]. The results are summarized in form of dependence of force and moment Fourier coefficients on the blade number (see Table 11.13 in [5]).

The Wereldsma approximation is based on the statistical regression analysis of measurements done for 40 ship models with four and five bladed propellers. To get detailed information the reader is referred to the original publication of [7].

Results obtained using engineering methods and presented in the paper are taken from [8].

Hybrid method

The hybrid CFD model developed in our previous work [1] has been described in the previous conference of NUTTS (NUTTS 2013 - see [2]), but a small summary will be written in this section. Hybrid model is based on the observation that the basic transport equations have the same form in LES and URANS

$$\frac{\partial \overline{u}_i}{\partial t} + \frac{\partial (\overline{u}_i \overline{u}_j)}{\partial x_j} = -\frac{\partial \overline{p}^*}{\partial x_i} + \frac{\partial (\tau^l_{ij} + \tau^t_{ij})}{\partial x_j}, \tag{1}$$

here we use the standard notation of p^* for the pseudo-pressure, and τ^l_{ij} and τ^t_{ij} for the laminar and turbulent stresses respectively. The computational domain in our model is dynamically (i.e. at each time step) divided into the LES and URANS regions. The key quantities of this decomposition are the integral length scale L and the extended LES filter Δ which are computed for each cell of the mesh. L is determined from the formula of Kolmogorov and Prandtl:

$$L = C \cdot k^{3/2}/\varepsilon \tag{2}$$

where k is the turbulent kinetic energy and ε is the dissipation rate and C is a certain empiric constant. The filter Δ is computed as $\Delta = \sqrt{0.5(d^2_{\max} + \delta^2)}$, where $d_{\max}$ is the maximal length of the cell edges $d_{\max} = \max(d_x, d_y, d_z)$ and $\delta = \sqrt[3]{(\text{the cell volume})}$ is the common filter width used in LES. A cell of the mesh belongs to one area or the other depending on the value of L relative to Δ: if $L > \Delta$ then the cell is in LES area, in other case it is in URANS region. The turbulent kinematic viscosity is smoothed between the LES and URANS regions. The wall functions are used in the near wall URANS region. The CFD calculations using both URANS and hybrid models were carried out with the OpenFOAM code.

Geometry and the numerical environment of the tanker KVLCC2

The doubled model of the KRISO tanker KVLCC2 with the scale 1/58 has been chosen as a test object since it is widely used in the shipbuilding community for CFD validations. The model has length of 5.517 m, breadth of 1 m, draught of 0.359 m and block coefficient of 0.8098. The study of the model has been performed for the constant velocity of $u_0 = 1.047$ m/s corresponding to the Reynolds number of $\mathrm{Re} = 5 \times 10^6$. The Froude number $\mathrm{Fn} = 0.142$ is small which makes it possible to neglect the water surface deformation effects. The propeller VP1356 used in our test has five blades ($Z = 5$), the diameter D of 0.17m, pitch ratio of 0.996, EAR (expanded area ratio) of 0.8, $D_{\mathrm{hub}}/D = 0.18$ and maximal skewness

of 32°. The propeller frequency n is 8 and 9.35 rotations per second. At $n = 9.35$ rps the thrust of the propeller is approximately equal to the ship resistance. The bare hull was studied with four gradually refined grids generated by Ansys ICEM and containing $7M$, $13M$, $25M$ and $45M$ of cells. The first computational node of first grid with $7M$ of cells was located at $y^+ = 6$ from the wall with a sufficient refinement in the propeller disc (see. Fig. 1(a)). All other grids were obtained from this grid by gradual refinement. For that the blocks in the boundary layer and the propeller disc (see Fig .1(b)) have been refined by multiplying the cell numbers in each block with a factor of 1.3 in all three directions (x, y, z). The first node for $13M$, $25M$ and $45M$ was, respectively, at $y^+ = 2.6, 1.6$ and $y^+ = 0.5$.

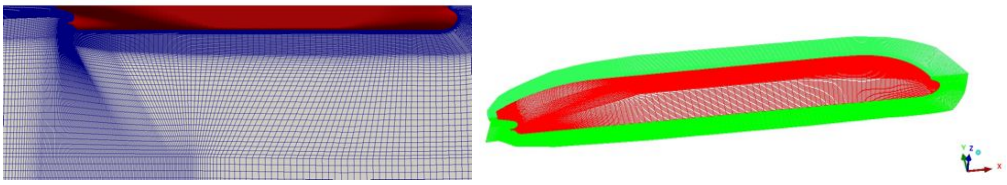

(a) Computational grid of KVLCC2 (b) Blocks of the boundary layer and the propeller disc.

Figure 1: Computational grid of KVLCC2 with 7 millions of cells.

The rotating propeller was calculated using the Arbitrary Mesh Interface (AMI) provided in OpenFOAM to model the interface between stator (hull) and rotor (propeller) grids. The system ship with rotating propeller was studied with fine ($22.5M$) grid. The stator grids containing $19.5M$ of cells have been generated using the Ansys ICEM software. The rotor grids have been generated using the snappyHexMesh-mesher provided by OpenFOAM and contain $3M$ cells. The grid of $22.5M$ has $y^+ \approx 0.1 - 3.5$ in the wall region of aftership and $y^+ \approx 3$ in the foreship area. The computations have been carried out with the fixed maximal Courant number of 4.0 for $n = 8$ rps and with $CO_{Max} = 40.0$ for $n = 9.35$ rps, which correspond to the time step $\approx 5.0 \times 10^{-5}$ s and $\approx 5.0 \times 10^{-4}$ s respectively. For 8 rps of the propeller the value of the rotation angle of the propeller for each time step is equal to 0.144°and 1.683°for 9.35 rps. The limited central differencing scheme has been used for all the terms in the momentum equation for the space discretization. The time discretization has been done using the Crank-Nicholson scheme. For the initialization of the flow in the computational domain the steady RANS solutions have been used.

Influence of grid resolution on velocity fluctuations in wake

Investigations were performed in the propeller plane at different radii from the propeller axis (see Fig. 2). Circumferential distributions of the r.m.s. of axial velocity fluctuations referred to the mean axial velocity in percent are shown at different radii and grid resolutions. The statistical data were gathered within 10 seconds of real time. The r.m.s. distributions are strongly fluctuating and the convergence in a classical sense is difficult to recognize. However, one can conclude that $7M$ cells grid is too coarse to resolve the fluctuations because of smoothing effect of big cells. When the cell number increases from $13M$ to $45M$ the r.m.s. level is stabilized at $r/R \leq 0.6$. The r.m.s distributions fluctuate around approximately the same level. At $r/R = 1$ there is the discrepancy between intermediate grid $13M$ and fine grids close to the peak region at $\phi \approx 50^0$ and $\phi \approx 310^0$. Since the peak region is very narrow, one can expect that this discrepancy is negligible for propeller loadings prediction. The only unsatisfactory results are documented at $50^0 < \phi < 125^0$ and $225^0 < \phi < 310^0$ at $r/R = 0.8$. The level of fluctuations is gradually reduced when the resolution grows. Taking these results into account further investigations with rotating propellers are performed for $19.5M$ grid cells around the hull excluding the propeller area. With the resources available to the authors the use of finer grids is non realistic for the hull with rotating propeller because of huge necessary computational time.

Unsteady loadings on propeller

The results for standard deviations of forces and moments are summarized in Table. 1. Standard deviations based on engineering methods were calculated using amplitudes of different harmonics published

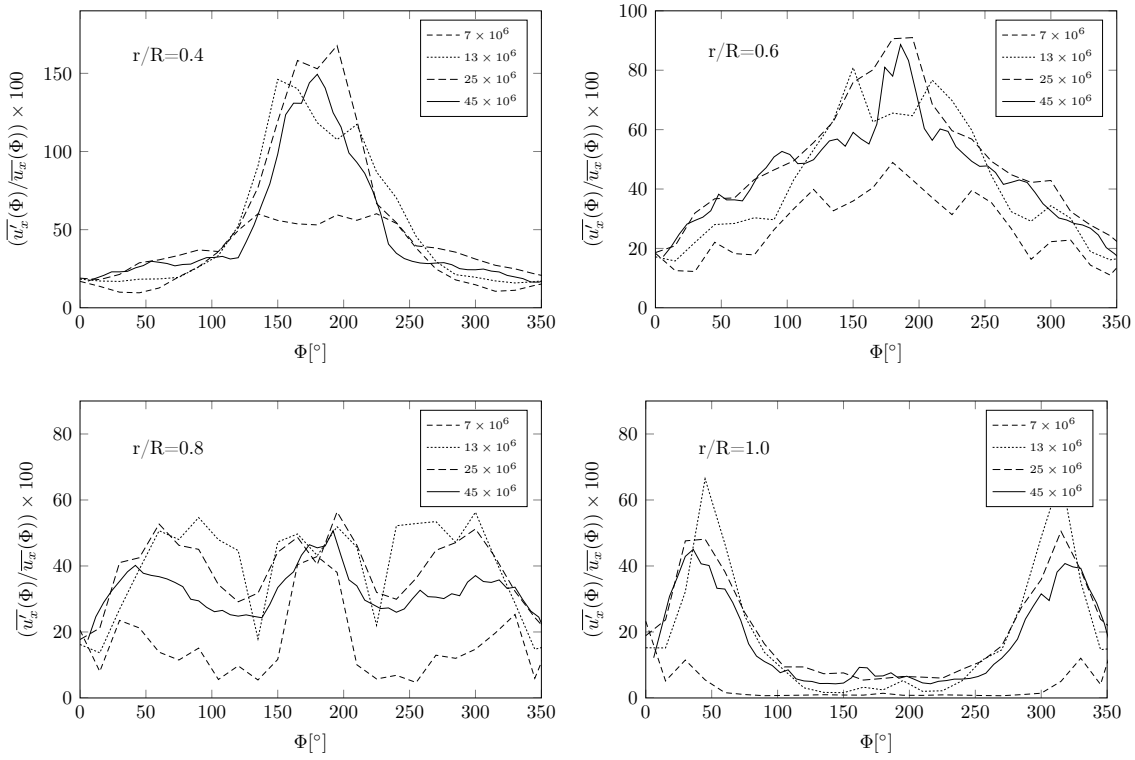

Figure 2: Axial velocity fluctuations along circles at different radii in the propeller plane.

in [8]:

$$AP_x = \sqrt{\overline{P_x'^2}} = \left[\lim_{T\to\infty} \frac{1}{T} \int_0^T \left(\sum_{k=1}^{N} A_k \sin(knZt + \phi_k) \right)^2 dt \right]^{1/2} \tag{3}$$

where A_k is the amplitude of $k-th$ mode, N is the number of harmonic modes (usually $N = 2$) and ϕ_k is the phase displacement. Amplitudes A_k are published in [8] for different blade numbers. Each amplitude is represented as the sum of a mean value which is valid for all possible ships and a deviation, i.e. $A_k = A_k^{mean} \pm A_k^{dev}$. A_k^{dev} accounts for the variation of A_k depending on ship types. Particularly, for full bottomed ships this reads $A_k^{max} = A_k^{mean} + A_k^{dev}$. Since the phase displacement has no influence on the standard deviation (it was tested), the results are presented for $\phi_k = 0$. The same procedure is applied to all forces and moments. All force standard deviations are referred to the mean thrust, whereas the moments deviations to the mean torque.

Method ⇒	Veritec	Wereldsma	Scheme B	CFD-our hybrid	
	mean	mean	mean	8 RPS	9.35 RPS
$P_x'/\overline{P_x}\%$	1.85 ±0.47	2.47 ±1.41	1.77 ±1.13	2.65	0.88
$P_y'/\overline{P_x}\%$	0.79 ±0.65	1.96 ±1.41	0.19 ±0.15	0.61	0.29
$P_z'/\overline{P_x}\%$	1.54 ±1.16	2.32 ±1.41	0.74 ±0.44	0.76	0.51
$M_x'/\overline{M_x}\%$	0.12 ±0.55	1.76 ±1.41	1.34 ±0.75	2.23	0.74
$M_y'/\overline{M_x}\%$	10.15 ±6.84	6.41 ±1.41	1.63 ±1.23	3.14	1.94
$M_z'/\overline{M_x}\%$	10.49 ±6.61	3.74 ±1.41	5.17 ±3.03	4.64	2.31

Table 1: Standard deviations of the forces and moments calculated using different approaches. P_x: thrust, P_y: vertical force, P_z: horizontal force, M_x: torque, M_y: horizontal moment, M_z: vertical moment.

The standard deviation of the thrust varies in the range between 1.85% and 3.89%, the vertical forces between 0.19% and 3.38%, the horizontal force between 0.74% and 3.74%, all referred to the mean thrust. For the torque, the results of all methods, except the Veritec approximation, are in a good

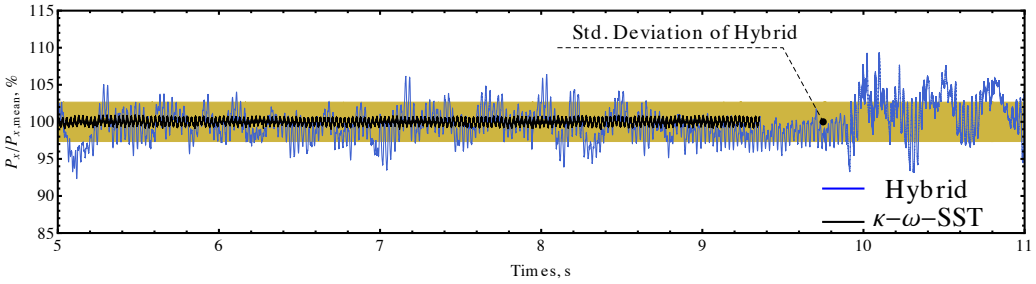

(a) 8 RPS

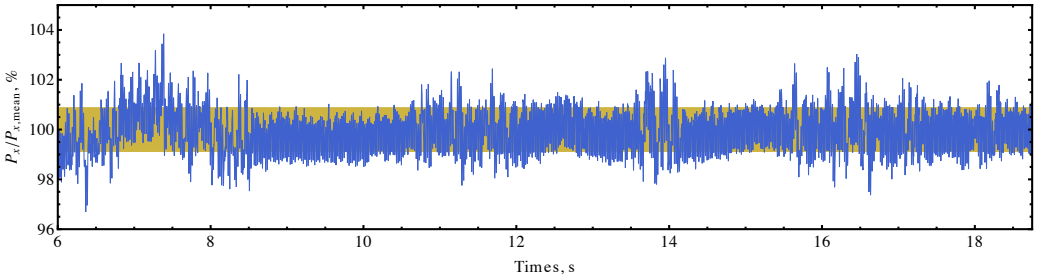

(b) 9.35 RPS

Figure 3: Variation of the thrust in time (22.5 M grid).

agreement with each other. Taking into account that the safety factor commonly used for the forces and moments variations in practical shaft calculations is taken a few times larger than that obtained from simple estimations, the discrepancy between the methods can be considered as insignificant. The situation with the horizontal AM_y and the vertical AM_z moment variations is more complicated. Results by the Veritec method substantially deviates from the results of the other methods. The estimation for the horizontal moment fluctuations around 2-3.2% percent has been obtained from hybrid methods and Scheme B approach, whereas the Wereldsma's estimation is around 7%. The vertical moment fluctuations is around 5% of the mean torque according to Wereldsma, Scheme B, whereas the Veritec method predicts up to 17 percent, which is more than three times as large as the others.

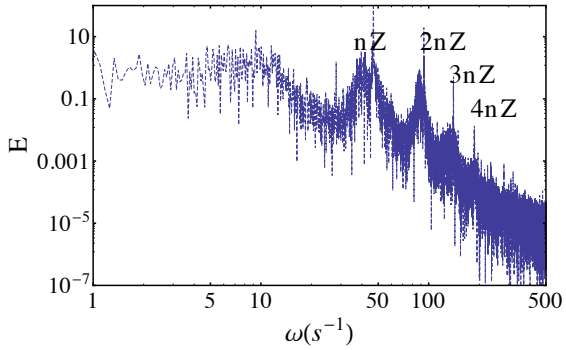

(a) Spectra of the thrust.

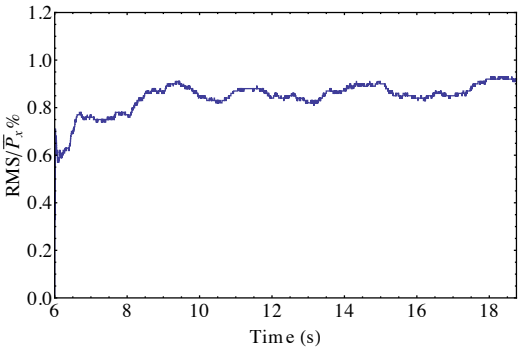

(b) Convergence of the thrust solution.

Figure 4: Spectra and convergence of the thrust solution obtained by hybrid model (22.5 M grid).

On the base of comparisons with CFD computations using modern hybrid methods one can conclude that the accuracy of predictions of standard deviations of forces and moments fluctuations on propellers provided by simple engineering methods like Wereldsma and Scheme B ones. can be considered as quite acceptable for practical purposes. The best agreement with CFD is attained for the Scheme B method. All engineering methods are not capable of predicting the peak loadings. Fig. 3 presents the time history of the thrust within 6 seconds. URANS computations with $k-\omega$ SST model show

regular periodic oscillations of small amplitude which is much less than that from hybrid method and engineering estimations. While the averaged propeller loadings and the standard deviations are reliably predicted by engineering methods the peak loadings on marine propellers of full bottomed ships can be detected only using hybrid techniques based on the combination of LES and URANS approaches. It can be supposed from the analysis of the literature [9] that the unsteady loadings are getting much larger during the maneuvering motions resulting in the damage of the shaft bearings. To our opinion, the LES or hybrid approaches are especially important for simulation of propeller hydrodynamics at transient motion conditions.

Fig. 4(a) presents the spectra of the thrust fluctuations. As seen five dominating blade passing frequencies up to $5nZ \sim 200$ Hz are resolved in our simulations. Fig. 4(b) shows standard deviations of thrust P_x versus time using 22.5M grids. As is shown the thrust standard deviations attain the mean value quickly in time.

Conclusion

The paper presents recent achievements in the development and application of the hybrid LES -URANS technique [1] for the prediction of the flow in the stern area and unsteady loadings on propellers of full bottomed ships. While our previous work [1] was dedicated to the calculations of the bare hull the focus of the present paper is the calculation of the whole system containing both the propeller and the hull with consideration of all interference effects. The unsteady loadings on the propeller of the KVLCC2 tanker have been calculated with numerical URANS and hybrid methods as well as with a few engineering approaches. On the base of comparison with the hybrid method results it is concluded that the accuracy of predictions of standard deviations of forces and moments fluctuations on propellers provided by simple engineering methods like Wereldsma and Scheme B ones can be considered as quite acceptable for practical purposes.

References

[1] Kornev, N., Taranov, A., Shchukin, E., & Kleinsorge, L. (2011). "Development of hybrid URANS-LES methods for flow simulation in the ship stern area." Ocean Engineering, 38(16), 1831-1838.

[2] Abbas N., Shevshuk I., Kornev N, Development and validation of a hybrid RANS-LES method for ship hydromechanics applications, NuTTS 2013: 16-th numerical towing tank symposium, Mülheim/Germany 2013.

[3] N. Abbas, N. Kornev, I. Shevchuk, P. Anschau, (2014). CFD prediction of unsteady forces on marine propellers caused by the wake nonuniformity and nonstationarity, submitted to Ocean Engineering.

[4] Voitkunski (Ed.), (1985). Handbook on ship theory. Vol. 1. pp. 564 – 572.

[5] Carlton, J. S., (2007). Marine Propellers and Propulsion. Butterworth - Heinemanns, Jordan Hill, Oxford OX2 8DP, USA.

[6] Noise and vibration Group, (1985). Vibration Control in Ships. VERITEC :Marine Technology Consultants (Norway), Oslo.

[7] Wereldsma, R., (1964). Propeller excited shaft and hull vibrations of single screw ships. Int. Shipbuilding Progress 11 (124), 547 – 553.

[8] Batrak, Y.A., Shestopal, V.P., Batrak, R.Y., (2012). Propeller hydrodynamic loads in relation to propulsion shaft alignment and vibration calculations. Proceedings of Propellers–Shafting 2012 Symposium, 10.1–10.14.

[9] Vartdal, B. J., Gjestland, T., Arvidsen, T. I., (2009). Lateral propeller forces and their effects on shaft bearings, First International Symposium on Marine Propulsion SMP09, Trondheim, Norway.

Shear Stress Effects in Cavitating Flows

Abolfazl Asnaghi, Andreas Feymark, Rickard E Bensow
abolfazl.asnaghi@chalmers.se, andreas.feymark@chalmers.se, rickard.bensow@chalmers.se
Department of Shipping and Marine Technology, Chalmers University of Technology, Gothenburg, Sweden

Cavitation has been categorized as the formation of vapour in a liquid when local static pressure of liquid falls below a critical pressure threshold. Based on the thermodynamic properties of the liquid, one can use the saturation pressure as the pressure threshold to estimate the inception and formation of cavitation. This definition, however, has some drawbacks. The thermodynamic saturation pressure is calculated in the conditions where the fluid is steady and in the equilibrium state. Therefore, the rupture of the liquid pocket is just due to the pressure tensile, and effects of shear stress caused by shear velocity are not included.

Some research has been done during the past decades to consider the effects of the shear stresses in the calculation of the pressure threshold [1-4]. Most of this was conducted in cavitating nozzle flows where the flow speed was very high and therefore the shear velocity magnitude was considerable [2]. In the current study the implementation of this approach in medium speed applications, e.g., cavitating propellers and foils are developed.

In what follows, concepts and derivation of the pressure threshold by considering the viscous shear stresses are presented and coupled with the transport equation model (TEM) for mass transfer modelling. For numerical simulation, the interPhaseChangeFoam solver of OpenFOAM open source package is modified and used. To validate the performed development, cavitating flow around the 3D twisted foil is performed. The Delft Twist11 foil, studied experimentally by Foeth [5, 6], generates cavitation which resembles propeller cavitation but in a more well defined and easily studied set up which makes it an attractive test case for evaluation of computational approaches for predicting cavitation.

The equations governing cavitating flows are the continuity, momentum, and mass transfer equations. In many practical problems related to the cavitation phenomena, temperature changes are negligible, and therefore the simulation of cavitation in isothermal condition will not have considerable effects on final results, and it is possible to neglect the energy equation. In the current study, a transport equation of volume fraction (TEM) is used to simulate distribution of the phases and the mass transfer between them. Both phases have been considered to be incompressible and isothermal which is a common approach also for cavitating flows in these flow regimes. The conservation equations of mass and momentum (in Cauchy format) for the effective fluid can be written as follows:

$$\frac{\partial \rho_m}{\partial t} + \frac{\partial \left(\rho_m u_i\right)}{\partial x_i} = 0 \tag{1}$$

$$\frac{\partial \left(\rho_m u_i\right)}{\partial t} + \frac{\partial \left(\rho_m u_i u_j\right)}{\partial x_j} = \frac{\tau_{ij}}{\partial x_j} + \rho_m g_i \tag{2}$$

The stress tensor in Newtonian fluids is conventionally written in the form of summation of pressure stress and shear stresses as below. In this derivation, it is assumed that the bulk viscosity of the fluid is equal to zero.

$$\tau_{ij} = -p\delta_{ij} + S_{ij} - \frac{2}{3}\mu \frac{\partial u_m}{\partial x_m}\delta_{ij} \tag{3}$$

$$S_{ij} = 2\mu D_{ij} \tag{4}$$

where p is the static pressure, μ the effective viscosity, S the viscous stress tensor, and D the deformation rate tensor (symmetric part of the velocity gradient), defined as $D_{ij} = \left(\partial u_i/\partial x_j + \partial u_j/\partial x_i\right)/2$.

For turbulence modelling, an implicit Large Eddy Simulation approach, ILES, is used [7-11]. The momentum equation in the LES model can then be written as:

$$\frac{\partial\left(\rho_m \overline{u_i}\right)}{\partial t}+\frac{\partial\left(\rho_m \overline{u_i}\,\overline{u_j}\right)}{\partial x_j}=-\frac{\overline{p}}{\partial x_i}+\frac{\partial}{\partial x_j}\left(\overline{S}_{ij}-B_{ij}\right)+\rho_m g_i \tag{5}$$

where the over bar denotes the low pass filtered quantities. In this equation, $B=\rho_m(\overline{u_i u_j}-\overline{u_i}\,\overline{u_j})$ is the subgrid stress tensor. In ILES, no explicit model is applied for *B*, instead the numerical dissipation is considered enough to mimic the action of *B* [7, 8]. As a result, for the momentum convection term, a blended scheme is used to provide appropriate numerical diffusion in the solution procedure.

In the TEM approach, the spatial distribution of water phases is specified using the volume fraction function. Based on the vapour volume fraction, mixture density and mixture viscosity are defined as Equation (6), where here alpha is the vapour volume fraction:

$$\rho_m=\alpha_v\rho_v+(1-\alpha_v)\rho,\qquad \mu_m=\alpha_v\mu_v+(1-\alpha_v)\mu_l \tag{6}$$

$$\frac{\partial\alpha_v}{\partial t}+\frac{\partial\left(\alpha_v u_i\right)}{\partial x_i}=S_\alpha \tag{7}$$

The source term of the vapour volume fraction equation, Equation (7), presents the rate of phase change between vapour and liquid phases. Different models have been proposed to represent the phase change rate, S_α, based on the fluid properties as well as the local flow properties. In the current study, the mass transfer model proposed by Sauer [12] is used, Equation (8), where average nucleus per liquid volume is set to $n_0=10^8$, and initial nuclei radius is $d_{Nuc}=10^{-4}$.

$$S_\alpha=sign(P_{sat}-P_{threshold})\frac{n_0}{1+n_0\frac{4}{3}\pi R^3}4\pi R^2\sqrt{\frac{2\left|P_{threshold}-P\right|}{3\rho_l}} \tag{8}$$

Using the saturation pressure as the pressure threshold for phase change in the cavitating flows is based upon the liquid rupturing at the static or quasi-static conditions. In these conditions, the static pressure in the major part of the liquid is much larger than the viscous shear stresses. Although this estimation, using the saturation pressure as the pressure threshold, has been used widely in numerical simulation of cavitation, it does not take into account the effects of the shear stresses in the liquid rupturing and initiating phase change [13, 14].

Therefore, in order to consider the viscous stresses in the liquid rupturing, the maximum eigenvalue of the stress tensor should be considered as the criteria on whether the fluid withstands rupturing or phase change, Equation (9). Note that in a stationary fluid, the eigenvalues of the stress tensor are the same, and equal to the static pressure.

$$\max(\tau_{ij})<p_{saturation} \tag{9}$$

$$\tau_{ij}=-p\delta_{ij}+S_{ij}=\begin{bmatrix}-p+S_{11} & S_{12} & S_{13}\\ S_{21} & -p+S_{22} & S_{23}\\ S_{31} & S_{32} & -p+S_{33}\end{bmatrix} \tag{10}$$

As it can be seen from Equation (10), calculation of the eigenvalues of the stress tensor is not an easy task and demands a significant computational effort. To simplify the calculation, one can use the same methodology used in the turbulence models here where the maximum viscous stress tensor is modelled by shear strain rate:

$$\dot{\gamma}=\sqrt{2D_{ij}D_{ij}} \tag{11}$$

Therefore, the magnitude of stress tensor in its principal coordinates can be estimated by the Equation (12):

$$\left|\tau_{ij}\right| = \left|-p\delta_{ij} + S_{ij}\right| \approx \left|-p\delta_{ij} + \mu\dot{\gamma}\delta_{ij}\right| \tag{12}$$

Using this simplification, the pressure threshold that determines the onset of cavitation in the flowing fluid can be expressed as:

$$p - \mu\dot{\gamma} \le p_{saturation}, \quad p_{threshold} \simeq \mu\dot{\gamma} + p_{saturation} \tag{13}$$

Obviously, this added term is important if either shear strain rate or effective viscosity is large enough, and comparable with the static pressure. For the flow around the foils, this is the case in the leading edge region, and for the flow around the propellers this is the case both in the tip and leading edge regions.

The geometry of the hydrofoil consists of a NACA0009 profile, with chord length, C ,equal to 150 mm, that has a spanwise varying angle of attack, ranging from -2 degree at the cavitation tunnel wall to 9 degree at the centre line and then back to -2 symmetrically with respect to the centre plane, with a total span of two chord length. Taking advantage of the symmetry only half of the domain is considered for numerical simulation. The domain extends 7C in the streamwise direction, starting 2C upstream of the leading edge and ending 4C behind the trailing edge. In the vertical direction, the domain extends 2 C, with the hydrofoil mounted in the centre.
The mesh consists of 2.7 million hexahedral cells. It has higher resolution near the leading edge where the gradients of the velocity and pressure are higher. Cell height of the near wall cell is measured to be $y^+ = 5$ on the most part of the suction side of the foil, according to the converged ILES solution of the wetted flow. In Figure (1), the hydrofoil and the mesh distribution are presented.

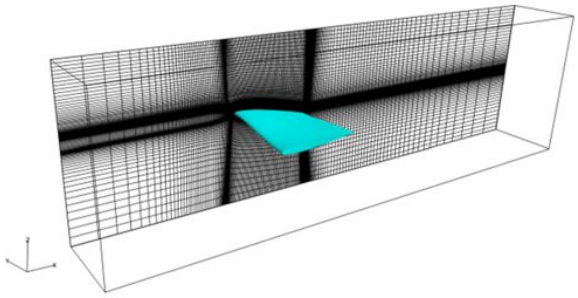

Figure 1: Computational domain used for numerical simulation of cavitation around Twist11

Standard inflow boundary condition is used as the inlet where the flow velocity is set equal to 6.97 m/s. At the outflow boundary a fixed pressure of 29kPa is used, regarding the outlet cavitation number equal to 1.07. At the upper and lower walls, a no-slip boundary condition is employed. Symmetry plane is used at the centre of the tunnel, and a no-slip condition is specified on the hydrofoil surface. The simulation is started with high outlet pressure which is gradually decreased to reach the specified outlet cavitation number.

One drawback of the TEM is that the final results can be sensitive to the coefficients of the mass transfer model. These coefficients mimic the phase change relaxation time (PCRT), and in the case that they are not set in an appropriate way to represents the flow nature, the cavity size and pressure distribution could be either over estimated or underestimated. Results shown in Figure (2a) exemplify results where the cavity size is under predicted. In this figure, Cc represents the condensation coefficient, and Cv represents the vaporization coefficient. Comparing to the experimental data, Figure (2d), it can be seen that both the cavity width at the leading edge and also the cavity volume are underestimated. Looking at the pressure distribution of this case, Figure (3a), shows that there is a negative pressure at the leading edge. This indicates that the mass transfer model was not able to use this potential to produce the vapour. In other word, in this case the vapour production relaxation time is set bigger than the flow time scale at the leading edge. This has led to that the liquid pockets

do not have enough time (comparing to the time they pass through the negative pressure regions) to transfer into vapour.

It has been stated that in the cavitating flow the production coefficient itself is large, as high as possible according to [15], to create near-instantaneous evaporation. The destruction term, however, allows for some retardation in the condensation. Therefore, the vaporization relaxation time scale should be set very small compared with the flow time scale which means using very high value for Cv, Figure (2b). Instantaneous vaporization means that the minimum pressure should be near the pressure threshold. So, for this case, Cv is set equal to 4000 which gives the minimum pressure close to the pressure threshold, Figure (3b).

Comparing Figure (2b) with experimental data indicates that using appropriate PCRT scale will provide more accuracy in predicting both the cavity width and cavity volume. Another advantage of using accurate PCRT is the location of the cavitation inception. In Figure (2a), the cavity starts at the 2.4% chord length after leading edge while in Figure (2b) cavity starts right at the leading edge which better matches the experimental results. Although in Figure (2b) the width of the cavity is predicted with reasonable accuracy, the volume of the cavity is still much lower than the experimental content, especially in the central region of the foil close to the leading edge.

(a) Cc=Cv =1, $p_{threshold} = p_{saturation}$

(b) Cc=1, Cv =4000 $p_{threshold} = p_{saturation}$

(c) Cc=1, Cv =4000 $p_{threshold} = \mu\dot{\gamma} + p_{saturation}$

(d) Experimental data

Figure 2: Comparison between numerical results and experimental data of cavitation around Twist11

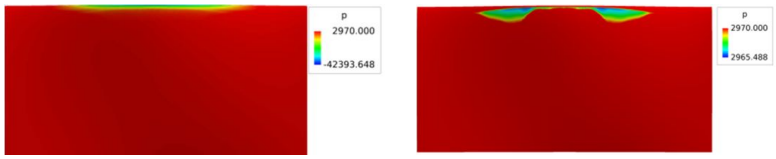

(a) Cc=Cv =1 $p_{threshold} = p_{saturation}$

(b) Cc=1, Cv =4000 $p_{threshold} = p_{saturation}$

Figure 3: Pressure distributions with different Cv values for cavitation around Twist11

In Figure (2c), numerical result of the modified pressure threshold based on the viscous stresses is presented. Comparison of Figure (2) panels (b) and (c) shows that the cavity width is not affected by this modification. The main change is the size of the separated cavity-vortex, and also the shape of the cavity at the centre parts, where the velocity gradients are very high comparing to the other regions.

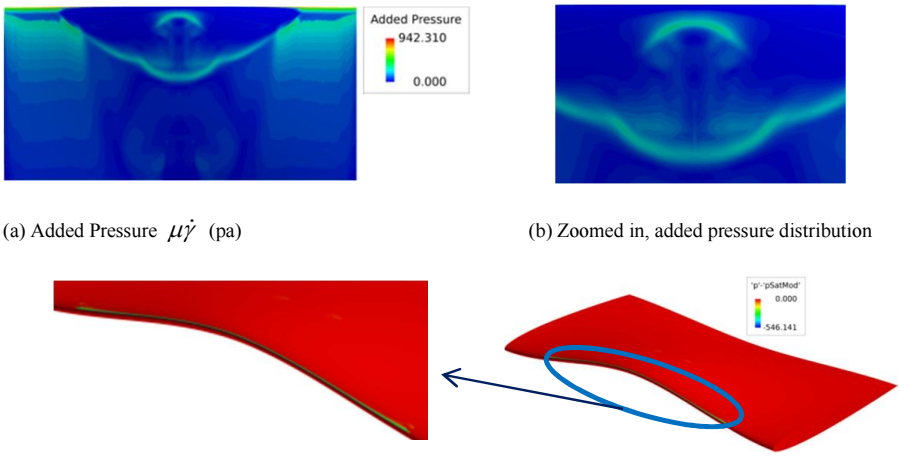

(a) Added Pressure $\mu\dot{\gamma}$ (pa)

(b) Zoomed in, added pressure distribution

Figure 4: Pressure distributions in different numerical settings for cavitation around Twist11

The pressure distribution of this case is however a little tricky since there is no fixed pressure threshold. In Figure (4a), the added pressure due to the consideration of viscous stresses is plotted. It can be seen that on the surface of the foil the added pressure is higher where the velocity strain is higher. Another issue is the effects of the symmetry boundary on the results. It can be seen from Figure (4b) that using symmetry boundary at the middle has added an extra constraint, seemingly influencing the solution. So, it seems necessary to investigate effects of this boundary in future work.

Looking at the distribution of difference between static pressure and pressure threshold which works as the potential for cavitation generation shows that even by using high value for Cv=4000, there are still some potential for cavitation formation which has not used. Comparing the magnitude of this unused potential (546 pa) with results presented in Figure (3), (5 pa), indicates that using constant coefficient for mimicking the phase change relaxation time is not ideal. One suggestion to overcome this would be to consider the correlation between the local flow time scales and the phase change relaxation time. However, this issue demands further investigation.

In this paper, numerical simulation of the unsteady cavitating flow around the Delft Twist11 foil is presented and compared with experimental data. Pressure threshold, which is the phase change criteria in the cavitating flows, is modified to consider effects of the viscous shear stresses in the liquid pocket rupturing and cavitation formation. Current results show that considering the viscous stress would significantly improve the accuracy of cavitation content prediction, especially at the regions where the velocity gradients are high enough. Moreover, obtained results indicates that using fixed phase change relaxation time scale would increase deviation between numerical results and the experimental data in the case that phase change phenomena interacts strongly with flow structure. In such conditions, the phase change will have different time scale depending on the local flow properties.

ACKNOWLEDGEMENTS

Financial support of this work has been provided by Rolls-Royce Marine through the University Technology Centre in Computational Hydrodynamics hosted at the Dept. of Shipping and Marine Technology, Chalmers. Computational resources have been provided by Chalmers Centre for Computational Science and Engineering, C3SE.

REFERENCES

[1] Martynov, S., 2005, "Numerical Simulation of Cavitation Process in Diesel Fuel Injectors," Ph.D. thesis, University of Brighton, Brighton.

[2] S. Som, S. K. Aggarwal, E. M. El-Hannouny and D. E. Longman, Investigation of Nozzle Flow and Cavitation Characteristics in a Diesel Injector, Journal of Engineering for Gas Turbines and Power, Volume 132, Issue 4, 2010
[3] Y.T. Shen, P.E. Dimotakis, Viscous and nuclie effects on hydrodynamic loading and cavitation of a NACA 66 (MOD) foil section, Journal of fluid engineering, ASME, 1989
[4] Youcef, AIT BOUZIAD. Physical modelling of leading edge cavitation: computational methodologies and application to hydraulic machinery. Fensh: Thesis, 2006.
[5] Foeth, E.J. (2008). 'The structure of three-dimensional sheet cavitation'. PhD Thesis, TU Delft.
[6] Foeth, E.J. & Terwisga, T.v. (2006). 'The structure of unsteady cavitation. Part I: Observation of an attached cavity on a three-dimensional hydrofoil'. 6th International Symposium on Cavitation, Wageningen, The Netherlands.
[7] Bensow, R.E. & Bark, G. (2010). 'Implicit LES predictions of the cavitating flow on a propeller'. J. Fluids Engng. 132.
[8] Lu, N.X., Bensow, R.E. & Bark, (2010) 'LES of unsteady cavitation on the Delft twisted foil'. J. Hydrodynamics 22(3).
[9] Bensow R.E. (2011). 'Capturing Secondary Cavitation A Step Towards Numerical Assessment of Cavitation Nuisance'. Ship Technology Research 58(2).
[10] Huuva, T. (2008). 'Large eddy simulation of cavitating and non-cavitating flow'. PhD Thesis, Chalmers university of Technology, Gothenburg
[11] Bensow, R.E & Fureby, C. (2007). 'On the justification and extension of mixed models in LES'. J. Turbulence 8(54).
[12] Sauer, J. (2000). 'Instation¨aren kaviterende Str¨omung – Ein neues Modell, baserend auf Front Capturing (VoF) and Blasendynamik'. PhD Thesis, Univ. Karlsruhe.
[13] Daniel D. Joseph, Cavitation and the State of Stress in a Flowing Liquid, Fourth International Symposium on Cavitation, CAV2001
[14] Daniel D. Joseph, Cavitation in a Flowing Liquid, Phys. Review, E., Volume 51, issue 3, 1995.
[15] Wikstrom, N. & Bark, G. 2003 Large Eddy Simulation for cavitating submerged objects. In Eighth International Conference on Numerical Ship Hydrodynamics.

Ship wake field analysis using a coupled BEMt-RANS approach

Charles Badoe[1*], *Alexander Phillips*[1] and *Stephen R Turnock*[1]

[1] Faculty of Engineering and the Environment, University of Southampton, Southampton, UK
Email: cb3e09@soton.ac.uk

** Corresponding author*

1. Introduction

The prediction of a ship's wake field and self-propulsion capabilities has traditionally been centered on experiments; however with the advancement in modern computing power, this can be achieved through the use of computational methods. An advantage with the use of CFD is its ability to provide insight into flow characteristics close to the wall, which are difficult to obtain through experiments. The most interesting and challenging aspect of using CFD in this analysis, is the influence of the propeller action and the unsteady hydrodynamic of the rudder working in the propeller wake. One approach to address the problem is to discretize the ship, propulsor and the rudder using unsteady RANS computations (Carrica et al., 2011). Due to the small time steps and high computational cost involved, simulations are often performed using representative propeller models or body force method. The level of complexities in the body force propeller approach varies from prescribing the body forces, Badoe et al., (2012), Phillips et al., (2010), through to coupling a more complex propeller performance code which accounts for the non-uniform inflow at the propeller plane, Phillips et al., (2009). There are several self-propulsion computations using body force propeller models reported in the literature. Banks et al., (2008, 2010) performed a RANS simulation of multiphase flow around the KCS hull form using a propeller model with force distribution based on the Hough and Ordway thrust and torque distribution (Hough and Ordway, 1965). Simonsen and Stern, (2003) coupled a body force propeller model based on potential theory formulation in which the propeller was represented by bound vortex sheets on the propeller disk and free vortices shed from the downstream of the propeller to a RANS code to simulate the manoeuvring characteristic of the Esso Osaka with a rudder.

In the present work an investigation is carried out into the sensitivity with which the wakefield of a container ship in calm water is resolved using a coupled BEMt-RANS sectorial approach.

2. Theoretical approach

2.1. RANS approach

The flow generated around the BEMt propeller model and hull can be modeled by the unsteady Reynolds averaged Navier-Stokes equations. Within the assumption of an incompressible fluid, the set of equations may be written in the form:-

$$\frac{\partial \overline{U_i}}{\partial x_i} = 0 \qquad [1]$$

$$\frac{\partial \overline{U_i}}{\partial t} + \frac{\partial \overline{U_i U_j}}{\partial x_j} = -\frac{1}{\rho}\frac{\partial \overline{P}}{\partial x_i} + \frac{\partial}{\partial x_j}\left\{\nu\left(\frac{\partial \overline{U_i}}{\partial x_j} + \frac{\partial \overline{U_j}}{\partial x_i}\right)\right\} - \frac{\partial \overline{u'_i u'_j}}{\partial x_j} + \overline{f_i} \qquad [2]$$

where x_i represents the Cartesian coordinates (X, Y, Z) and U_i are the Cartesian mean velocity components ($\overline{U_x}$, $\overline{U_y}$, $\overline{U_z}$). The Reynolds stress is expressed as ($\overline{u'_i u'_j}$) and must be modeled using an appropriate turbulence model.

2.2. BEMt propeller model and coupling methodology

BEMt is a method of modelling the performance of tidal turbines, (Mikkelsen, 2003) and ship propellers, (Phillips, 2009). The method combines both the blade element theory and the momentum theory. By combining these two theories, some of the difficulties involved in the calculation of the induced velocity of the propeller are addressed. Solution to this problem can be achieved if the part of the propeller between r and (r+∂r) is analysed by matching forces generated by the blade elements, as 2D lifting foils to the momentum changes occurring through the propeller disc between these radii. An actual propeller is not uniformly loaded as assumed by Rankine and Froude actuator disc model, thus to analyze the radial variation of loads along the blade the flow field is divided into radially independent annulus stream tube.

An existing BEMt code (Molland and Turnock, 1996) was modified and coupled to a RANS solver, whereby within the RANS mesh the propeller is represented as a cylindrical domain with diameter equal to that of the propeller diameter, D and a length of 0.1D. The propeller is adapted to the hull wake by employing a sectorial approach where the propeller domain is sub divided into a series of nC circumferential, and nR radial slices along the blade. An example of a BEMt mesh is presented in Fig. 1. A brief coupling procedure is presented as follows:

1. A steady state RANS computation is first performed with the body force terms set to zero.
2. The resulting local nominal wake fraction is determined for each radius by calculating the average mean circumferential velocity at the corresponding radius. This procedure captures the influence of the rudder and hull on the flow through and across the propeller disc.

$$W_T{}'' = \frac{1}{2\pi r} \int_0^{2\pi} \left(1 - \frac{U}{U_a}\right) r \, \partial\theta \qquad [3]$$

   where U signifies the axial velocity at a given nC circumferential, and nR radial location.
3. The BEMt propeller code iterates to find the local thrust and torque for nR radial and nC circumferential locations based on the local nominal wake fraction, the inflow speed and the rps.
4. The local thrust and torque are assumed to act uniformly over the circumference corresponding to each radial slice. They are then converted into axial and tangential momentum sources and distributed over the nR radial and nC circumferential slices respectively.
5. The Simulation is then started from the naked hull and rudder solutions but now with the added momentum sources until convergence is achieved.
6. The effective wakefield is defined by repeating steps 2 to 5 to find the total wakefield then subtracting the propeller induced velocities calculated from the BEMt code.

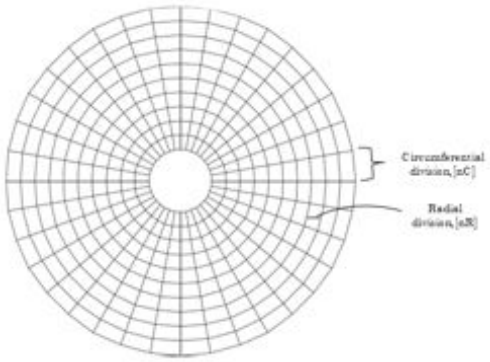

Fig. 1: BEMt propeller mesh showing radial, nR, and circumferential, nC, subdivisions

3. Ship model wake field analysis case study

3.1. Details of experiment

The case considered is the self-propelled KRISO container ship (see Fig. 2 and Table 1) in calm water conditions (Larsson et al., 2010). The MOERI scale KCS hull model, designed at KRISO and tested at SRI, (Fujisawa et al., (2000) was used for this study. Measurements of local velocity field on the MOERI KCS hull was carried out at SRI's towing tank (400m long x 18m breadth x 8m depth) at Froude number Fn=0.26 under even keel conditions. The rate of the propeller model was set at 9.5rps and self-propulsion condition at "ship point". Full details of the experimental conditions and data can be found at Fujisawa et al., (2000).

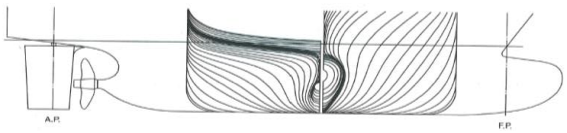

Fig. 2. Body plan and side profile of the KCS ship model, source: Fujisawa et al., (2000).

3. Simulation setup

Numerical solution of equations (1) and (2) was carried out using the open source RANS solver OpenFOAM, which is designed to solve problems in mechanics of continuous mediums; see Jasak (1996)

for more details on introduction and numeric used in OpenFOAM. The steady RANS equations were solved using a cell centered finite volume method (FVM). Discretization of the convection terms was achieved using Gauss linear second order upwind and the diffusion terms were treated using the central difference scheme. The SIMPLE algorithm was used for the pressure-velocity coupling. The pressure correction equation was under relaxed with a factor of 0.3, which was found as a compromise between stability and convergence speed.

The SST k-ω model has been successfully used for this purpose of hull-propeller-rudder interaction and wakefield analysis, (Larsson et al., 2010) making it a natural choice for the study discussed herein.

Table 1: Principal dimensions of the KCS model and propeller.

Dimensions	Full scale	Model scale MOERI
Scale	1.00	31.5994
L_{PP} (m)	230.0	7.2785
B_{WL} (m)	32.2	1.0190
D (m)	19.0	0.5696
T (m)	10.8	0.3418
Displacement (m^3)	52030	1.6497
Rudder type	SB horn rudder	-
Lat. area (m^2)	54.45	-
Propeller type	FP	FP
Number of blades, N	5	5
Diameter (m)	7.9	0.250
P/D at 0.7R	0.997	0.9967
Ae/Ao	0.800	0800
Rotation	Right	Right
Hub ratio	0.180	0.1800

4.1. Boundary Conditions

The inflow and outflow plane were located 1.2LPP in front of and 2.5LPP behind the hull respectively. The hull, rudder and propeller were modelled as no-slip walls, the sides and bottom of the domain were treated using slip boundary condition. The influence of free surface was not included in the simulation due to the increase cost in computation hence the free surface was modelled with a symmetry plane.

4.2. Grid generation

Unstructured, predominantly hexahedral grids with local refinements around no slip walls were used in the study. All grids were created using blockMesh and snappyHexMesh utilities forming part of the OpenFOAM libraries. The grids were congregated in the regions of the stern, bow, near the hull surface and the free surface. Ten to twelve elements were used to capture the boundary layer of the hull and rudder yielding an approximate y^+ of 60 for the hull and 30 for the rudder. The total number of grids used was approximately 5 million. Fig. 3 shows the mesh resolution for the bow and stern.

Fig. 3. KCS bow and stern mesh.

5. Results

5.1 Propeller Open water prediction

The open water performance shown in Fig. 4 calculated from the BEMt propeller code is compared with values from SRI. The trend in KT plots highlights the good agreement of the predicted thrust of the propeller. The BEMt model showed an over prediction in torque ($10K_Q$), and the discrepancies increased as the propeller advance coefficient (J) reduces. This

is not unusual especially when using momentum theory in the numerical prediction of propeller open water conditions. This has also been reported by Uto, (1993) who carried out RANS simulations involving marine propellers. These over predictions might be unavoidable due to experimental conditions such as tunnel wall, inflow speed non-uniformity and hub and boss configurations which do not conform to CFD simulations. For the effective advance speed of interest for this work (nominal J=0.7) the agreement for KT and 10 KQ was excellent with difference of less than 4%.

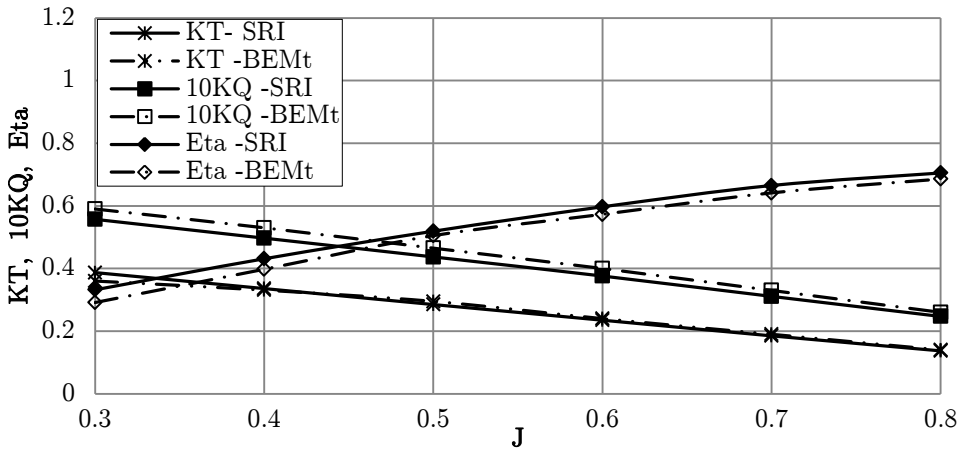

Fig. 4. Comparison of propeller characteristics in open water. Experiments data Fujisawa et al., (2000).

5.2 Nominal wakefield predictions

The prediction of a ships nominal wakefield is important since it provides a good initial estimate for the BEMt-RANS propeller model. The local velocity field without the working propeller model at an even keel 0.25D behind the propeller plane is compared with that of SRI in Fig. 5. The symmetry with respect to the ships centreline is well predicted compared to experiments up to u ≈0.7. The diffusive contour lines of u ≈0.8&0.9 at the top part of the propeller outer radius (both port and starboard) are likely the result of insufficient mesh resolution around that region. The distortion in the velocity, i.e. the "hook shape" is very small compared to that of the experiment. Other distinct flow features such as the weak vortex flow found on both sides near the upper corner of the propeller boss and the downwards flow found near the centreline above the shaft were accurately predicted. The averaged nominal wake 1-wn was 1% over estimated at 0.720 compared to SRI's value of 0.712.

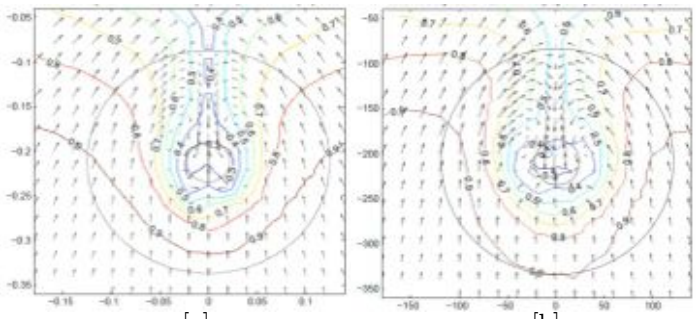

[a] [b]

Fig. 5: Local velocity field (u contour & v-w vectors) 0.25D behind propeller plane (x/L=0.491), Fr 0.26 without propeller [a] Fine grid, [b] Experiment, SRI.

5.3 Sensitivity studies

Sensitivity studies were carried on the BEMt model to determine the number of radial nR, and circumferential, nC, subdivisions to effectively capture the wake field with the working propeller. A series of radial subdivisions, nR =10, 20, 40 and circumferential, nC subdivisions from 10-360 were used. It can be seen from the convergence plot in Fig. 6 that nC converges at about 100 subdivisions. The plots in Fig. 7 were then created by fixing nC to 180 and the varying nR. The plots were taken with the working propeller. It can be seen from the plots that when nR > 20 the wake is smeared out. Not enough thrust is generated by the BEMt beyond this point. The reason for this behaviour may is yet to be established, nevertheless the wake field is predicted reasonably well by using nR=20 and nC =180

(Fig. 7b). By comparing Fig. 7b to that of a BEMt model which assumes an average wakefield as in Fig. 7d, the superiority of the sectorial approach is clearly illustrated. The sectorial approach is seen to be more consistent with a real propeller hydrodynamic influence on the inflow (Fig. 7e). The approach does not use an average circumferential distribution but rather takes into account the local thrust and torque at each radial and circumferential location in the propeller plane. This results in an asymmetry in the flow field.

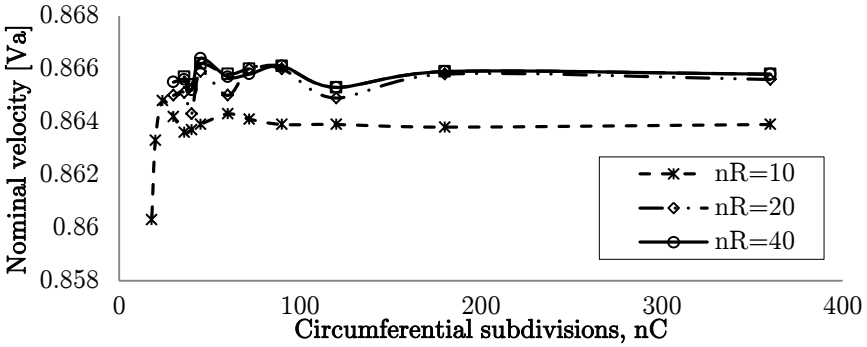

Fig.6 : Convergence of nominal velocities for various radial, nR, and circumferential, nC, subdivisions.

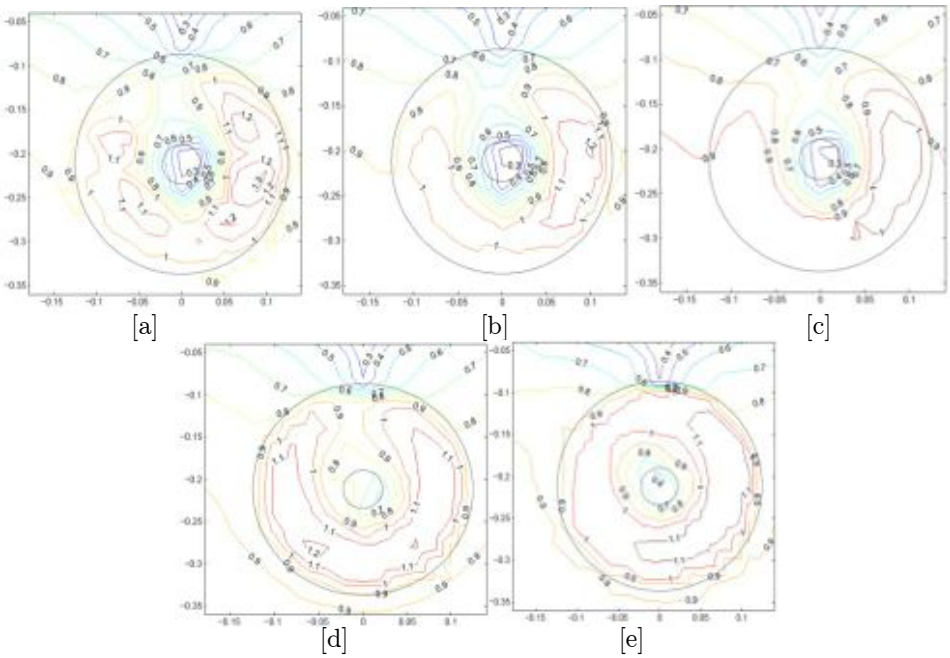

Fig. 7: BEMt sensitivity studies for local velocity field (u contour) 0.25D behind propeller plane (x/L=0.491), Fr 0.26 with [a] nR =10 [b] nR =20 [c] nR =40 [d] Averaged wake [e] Experiment, SRI, at n_p = 9.5rps.

5.3 Self-propulsion parameters

The self-propulsion parameters shown in Table 2 also compares well with the experiment. It should however be borne in mind that propeller forces are dependent on the inflow conditions (bare hull wake) hence a slight over-prediction in the hull wake will result in an increased inflow velocity to the propeller, causing an increase in propeller forces hence the over-prediction in the thrust and torque values.

Table 2: Self-propulsion parameters for KCS in fixed condition.

Parameter	BEMt	SRI	*E*%D
K_T	0.1830	0.1703	+7%
K_Q	0.0315	0.0288	+9%

NB: Tabulated results obtained using nR =20& nC =180 as shown in Fig. 6b.

6. Conclusions

A BEMt-RANS coupling methodology has been outlined to analyse the wakefied of a containership in calm water conditions. These initial results have indicated that the sectorial approach described has much merit for capturing many aspects of wakefield of ships in calm water conditions. The wakefield was poorly predicted when nR>20. The reason for this behaviour is yet to be established but one possible reason might be due to the mapping of data from the BEMt to the RANS mesh. There is still much scope for detailed analysis of the sectorial approach and the empirical relations used in the BEMt code.

References

Badoe, C., Phillips, A.B. and Turnock, S.R., 2012. Initial numerical propeller rudder interaction studies to assist fuel efficient shipping, in 'Proceedings of the 15th Numerical Towing Tank Symposium, 7-9 October, Cortona Italy'.

Banks, J., Phillips, A.B., Turnock, S.R. and Bull, P.W., 2010. RANS simulations of multiphase flow around the KCS hull form. In, Gothenburg 2010; A workshop on CFD in ship hydrodynamics 08-10 December.

Carrica, P.M., Alejandro, M., and Stern, F., 2011. Full scale self-propulsion computations using a discretized propeller for the KRISO container ship KCS. Journal of computers and fluids marine science and technology, 51, pp.35-47.

Fujisawa, J., Ukon, Y., Kume, K., and Takeshi, H., 2000. Local velocity measurements around the KCS Model (SRI M.S. No. 631) in the SRI 400m Towing Tank, Ship Perf. Div. Rep. No. 00-003-2, SRI, Tokyo, Japan.

Goldstein, S., 1929. On the Vortex Theory of Screw Propellers, Proc. of the Royal Society, 123, 440, (A).

Hough, G.R. and Ordway, D.E., 1965. The generalized actuator disc. Developments in theoretical and applied mechanics, 2, 317-336.

Jasak, H., 1996. Error analysis and estimation for the finite volume method with applications to fluid flows, Ph.D thesis, Imperial College of Science, Technology and Medicine, University of London.

Larsson, L., and Zou, L., 2010. CFD prediction of local flow around the KVLCC2 tanker in fixed condition. A Workshop on Numerical Ship Hydrodynamics: The Gothenburg 2010 Workshop December 8-10, 2010.

Menter, F.R., 1994. Two-equation eddy viscosity turbulence models for engineering applications. AIAA journal, 32(8), pp.1598–605.

Mikkelsen, R., 2003. Actuator Disc Methods Applied to Wind Turbines, Ph.D thesis, University of Denmark.

Molland, A.F., and Turnock, S.R., 1996. A compact computational method for predicting forces on a rudder in a propeller slipstream. Transactions of the Royal Institution of Naval Architects, 138, pp.227–244.

Phillips, A.B., Turnock, S.R. and Furlong, M.E., 2008. Urans simulation of static drift and dynamic manoeuvres of the kvlcc2 tanker. In. SIMMAN 2008: workshop on verification and validation of ship manoeuvring simulation methods, Lyngby, Denmark, 13-17 April 2008.

Phillips, A.B., Turnock, S.R. and Furlong, M.E., 2009. Evaluation of manoeuvring coefficients of a self-propelled ship using a blade element momentum propeller model coupled to a Reynolds averaged Navier-Stokes flow solver. *Journal of ocean engineering*, 36(15-16), pp.1217-1225.

Phillips, A.B., Turnock, S.R. and Furlong, M.E., 2010. Accurate capture of rudder-propeller interaction using a coupled blade element momentum-RANS approach. Journal of Ship Technology Research, 57(2), pp.128–139.

Simonsen, C., and Stern, F., 2003. Verification and Validation of RANS manoeuvring simulation of Esso Osaka: effects of drift and rudder angle on forces and moments. Journal of Computers and Fluids, 32, pp.1325-1356.

Uto, S., 1993. Computation of incompressible flow around a marine propeller, Journal of Naval Architecture 173.

Developing tools for assessing bend-twist coupled foils

J. Banks*, L. Marimon Giovannetti, S.R. Turnock, S.W. Boyd
*J.Banks@soton.ac.uk

1 Introduction

There are many applications where the ability of a foil to passively adapt to the experienced fluid loading could be advantageous. This includes wind or tidal turbine blades, high performance hydrofoils for sailing yachts, or marine propellers. If these foils could naturally adjust their angle of attack as the flow speed varies their efficiency could be improved without the need for active control systems (Nicholls-Lee & Turnock, 2007). The use of composite materials provides the opportunity to tailor the bend twist coupling of a structure to achieve these goals (P. Veers & Bir, 1998).

To allow such foils to be designed and assessed numerical tools such as finite element analysis (FEA) and computational fluid dynamics (CFD) will need to be coupled together in fluid-structure interaction (FSI) simulations, but currently there is a lack of a full coupling between the two for passive adaptive composites. In isolation there are many methods for the validation of FEA and CFD. However, there is a lack of experimental validation data for FSI investigations.

This paper details a set of experimental tests conducted on a NACRA F20 curved dagger board in the University of Southampton's RJ Mitchell wind tunnel. Digital image correlation (DIC) was used to measure the full field deflection at the board tip and particle image velocimetry (PIV) was used to capture the position and strength of the tip vortex. Preliminary CFD simulations of the rigid experimental geometry are compared to this data.

2 Experimental Data

The experiments were conducted in the 3.5 m x 2.4 m RJ Mitchell wind tunnel at the University of Southampton. This closed circuit tunnel operates at wind speeds of 4 to 40 ms^{-1} with less than 0.2% turbulence. A six component Nutem load cell balance is mounted on a turntable in the tunnel roof. This allows forces and moments to be measured in the turntable axis system about the balance centre 1.27 m below the tunnel roof. Figure 1 shows the cross-section of the wind tunnel at the position of the dynamometer.

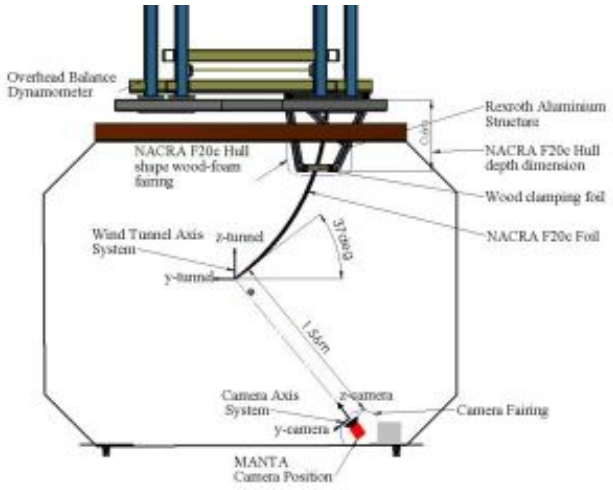

Figure 1 - Wind tunnel working section diagram.

2.1 Aerodynamic forces

The forces were measured at 1kHz and converted into the tunnel axis system to provide sideways lift coefficient (C_L), vertical force coefficient (C_Z) and drag coefficient (C_D).

An initial angle of attack sweep was completed to determine the zero lift condition of the board, and therefore the true zero degrees angle of attack (AoA) position allowing for board misalignment within the clamping structure. This determined the board was misaligned by 1.44 degrees from the turntable.

2.2 Board deflection

A stereo DIC system was set up in the wind tunnel allowing 3D deflection data to be captured within a 0.3x0.3m field of view at the board tip.

A background to this methodology and full details of this experimental setup can be found in (Giovannetti, Banks, Soubeyran, Turnock, & Boyd, 2014)

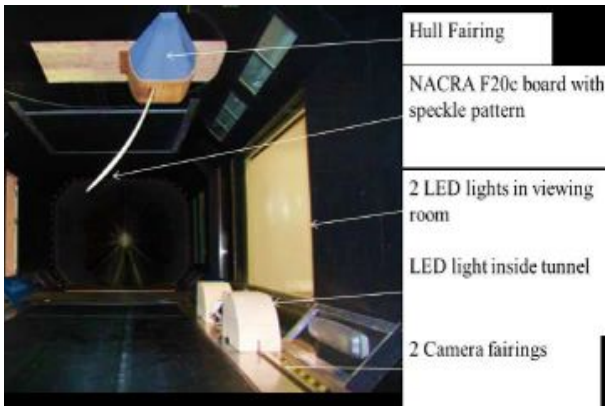

Figure 2 - DIC set up

2.3 Flow field measurement

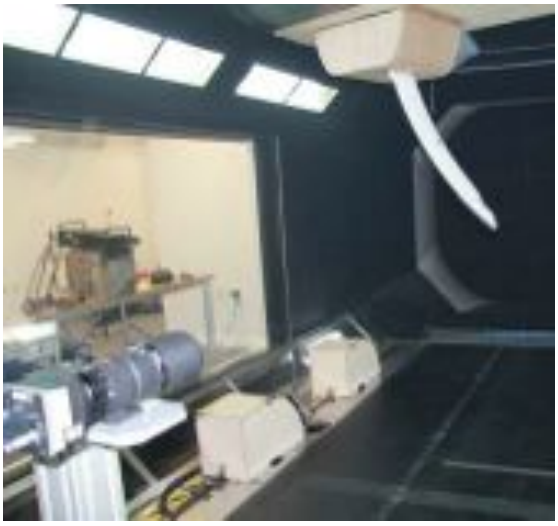

Figure 3 - PIV set up.

Particle image velocimetry allows two components of the fluid velocity to me measured on a plane using a single camera. Two images are taken of particles moving through a thin laser sheet, allowing the particle displacement, and therefore velocity, to be calculated (Raffel, Willert, Wereley, & Kompenhans, 2007).

A laser sheet was set up one chord (0.25m) behind the trailing edge of the foil and perpendicular to the flow direction. A 4 MP camera was positioned directly behind the board tip, with a 200mm Nikon lens providing a 0.2x0.2m field of view. Seeding particles were introduced into the tunnel using a smoke machine on a timer. The time between the two image frames was set to ensure that the majority of particles were observed in both frames. Then a series of 200 pairs of images were taken at a constant frame rate.

Two different angles of attack, 8.5 and 18.5 deg, were investigated at a range of wind speeds. The images were processed using the LaVision software DaVis.

3 Numerical simulations

Preliminary CFD investigations have focused on replicating the experimental results from the wind tunnel. Initially this has focused on simulating the un-deformed board geometry, along with the hull fairing. This will allow the impact of the blade deflection to be assessed by also simulating the deformed geometry at a later date.

3.1 Theoretical approach

A finite volume method is adopted for a single phase fluid. This method is derived from the surface integration of the conservative form of Navier Stokes' equations over a control volume. The incompressible Reynolds averaged Navier-Stokes (RANS) equations, written in tensor form, are defined as

$$\frac{\partial(\rho U_i)}{\partial t}+\frac{\partial(\rho U_i U_j)}{\partial x_j}=-\frac{\partial P}{\partial x_i}+\frac{\partial}{\partial x_j}\left[\mu\left(\frac{\partial U_i}{\partial x_j}+\frac{\partial U_j}{\partial x_j}\right)\right] - \frac{\partial}{\partial x_j}\left(\rho\overline{u'_i u'_j}\right)+f_i \qquad \text{3-1}$$

and

$$\frac{\partial U_i}{\partial x_i}=0 \qquad \text{3-2,}$$

for momentum and mass continuity respectively.

The effect of turbulence is represented in equation 3-1 by the Reynolds stress tensor $\rho\overline{u'_i u'_j}$ and is modelled using the k-omega SST turbulence model contained within OpenFOAM-2.2 (OpenFOAM®, 2011).

The SST model blends a variant of the k-ω model in the inner boundary layer and a

transformed version of the k-ε model in the outer boundary layer and the free stream (Menter, 1994).

3.2 Numerical model

A steady state solver was initially used with the solver settings and simulation parameters found in Table 3-1.

Table 3-1 - Numerical settings

Property	Mesh
Type of mesh	Unstructured (Hexahedral)
No. of elements	Approximately 7-8M
y+ on the foil	1-60
Domain Physics	kOmegaSST turbulence model, Automatic wall function
Boundary physics:	
Inlet	Free stream velocity of 30m/s
Outlet	Zero gradient
Bottom/side/top wall	Wall with free stream velocity
Board and fairing	Wall with no slip condition
Solver settings:	
Grad (U) Scheme	Gauss linear
Div (U)	Gauss limitedLinearV 1
Pressure coupling	SIMPLE
Convergence criteria	P 1e-7, U 1e-6, k 1e-8, omega 1e-8
Processing Parameters:	
Computing System	Iridis 4 Linux Cluster (University of Southampton)
Run type	Parallel (32 Partitions run on 2x16 core nodes each with 23 Gb RAM)

3.3 Meshing Technique

The simulation domain replicates the dimensions of the RJ Mitchel wind tunnel with 8 m upstream of the foil and 12 m downstream. The hull fairing is included to replicate the same flow over the board as in the experiment.

An unstructured hexahedral mesh around the foil was created using the snappyHexMesh utility within OpenFOAM. Firstly a coarse block mesh of hexahedral cells is created, using the blockMesh utility, defining the size of the domain and the initial cell size in each direction. Specific areas within the domain are then specified for mesh refinement in progressive layers. For each layer of refinement conducted each cell within the specified region is split into 8 equal parts, doubling the mesh density in all directions. Regions of refinement were placed around the foil, fairing and an estimated wake path. Two boundary layer elements are also grown out from the foil surface mesh. This localised refinement process results in a general mesh structure and boundary layer refinement that can be seen in Figure 4.

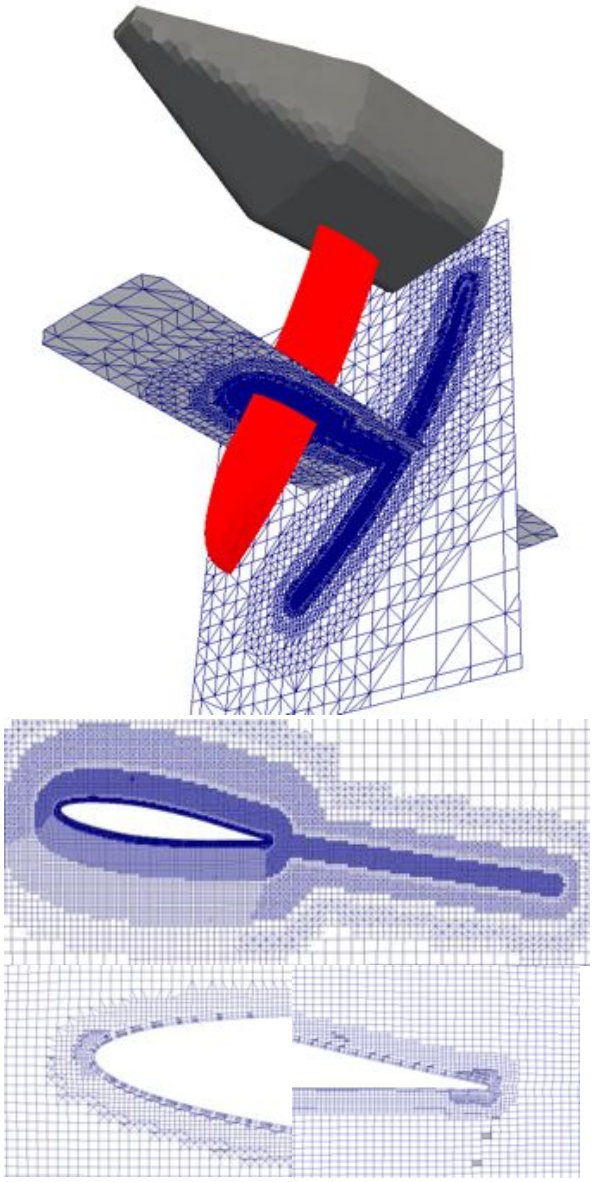

Figure 4 - Mesh structure

4 Results

An over view of the experimental results obtained in the wind tunnel is presented here and compared with preliminary CFD results.

4.1 Force comparison

The force coefficients from the CFD simulations are compared with experimental results in Figure 6. In general there is good agreement for the lift and drag coefficients for angles of attack less than 10 degrees. However a general trend of slightly over predicting the lift and under predicting the drag can be observed. In this region the flow is mainly attached with separation just starting to occur at an angle of attack of 8.5 degrees. This can be observed in the surface streamlines and y^+ distribution presented in Figure 5. The aligned flow and high y^+ over the majority of the suction side of the foil indicates that the flow is mainly attached for the first two thirds of the chord but with some separation towards the trailing edge. Some larger unsteady regions of separation can be observed towards the root of the board, potentially caused by the flow over the hull fairing.

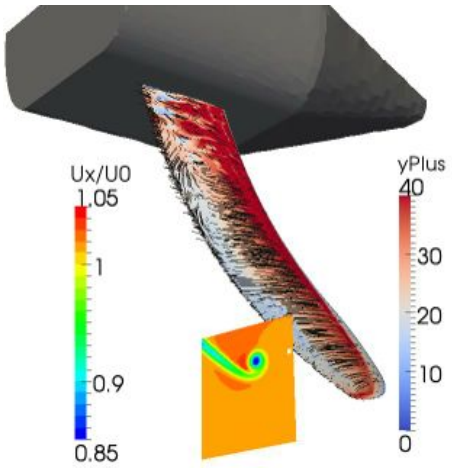

Figure 5 - y+ values on the board surface with AoA = 8.5 deg, with normalised axial velocity displayed on the PIV plane.

For large angles of attack, where the flow if fully separated, a large discrepancy is seen between the CFD and experimental data. It should be noted that the unsteady flow regime created by large amounts of separation requires an unsteady flow solver to accurately capture the flow physics.

A significant difference is also observed in the vertical force coefficient, Cz. As an assessment of board pitch angles was not completed in the wind tunnel it is possible that there was an error in the vertical alignment of the board in its clamps. The potential impact of this error should be investigated further using CFD simulations.

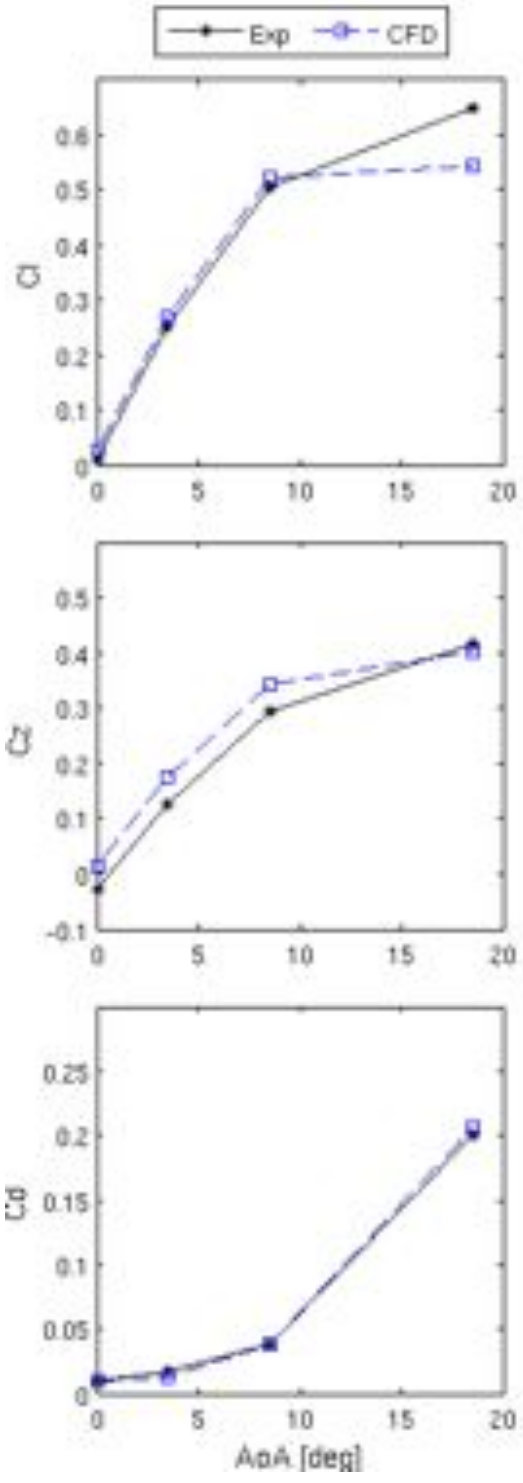

Figure 6 – Comparison of CFD force prediction against experimental data.

4.2 Deflection data

An example of the board tip deflection data obtained from the DIC system in the wind tunnel is provided in Figure 7. It is intended that both

this and twist data gathered and presented in (Giovannetti et al., 2014) can be used to generate deflected foil geometries allowing the impact of board bend and twist on performance to be assessed.

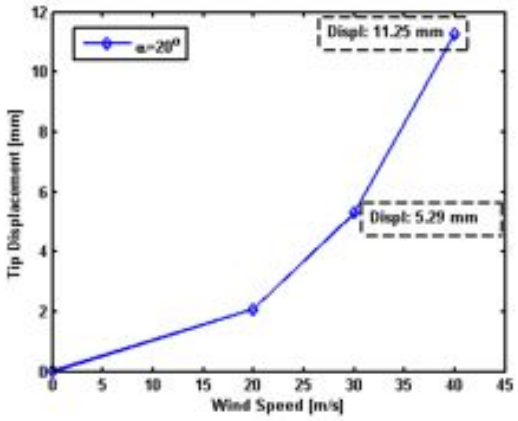

Figure 7 - Board tip deflection for an AoA of 18.5 deg.

4.3 Flow field comparison

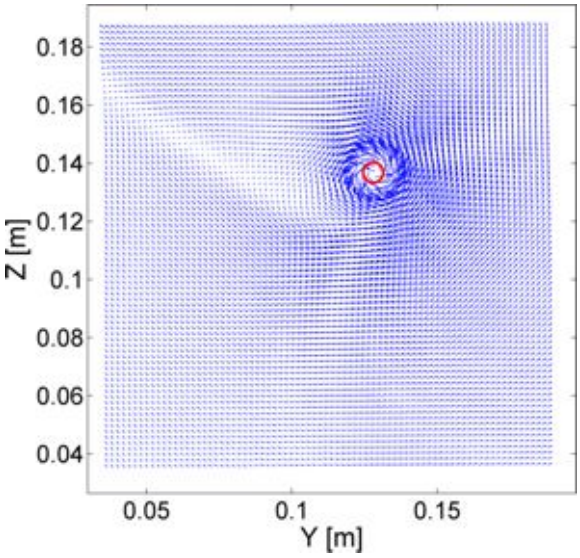

Figure 8 - Mean experimental velocity vector field, for AoA = 8.5 deg, with highlighted vortex centre.

An example of the mean transverse velocity vector field measured using the PIV system is provided in Figure 8. The basic VORTFIND algorithm, originally presented in (Pemberton R, Turnock S, Dodd T, 2002), was used to locate the centre of the tip vortex in the 200 vector fields produced for each experimental configuration The algorithm ranks which vectors are closest to the vortex centre using criteria defined in (Phillips & Turnock, 2013). The average position of the 10 closest vectors was then taken as the vortex position for each vector field. The average vortex position was then calculated and is highlighted in Figure 8.

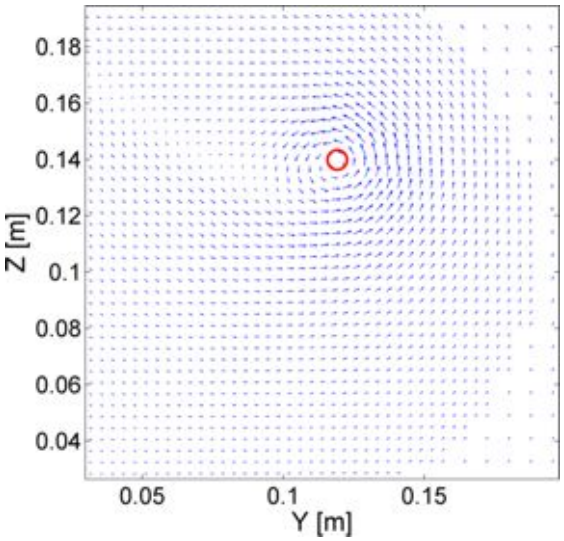

Figure 9 - CFD vector field for AoA = 8.5 deg, each vector represents 1 cell.

To compare the CFD results with the experimental flow field data the velocity components were sampled on the same plane as the laser sheet, see Figure 10. It appears that there is a slight discrepancy in the position of the vortex, possibly due to the experimental board deflection, however a much greater difference is observed in the local vortex velocities. This can be assessed by calculating the mean tangential velocity magnitude for different radiuses away from the vortex centre, see Figure 11.

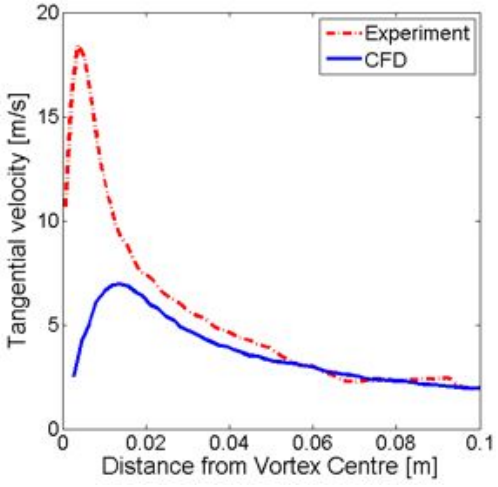

Figure 10 – Mean Tangential velocity for an AoA = 8.5 deg

It is clear that the vortex structure near the core is not well captured in the CFD. This is most likely due to lack of mesh density in this region, which can be observed in the vector spacing in Figure 9.

Both the mean and distribution of the experimental tip vortex position can be seen for different wind speeds and angles of attack in Figure 11. The impact of flow separation on the variability of the vortex position can be seen as the AoA increases. The impact of the board deflection can also be seen on the tip vortex position, especially for AoA = 18.5 deg.

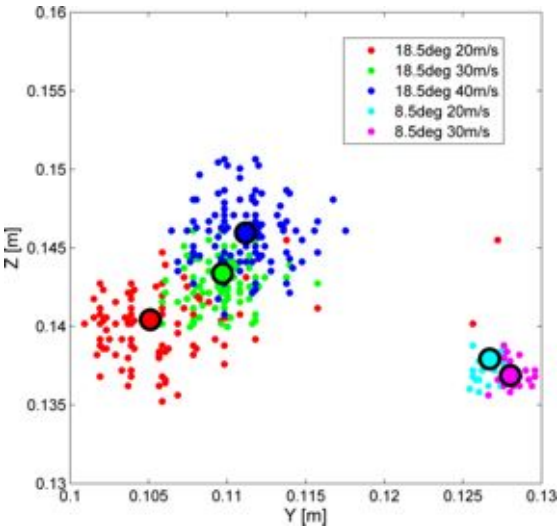

Figure 11 - Distribution of experimental tip vortex position for different wind speeds and angles of attack, with mean position highlighted by black ring.

5 Conclusions

A detailed set of experiments has been conducted providing validation data for both the structural response and fluid dynamic flow for a new fluids structure interaction test case. Preliminary CFD results are compared against these and significant future areas of improvement are identified.

6 Acknowledgements

The authors would like to thank the help of the TSRL team, Dave Hollis from LaVision, the RJ Mitchell wind tunnel staff and the research funding from the EPSRC (grant number EP/009876/1).

7 References

Giovannetti, L. M., Banks, J., Soubeyran, X., Turnock, S. R., & Boyd, S. W. (2014). Full-field deformation response of a high performance foil under fluid loading using Digital Image Correlation. *Ready for submission*.

Menter, F. R. (1994). Two-equation eddy-viscosity turbulence models for engineering applications. *AIAA-Journal*, *32*(8), 269–289.

Nicholls-Lee, R. F., & Turnock, S. R. (2007). Enhancing Performance of a Horizontal Axis Tidal Turbine using Adaptive Blades. In *OCEANS 2007 - Europe* (pp. 1–6). Aberdeen: Ieee. doi:10.1109/OCEANSE.2007.4302437

OpenFOAM®. (2011). *OpenFOAM – The Open Source CFD Toolbox- User Gide, Version 2.01*. Retrieved from www.openfoam.org

P. Veers, & Bir, G. (1998). Aeroelastic tailoring in wind-turbine blade applications. In *Windpower'98, American Wind Energy Association Meeting and Exhibition*. Bakersfield, California. Retrieved from http://windpower.sandia.gov/other/AWEA4-98.pdf

Pemberton R, Turnock S, Dodd T, R. E. (2002). A novel method for identifying vortical structures. *Journal of Fluids and Structures*, *16*(23), 1051–1057.

Phillips, A., & Turnock, S. (2013). Application of the VORTFIND algorithm for the identification of vortical flow features around complex three-dimensional geometries. *International Journal for Numerical Methods in Fluids*, *71*(11), 1461–1474. doi:10.1002/fld.3720

Raffel, M., Willert, C., Wereley, S., & Kompenhans, J. (2007). *Particle Image Velocimetry*.

Numerical Analysis of Propeller-induced Pressure Pulses in Wakes Modified by Improvement Devices

T. BUGALSKI[1] AND J. A. SZANTYR[2]

[1] Ship Design and Research Centre SA (CTO), Szczecinska 65, 80-392 Gdansk, Poland
[2] Gdansk University of Technology, Narutowicza 11/12, 80-233 Gdansk, Poland

The research presented in this paper is related to the European Commission project STREAMLINE, which was concerned with the hydrodynamic performance of a 7000 ton chemical tanker [1]. The model of this ship was equipped with several different flow-modifying devices and tested in a model basin. The tests covered the resistance and propulsion performance of the ship and the unsteady aspects of propeller operation. This paper concentrates on the influence of the wake-improvement devices, such as: vortex generators, pre-swirl stators and boundary layer alignment devices, on the propeller-induced pressure pulses. Altogether four different wake fields are considered in the analysis: the original hull wake, a vortex generator, a pre-swirl stator and a boundary layer alignment device. The objective of the analysis was to determine and compare propeller-induced pressure pulses. Two propellers were included in the analysis: the reference propeller P0 originally designed for the ship and the propeller P3 of a modified, improved design.
The analysis was performed almost entirely by numerical computations. Only the calculations for the original hull equipped with propeller P0 could be directly compared with pressure pulses measured on the ship model in a circulating water channel. The results if the analysis are presented in the following sections of this paper. All results given in this paper refer to model scale and the scale of the models is 1:16.5.

Wake improvement devices and their effect on the wake structure

The ship considered in this analysis is the 7000 ton chemical tanker with the length between perpendiculars of 94m, breadth of 15.4m, draft of 6m, block coefficient of 0.786 and the volume displacement of 6827m^3. The photograph of the stern part of the original hull H0 and the map of the resulting wake velocity field are shown in Fig. 1. The velocity field of the wake seems to be typical for this category of ships and it is reasonably favourable from the point of view of unsteady propeller operation. Consequently, no high intensity of unsteady cavitation phenomena and high induced pressure pulses may be expected.

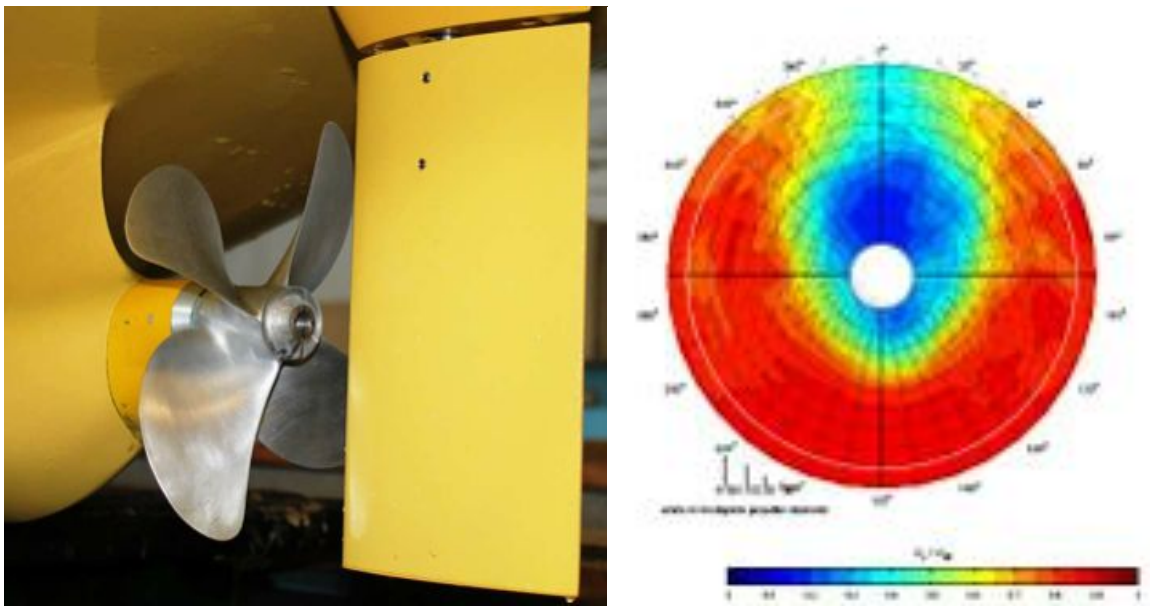

Fig. 1 Photograph of the original hull H0 with propeller P0 and basic rudder and map of the wake velocity field

The vortex generators VG6 were located on both sides of the stern and inclined at an angle of 9 degrees with respect to the waterline. The photograph of the stern with vortex generators VG6 is shown in Fig. 2, together with the map of the resulting wake velocity field. Now the wake peak visible in the upper part of the wake in Fig. 1 is significantly modified, creating a wide region of almost uniform velocity. Moreover, the iso-wake lines in this region have an almost circumferential direction. This should have a marked positive effect on the unsteady operation of propellers.

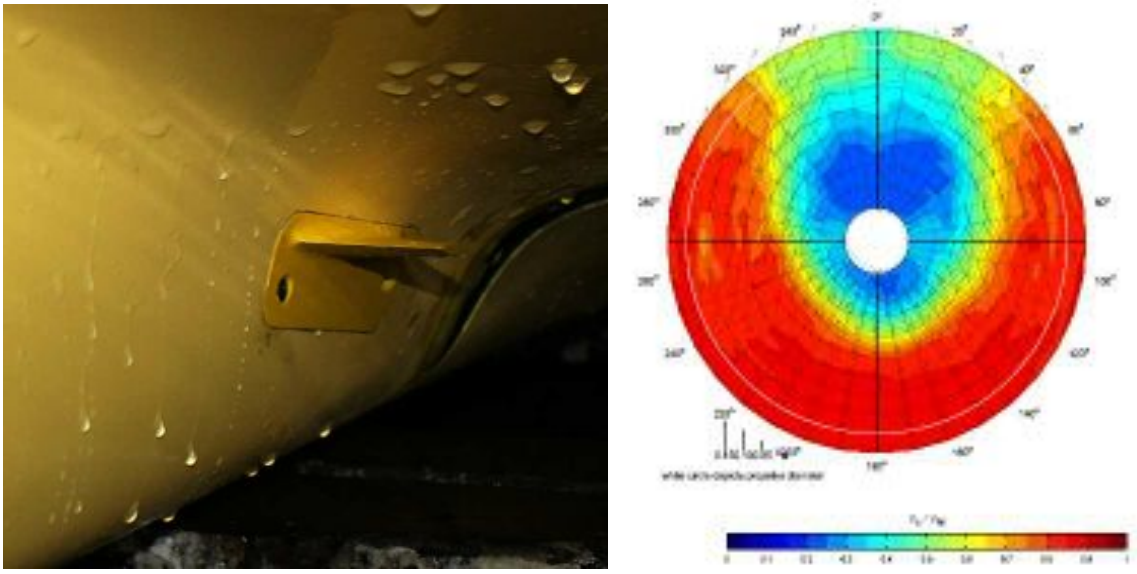

Fig. 2 Photograph of the hull with vortex generators VG6 and map of the wake velocity field

Another type of wake improving devices were the Pre-Swirl Stators (PSS), which were intended first of all to increase the propulsive efficiency. Several configurations of these were tested and finally the one with three stator vanes fitted on the port side of the hull was selected. The photograph of the stern with PSS is shown in Fig. 3, together with the map of the resulting wake velocity field.

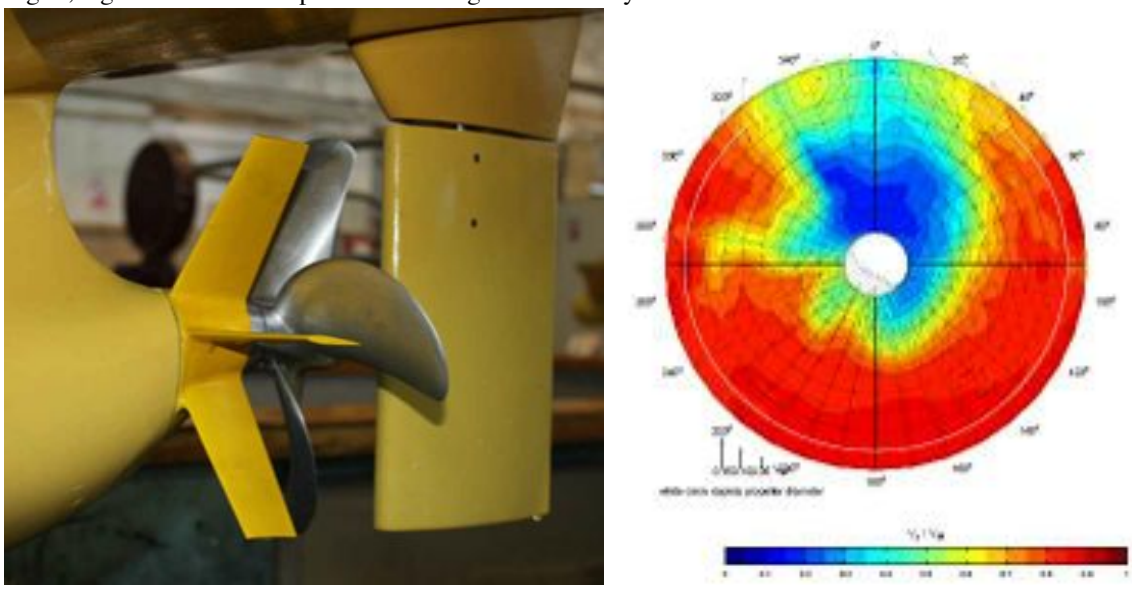

Fig. 3 Photograph of the hull with Pre-swirl Stator PSS and map of the wake velocity field

Now the main upper peak of the wake is weaker in the top region, but much more intensive and extended towards the starboard side in the region right above the shaft.
At the same time an additional peak has appeared of the port side at approximately 270 degrees position. This should not result in the rise of unsteady cavitation and induced pressure pulses, but it may amplify higher harmonics of the unsteady shaft forces.
Another type of wake improvement devices was the Boundary Layer Alignment Device (BLAD). It consisted of a couple of spoilers fitted to both sides of the stern part of the hull. Their objective was to prevent thickening of the hull boundary layer in front of the propellers. The photograph of the stern equipped with BLAD is shown in Fig. 4, together with the map of the resulting wake velocity field. The map of the wake does not indicate any decrease on the hull boundary layer thickness. At the same time a quite wide area of retarded flow has appeared in the region right above the shaft. These modifications of the original wake distribution cannot be regarded as positive from the point of view of the unsteady propeller operation.

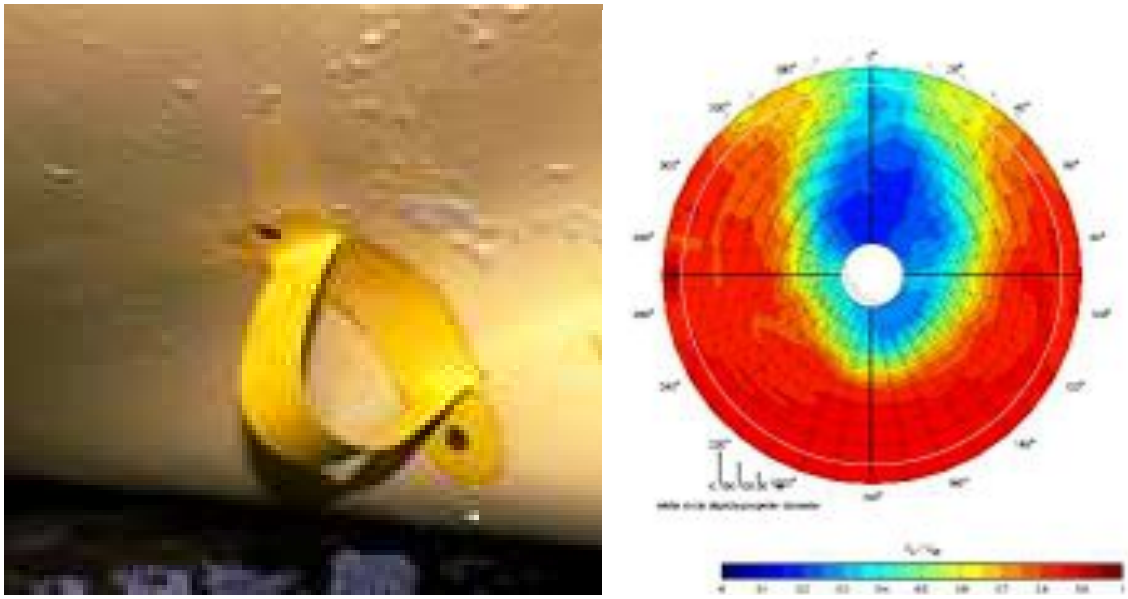

Fig. 4 Photograph of the hull with Boundary Layer Alignment Device BLAD and map of the wake velocity field

Propellers included in the analysis

Both propellers considered in the analysis were four bladed and they had the same full scale diameter of 3.8 [m]. Their detailed geometry is presented in Figs. 5 and 6. Comparison of both propeller designs shows that the most significant difference between them is the higher hydrodynamic blade tip loading of propeller P3 with respect to the propeller P0. It is visible both in the increased blade pitch and increased mean line camber of the blade sections in this region. This increases the risk of unsteady cavitation. This risk may be further aggravated by a reduction of the expanded blade area ratio from 0.5809 for the propeller P0 to 0.5208 for the propeller P3and it may cause an inferior unsteady performance of propeller P3.

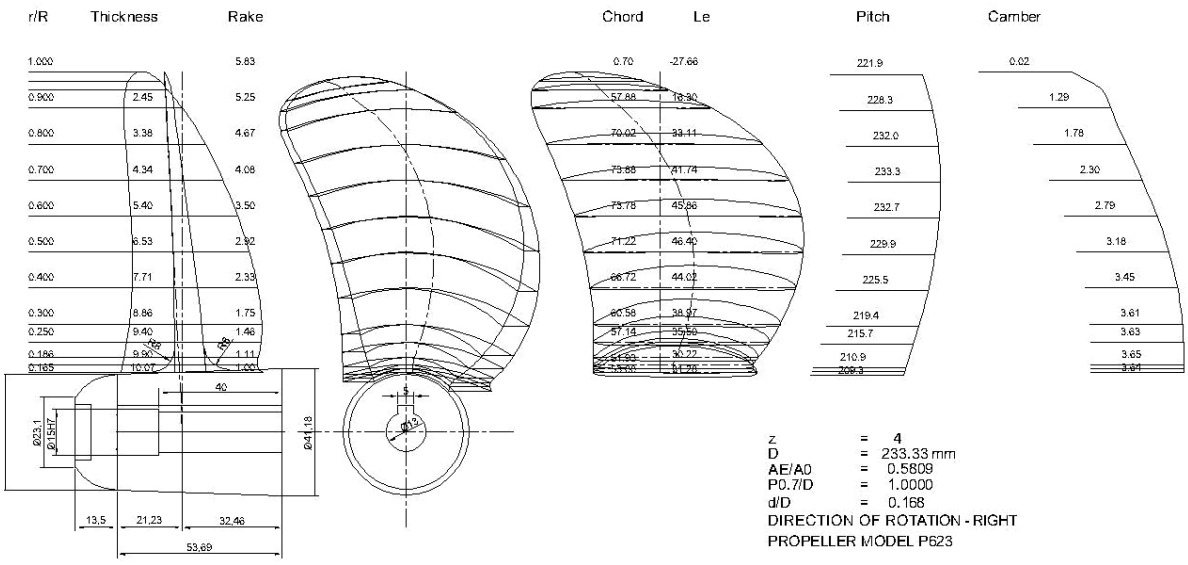

Fig. 5 Drawing of the reference propeller P0

Results of calculations and comparison with experiments

Calculations reported in this paper were performed using the newly modified computer program DUNCAN [2,3]. This program is based on the deformable lifting surface theory and it is capable of calculating for the propeller operating in the three-dimensional non-uniform velocity field the time-dependent pressure distribution of the propeller blades, the unsteady cavitation extent on the propeller including sheet, bubble and vortex

cavitation, the fluctuating bearing forces and the pressure pulses generated by the cavitating propeller in the prescribed points.

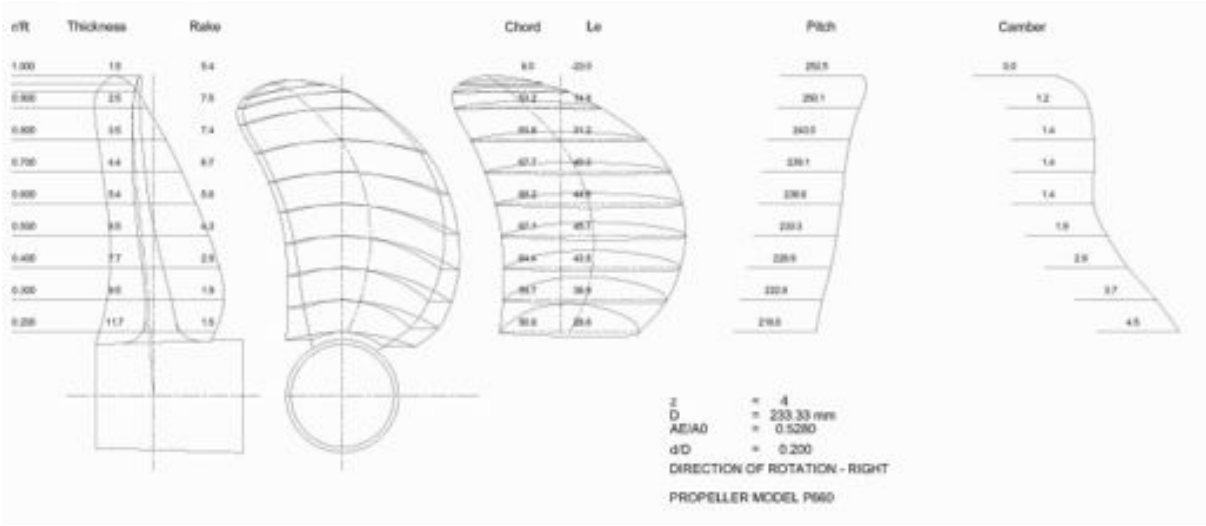

Fig 6 Drawing of the designed propeller P3

Unfortunately, the corresponding experimental results in model scale were available only for the hull H0 with propeller P0. In these experiments the measurements of the pressure pulsations in 17 points on the stern part of the ship hull. The locations of theses points are shown in Fig. 7. As the program allowed for 16 computation points only, and furthermore, the measurements were performed with the rudder in place while the computations did not include the rudder, it was decided to disregard in calculations point no. 1, located closest to the rudder.
All calculations were performed for the ship speed of 15.0 knots and the cavitation number equal to σ_N=2.632.During calculations in the different wake velocity fields the input ship speed was adjusted to produce the same thrust coefficient equal to K_T=0.2649. In this way all the computations of the unsteady parameters of operation of both propellers in all analysed wake fields may be regarded as comparable.

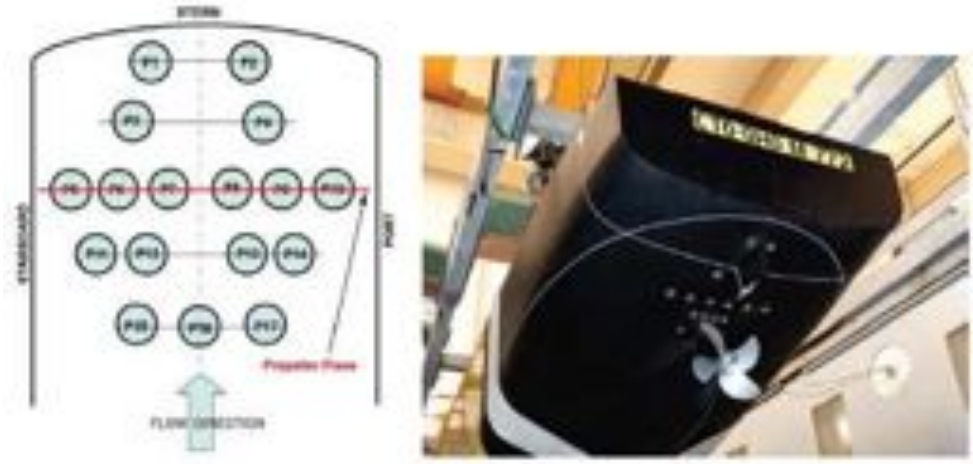

Fig. 7 Location of points for measurement and calculation of the propeller-induced pressure pulses

Fig. 8 shows the comparison of the calculated and experimentally measured blade frequency harmonic amplitudes of the pressure pulses in model scale. The calculated results are visibly higher than the results of corresponding measurements, however both sets of results give values which are well within the acceptable range for this kind of ship. Several reasons for the discrepancy between measurements and calculations may be suggested:
- overestimation of the maximum extent and volume of the pulsating sheet cavity in the calculations, which leads to an overestimation of the maximum amplitudes of the pressure pulses,
- absence of the rudder in the calculations,

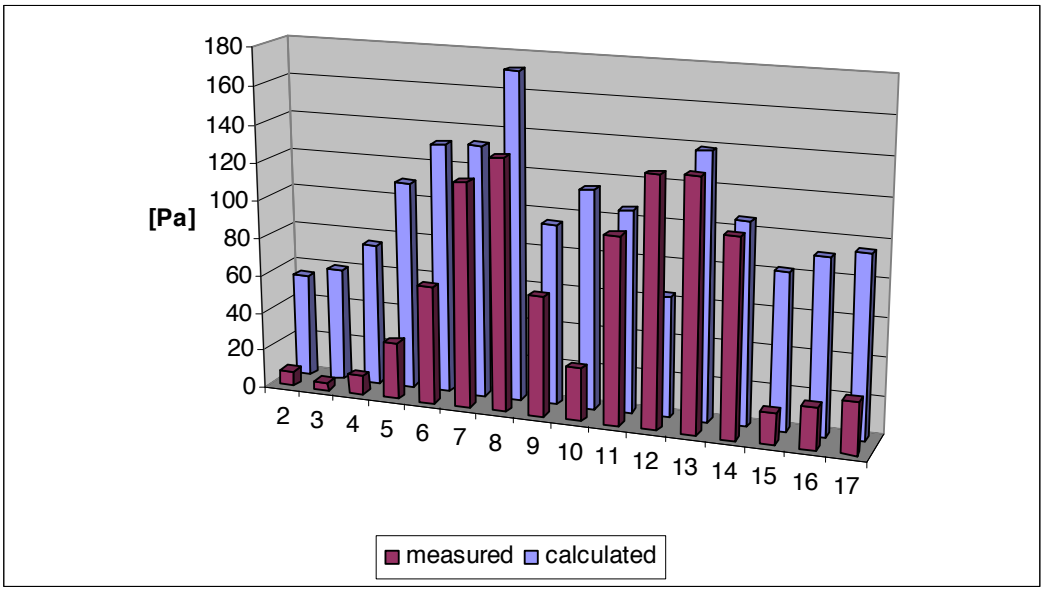

Fig. 8 Comparison of the measured and calculated blade frequency amplitudes of the pressure pulses generated by the propeller P0 behind the hull H0

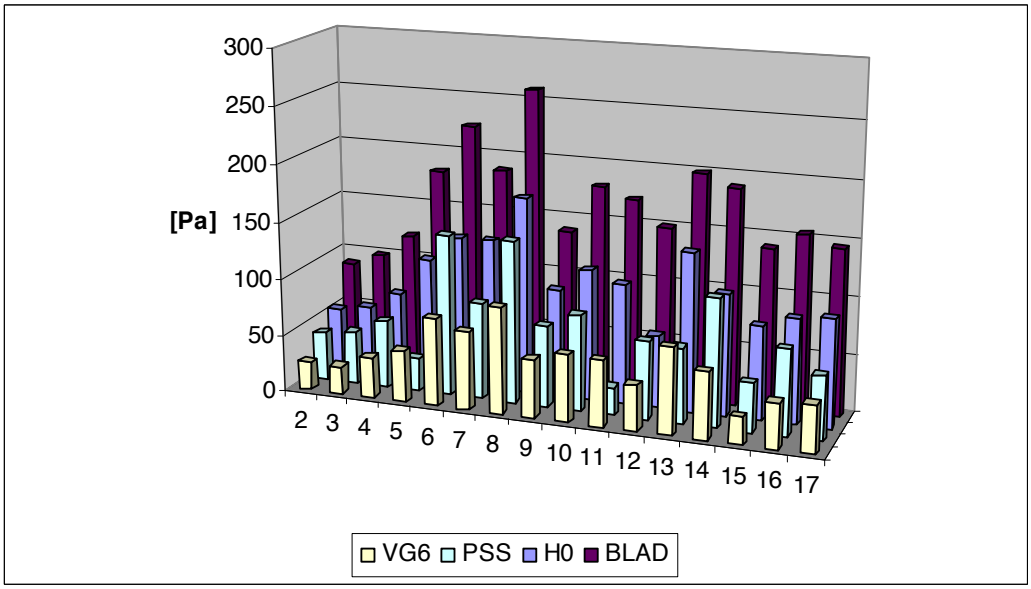

Fig. 9 Comparison of the calculated blade frequency amplitudes of the pressure pulses generated by the propeller P0 behind the hulls H0, VG6, PSS and BLAD

- measurements were conducted in the limited space of the circulating water channel, while the calculations assumed unlimited space (except hull surface as the only rigid boundary).

The following figures, Figs. 9 and 10, show only the results of calculations. They present the comparison of the blade frequency harmonic amplitudes of the pressure pulses for both propellers P0 and P3 in all analysed wake velocity fields H0, VG6, PSS and BLAD.

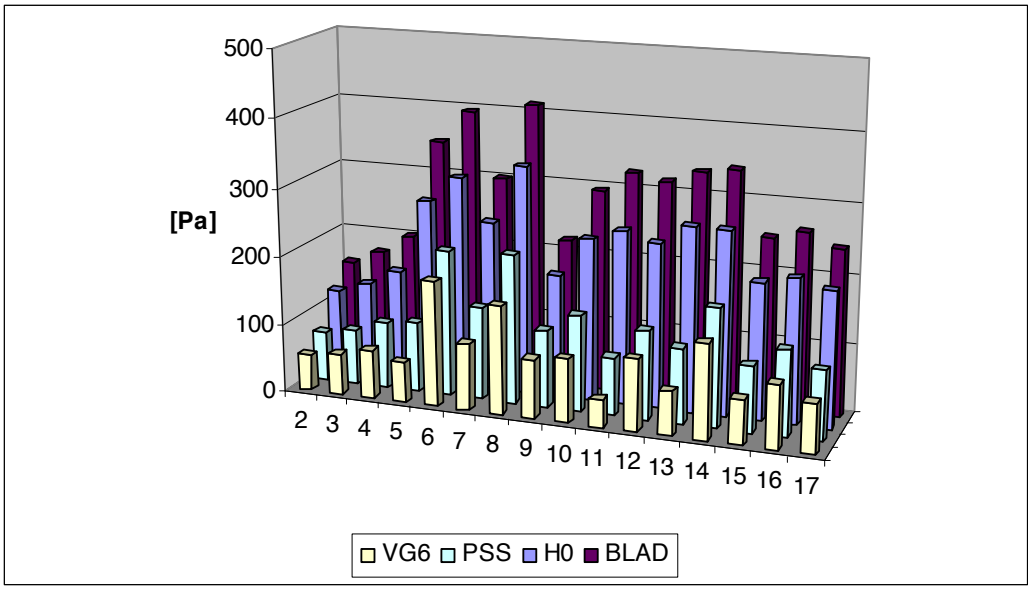

Fig. 10 Comparison of the calculated blade frequency amplitudes of the pressure pulses generated by the propeller P3 behind the hulls H0, VG6, PSS and BLAD

Conclusions

The following conclusions may be drawn from the analysis of the above presented results:

- The computed blade frequency harmonic amplitudes of the pressure pulses for the hull H0 and propeller P0 are visibly higher than the values measured experimentally in the circulating water channel. However, both computed and measured amplitude values are rather low and they would be regarded as acceptable for this type of ship.
- The spatial distribution of pressure pulses amplitudes over the stern area in calculations and measurements shows visible differences. The calculated results are much closer to the measured values in the points located near the propeller, while the calculations overestimate the pressure amplitudes more significantly in the regions farther from the propeller. This may result from an overestimation of the calculated maximum size of the pulsating sheet cavity.
- The most effective reduction of the blade frequency harmonic amplitudes of the pressure pulses is achieved with the vortex generators VG6. Next best results are obtained with the Pre-Swirl Stator. Application of the Boundary Layer Alignment Device BLAD increases the blade frequency harmonic amplitudes.
- In all cases the blade frequency harmonic amplitudes of the pressure pulses for the propeller P3 are significantly higher than the corresponding values for the original propeller P0. This follows from a rather unusual geometry of the propeller P3 as compared to the propeller P0
- Considering all results of calculations presented in this paper the vortex generator VG6 should be considered as the most effective device as far as the unsteady performance of the propeller is concerned.

Acknowledgement

The experimental results presented in this paper have been obtained in STREAMLINE project. The STREAMLINE project is a collaborative R&D project, partly funded by the7th Framework Programme of the European Commission. The authors would like to express their gratitude for the possibility of using these results in preparation of this paper.

References

[1] Di Felice F., Falchi M., Aloisio G., Pecoraro A., Salvatore F., Bugalski T.: Deliverable D21.11 –Results of Model Tests on Optimized Configurations. STREAMLINE project Technical report, INSEAN and CTO, 2013.

[2] Glover E.J., Szantyr J. A.:The Analysis of Unsteady Propeller Cavitation and Hull Surface Pressures for Ducted Propellers, Trans. RINA, Vol. 132, 1990.

[3] Szantyr J. A.: User Instructions for the Program DUNCAN2012 for the Analysis of Ducted Propeller Operation in the Non-uniform Velocity Field, Technical Report of CTO SA No RH-2012/T-123 (in Polish), 2012.

RANSE Simulations for the Effect of Welds on Ship Resistance

Cosmin Ciortan (DNV GL), Hovik/Norway, cosmin.ciortan@dnvgl.com
Volker Bertram (DNV GL), Hamburg/Germany, volker.bertram@dnvgl.com

DNV GL has launched a service which shall help yards and owners getting hulls built as designed. The service is called Build2Design (B2D), *Ciortan and Sun (2014)*. For the yard, the benefit is that a third party certifies the build quality; for the owner, the benefit is the increased confidence that the hull will perform as intended. In addition to this, for tier-2 yards, which have lower quality standards, B2D helps with improving build quality and hence better position the yards in the market. B2D touches on a variety of aspects which concern production details with relevance to hydrodynamic performance:

- Plate buckling
- Weld seams
- Anodes (placement and shape)
- Draft marks
- Bilge keel alignment

All numerical simulations are performed using Star-CCM+ of CD-adapco. This state-of-the-art RANSE code is based on the finite volume method. This paper focusses on the analyses for the weld seams.

The standard test case concerned a flat plate field with butt welds. The plate field was 5000 mm and the initial weld height 3 mm, both typical values for North European ship yards. Later, the height of the welds is increased at 5, 7 and 9 mm, values used in tier-2 yards. The width of the plate is about 9 cm, suitable for a 2D-like study. The weld seam is approximated by an arc of a circle. Three ship speeds were used: 12, 16 and 20 kn (6.17, 8.23 and 10.288 m/s, respectively). A physical turbulence stimulator (blade of 50 mm height) was arranged 4 plate lengths upstream of the test plate section.

Systematic numerical studies were performed to look at the influence of parameters of the computational model and at the influence of weld geometry and ship parameters.

The investigated parameters of the computational model included:

- Type of simulation (transient or steady state). The initial thinking was to run the simulations in steady state, since no significant transient effects were expected. However, the convergence was quite poor, and therefore the simulations were all performed in transient, which greatly improved the convergence.
- Mesh size: For mesh convergence, the influence of y^+ on results was checked for values smaller than 1 (as recommended for capturing separation on rounded structures), and ~50 (with wall functions). For the drag on the plate, the results are almost insensitive, but for the drag on the welding, $y^+=50$ gives roughly half the weld seam drag than $y^+<1$. Since separation from the weld is expected, and the size of the welds is small, a value of $y^+<1$ is used for all simulations. Dividing the cell size in half did not change the drag values. For the subsequent variations, the "coarse" mesh with roughly 2,000 cells on the surface of the plate field was used.
- Time step size. Several time step sizes were used in order to check the sensitivity of the solution. A final time step of 0.01 s, with 8 inner iterations, is used
- Turbulence model: standard and realizable k-ε, standard k-ω, SST, and Spalart-Allmaras. All turbulence models gave results that were quite close, except for standard k- ε model, which calculated a higher drag. For the subsequent variations, we used then the Spalart-Allmaras, which gave results somewhat near the average of the other three turbulence models (realizable k-ε, standard k-ω, and SST).

The investigated weld geometry and ship parameters included:

- Weld height: 3 mm, 5 mm, 7 mm, 9 mm
- Plate field length: 5000 mm
- Number of welds: 2
- Weld width: 13.5 mm (corresponding to 20 mm plate thickness)
- Ship speed: 12 kn, 16 kn, 20 kn

Star-CCM+ was used for performing the simulations. Trimmed meshes were used, with $y^+<1$ next to the wall. Prism cells were used on the walls, for a height of 10 cm using 40 layers, over the whole length of the domain. This is deemed sufficient for capturing the velocity distribution in the boundary layer. Fig.1 shows a mesh detail near the welding.

Two plate fields are simulated, in order to check the influence of successive fields on each other. The domain extends for 18 L upstream of the first plate field; 20 L downstream of the second plate field (total length, including plates, 40 L); and 2.2 L in vertical direction. Extrusion (gradual increase in cell length) was used towards the outlet, in order to damp the solution and avoid possible boundary effects. A physical turbulence stimulator (blade of 50 mm height) was arranged 4 plate lengths upstream of the test plate section. A fine mesh region (extending 4 blade heights upstream, 15 blade heights downstream, and 4 blades heights above) was used in order to capture the turbulent flow structures generated by the blade. The results are summarized in Table I.

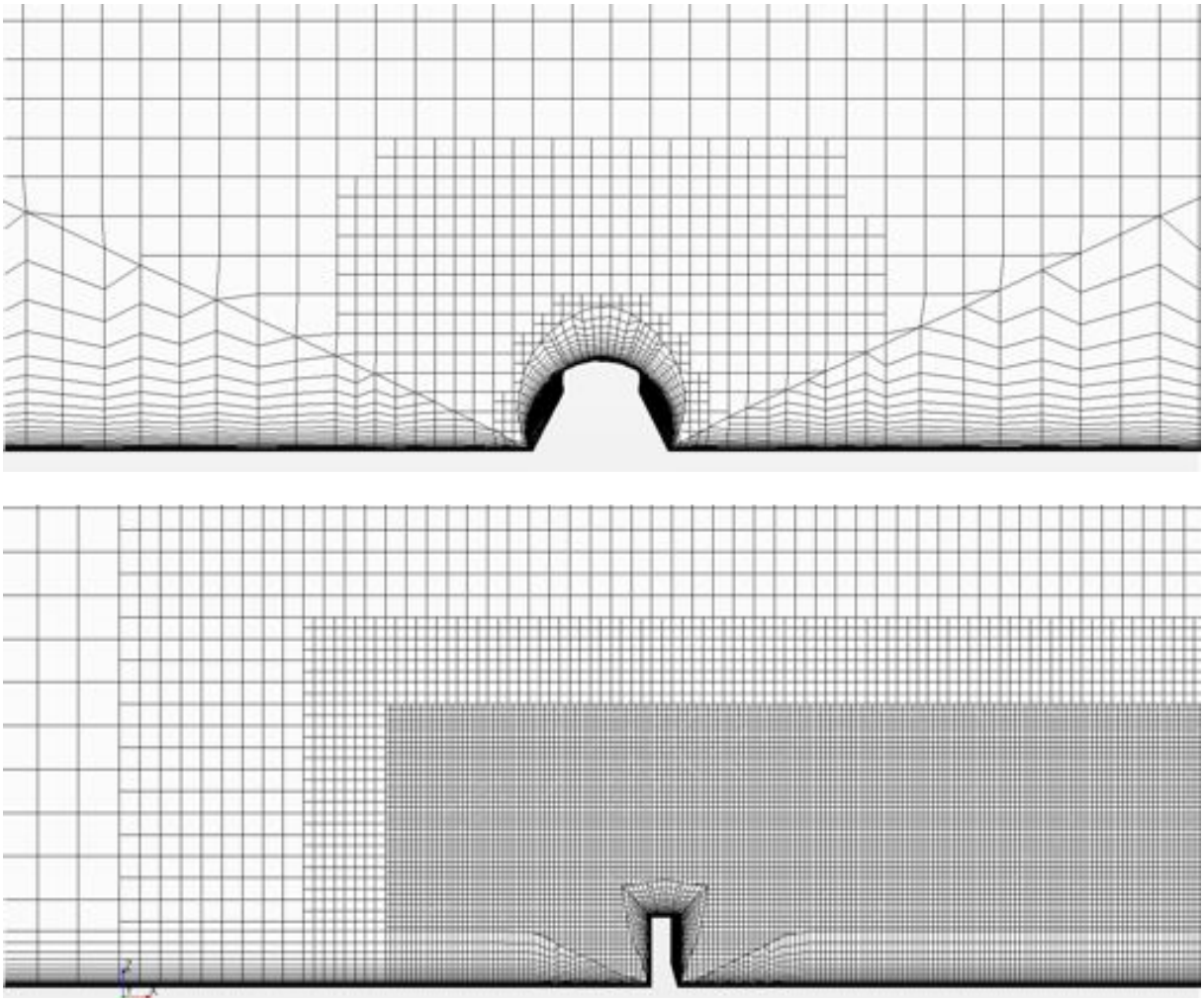

Fig.1: Mesh around a welding (up) and turbulence stimulator (down), detail

Table I: Resistance [N] of the welds and plates for several welding heights; PR = plate resistance, WR = weld resistance, W/P = weld/plate resistance

PLATE 1												
Weld height	3 mm			5 mm			7 mm			9 mm		
Speed	PR	WR	W/P	PR	WR	W/P	PR	WR	W/P	PR	WR	W/P
12 kn	13.33	0.568	4.3%	13.31	1.482	11.1%	13.27	2.55	19.2%	13.24	3.66	27.6%
16 kn	22.85	0.955	4.2%	22.81	2.505	11.0%	22.755	4.44	19.5%	22.70	6.39	28.1%
20 kn	34.72	1.444	4.2%	34.67	3.910	11.3%	34.58	6.98	20.2%	34.49	9.85	28.6%
PLATE 2												
Weld height	3 mm			5 mm			7 mm			9 mm		
Speed	PR	WR	W/P	PR	WR	W/P	PR	WR	W/P	PR	WR	W/P
12 kn	13.19	0.575	4.4%	12.88	1.464	11.4%	12.55	2.58	20.5%	12.24	3.65	29.8%
16 kn	22.65	0.969	4.3%	22.13	2.505	11.3%	21.54	4.46	20.7%	21.00	6.36	30.3%
20 kn	34.44	1.470	4.3%	33.65	3.748	11.1%	32.75	6.83	20.8%	31.97	9.80	30.7%

The results indicate that the influence of the plates on each other is negligible (and likewise as regards the welds). The negligible differences in forces between plate 1 and plate 2 suggest that one can consider the force on each plate as constant.

The welds contribute significantly to the resistance. For 3 mm weld height (good EU, Korean or Japanese yard), the welds have 4-5% of the resistance of the plate. This increases to ~11% for 5 mm weld height, ~20% for 7 mm (poor shipyard standard as found in developing countries). For a large tanker, assuming 10% of the welds are poorly welded (7 mm height), this may translate to 100,000 USD/a in added fuel costs!

The drag coefficient is calculated as follows:

$$C_D = \frac{F}{\frac{1}{2}\rho A v^2}$$

F represents the drag force, ρ the fluid density, A the reference area (of plate or weld), and v the upstream inflow speed.

Does the drag coefficient depend on speed? This was one of the questions that we posed ourselves. Table II provides results. Since the force on the plate does not depend on the welding height, the plate drag coefficient (CDP) is presented only as function of speed. The weld drag coefficient (CDW) depends on both speed and weld-height and is presented accordingly.

Table II: Drag coefficients for plate and welds

Speed	CDP	CDW 3 mm	CDW 5 mm	CDW 7 mm	CDW 9 mm
12 kn	0.00146	0.0204	0.0532	0.0914	0.131
16 kn	0.00140	0.0193	0.0506	0.0897	0.129
20 kn	0.00137	0.0187	0.0505	0.0902	0.127

The plate drag coefficient reduces with speed, as expected. (Plate friction coefficients decrease slightly with Reynolds number (or speed), see e.g. the ITTC'57 formula). For the welds, the trend is the same, with the exception of the 7 mm weld, where drag increases (albeit slightly) from 16 to 20 kn. This is probably due to numerical errors and not a physical effect.

In conclusion, the resistance of welds is significant compared to the resistance of the plate field. From an industry perspective, the study shows that important gains can be achieved in relatively simple ways, on (until now) neglected parts of the ship.

Acknowledgements

We gratefully acknowledge the extensive team contributions from our colleagues Frank Lumpitzsch and Jaeouk Sun.

References

CIORTAN, C.; SUN, J. (2014), *Energy efficient design of ship appendages*, 2nd Int. Conf. Maritime Technology and Engineering (MARTECH), Lisbon

A fish shoal algorithm for global derivative-free simulation-based ship design optimization

Matteo Diez[1], Andrea Serani[1,2], Umberto Iemma[2], Emilio F. Campana[1]

[1]CNR-INSEAN, Natl. Research Council-Marine Technology Research Inst., Rome, Italy (matteo.diez@cnr.it)

[2]Roma Tre University, Dept. of Engineering, Rome, Italy

1 Introduction

The paper presents a nature-inspired derivative-free global optimization method, namely the fish shoal algorithm (FSA), for solving engineering optimization problems with costly objective functions. The method is intended for unconstrained single-objective maximization and is based on a simplified social model of a fish shoal in search for food. Derivative-free global optimization approaches are usually preferred to derivative-based local approaches, when objectives are noisy, derivatives are unknown and the existence of multiple local optima cannot be excluded, as often encountered in simulation-based design (SBD) optimization. When global techniques are used with CPU-time expensive solvers, the optimization process is computationally expensive and its effectiveness and efficiency remain an algorithmic and technological challenge. Nature-inspired algorithms, such as particle swarm optimization [1], firefly algorithm [2], cuckoo search [3], have been widely studied and used as heuristic methods for global derivative-free optimization, combining effectiveness and efficiency of the overall optimization.

Herein, FSA is formulated starting from the dynamics of a single individual belonging to a fish shoal in search for food, and subject to a shoal attractive force and a food-related attraction force. Effectiveness and efficiency of FSA are influenced by the choice of three main parameters: (a) the number of individuals interacting during the optimization, (b) the initialization of the shoal in terms of initial location and velocity, and (c) a set of coefficients controlling the shoal dynamics. The objective of the present work is the identification of the most effective and efficient parameters for FSA, for use in SBD optimization for ship design.

The approach includes a parametric analysis using 60 analytical test functions [4, 5] characterized by different degrees of non-linearities and number of local minima, with full-factorial combination of: (a) number of individuals, using power of two per number of design variables; (b) initialization of the shoal, in terms of initial position and velocity, by Hammersley distributions [6]; (c) twenty-seven different set of coefficients. Box constraints are treated by an inelastic-wall approach [7]. Three absolute metrics are applied for the evaluation of the algorithm performances, based on the distance between FSA-found and analytical optima. The most significant parameters among (a), (b) and (c) are identified, based on the associated relative variability of the results [8]. The most promising parameters for FSA are identified and the performance of FSA is compared with a deterministic particle swarm optimization, D-PSO [8]. Finally, FSA is applied to three ship design single-objective unconstrained problems, pertaining to the barehull optimization of the Delft catamaran in calm water and waves. Specifically, a four dimensional shape modification space [9] is used and the objective functions considered are (i) the total resistance in calm water at Fr=0.5 [9], (ii) the expected value of the total resistance in wave at sea state 5, including variable speed [10], and (iii) the ship operability in the North Pacific Ocean, considering variable speed and sea state [10]. Numerical experiments are performed using a URANS-simulations-trained metamodel, based on stochastic radial basis functions [11].

2 Fish shoal algorithmn (FSA)

Consider the dynamics of the j-th shoal individual, subject to a shoal attraction force, δ_j, and an attraction force related to the knowledge of food distribution, φ_j:

$$m\ddot{x}_j = -\xi\dot{x}_j + \delta_j + \varphi_j \tag{1}$$

where m is the individual mass, ξ is a damping coefficient, and

$$\delta_j = k\sum_{i=1}^{n_p} r_{ij}\hat{u}_{ij}, \qquad \varphi_j = h\sum_{i=1}^{n_p} \frac{2\Delta f_{bi,j}}{1+\sqrt{r_{bi,j}}}\hat{u}_{bi,j}, \tag{2}$$

with

$$r_{ij} = \|x_i - x_j\|, \qquad \hat{u}_{ij} = \frac{x_i - x_j}{r_{ij}}, \qquad \Delta f_{bi,j} = \frac{f(x_{b,i}) - f(x_j)}{R_f}, \qquad r_{bi,j} = \|x_{bi} - x_j\|, \qquad \hat{u}_{bi,j} = \frac{x_{bi} - x_j}{r_{bi,j}} \tag{3}$$

where k and h are coefficients controlling the attraction forces intensity, x_j is the vector-valued position (of dimension N_{dv}) of the j-th individual, f is the objective function (to be maximized) representing the food distribution, x_{bi} is the best location ever visited by the i-th individual, and R_f is a normalization factor.

Finally, using explicit Euler integration and setting $m = 1$ yield the FSA iteration as

$$\begin{cases} v_j^{k+1} = (1 - \xi \Delta t) v_j^k + \Delta t (\delta_j + \varphi_j) \\ x_j^{k+1} = x_j^k + v_j^{k+1} \Delta t \end{cases} \tag{4}$$

where x^k and v^k represent the individual position and velocity vector at the k-th iteration, respectively.

It may be noted that, under the condition ξ, $k =$ constant, for all individuals, the system's eigenvalues for Eq. (1) equal $\lambda = -\xi/2 \pm \sqrt{(\xi/2)^2 - kN_s}$, where N_s is the shoal size (number of individuals).

3 FSA implementation and evaluation metrics

FSA parameters are defined as follows. Their full-factorial combination is taken into account, resulting in 243 setups. Specifically, the number of individuals is defined as $N_s = 2^m \cdot N_{dv}$, with $m \in \mathbb{N}[2,4]$, therefore ranging from $4 \cdot N_{dv}$ to $16 \cdot N_{dv}$. The initialization of individuals location follows a Hammersley sequence sampling (HSS) [6]. HSS equation is applied to three different regions, namely: (A) the entire optimization domain, (B) the domain bounds, and (C) domain and bounds combined together. A non-null initial velocity is used, following [9]. Provided that all the design variables are normalized such that $0 \leq x \leq 1$, the following positions are used for the coefficients controlling the shoal dynamics: $\xi = 1, 0.1, 0.01$; $k = h = q/N_s$, with $q = 1, 10, 100$; $\Delta t = 2/(p\,|\lambda|)$, where $|\lambda| = \sqrt{kN_s} = \sqrt{q}$ with $p = 1, 10, 100$ (derived from stability condition of explicit Euler integration of the system's free-vibrations). Box constraints are handled using an inelastic-wall method [7].

All numerical tests presented herein are minimization problems and are solved by Eq. (4), changing the sign of φ_j. Three absolute performance criteria are used as evaluation metric, and defined as follows:

$$\Delta_x = \frac{\|x_{\min} - x^\star_{\min}\|}{\sqrt{N_{dv}}}, \qquad \Delta_f = \frac{f_{\min} - f^\star_{\min}}{f^\star_{\max} - f^\star_{\min}}, \qquad \Delta = \sqrt{\frac{\Delta_x^2 + \Delta_f^2}{2}} \tag{5}$$

Δ_x is the root mean square of the normalized Euclidean distance of FSA-found ($x_{\min}$) from analytical minimum ($x^\star_{\min}$); Δ_f is the associated normalized distance in the image space, where $f_{\min}$ is the FSA-found minimum, $f^\star_{\min}$ is the analytical one, and $f^\star_{\max}$ is the analytical maximum in the research space [8].

4 Numerical results

Sixty analytical test functions are used. They include simple unimodal, highly complex multimodal and not differentiable problems (see e.g., [8]), with dimensionality ranging from two to twenty. Results are included in Figs. 1 to 4. Specifically, Figs. 1 and 3, show the performances of FSA versus the budget of function evaluations, in terms of Δ_x, Δ_f, Δ, for $N_{dv} < 10$ and ≥ 10 respectively. Average values are presented, conditional to number of individuals, individuals initialization, ξ, q and p coefficients respectively. Figures 2 and 4 show the relative variance σ_r^2 of Δ_x, Δ_f, Δ for $N_{dv} < 10$ and ≥ 10 respectively, retained by each FSA parameter. The coefficient p is found the most important parameter for $N_{dv} < 10$, whereas the individuals initialization is found the most significant parameters for $N_{dv} \geq 10$. The number of particles is shown to be the least important. The best-performing implementation on average (considering all test functions) corresponds to a number of individuals N_s equal to 16 times the number of design variables N_{dv}, an individuals initialization over the variables domain (A), and a set of coefficients corresponding to: $\xi = 0.1$, $q = 10$ and $p = 1$. Figures 5a and 5b show the performance of the associated FSA, compared to D-PSO [8]. FSA is slightly better then D-PSO for problems with $N_{dv} < 10$, especially for high budgets, while FSA performs always better than D-PSO for problems with $N_{dv} \geq 10$.

Best-performing FSA is applied to the ship design problems, and compared with D-PSO [8]. For each problem, FSA results are comparable with D-PSO in terms of convergence and design variable value as is shown in Fig. 6 and 7 respectively, although some difference may be identified. The maximum difference in terms of global optimum value for problems (i) and (ii) does not exceed 1%, while FSA and D-PSO found the same result for problem (iii).

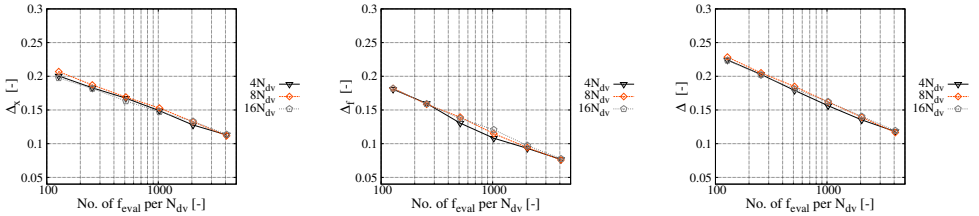

(a) Average performance, conditional to number of individuals

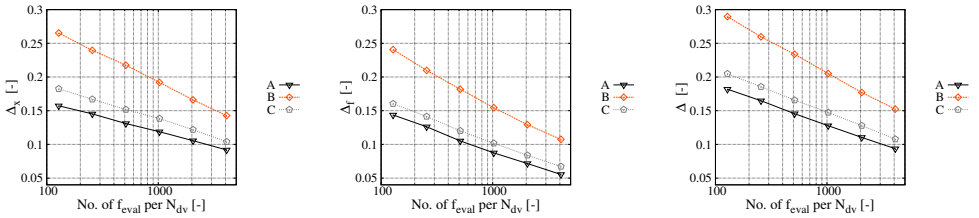

(b) Average performance, conditional to individuals initialization

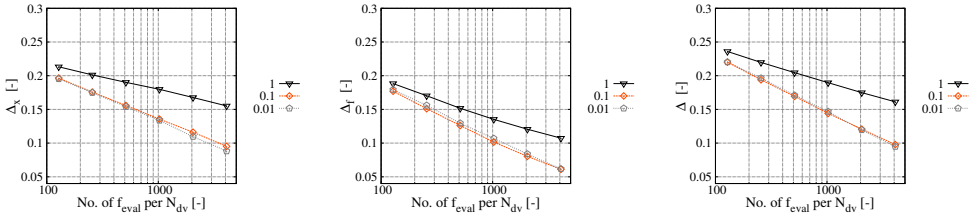

(c) Average performance, conditional to coefficient ξ

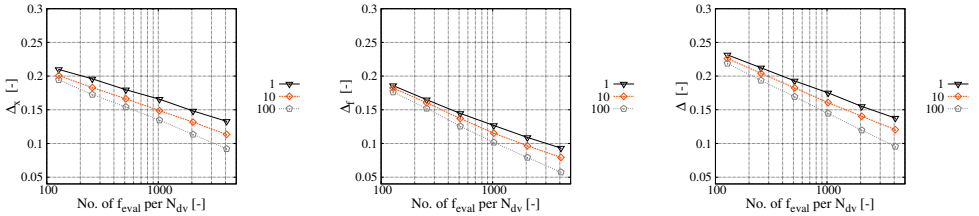

(d) Average performance, conditional to coefficient q

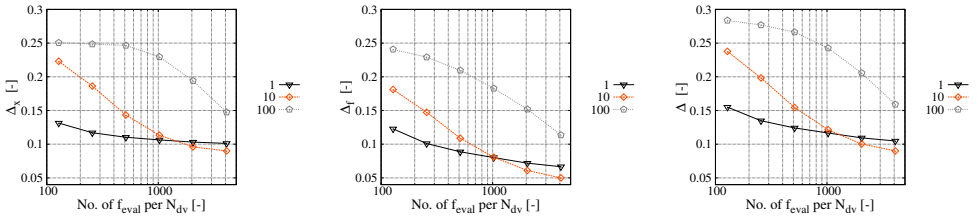

(e) Average performance, conditional to coefficient p

Figure 1: FSA average performance for $N_{dv} < 10$

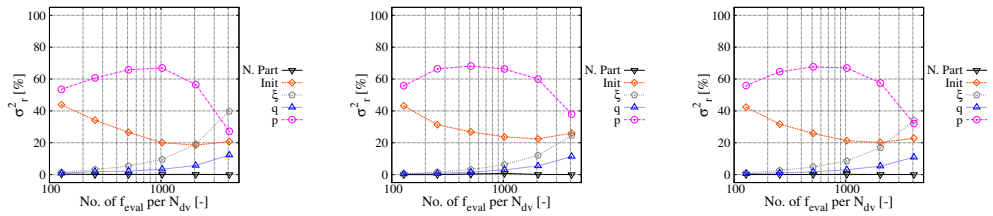

(a) Δ_x (b) Δ_f (c) Δ

Figure 2: $\sigma_r^2(\%)$ of FSA for $N_{dv} < 10$

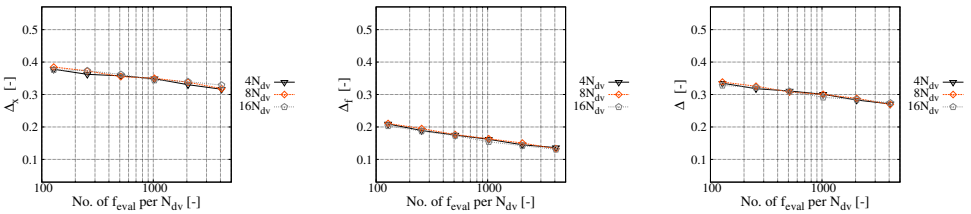

(a) Average performance, conditional to number of individuals

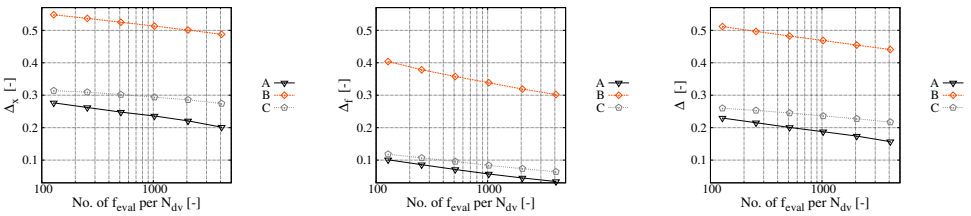

(b) Average performance, conditional to individuals initialization

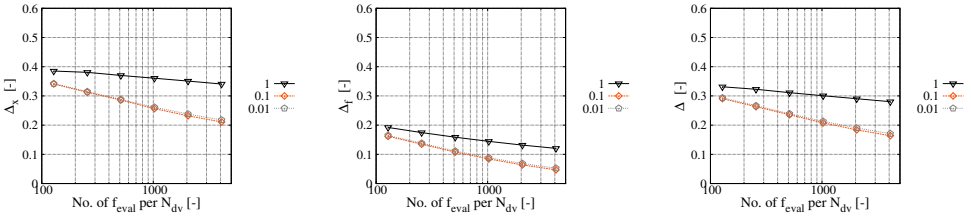

(c) Average performance, conditional to coefficient ξ

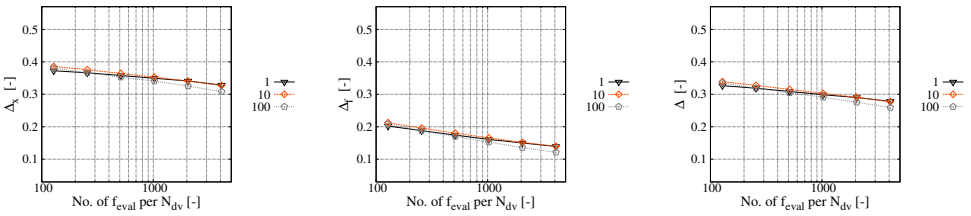

(d) Average performance, conditional to coefficient q

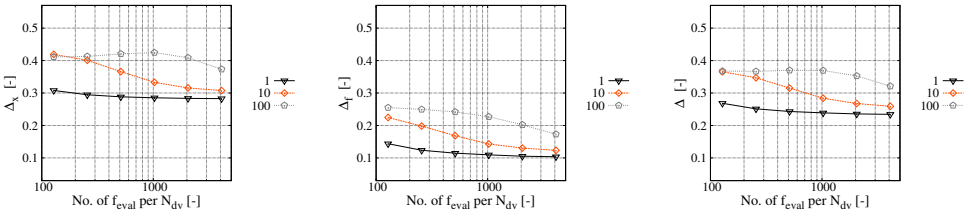

(e) Average performance, conditional to coefficient p

Figure 3: FSA average performance for $N_{dv} \geq 10$

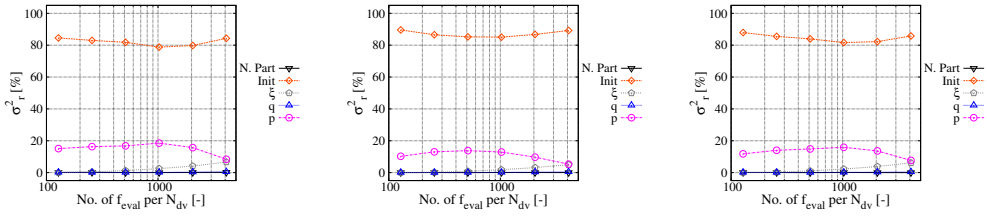

(a) Δ_x (b) Δ_f (c) Δ

Figure 4: $\sigma_r^2(\%)$ of FSA for $N_{dv} \geq 10$

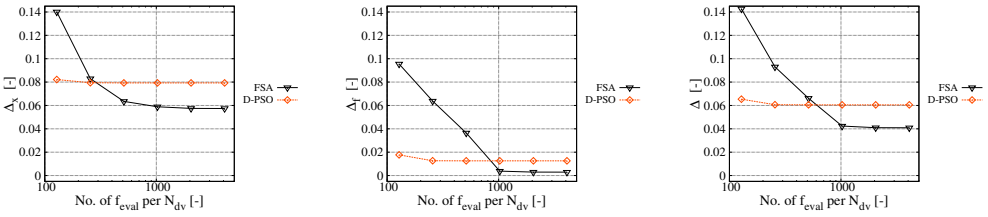

(a) $N_{dv} < 10$

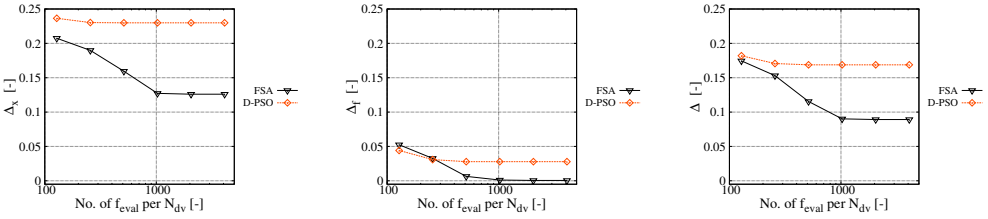

(b) $N_{dv} \geq 10$

Figure 5: Performance of FSA, compared to D-PSO

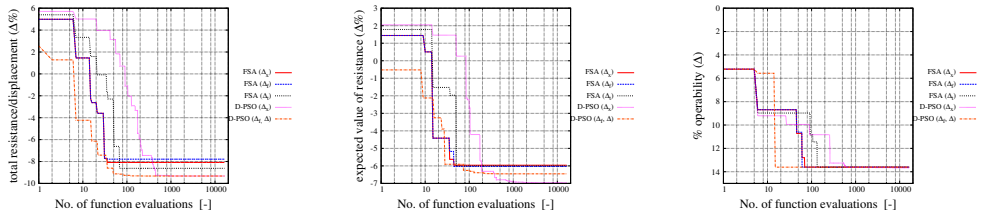

(a) (b) (c)

Figure 6: Convergence of FSA, compared with D-PSO

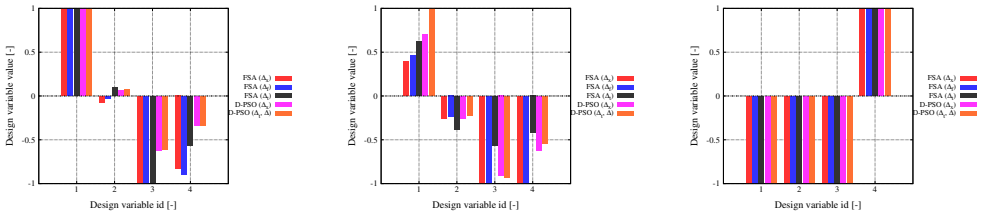

(a) (b) (c)

Figure 7: Comparison between optimal design variables of FSA and D-PSO

5 Conclusions and future work

A fish shoal algorithm for global derivative-free optimization has been presented for simulation-based ship design problems. This is based on a simplified social model of a fish shoal in search for food. A parametric analysis has been conducted using 60 analytical test functions and three evaluation metrics, varying the number of individuals, their initialization, and the coefficient set controlling the shoal dynamics. All possible combinations of FSA implementations led to 243 optimizations for each function. The coefficient p, which defines the time step, has been found the most significant FSA parameter for $N_{dv} < 10$, while for $N_{dv} \geq 10$ the shoal initialization is found the most significant. The number of individuals has been found with a little influence on the FSA performance, compared to other parameters (at least for current studies). The most promising FSA setup has been identified and corresponds to: a number of individuals N_s equal to 16 times the number of design variables N_{dv}; a shoal initialization with a distribution over the whole design variables domain; and a set of coefficient corresponding to: $\xi = 0.1$, $q = 10$ and $p = 1$. FSA has been found slightly better than D-PSO for $N_{dv} < 10$ (especially for high budgets) and always better for $N_{dv} \geq 10$. The best performing FSA has been applied to three four-dimensional ship SBD optimization problem aimed at (i) total resistance in calm water at Fr=0.5, (ii) expected value of the total

resistance in wave at sea state 5, including variable speed, and (iii) ship operability in the North Pacific Ocean, for the Delft catamaran. The ship design problems shown comparable results between FSA and D-PSO. Future work includes the extension of current studies to larger size shoals (by increasing N_s). Different formulations for the food-related attraction force φ will be also investigated, as well as the possibility of changing mass and damping dynamically during the optimization.

Acknowledgments

The present research is supported by the US Navy Office of Naval Research, grant N00014-11-1-0237, and Office of Naval Research Global, NICOP grant N62909-11-1-7011, under the administration of Dr Ki-Han Kim and Dr Woei-Min Lin, and by the Italian Flagship Project RITMARE, coordinated by the Italian National Research Council and funded by the Italian Ministry of Education, Research Program 2011-2013.

References

[1] J. Kennedy, R.C. Eberhart, Particle swarm optimization, in: *Proc. IEEE Conf. on Neural Networks, IV*, Piscataway, NJ, 1995, pp. 1942-1948.

[2] X.S. Yang, *Nature-Inspired Metaheuristic Algorithms*, first ed. Luniver Press, Frome, 2008.

[3] X.S. Yang, S. Deb, Cuckoo search via Levy flights, in: *Proceedings of World Congress on Nature and Biologically Inspired Computing (NaBic 2009)*, IEEE Publications, USA, pp. 210-214, 2009

[4] S. Lucidi, M. Piccioni, Random Tunneling by Means of Acceptance-Rejection Sampling for Global Optimization, *Journal of optimization theory and applications*, Vol. 62, N. 2, August 1989, pp. 255-277.

[5] E.F. Campana, G. Fasano, A. Pinto, Dynamic analysis for the selection of parameters and initial population, in individual swarm optimization, *Journal of Global Optimization*, November 2010, Volume 48, Issue 3, pp. 347-397.

[6] T.T. Wong, W.S. Luk, P.A. Heng, Sampling with Hammersley and Halton Points, *Journal of Graphics Tools*, 1997, pp. 9-24.

[7] S. Helwig, J. Branke, S. Mostaghim, Experimental Analysis of Bound Handling Techniques in Particle Swarm Optimization, *IEEE Transactions on Evolutionary computation*, Vol. 17, No. 2, April 2013.

[8] A. Serani, M. Diez, C. Leotardi, D. Peri, G. Fasano, U.Iemma, E.F. Campana, On the use of synchronous and asynchronous single-objective deterministic Particle Swarm Optimization in ship design problems, *International Conference in Engeneering and Applied Sciences Optimization*, Kos, Greece, June 4-6, 2014.

[9] X. Chen, M. Diez, M. Kandasamy, Z. Zhang, E.F. Campana, F. Stern, High-fidelity global optimization for shape design by dimensionality reduction, metamodels and deterministic individual swarm, *Engineering Optimization*, in press, 2014. DOI:10.1080/0305215X.2014.895340.

[10] Diez, M., Chen, X., Campana, E.F., Reliability-based robust design optimization for ships in real ocean environment, *12th International Conference on Fast Sea Transportation*, FAST2013, Amsterdam, The Netherlands, 2013.

[11] S. Volpi, M. Diez, N.J. Gaul, H. Song, U. Iemma, K K. Choi, E.F. Campana, F. Stern, Development and validation of a dynamic metamodel based on stochastic radial basis functions and uncertainty quantification, *Structural Multidisciplinary Optimization*, in press, 2014. DOI: DOI 10.1007/s00158-014-1128-5.

Simulation cases for verification of flow noise prediction in the parameter range of interest for naval applications.

Andreas Feymark[1], Mattias Liefvendahl[1,2], Rickard E Bensow[1]
([1]Chalmers University of Technology, Sweden; [2]Swedish Defence Research Agency, FOI)

Flow-generated noise is, for some parameter ranges, an important contribution to the total underwater noise from a ship. Its investigation is of importance both concerning the radiated noise and the self-noise (i.e. interference with acoustic sensors on the ship). A considerable amount of research has been carried out on semi-empirical methods for the estimation of strength and frequency content of sources, see [1] for a comprehensive review. A more recent, and very significant line of development, is to employ CFD to investigate the flow mechanisms responsible for noise generation. Unsteady methods, such as LES, are of particular importance for this purpose. We will present a Ffowcs Williams-Hawkings based approach, quite similar to that used in [2], in which the sources will be computed by integration over so-called porous surfaces. The approach has been implemented by the authors in OpenFOAM and results for test problems will also be reported.

As compared to aeroacoustics, we are interested in a range of much lower Mach-numbers. One effect of this is that the relative source strength of different mechanisms is completely different between aero- and hydroacoustics. In particular, surface sources are more important in hydroacoustics. One aspect of this is that the established test cases of aeroacoustics are not suitable for hydroacoustics, and furthermore there is no well-established validation procedure for the hydroacoustic case. We will present preliminary noise prediction results for a range of test cases including; (i) A small sphere radiating as a pure mono-, di- or quadrupole; (ii) Vortex shedding from a cylinder in cross-flow (for Ma<<1), and; (iii) The propeller in open water condition which also was considered in [2]. The presentation will include a discussion of the suitability of these test cases for validation and benchmarking of this type of noise prediction tools.

References

[1] W. K. Blake, “Aero-hydroacoustics for ships”, Vol. I and II, DTNSRDC-84/010, David Taylor Research Center, 1984.

[2] S. Ianniello, R. Muscari and A. Di Mascio, “Ship underwater noise assessment by acoustic analogy. Part I: Nonlinear analysis of a marine propeller in a uniform flow”, J. Mar. Sci. Technol., vol.18, pp. 547-570, 2013.

OpenFOAM investigations of a flushed water-jet inlet performance

Authors:

A. Gattoronchieri	University of Genova	-mail a.gattoronchieri@gmail.com
C. Cravero	University of Genova	-mail cravero@unige.it

INTRODUCTION

In the last two decades, pulled by the growing market of the fast craft, the water-jet and its interaction with the hull has been widely studied [1, 2]. The water-jet inlet is fundamental for the overall propulsion performance, various experimental and numerical results have been published and it's still a hot topic for engineers. The necessity of considering the three-dimensional viscous flows in the numerical simulations has been pointed out by Bulten [2] and previous authors. The here reported study involves an intense simulation campaign aimed at the understanding of the capability of the open source CFD code OpenFOAM to predict the flow features in a flushed water-jet inlet. The well documented experimental campaign presented by Brandner and Walker in 2007 [4] has been chosen as a benchmark for the numerical simulation.

EXPERIMENTAL SETUP

The experiments has been carried out in the AMC Tom Fink Cavitation Tunnel, a closed-circuit variable-pressure water tunnel. The general arrangement of the experimental setup is reported in Figure 1. More detailed information on the tunnel and water-jet inlet test loop are given in Brandner and Walker [3]
The experiments have been carried out with both natural test section boundary layer and thickened boundary layer. The thickened boundary layer has been generated with a saw-toothed fence chosen from a range of devices tested by Brandner and Walker (2001). This device produces a 30 mm increment of the natural boundary layer thickness that was 20 mm maintaining a turbulence and velocity distribution similar to those generated on a flat plate. The boundary layer thickness and velocity distribution have been measured in two different locations, named upstream and ramp, by means of 1.6 mm diameter total head tube and wall static tap in the plane of the tube tip. The model has been fitted with 17 wall tappings on the centerline of the ramp and upper half of the duct to measure the longitudinal distribution of static pressure over the entire inlet length. Furthermore three pressure tappings have been placed at the lip inlet to evaluate the lip incidence and a rotatable pipe length instrumented with Pitot rakes, three-hole cobra probes and pressure tappings, have been fitted downstream of the inlet to investigate the flow properties at the notional pump face, where the duct diameter is 150 mm. The location of model inlet instrumentation and the boundary layer thickener are shown in Figure 2 together with overall dimensions of the test section. Full details of the instrumentations are reported in the original paper. The most significant experimental condition has been chosen for the CFD simulations Rn 1x106, temperature 17° C and IVR values 1.0, 1.5, 2.0.

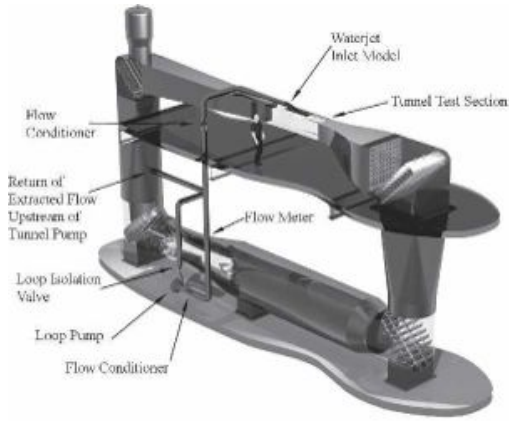

Figure 1: Water-jet test loop

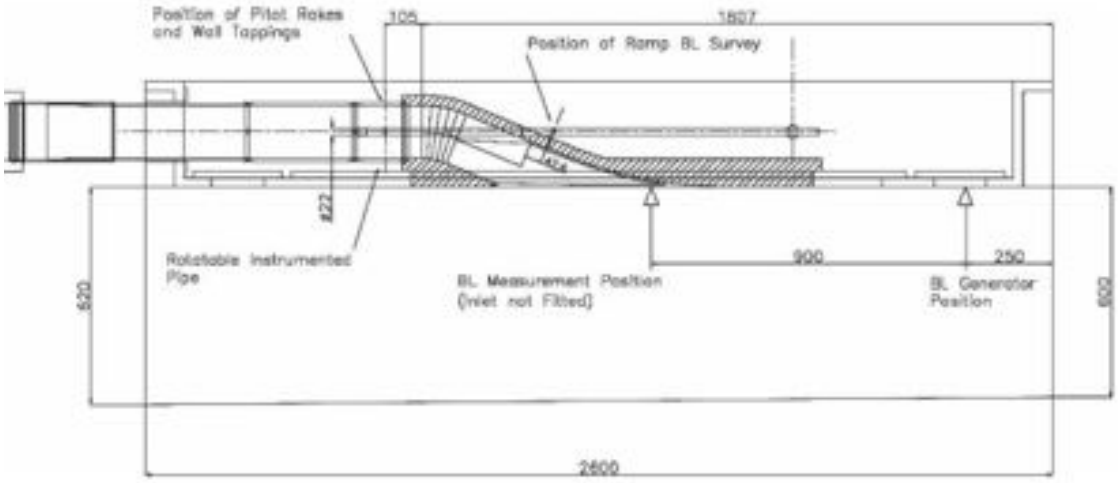

Figure 2: Test section and location of model instrumentations and boundary layer thickener

NUMERICAL MODEL

A computational domain coincident with the test section has been chosen for the simulations in order to reduce the computational costs and the outlet water-jet boundary has been extend to prevent the influence of the boundary conditions on the measurement's sections. A hybrid hexahedral-tetrahedral meshing techniques has been considered and a mesh sensitivity study has been carried out together with the testing of different turbulence models (Lien Cubic Low Reynolds k-epsilon, k-Omega-SST, Spalart-Allmaras) to understand their effect on flow separation prediction. The commercial software ANSYS mesh has been used to generate several meshes with different refinements varying between 0.5 and 3.5 millions of elements. Special attention has been paid to the prism layer generation: the total thickness have been defined in function of the expected boundary layer height, as visible in Figure 4, meanwhile the Y+ has been varied to satisfy the requirements of different wall treatment. The results achieved with the wall functions and with the low-Reynolds models have been compared in an earlier stage and this second approach has been adopted for further simulations.

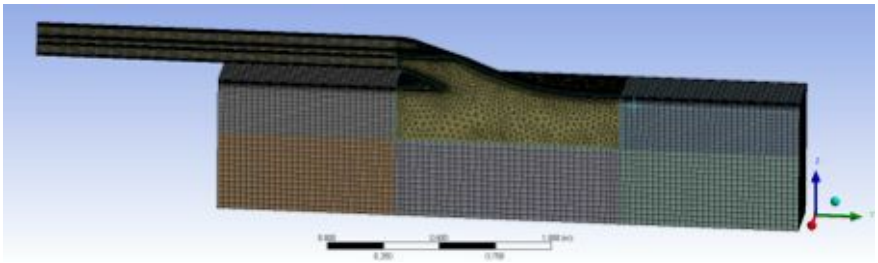

Figure 3: simulation domain meshed with hybrid hexahedral-tetrahedral meshing techniques

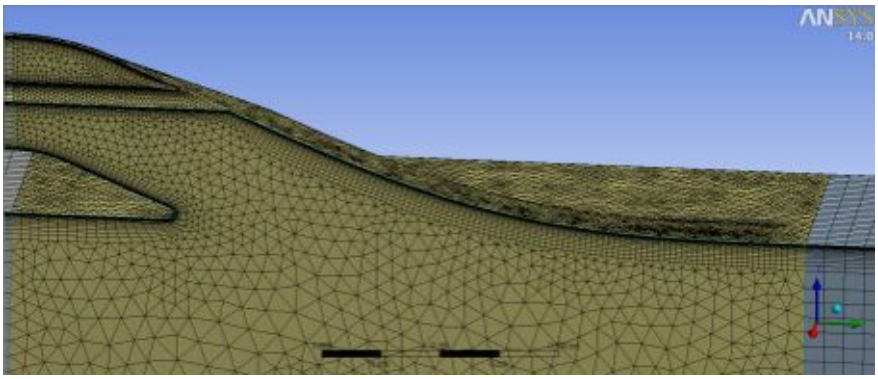

Figure 4: Detail of the prism layer

The open source CFD code OpenFOAM has been chosen for the simulation campaign. The simulations have been initialized with a potential flow solution and then performed as steady state RANSE with simpleFoam. The usual linear-upwind interpolation scheme has been chosen. Some parameters have been used to monitor the convergence: the residuals, the trend of ramp and shaft's force coefficient and the development of the boundary layer velocity distribution.

RESULTS

It has been proven by Walker and Brandner that the flow pattern in the inlet duct is strictly related to upstream boundary layer. For these reasons, in order to obtain a similar velocity profile at the upstream location the velocity distribution at inlet has been calculated with the flat plate theory and set as numerical boundary. Figure 5 shows the comparison between the boundary layer at upstream point calculated with uniform and non-uniform velocity inlet distributions together with the experimental values for the natural boundary layer case. This correction is necessary to take into account the cavitation tunnel boundary layer, for the natural case, and also the effects of the thickener for the triggered configurations.

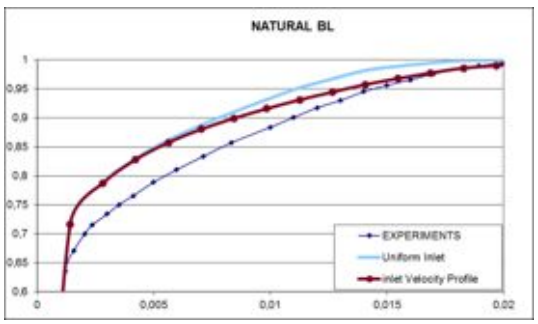

Figure 5: upstream boundary layer for different inlet boundary conditions

Figure 6 and 7 present the comparison between the numerical and experimental boundary layer velocity distributions for the natural boundary layer and thickened boundary layer respectively. Taking into account that the computed upstream boundary layer presents some difference with the measured one, especially in the lower zones, the

velocity profile calculated at the ramp for the different IVR are in good agreement with the experimental results. The flow separation that occurs for IVR=2 for the natural boundary layer is well predicted whereas for the thickened boundary layer the computed velocity distributions differs from the experimental data. In the simulations shown in figure 7, the downstream pressure gradient, related to the IVR, influences the upstream boundary layer.

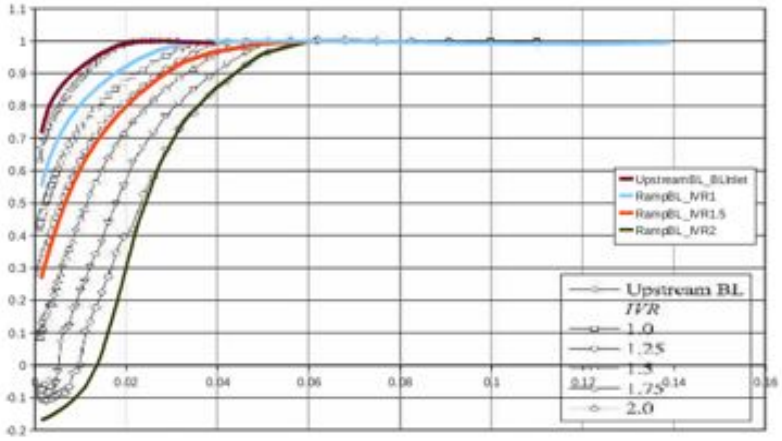

Figure 6: Ramp boundary layer velocity profiles with natural wall boundary layer

Figure 8 shows the distribution of the axial velocity measured along a vertical line located at the notional pump face divided by the average outlet velocity for the natural boundary layer. The numerical simulations confirm what has been pointed out in the experimental results, the IVR=1 produces the best flow uniformity among the three simulated values, Brandner and Walker identified the optimum at 0.75, otherwise at higher IVR there is a deficit at the top of the disc (left side of the chart). The agreement between the CFD and the experimental results is really good on the bottom of the duct for all inlet velocity ratio whereas on the top the accuracy of the numerical results decreases for higher IVR. Even if the general trend is well captured the CFD over estimates the regions of separated flow. This is even more evident in Figure 9 where the experimental results highlight a larger influence of the boundary layer in the flow separations. These results confirm the difficulties in the prediction of the flow separation pointed out in Figure 7.

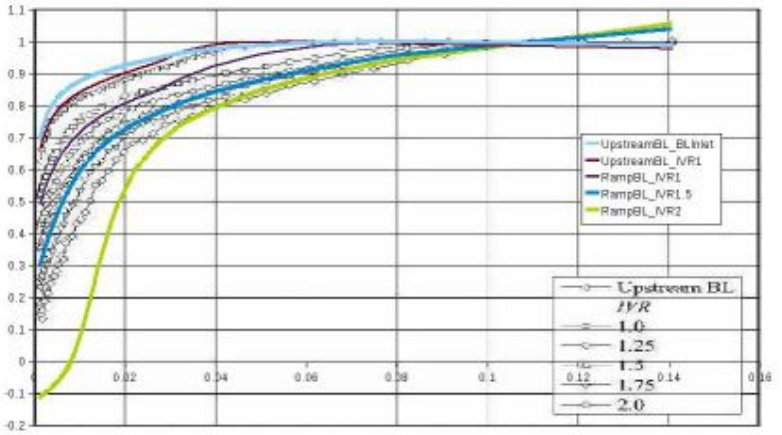

Figure 7: Ramp boundary layer velocity profiles with thickened wall boundary layer

Figures 10 and 11 show the ramp/duct upper centerline pressure coefficient distribution from the toe of the ramp to the notional pump face with surface arc length, x, for the natural and thickened boundary layer cases, respectively. This results are of particular interest because the ramp pressure gradient is a major factor affecting ramp separation and at the same time provides an additional information to evaluate the reliability of the numerical solution. The value at the toe of the ramp point out that some difference are already present in the upstream field. This difference can be due to the approximations made in the inlet boundary condition but also to some small difference in the curvature of the first part of the upper wall. This second hypothesis seems to be confirmed by the pressure gradient in the first 300 mm of the duct. The pressure gradient before of the shaft intersection is well predicted for smaller IVR with both the wall boundary layer. On the other hand for IVR = 2 the pressure coefficient is over predicted for the taps along the ramp except for the last before the shaft intersection. The value measured by the last tap for the higher IVR has been identified by Brandner and Walker as “the ultimate limit on pressure rise before separation occurs”. In the numerical simulation this value is reached in an earlier point along the ramp and is maintained almost constant until the shaft intersection. This results confirm the limit value for the pressure coefficient identified in the experimental results

and quantify the over prediction of the separation point. For IVR= 1.5 the pressure gradient before the shaft intersection has been correctly predicted for the thickened boundary layer, whereas for the natural boundary layer the value has been over predicted. After the shaft intersection the pressure coefficient calculated for the two higher IVR is in really good agreement with the experimental results. The positive pressure gradients for IVR=2 indicate the presence of a separated/low-speed zone that is no longer present at IVR=1.5. The pressure coefficient distribution for the smallest inlet velocity ratio is due to the interaction between the shaft's wake and the duct bend; in this case a the steady state simulation is not adequate close to the shaft but overall good agreement with the experiments is obtained. The pressure rise achieved in correspondence of the pump face, which is fundamental for the pump cavitation number, is always correctly predicted.

The contour of the total pressure coefficient, reported in figure 12 and 13, show that the total pressure gradients have been slightly over predicted especially for the thickened boundary layer at higher IVR, however increasing the upper limit of the Cp contour (of a value always smaller than 0.1), it is possible to observe that the flow pattern has been well captured by the numerical solutions. The differences are acceptable considering the inlet condition approximations. Similar behavior has been observed for the contour of the ratio between the local axial velocity and the mean outlet velocity, not presented here for the sake of shortness.

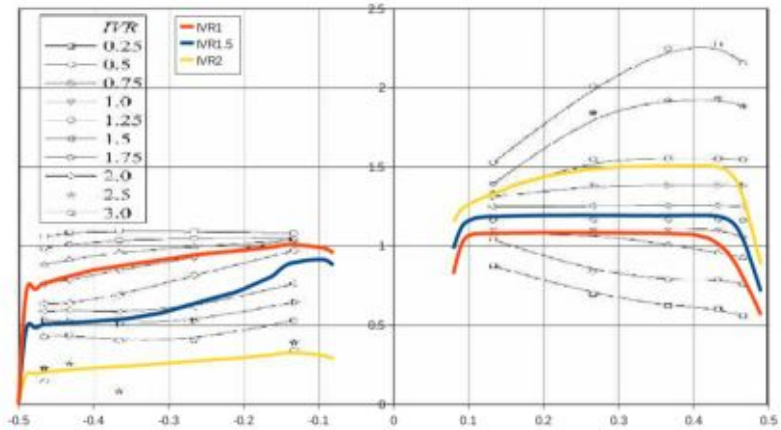

Figure 8: Pump face vertical distribution of axial velocity for natural boundary layer

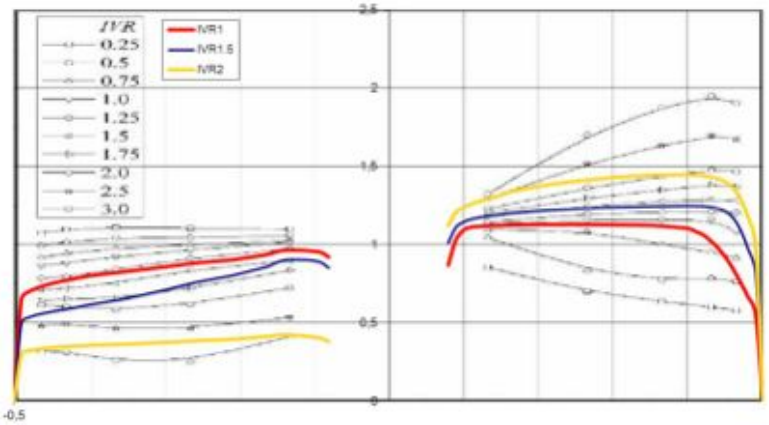

Figure 9: Pump face vertical distribution of axial velocity for thickened boundary layer

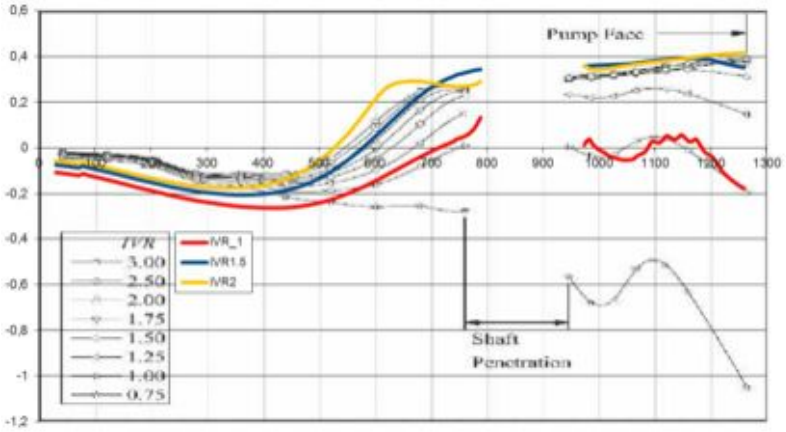

Figure 10: Ramp pressure coefficient Cp with natural wall boundary layer

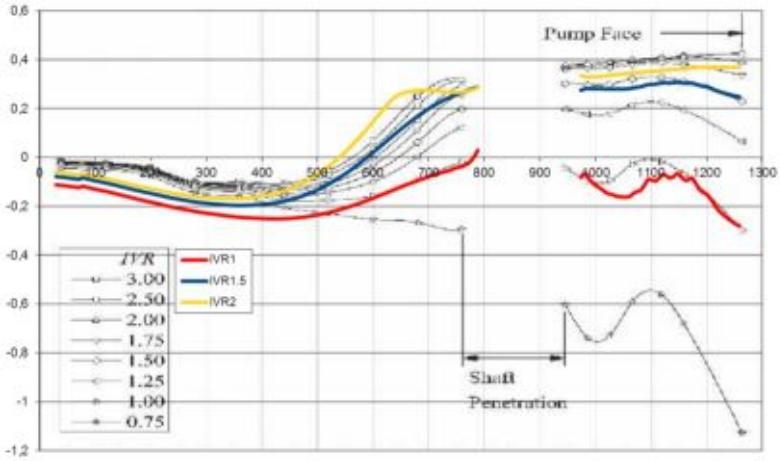

Figure 11: Ramp pressure coefficient Cp with thickened wall boundary layer

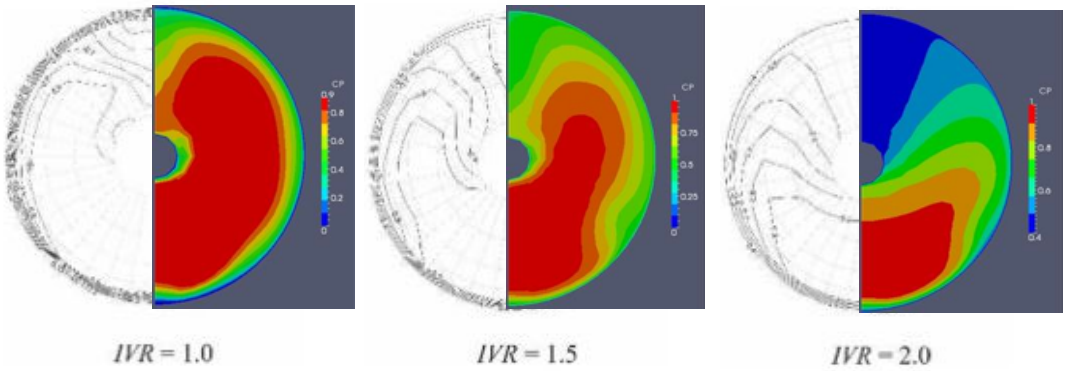

Figure 12: Pump face total pressure coefficient distributions with natural wall boundary layer

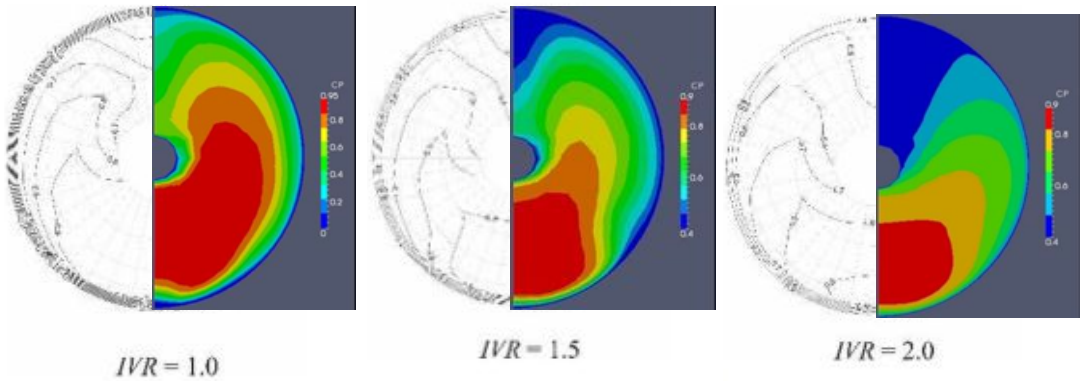

Figure 13: Pump face total pressure coefficient distributions with thickened wall boundary layer

In Figure 14 the ratio between the local velocity magnitude and the free stream velocity is plotted at different IVR to visualize the influence of the boundary layer thickness on the velocity distribution at the symmetry plane. In this figure it is also possible to observe the reduction of the boundary layer thickness in correspondence of the upstream measurements points due to the curvature of the upper wall. The stagnation point can be easily identified especially for the highest IVR when it moves towards the top of the lips and the velocity gradient in the lower part becomes stronger. This phenomena is less evident for the thickened boundary layer case because the ingested flow is more uniform.

A numerical evaluation of the scale effect in case of installation of a different pump has been made as a preliminary step for a future development of this activity. The inlet geometry has been scaled by a factor 1.967, the pump flow rate has been imposed at IVR=1.5 and then adjusted to obtain the different IVR value. The above choice lead to a Reynolds number of $3x10^6$. Two different wall boundary layers have been tested and the total thickness has been scaled geometrically in order to maintain the same ratio with the inlet diameter. No relevant scale effects have been detected except for a reduction of the low speed/separation zones and consequently the rise of the pressure coefficient at the pump inlet for IVR > 1.5. The higher Reynolds number is the main factor for the smaller separation detected in the scaled model. This is in accordance with the trend identified by Brandner and Walker for the range of Re between $0.5x10^6$ and $1.5x10^6$.

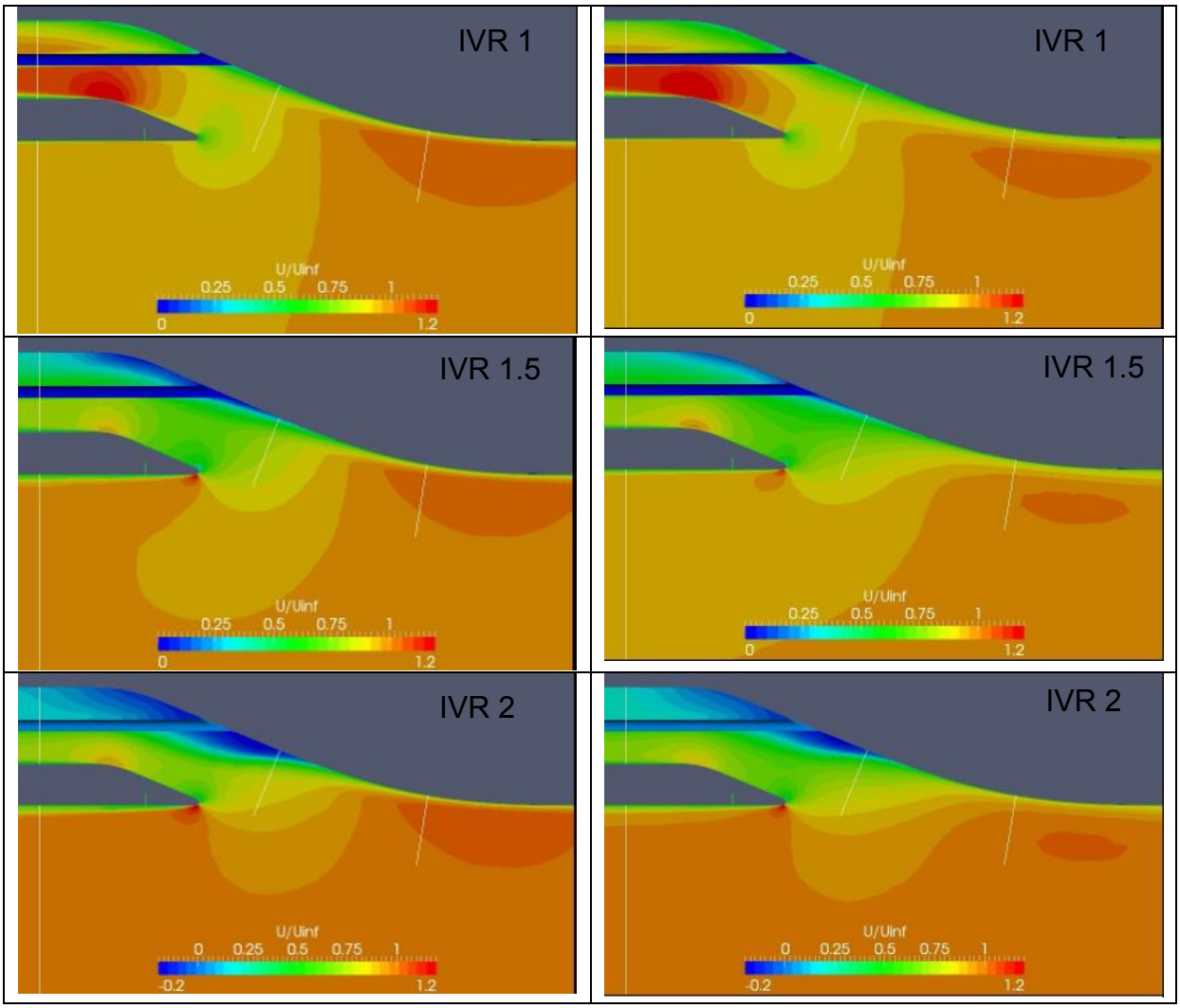

Figure 14: velocity distribution at the symmetry plane for natural and thickened boundary layer, left and right side respectively, measured at IVR 1, 1.5, 2.

FUTURE DEVELOPMENTS

A numerical cavitation model is currently under investigation to simulate the dynamic sheet cavities on the inlet lip reported by Brandner and Walker. The influence of the flow pattern generated by the water-jet inlet on the performance of a mixed flow pump will be evaluated.

ACKNOWLEDGMENTS

The authors wish to acknowledge the supervision of prof. Rickard Bensow, the assistance of Mr. Joel Guerrero in the OpenFOAM setup and the support of Termomeccanica Pompe Spa.

REFERENCES

1. Tom J.C. Van Terwisga, 1997: Waterjet-hull interactions, PhD Tesis Delft University
2. Brandner, P. A. and Walker, G.J., 2001: A waterjet test loop for the Tom Fink Cavitation Tunnel, proceedings, Waterjet Propulsion Conference III, RINA, February 20, Gothenburg, Sweden, paper no. 1, 11 pp.
3. Norbert Willem Herman Bulten, 2006: 'Numerical Analysis of a Waterjet Propulsion System Norbert Willem', Phd Thesis
4. Brandner, P. A. and Walker, G.J. 2007: An Experimental Investigation Into the Performance of a Flush Water-Jet Inlet, Journal of Ship Research, Vol. 51, No. 1, March 2007, pp. 1–21

Potential of Chaotic Iterative Solvers for CFD

J. Hawkes[a,c*], G. Vaz[b], S. R. Turnock[c], S. J. Cox [d], A. B. Phillips[c]

[a]MARIN Academy; [b]Research and Development Department; MARIN, Wageningen, NL.
[c]Fluid Structure Interactions (FSI); [d]Computational Engineering and Design (CED);
University of Southampton, UK.

1 Introduction

Computational Fluid Dynamics (CFD) has enjoyed the speed-up available from supercomputer technology advancements for many years. In the coming decade, however, the architecture of supercomputers will change, and CFD codes must adapt to remain current.

Based on the predictions of next-generation supercomputer architectures it is expected that the first computer capable of 10^{18} floating-point-operations-per-second (1 ExaFLOPS) will arrive in around 2020. Its architecture will be governed by electrical power limitations, whereas previously the main limitation was pure hardware speed. This has two significant repercussions [14, 17, 25]. Firstly, due to physical power limitations of modern chips, core clock rates will decrease in favour of increasing concurrency. This trend can already been seen with the growth of accelerated "many-core" systems, which use graphics processing units (GPUs) or co-processors. Secondly, inter-nodal networks, typically using copper-wire or optical interconnect, must be reduced due to their proportionally large power consumption. This places more focus on shared-memory communications, with distributed-memory communication (predominantly MPI - "Message Passing Interface") becoming less important.

The current most powerful computer, Tianhe-2 [26], capable of 33 PFlops, consists of 3,120,000 cores. The first exascale machine, which will be 30 times more powerful, is likely to be 300-times more parallel – which is a massive acceleration in parallelization compared to the last 50 years. This concurrency will come primarily from intra-node parallelization. Whereas Tianhe-2 features an already-large O(100) cores per node, an exascale machine must consist of O(1k-10k) cores per node.

CFD has benefited from *weak scalability* (the ability to retain performance with a constant elements-per-core ratio) for many years; its *strong scalability* (the ability to reduce the elements-per-core ratio) has been poor and mostly irrelevant. With the shift to massive parallelism in the next few years, the strong scalability of CFD codes must be investigated and improved.

In this paper, a brief summary of earlier results [12] is given, which identified the linear-equation system solver as one of the least-scalable parts of the code. Based on these results, a chaotic iterative solver, which is a totally-asynchronous, non-stationary, linear solver for high-scalability, is proposed. This paper focuses on the suitability of such a solver, by investigating the linear equation systems produced by typical CFD problems. If the results are optimistic, future work will be carried out to implement and test chaotic iterative solvers.

2 ReFRESCO

The work presented in this paper focuses on the development of ReFRESCO – a typical viscous-flow CFD code. ReFRESCO solves multiphase, unsteady, incompressible flows with the Reynolds-Averaged Navier Stokes (RANS) equations, complemented with turbulence models, cavitation models and volume-fraction transport equations for different fluid phases [27]. ReFRESCO represents a general-purpose CFD code, with state-of-the-art features such as moving, sliding and deforming grids and automatic grid refinement – but has been verified, validated and optimized for numerous maritime industry problems.

The RANS equations are discretized in strong conservation form using a finite-volume approach with cell-centred collocated variables. The SIMPLE algorithm is used to ensure mass conservation, with pressure-weighted interpolation (PWI) to tackle pressure-velocity decoupling issue arising from the collocated arrangement [16].

Time integration is performed implicitly with first or second-order backward schemes. At each time step, the non-linear system for velocity and pressure is linearized with Picard's method – and a segregated method applied. All non-linearity is tackled by means of an iterative process so-called the outer loop. For each outer-loop iteration, and for each transport equation, an algebraic system of linear equations is solved iteratively until a prescribed residual decay is achieved.

All numerical schemes used to discretize the transport equations (convection schemes, diffusion, gradients, non-orthogonality corrections, eccentricity corrections) apply their low-order contributions implicitly, to the left-hand side of the equation system; and their higher-order contributions explicitly, to the right-hand side of the system, using values from the previous outer loop.

The code is parallelized using MPI and sub-domain decomposition. The grids are partitioned in sub-domains, each one having a layer of common cells so-called ghost-cells. Each of these sub-domains is calculated in its own MPI process. The ghost-cells are treated as normal cells, as far as the numerical algorithms are concerned, and are therefore handled implicitly.

ReFRESCO is currently being developed at MARIN (Netherlands) [8] in collaboration with IST (Portugal) [22], the University of Sao Paulo (Brazil) [24], the Technical University of Delft (the Netherlands) [16], the University of Groningen (the Netherlands) [4] and recently at the University of Southampton (UK) [12].

* *corresponding author's e-mail*: J.Hawkes@soton.ac.uk

3 Strong Scalability Investigation

In previous work [12], ReFRESCO was profiled using *Score-P* [28] to extract timings from the code and its relevant functions. In a CFD code, these functions can be grouped together into the following categories, giving a breakdown of the code (see figure 1.a for illustration):

- **Assembly** – the assembly of each inner-loop linear equation system, including discretization, linearization and face-value interpolation for each transport equation.
- **Solve** – the iterative solving of the linear equation system for each transport equation, in each outer loop.
- **Gradients** – the calculation of gradient values at cell centres, using Gauss theorem.
- **Exchange** – MPI data exchange of cell-centred variables and gradients across ghost cells.
- **Other** – the remainder of the above, including initialization routines.

The results of a typical breakdown, using the well-known KVLCC2 case[2], are shown in figure 1, where the "speedup" is defined as the relative decrease in wall-time with N cores compared to the serial or single-node (16 cores) runtime. The results of the nodal speedup (1.b) show relatively good scalability (up to ≈40k cells-per-core), but hide the intra-node inefficiencies which are important for next-generation machines (with high intra-node parallelization). Graphs which show the speed-up relative to the single-core run-time (1.c) are thus more useful.

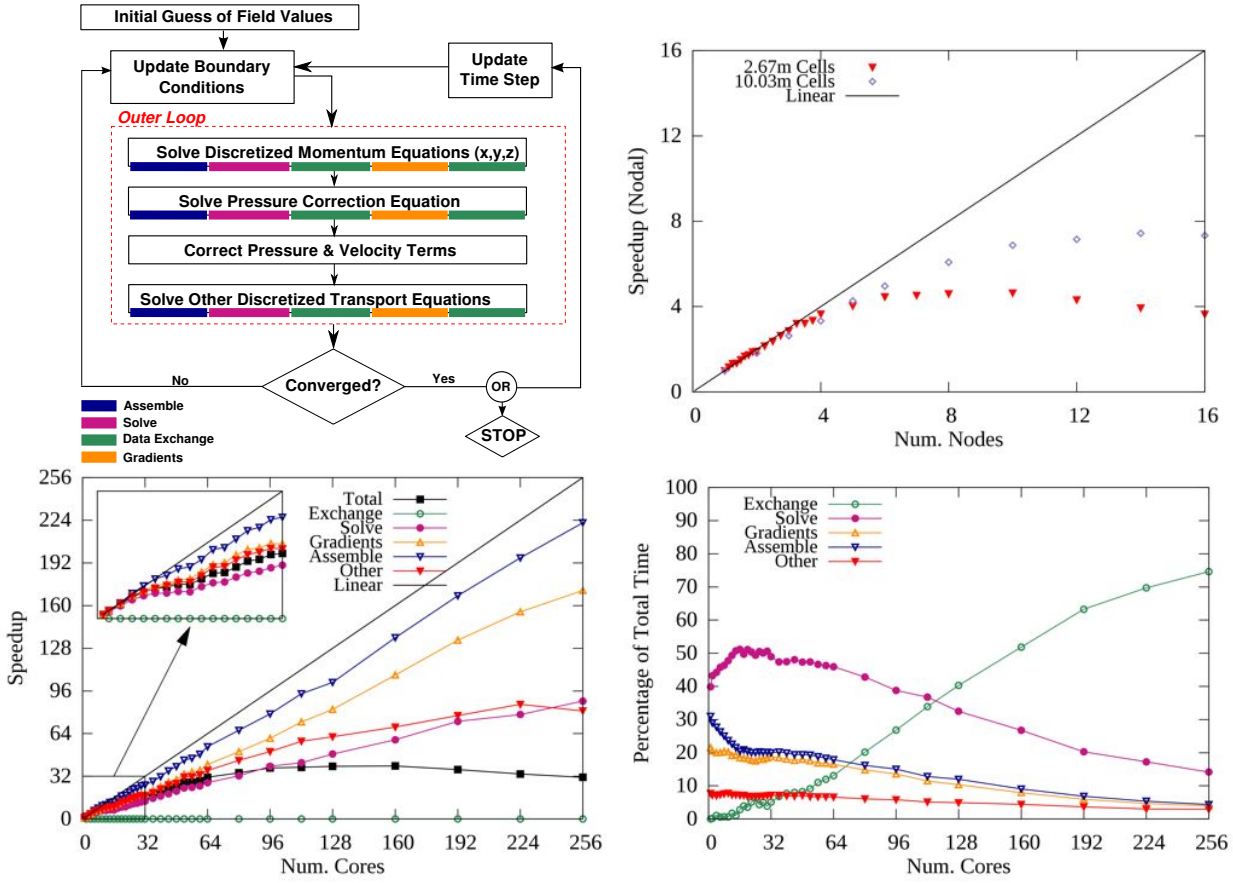

Figure 1: (a) An illustration of the SIMPLE algorithm, with colour-coding relating the various profiled functions of the code. (b) Total scalability of ReFRESCO normalized to single-node runtime, with two different grid sizes. (c) Scalability breakdown of a typical simulation showing the profiled functions individually and (d) the proportions of execution time spent in those routines [12].

The scalability graph (1.c) shows that *assembly* and *gradient* computations scale well, and the relative proportions graph (1.d) shows that these routines account for a very small proportion of run-time. The *other* routines do not scale so well, but are a small contribution to total run-time, so are of little concern.

The *solve* routines are an area for improvement. They exhibit poor scalability and take considerable amounts of total runtime, with particularly poor performance at the shared-memory level due to memory bandwidth or latency. Similarly, the *exchange* routines, which exhibit inverse scalability, are also a concern at the distributed-memory level. The data exchange is performed using MPI functions, and possibilities to improve this include switching to a hierarchical parallelization scheme (*i.e.* MPI + OpenMP) – as in [9, 10].

Up to ≈24k cells-per-core the iterative solver is the main limitation to scalability and should form the focus of future work, particularly as shared-memory parallelization grows. However, the data exchange issues are also an interesting area for further research and should not be neglected.

[2]KRISO Very Large Crude Carrier 2: half-body; two-equation κ-ω shear-stress transport (SST) turbulence model [21]; single-phase; based on wind-tunnel experiments [18]; 1000 outer loops; 2.67m structured grid.

4 Background to Iterative Solvers

The results shown in figure 1 used a Krylov subspace solver (GMRES - Generalized Minimal Residual method) with a Block Jacobi pre-conditioner [3]. Other Krylov methods such as BiCGStab (Bi-Conjugate Gradient Squared Stabilized) were tested with similar results. Other pre-conditioners were also tested, but Block Jacobi was (by far) the most scalable [12].

The Krylov solvers are powerful, but create a bottleneck due to the computation of inner products, which require global communication and synchronization in the form of MPI reductions. Efforts have been made to reduce the synchronization penalty of the Krylov solvers (down from two synchronized reductions to one, per iteration), with considerable improvements, but the bottleneck remains [20, 29].

By returning to simple, so-called stationary methods, it may be possible to obtain better performance in the limits of strong scalability. The task of a stationary solver (or, indeed, any iterative solver), for each transport equation in each outer loop, is to solve $\mathbf{Ax} = \mathbf{b}$, where $\mathbf{x}$ is the unknown solution vector, $\mathbf{A}$ is an n-by-n sparse coefficient matrix, $\mathbf{b}$ is the constant right-hand-side (RHS) vector, and n is the number of elements.

Beginning with an initial guess for $\mathbf{x}$, the system can be solved iteratively:

$$\mathbf{x}^k = -\mathbf{D}^{-1}(\mathbf{L}+\mathbf{U})\mathbf{x}^{k-1} + \mathbf{D}^{-1}\mathbf{b} \tag{1}$$

where $\mathbf{D}$ is the diagonal of $\mathbf{A}$, and $\mathbf{L}/\mathbf{U}$ are the lower- and upper-triangles respectively. The notation k represents the iteration number. This is the Jacobi method, and the matrix $\mathbf{D}^{-1}(\mathbf{L}+\mathbf{U})$ is the iteration matrix, $\mathbf{M}$. Each equation (from 1 to n) can be solved (*a.k.a.* relaxed) independently as follows:

$$x_i^k = \left(-\sum_{\substack{j=1 \\ j\neq i}}^{n} a_{ij}x_j^{k-1} + b_i \right) / a_{ii}, \quad i = 1, \ldots, n. \tag{2}$$

where a, x and b are the individual components of $\mathbf{A}$, $\mathbf{x}$ and $\mathbf{b}$ respectively. At the end of each iteration the new values of $\mathbf{x}$ must be globally communicated before the next iteration can begin.

See Barrett et al. [5] for more information on a variety of iterative solvers – Krylov, stationary and otherwise.

5 Chaotic Iterative Solver

In 1969, Chazan & Miranker [7] proposed the concept of *Chaotic Relaxation* whereby several processes (distributed-memory processes or shared-memory threads) never synchronize. Instead, the processes freely pull values of off-diagonal $\mathbf{x}$ from memory whenever they are required, and push new values for the diagonal x_i whenever they have been relaxed. In this way, each relaxation uses the values of $\mathbf{x}$ from the latest iteration that is available – this could be several iterations behind the current relaxation iteration ($s = 1,\ldots,$n), or even ahead of it ($s < 0$):

$$x_i^k = \left(-\sum_{\substack{j=1 \\ j\neq i}}^{n} a_{ij}x_j^{k-s} + b_i \right) / a_{ii}, \quad s < s_{max}, \quad i = 1, \ldots, n. \tag{3}$$

The order in which the n equations are relaxed is completely arbitrary. With this scheme, processes never need to wait for each other. Although communication must still occur, it can be entirely *asynchronous*, thereby making efficient use of memory bandwidth and computational resources. Processes may even iterate multiple times on the same data if memory bandwidth is completely saturated, making the best use of the available hardware. Whilst this method is based on the stationary Jacobi method, s can vary between iterations implying that chaotic methods are actually non-stationary.

Chazan & Miranker proved that this iterative scheme will converge for any real iteration matrix if $\rho(|\mathbf{M}|) < 1$ so long as s_{max} is bounded. $\rho(\cdot)$ denotes the *spectral radius* (the absolute value of the maximum eigenvalue) and $|\cdot|$ represents a matrix where all the components have been replaced with their absolute values. The implications of s_{max} being bounded is simply that if two relaxations take different amounts of time (either due to imbalanced hardware or relaxation complexity), they cannot be left completely independent indefinitely, such that s could potentially become infinite. Baudet [6] went on to prove that $\rho(|\mathbf{M}|) < 1$ is a necessary condition for convergence for any $s_{max} \leq k$. Baudet denoted the relaxation method where $s = 0, ..., k$ as an *asynchronous method* but the terms "chaotic" and "asynchronous" are often used interchangeably. Bahi [2] further showed that $\rho(|\mathbf{M}|) = 1$ is also valid, if $\mathbf{M}$ is singular and s_{max} is bounded.

Preconditioning of $\mathbf{A}$ usually serves to reduce the condition number and spectral radius of the equation system; however, preconditioning is rarely applied to simpler solvers, since almost all preconditioners are more complex than the solver itself.

At their conception, chaotic methods were considerably ahead of their time. Although created specifically for parallel computing, the concurrency of state-of-the-art supercomputers in 1969 was too small to utilize the methods efficiently. With new architectures, the true potential of chaotic methods may be realized. Anzt et al. [1] begins to show the use of chaotic or asynchronous methods on a modern architecture, using the GPU to perform block-relaxations. Despite the intrinsic loss in global convergence rates, Anzt et al. showed that chaotic iterative methods provided a boost in real-time convergence rates compared to standard stationary methods

(*i.e.* Jacobi) – although comparisons to the more advanced Krylov methods were not performed, and the chosen matrices were not derived from CFD applications.

Chaotic methods provide a means to exploit massive parallelism due to the absence of synchronization points. They are also implicitly heterogeneous, allowing seamless cooperation between CPUs, GPUs or co-processors running at different speeds – allowing all computational resources to be used to maximum capacity with little concern for load-balancing. The convergence criteria, $\rho(|\mathbf{M}|) < 1$, is stricter than that of standard stationary methods which only require $\rho(\mathbf{M}) < 1$, and stricter still than the oft-used Krylov methods (which have no such requirements). The following section aims to determine if a range of standard CFD test cases will produce matrices that satisfy the criteria – the results of which will determine whether chaotic solvers are worth implementing and investigating.

6 Suitability of CFD Equation Systems

In this section, un-preconditioned matrices are extracted from a number of test cases. The matrices are analyzed to obtain key statistics and determine their suitability to chaotic methods.

For each matrix, it is possible to plot the connectivity graph, following the methods of Hu [15] – this gives a qualitative, visual insight into the sparse matrices by graphically connecting the elements of the matrix. The largest eigenvalues of $|\mathbf{M}|$ can be found using ARPACK [19] routines, and plotted in an Argand diagram – for $\rho(|\mathbf{M}|) < 1$ all eigenvalues must lie within a unit circle. The sparsity pattern of the matrix $\mathbf{A}$ may also be plotted directly to give qualitative clues on the matrix structure.

Assuming a satisfactory spectral radius, the *condition number* (the ratio of the largest to smallest eigenvalue) of the original matrix $\mathbf{A}$ can be used to assess the difficulty of convergence ($\propto$ number of iterations required). The condition number is computed using a 1-norm condition estimator [11].

As explained in section 2, all higher-order influences on the linear equation system are shifted to the RHS (the $\mathbf{b}$ vector) – which strongly decouples many common user settings (such as discretization scheme) from the format of the iteration matrix $\mathbf{M}$.

Changes in element-count and geometry may have a more profound effect on the matrices, and special equations (such as volume-fraction and cavitation equations) should also be examined. Thus the following test cases are chosen for increasing geometric complexity and their additional equations.

- **Lid-Driven Cavity Flow** (LDCF) on a number of 2D structured grids (225, 14.4k, 1m elements); no turbulence model; see [16].
- **NACA0015** hydrofoil (15° angle-of-attack) on a two-dimensional multi-block structured grid (28k elements) with a two-eqn. κ-ω SST turbulence model [21]; see [23].
- **KVLCC2** (half-body, no free surface, single-phase) on a three-dimensional multi-block structured grid (317k elements) and a hexahedral unstructured grid (**U**) with hanging nodes (167k elements); κ-ω SST turbulence; see [12].
- **NACA0015(C)**, as before, but with a Sauer-modified cavitation model; κ-ω SST turbulence; see [13].
- **Dambreak**, a homogeneous two-phase, three-dimensional problem with a simple structured grid (16k cells) with a volume-fraction equation; no turbulence; see [27].
- **Cylinder**, low Reynold's number, unsteady (10 timesteps) on a structured grid (4.3k elements); no turbulence; poor initial flow estimation; see [24].

The matrices were extracted at outer loops 1, 5, 10, 50 and 100. The momentum equations (in x, y and z) are identical, due to the way in which they are assembled. The differences between $\rho(|\mathbf{M}|)$ and $\rho(\mathbf{M})$ were negligible, implying that $\mathbf{M}$ is mostly positive.

Figure 2 shows the qualitative view of the simple 2D LDCF, the more complex 2D hydrofoil, and the 3D KVLCC2 case at the 5^{th} outer loop. The connectivity graphs show resemblance to the underlying geometry and mesh structure – for example, the NACA0015 connectivity resembles the O-grid from which it arose.

The sparsity patterns are interesting from a computational perspective, since they highlight communication patterns when the matrix is split into parallel blocks. Where off-diagonal components of an equation are spread out, more cross-communication between processes is required – since the variables will be stored in parts of memory not directly accessible. The sparsity is closely related to the structure of the grid and the cell-numbering – the more complex KVLCC2 case is highly complex compared to the cartesian, structured LDCF grid.

Table 1 shows the quantitative results from all the test cases, taking the maximum values of all the extracted outer loops. The condition number appeared to be higher for more complex cases, such as the 3D KVLCC2 case, although there was little correlation with flow features or mesh structure. In all cases, $\rho(|\mathbf{M}|) \leq 1$, meeting the requirements for chaotic solvers.

The pressure equation, which takes a Poisson-equation format, was singular for the LDCF and Dambreak case, where only Neumann boundary conditions are applied. In all the other cases, a Dirichlet condition on the outflow reduced the spectral radius, although it was still close to one. In the LDCF-225 case and the first timestep of the unsteady cylinder, the spectral radius was also very high – these cases both feature complex flows with simple initial-flow estimations and coarse meshes; this large discrepancy and poor resolution could be the reason for the the near-singular matrices (however, the condition number was still low).

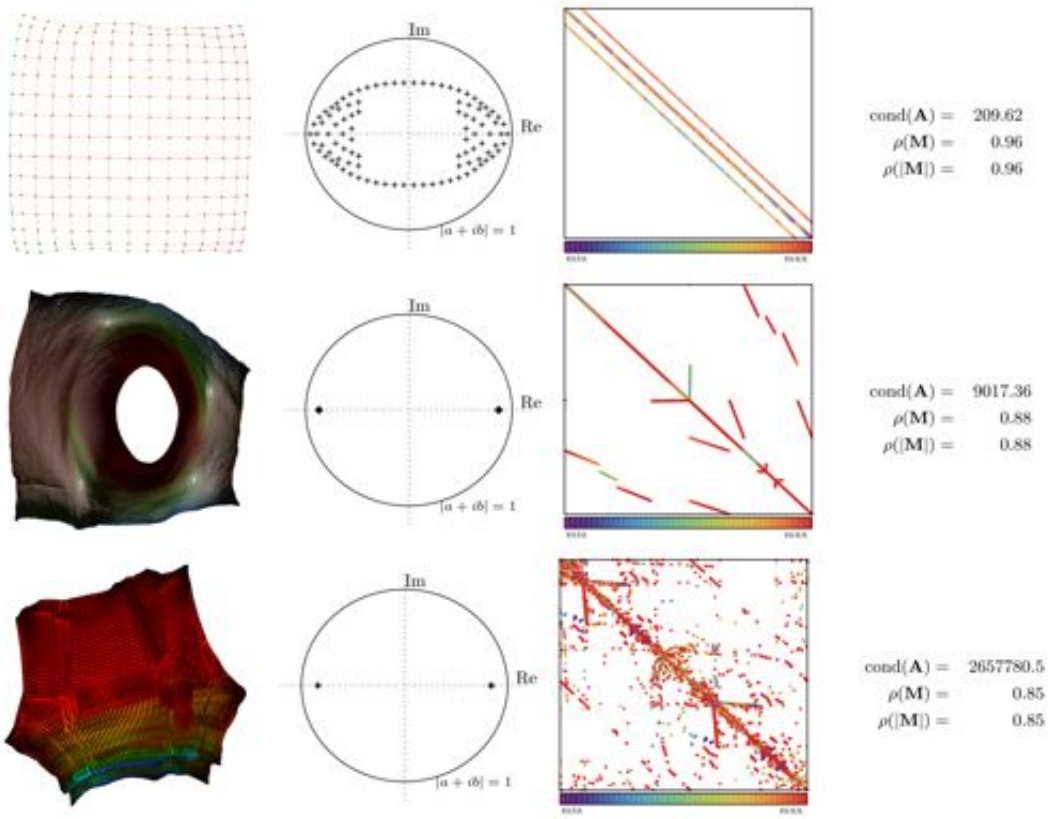

Figure 2: Connectivity, 100 largest eigenvalues, sparsity and statistics for the momentum equation (outer loop 5). [Top] LDCF-225, [Middle] NACA0015-28k and [Bottom] KVLCC2-317k.

Additional matrices for the KVLCC2 case (up to 2.67m elements) and a 21.7m-element INSEAN E779A propeller (with sliding interface) were tested, but could not be fully post-processed due to memory requirements – nonetheless, the original matrices ($\mathbf{A}$) were diagonally dominant: a sufficient condition for $\rho(|\mathbf{M}|) < 1$.

Table 1: Quantitative results for a range of test matrices, showing condition number and spectral radius for momentum-, pressure-, turbulence- and free-surface-/cavitation-equations.

	Mom.		Pres.		Turb. 1		Turb. 2		V.F./Cav.	
	cond($\mathbf{A}$)	$\rho(\|\mathbf{M}\|)$	cond($\mathbf{A}$)	$\rho(\|\mathbf{M}\|)$	cond($\mathbf{A}$)	$\rho(\|\mathbf{M}\|)$	cond($\mathbf{A}$)	$\rho(\|\mathbf{M}\|)$	cond($\mathbf{A}$)	$\rho(\|\mathbf{M}\|)$
LDCF-225	210	0.955	9.4·e17	1.000						
LDCF-14.4k	7	0.500	2.1·e18	1.000						
LDCF-1m	4	0.500	2.9·e19	1.000						
NACA0015	9.0·e3	0.884	6.53·e6	0.999	4.5·e3	0.849	4.8·e3	0.851		
NACA0015(C)	6.3·e3	0.734	4.67·e6	0.999	5.1·e3	0.688	5.2·e3	0.690	2.3·e8	0.240
KVLCC2	2.6·e6	0.845	2.63·e8	.9999	1.2·e7	0.588	1.2·e7	0.594		
KVLCC2 (unst.)	5.2·e6	0.810	5.4·e7	.9999	8.3·e6	0.726	7.7·e6	0.728		
Dambreak	105	0.048	5.6·e18	1.000					7	0.048
Cylinder (t=1)	111	.9999	1.1·e6	.9999						
Cylinder (t=2–10)	4.4·e2	0.520	1.1·e6	.9999						

7 Conclusion

Chaotic iterative solvers have been proposed as a means to improve the scalability of a typical CFD code, in preparation for a paradigm-shift towards massive parallelization in supercomputing architectures. The removal of synchronization points from one of the major bottlenecks in the code (the *solve* routines) could lead to a vast improvement in scalability, although the loss in convergence rate which compromises the speed-up is difficult to predict. The matrices which the chaotic solver would be required to solve have been extracted and evaluated, and it has been determined that necessary and sufficient conditions for convergence have been satisfied.

Future work will focus on implementing a chaotic solver in a hierarchical parallel environment (MPI & OpenMP & GPU/coprocessor). At the shared-memory (OpenMP) level, issues associated with double-precision atomic operations and intra-core cache-coherency will be encountered; and methods must be investigated to hide any cache latency that may occur. Maintaining true asynchronicity across memory-boundaries (for example, across nodes, using MPI) will also be a unique challenge – since most MPI communications require at least two nodes to synchronize. One-sided MPI operations may be investigated to allow direct access to non-shared memory. Similarly, true asynchronicity between host processes and attached GPUs/coprocessors must be achieved – perhaps by assigning processes on the host processor purely for these communications.

From a numerical perspective, it is best if each equation in the system is iterated the same number of

times/at the same speed (*i.e.* the equations do not become too out-of-synch). Regulating this, by moving equations to different processes dynamically, may be beneficial for overall performance and may be necessary for convergence when the pressure equation is singular.

Above all, however, is the intrinsic difficulty of debugging a chaotic scheme. As soon as instrumentation points are added, the chaotic order of the process changes – indeed, every time the process is run, different numerical results and convergence rates may be obtained.

Chaotic methods introduce a number of unique challenges, but could create a significant speed-up for CFD on current and next-generation supercomputers. Whilst it has been shown that the chaotic methods will converge for the relevant equations, it remains to predict their real-world performance for CFD applications; and to implement and test them successfully.

References

[1] Anzt, H., Tomov, S., Dongarra, J. & Heuveline, V. (2013, December). A Block-Asynchronous Relaxation Method for Graphics Processing Units. *Journal of Parallel and Distributed Computing*, 73(12):1613–1626.

[2] Bahi, J. (2000). Asynchronous Iterative Algorithms for Nonexpansive Linear Systems. *Journal of Parallel and Distributed Computing*, 60:92–112.

[3] Balay, S., Abhyankar, S., Adams, M. F., Brown, J., Brune, P., Buschelman, K., Eijkhout, V., Gropp, W. D., Kaushik, D., Knepley, M. G., McInnes, L. C., Rupp, K., Smith, B. F. & Zhang, H. (2013). PETSc Users Manual. Technical Report ANL-95/11 - Revision 3.4, Argonne National Laboratory. `http://www.mcs.anl.gov/petsc`.

[4] Bandringa, H., Verstappen, R., Wubbs, F., Klaij, C. & Ploeg, A. (2012, October). On Novel Simulation Methods for Complex Flows in Maritime Applications. *Numerical Towing Tank Symposium (NUTTS)*, Cortona, Italy.

[5] Barrett, R., Berry, M., Chan, T. F., Demmel, J., Donato, J., Dongarra, J., Eijkhout, V., Pozo, R., Romine, C. & der Vorst, H. V. (1994). *Templates for the Solution of Linear Systems: Building Blocks for Iterative Methods, 2nd Edition*. SIAM, Philadelphia, PA.

[6] Baudet, G. M. (1978, April). Asynchronous Iterative Methods for Multiprocessors. *J. ACM*, 25(2):226–244.

[7] Chazan, D. & Miranker, W. (1969, April). Chaotic Relaxation. *Linear Algebra and its Applications*, 2(2):199–222.

[8] Eca, L. & Hoekstra, M. (2012, August). Verification and Validation for Marine Applications of CFD. *29th Symposium on Naval Hydrodynamics*, Gothenburg, Sweden.

[9] Gorobets, A., Trias, F. & Oliva, A. (2013, December). A Parallel MPI+OpenMP+OpenCL Algorithm for Hybrid Supercomputations of Incompressible Flows. *Computers & Fluids*, 88:764–772.

[10] Gropp, W. D., Kaushik, D. K., Keyes, D. E. & Smith, B. F. (2001, March). High-Performance Parallel Implicit CFD. *Parallel Computing*, 27(4):337–362.

[11] Hager, W. W. (1984). Condition Estimates. *SIAM Journal on Scientific and Statistical Computing*, 5:311–316.

[12] Hawkes, J., Turnock, S. R., Cox, S. J., Phillips, A. B. & Vaz, G. (2014, October). Performance Analysis Of Massively-Parallel Computational Fluid Dynamics. Submitted to *The 11th International Conference on Hydrodynamics (ICHD)*, Singapore.

[13] Hoekstra, M. & Vaz, G. (2009, August). The Partial Cavity on a 2D Foil Revisited. In proceedings of the *7th International Symposium on Cavitation*, Ann Arbor, MI, USA.

[14] Horst, S. (2013, May). Why We Need Exascale And Why We Won't Get There By 2020. *Optical Interconnects Conference*, Santa Fe, New Mexico, USA.

[15] Hu, Y. (2005). Efficient, High-Quality Force-Directed Graph Drawing. *Mathematica Journal*, 10(1):37–71.

[16] Klaij, C. & Vuik, C. (2013). Simple-Type Preconditioners for Cell-centered, Collocated, Finite Volume Discretization of Incompressible Reynolds-averaged Navier-Stokes Equations. *International Journal for Numerical Methods in Fluids*, 71(7):830–849.

[17] Kogge, P., Bergman, K., Borkar, S., Campbell, D., Carlson, W., Dally, W., Denneau, M., Franzon, P., Harrod, W., Hill, K., Hiller, J., Karp, S., Keckler, S., Klein, D., Lucas, R., Richards, M., Scarpelli, A., Scott, S., Snavely, A., Sterling, T., Williams, S. & Yelick, K. (2008, September). ExaScale Computing Study: Technology Challenges in Achieving Exascale Systems. *DARPA IPTO*.

[18] Lee, S., Kim, H., Kim, W. & Van, S. (2003). Wind Tunnel Tests on Flow Characteristics of the KRISO 3,600 TEU Container Ship and 300K VLCC Double-Deck Ship Models. *Journal of Ship Research*, 47(1):24–38.

[19] Lehoucq, R. B., Sorensen, D. C. & Yang, C. (1998). *ARPACK Users' Guide: Solution of Large-Scale Eigenvalue Problems by Implicitely Restarted Arnoldi Methods*. SIAM, Philadelphia, PA, USA.

[20] Maheswaran, M., Webb, K. & Siegel, H. (1998, August). Reducing the Synchronization Overhead in Parallel Nonsymmetric Krylov Algorithms on MIMD Machines. In proceedings of *International Conference on Parallel Processing*, Minneapolis, Minnesota, USA.

[21] Menter, F., Kuntz, M. & Langtry, R. (2003, October). Ten Years of Industrial Experience with the SST Turbulence Model. In *Turbulence, Heat and Mass Transfer 4*. Antalya, Turkey.

[22] Pereira, F., Eca, L. & Vaz, G. (2013, June). On the Order of Grid Convergence of the Hybrid Convection Scheme for RANS Codes. In proceedings of *CMNI*, Bilbao, Spain.

[23] Rijpkema, D. R. (2008, November). Numerical Simulation of Single-Phase and Multi-Phase Flow over a NACA 0015 Hydrofoil. M.Sc. Thesis, Delft University of Technology, Faculty of 3ME.

[24] Rosetti, G., Vaz, G. & Fujarra, A. (2012, July). URANS Calculations for Smooth Circular Cylinder Flow in a Wide Range of Reynolds Numbers: Solution Verification and Validation. *Journal of Fluids Engineering, ASME*, page 549.

[25] Shalf, J. (2013, October). The Evolution of Programming Models in Response to Energy Efficiency Constraints. *Oklahoma Supercomputing Symposium*, Norman, Oklahoma, USA.

[26] Top 500 List (Acc. 2013, February). `http://www.top500.org`.

[27] Vaz, G., Jaouen, F. & Hoekstra, M. (2009, May–June). Free-Surface Viscous Flow Computations: Validation of URANS Code FRESCO. *28th International Conference on Ocean, Offshore and Arctic Engineering (OMAE)*, Honolulu, Hawaii.

[28] VI-HPS, Score-P, v.1.2.3 (Acc. 2013, November). `http://www.vi-hps.org/projects/score-p`.

[29] Zuo, X.-Y., Zhang, L.-T. & Gu, T.-X. (2014, December). An Improved Generalized Conjugate Residual Squared Algorithm Suitable for Distributed Parallel Computing. *Journal of Computational and Applied Mathematics*, 271:285–294.

RANS simulations of cavitating propeller flows

Tobias Huuva, Simon Törnros

tobias.huuva@catpropulsion.com, simon.tornros@catpropulsion.com

Caterpillar Propulsion Production AB

Background

Cavitation is the phenomena of phase change, from liquid to vapor, due to a local pressure decrease. It is an important phenomena for turbo machinery operating in water such as marine propellers, pumps and turbines. Cavitation extent is crucial to control and limit when designing a propeller as it may induce vibrations, erosion as well as performance degradation.

Experiments are useful for predicting pressure pulses and visual estimations of cavitation extent but may be expensive and time consuming. Numerical tools on the other hand can more easily be applied in early design stages for verification and optimization. Numerical methods based on potential flow are commonly used in industry to estimate cavitation extent and pressure pulses but lacks potential of predicting detailed flow phenomena. Viscous CFD utilizing Unsteady Reynolds Averaged Navier Stokes (URANS) is capable of predicting cavitation including flow detail and dynamics (Sipilä, 2011), (Grekula & Li, 2008). Although the level of detail is lower compared to Large Eddy Simulation (LES) (Lu, Bark, & Bensow, 2012), the significant lower computational cost makes RANS a suitable method for industrial usage.

Objective

The objective of this study is to simulate cavitating propeller flow using an in-house developed CFD methodology with regard to cavitation extent and cavitating performance.

Test cases

The well-known Potsdam Propeller Test Case (PPTC) is a five bladed controllable pitch model propeller with high design pitch and moderate skew. The PPTC propeller can be seen in Figure 1.

Figure 1 PPTC in test configuration (Heinke, 2011)

Geometrical data of the propeller can be seen in Table 1.

Table 1 PPTC geometrical properties

Diameter	D	[m]	0.250
Design pitch ratio	$P_{0.7}/D$	[-]	1.635
Expanded area ratio	EAR	[-]	0.779
Skew	Θ_{EXT}	[°]	18.837
Hub ratio	d_h/D	[-]	0.300
No. of blades	Z	[-]	5

© 2014 Caterpillar. All Rights Reserved. CAT, CATERPILLAR, BUILT FOR IT, their respective logos, “Caterpillar Yellow,” the “Power Edge” trade dress as well as corporate and product identity used herein, are trademarks of Caterpillar and may not be used without permission.

The experimentally analyzed test conditions by SVA Potsdam GmbH (Heinke, 2011) are used in this study, at thrust identity, and can be seen in Table 2.

Table 2 Cavitating condition for the PPTC propeller

Case	#	[-]	1	2	3
Advance ratio	J	[-]	1.019	1.269	1.408
Cavitation no.	σ_n	[-]	2.024	1.424	2.00
Rot. speed	n	[s^{-1}]	24.987	24.986	25.014
Thrust coeff.	K_T	[-]	0.387	0.245	0.167
Density	ρ	[kg/m^3]	997.44	997.44	997.37
Kin. viscosity	v	[m^2/s]	9.337×E-7	9.337×E-7	9.272×E-7

In addition to simulation of the PPTC propeller a Cat® azimuth thruster, Figure 2, will be analyzed as well. The azimuth thruster is a propulsion system which is rotatable around a vertical axis. In this case, the thruster unit is equipped with a nozzle. The nozzle improves performance at low speed and high power, typical for a ship operating in bollard pull or towing mode such as a tug boat or anchor handler.

Figure 2 Cat® azimuth thruster

Geometrical properties of the azimuth thruster can be seen in Table 3.

Table 3 Geometrical properties of the azimuth thruster

Diameter	D	[m]	2.3
No. of blades	Z	[-]	4
Sense of rotation		[-]	Left
Nozzle		[-]	Yes
Type		[-]	Azimuth CPP

The full scale thruster is analyzed in open water with regard to cavitating performance in towing condition specified in Table 4.

Table 4 Cavitating condition for the azimuth thruster

Advance ratio	J	[-]	0.24
Inlet velocity	V	[kn]	5×(1-0.12)
Rot. speed	n	[rpm]	250
Cavitation no.	σ_n	[-]	2.6

© 2014 Caterpillar. All Rights Reserved. CAT, CATERPILLAR, BUILT FOR IT, their respective logos, “Caterpillar Yellow,” the “Power Edge” trade dress as well as corporate and product identity used herein, are trademarks of Caterpillar and may not be used without permission.

Methodology

In this study a RANS CFD code, based on the finite volume C++ library OpenFOAM, is used for simulating the cavitating flow. The incompressible solver utilizes a volume of fluid (VOF) approach for dealing with the two phases. The cavitation phenomena is modelled by applying the mass transfer model by Kunz (Kunz, o.a., 1999). Turbulence is dealt with using an URANS approach with a modified Renormalization Group Theorem (RNG) k-ε model. A damping function of the turbulent viscosity in the mixture region constitutes the modification. The purpose of the damping function is to compensate for the otherwise previously experienced underestimated unsteadiness of cavity dynamics (Reboud, Coutier-Delgosha, & Fortes-Patella, 2002). The damping function, equation 1, replaces the density in the expression for turbulent viscosity as shown in equation 2.

$$f(\rho) = \rho_v + \frac{(\rho_m - \rho_v)^{10}}{(\rho_l - \rho_v)^9} \qquad (1)$$

$$\mu_t = f(\rho)\, C_\mu \frac{k^2}{\varepsilon} \qquad (2)$$

Wall functions are applied to reduce the necessary discretization resolution near the walls. The computational domains are discretized using the commercial software ANSA by BETA CAE. The discretization of the PPTC propeller is done for only one fifth of the propeller, taking advantage of the cyclic geometry of the propeller by using cyclic boundary conditions utilizing Arbitrary Mesh Interpolation (AMI). The rotation of the propeller is achieved by rotating the whole domain. The domain can be seen in Figure 3.

Figure 3 Computational domain for PPTC propeller

The surface mesh is made out of triads and the volume mesh starts from the propellersurface with prism layers followed by a transition zone of pyramids to hexahedrals. The mesh consists of a total amount of 2.3M cells and can be seen near the blade in Figure 4.

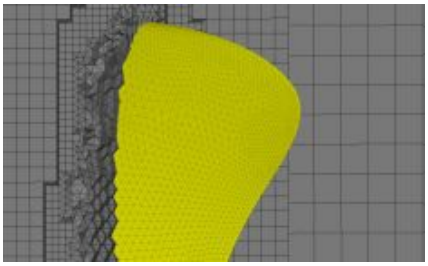

Figure 4 Surface and volume mesh for the PPTC propeller

© 2014 Caterpillar. All Rights Reserved. CAT, CATERPILLAR, BUILT FOR IT, their respective logos, “Caterpillar Yellow,” the “Power Edge” trade dress as well as corporate and product identity used herein, are trademarks of Caterpillar and may not be used without permission.

The azimuth thruster is discretized into 6M polyhedral cells. The gap between the blade tip and nozzle is included and rotation is achieved by rotating a zone containing the hub and propeller blades. The interfaces between the rotor (inner volume) and stator (outer volume) are sliding using AMI. The meshed thruster unit can be seen in Figure 5.

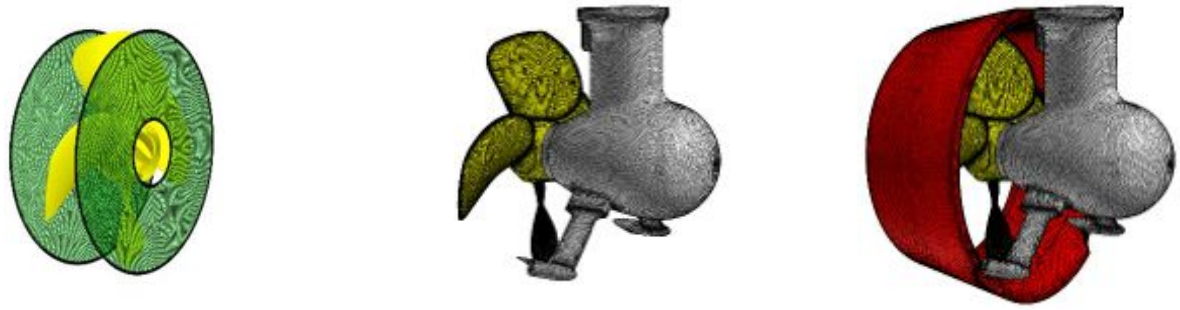

Figure 5 Surface meshed azimuth thruster unit and sliding interface (left)

The thruster unit is connected to a vertical shaft, which extends upwards all the way to the cylindrical domain boundary (Figure 6).

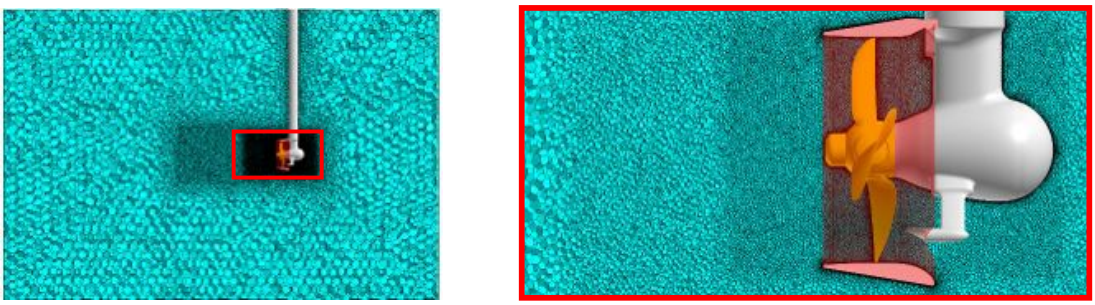

Figure 6 Cut through volume mesh

Results

To achieve thrust identity for the PPTC propeller it was necessary to lower the inlet speed in all of the three cases, yielding lower advance ratio as can be shown in Table 5.

Table 5 Changed advance ratio to gain thrust identity for the PPTC propeller

Case	Δ J [%]
1	-1.14
2	-1.03
3	-1.13

© 2014 Caterpillar. All Rights Reserved. CAT, CATERPILLAR, BUILT FOR IT, their respective logos, “Caterpillar Yellow,” the “Power Edge” trade dress as well as corporate and product identity used herein, are trademarks of Caterpillar and may not be used without permission.

Cavitation extent shown by isosurfaces three values of liquid volume fractions (0.2, 0.5, and 0.8) is shown below in Figure 7.

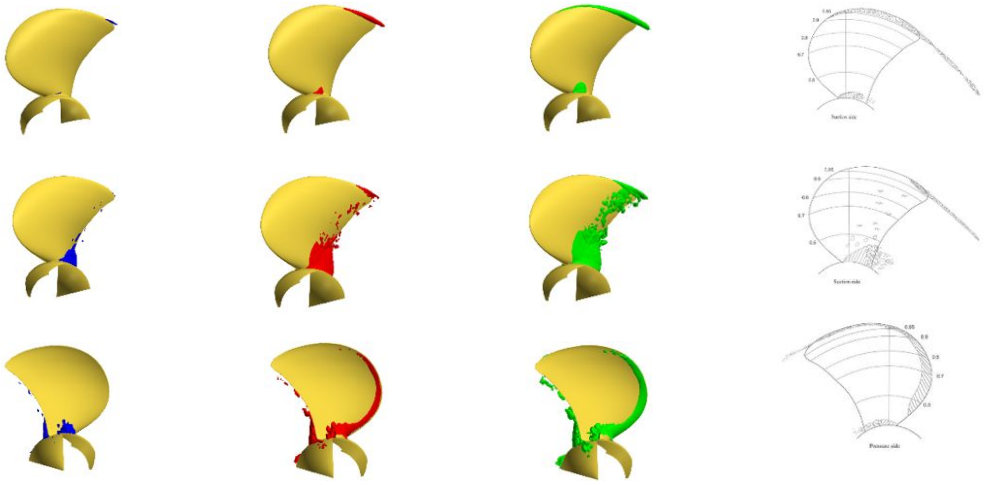

Figure 7 Cavitation extent for the three cases (rows) for three isosurfaces (columns) and experimental results (rightmost column)

The tip vortex and root cavitation in case 1 are both captured, with best resemblance for a volume fraction of 0.5. In case 2, the root cavitation and is over predicted for liquid volume fraction 0.5 and 0.8 while the tip vortex cavitation is under predicted for volume fraction 0.2. The (unsteady) bubble cavitation is captured of reasonable extent for volume fraction 0.5. The sheet cavitation on the pressure side in case 3 is captured for liquid volume fraction of 0.5 and 0.8, although the root cavitation is over predicted. The tip vortex cavitation is not present for any of the isosurfaces. The thrust from the propeller is decreased in cavitating condition, as seen in Table 6.

Table 6 Cavitation effect on thrust coefficient

	$\frac{K_{T,cavitating}}{K_{T,wetted}}$ [%]	
	Exp.	Sim.
Case 1	96.25	97.96
Case 2	84.25	99.4
Case 3	81.56	88.74

The propeller on the azimuth thruster shows cavitation extent as seen in Figure 8. Note that the pressure distribution on the azimuth thruster is including the effect of gravity.

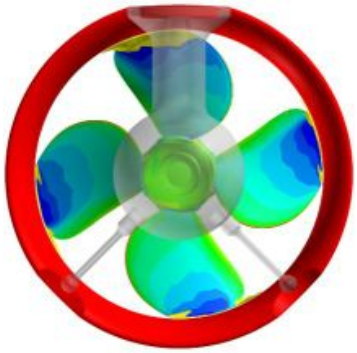

Figure 8 Cavitation isosurface (yellow) on the azimuth thruster

© 2014 Caterpillar. All Rights Reserved. CAT, CATERPILLAR, BUILT FOR IT, their respective logos, “Caterpillar Yellow,” the “Power Edge” trade dress as well as corporate and product identity used herein, are trademarks of Caterpillar and may not be used without permission.

The azimuth thruster is cavitating near the tip at all four blades, the top blade is however experience more cavitation than the others. This is expected as the pressure increases with depth due to the presence of gravity as well as the wake due to the azimuth structure ahead of the blades yields higher loading on the top blade.

Discussion and conclusions

All present types of cavitation are captured in the PPTC case. Tip vortex cavitation, bubble cavitation, sheet cavitation and root cavitation are all present in the simulation. The results shows inconsistency in best suitable isosurface value to reproduce the visual observed cavitation extent. The under predicted tip vortex cavitation may be due to insufficient spatial resolution. According to the experience of the authors, an improvement of the cavitating results could be achieved by using a polyhedral mesh rather than the currently applied hybrid mesh for the PPTC propeller.

The cavitating azimuth shows cavitation on the suction side near the tip and in the tip gap volume. The effect of gravity as well as the wake from the azimuth structure can be observed in the increased amount of cavitation on the top blade.

References

Grekula, M., & Li, D. Q. (2008). Prediction of dynamic shedding of cloud cavitation on a 3D twisted foil and comparison with experiments. *27th Symposium on Naval Hydrodynamics*, (pp. 1-17). Seoul.

Heinke, H. J. (2011). *Potsdam Propeller Test Case Cavitaiton Tests with the model propeller VP1304.* SVA Potsdam model basin.

Kunz, R. F., Boger, D. A., Chyczewski, T. S., Stinebring, D. R., Gibeling, H. J., Venkateswaran, S., & Govindan, T. R. (1999). A Preconditioned Navier Stokes Method for Two-Phase Flows with Application to Cavitation Problems. *Proceedings of 14th AIAA CFD Conference*, (pp. 849-875). Norfolk.

Lu, N., Bark, G., & Bensow, R. (2012). Numerical simulations of the cavitating flow on a marine propeller. *Eight Symposium on Cavitation*, (pp. 338-343). Singapore.

Reboud, J. L., Coutier-Delgosha, O., & Fortes-Patella, R. (2002). Simulation of unsteady cavitation with a two equation turbulence model including compressibility effects. *Journal of Turbulence.*

Sipilä, T. (2011). *RANS analyses of cavitating propeller flows.* Espoo: VTT.

© 2014 Caterpillar. All Rights Reserved. CAT, CATERPILLAR, BUILT FOR IT, their respective logos, “Caterpillar Yellow,” the “Power Edge” trade dress as well as corporate and product identity used herein, are trademarks of Caterpillar and may not be used without permission.

A comparison of CFD and wind tunnel tests for exhaust gas dispersion analysis of an Aframax tanker

Kavyashree Kalaskar, Stewart Whitworth, Dejan Radosavljevic
Lloyds Register, London
kavyashree.kalaskar@lr.org, stewart.whitworth@lr.org

Introduction

Exhaust gas emissions have become a major concern in terms of environmental impact in the recent years. In addition to maintaining low emission requirements, the ship builders have to account for the long term and short term exposure limits of harmful gases on and around the ship. The exhaust gases that are expelled from the ship funnels could easily flow into deck and cabin areas through air intakes and vents. This affects the quality of air for the cabin crew, potentially creating an unsafe working environment. Ship yards have to ensure that the exposure limits of these harmful gases are within the health and safety standards. Traditionally, wind tunnel experiments are conducted to predict the smoke dispersion and measure the concentration of harmful gases.

This paper describes the results obtained for exhaust gas dispersion analysis of an Aframax tanker. It shows a comparison of results obtained from both CFD and wind tunnel tests.

Objective and Scope of Work

Exhaust gas dispersion analysis was conducted to determine the concentration levels of sulphur dioxide (SO_2). These were monitored at fresh air intake inlets and vents on the ship deck through which the cabin air is circulated. The analysis was conducted on several design configurations with various deckhouse and funnel combinations. It was established whether the concentrations are within the safe operating limits for a range of wind speeds and wind angles. The CFD results were then compared with the data obtained from the wind tunnel tests.

Methodology

A 3D CAD model of the ship is provided in Figure 1. The flow of air around the vessel, as well as the expulsion of SO_2 from the ventilation pipes, was simulated using the commercial Computational Fluid Dynamics (CFD) software STAR-CCM+ [1].

The rectangular domain extended one ship length upwind from the bow and three ship lengths downstream of the vessel. The upstream boundary, as well as the sides and the top, were set as inlet boundaries. The downstream boundary was set as a pressure outlet and the bottom of the domain as a no-slip wall. An overview of the computational domain is provided in Figure 2.

The computational domain was discretised using a trimmed-cell mesh, comprised predominantly of hexahedrons aligned with the direction of the nominal flow. This way, the mesh-induced numerical diffusion is kept to a minimum. Prism layers with wall $30 < y+ < 100$ were used on all wall boundaries, to capture the boundary layer flow. The region around the funnel and the deckhouse were further refined to capture the flow features accurately. The total cell count for the domain was roughly 2.5 million cells. Figure 3 shows a view of the mesh of the entire domain and the refinement areas near to the ship.

For all the ship scale simulations, a stable atmospheric boundary layer (ABL) flow was established prior to the expulsion of exhaust gases. The ABL was modelled using the

logarithmic law [1] for sheared inflow, turbulence kinetic energy and turbulence dissipation. The exhaust gas was expelled into the ventilation pipe using a uniform inflow condition with the given mass flow rates and temperatures.

To model the dispersion correctly, a gas mixture composition of CO_2, H_2O, N_2, O_2 and SO_2 was used based on real data for diesel engine emissions. All the simulations were run at sea-going conditions and monitored for long term exposure limit of SO_2, 2ppm (parts per million). The flow was run as steady compressible, multi-component, non-reacting gas flow with RANS k-ε turbulence model.

Results and Discussion

Ship scale simulations

The ship scale simulations were run at a Reynolds number of ~10^8. Figures 4 and 5 show the contour plots at two different wind speeds - 20 and 30 knots for wind angles 60º, 90º and 150°.

At 20 knots, the concentration spread is higher at 60° when compared to 90° or 150°. With increase in speed to 30 knots, the concentration spread decreases for 60° and 90° whereas at 150°, it increases considerably towards the starboard deck. At 30 knots, the flow interacts with the funnel strongly with a higher velocity field thereby creating a larger downstream flow field towards the starboard deck. This shows the unstable nature of smoke dispersion and how variable it is at different wind speeds and wind angles. Due to this unpredictable behaviour, it is suggested to conduct smoke dispersion simulations up to 5 wind speeds and a full 360° sweep of angles to cover all the critical conditions.

Even though the smoke is dispersed all over the deck, it was found that the SO_2 concentrations were less than 2ppm near the intakes and vents at all conditions.

Wind Tunnel Test comparison

The wind tunnel experiments were conducted by a well reputed company with high standard facilities and several years of experience in performing concentration measurements. The model used in the tests had a scale ratio of 1:175. The tests were conducted in a boundary layer wind tunnel of length 20m. To compare the CFD results with the wind tunnel tests, model scale simulations were run at Reynolds number ~10^5 with the same set up and inputs used in the wind tunnel.

Initially, as a first step of validation, the wind loads comparison was performed without any smoke dispersion. The force coefficients were calculated from each CFD simulation run and compared with the force coefficients obtained from the wind tunnel tests. This ensured that the CFD represented the scenario modelled in the wind tunnel closely and accurately.

Figure 6 shows the results from both CFD and wind tunnel tests for the force coefficients at 3 wind angles. The results show that the CFD analysis is in good correlation with the experimental results. The slight differences arise due to the additional superstructure features like masts etc. included in the test model near the walkways and in the aft section of the deckhouse. These are not included in the CFD model as they generate negligible effects for dispersion studies. In spite of these differences, the force coefficients obtained are very similar and represent similar force fields in both the model scale CFD analysis and the wind tunnel tests. This confirms that the CFD modelling is set up accurately to replicate the conditions in the wind tunnel.

The model scale dispersion analysis was set up with combined sea wind profile using a power law exponent of 0.105. The velocities for the tunnel speed and the exhaust were scaled by Froude scaling. The mixture used for exhaust gas composition was Air and Helium as used in the wind tunnel. The results were compared at fresh air intake positions.

Figure 7 shows the SO_2 concentrations at two wind speeds and wind angles. The charts show a comparison of model scale CFD, ship scale CFD and wind tunnel test results. The absolute concentrations in all the cases remain below the long term exposure limit of 2ppm. However, the concentrations vary significantly between the ship scale, model scale and experiments. It is important to note that even though the force coefficients were matched well between the model scale CFD and experiments, the concentration values vary to a higher extent. This could be due to the turbulence intensity being different within the tunnel and the CFD flow domain, accuracy of measurement techniques used or other conditions which are unknown at the moment. This needs to be confirmed with further testing at different conditions.

However, when compared with the ship scale simulations itself, the experimental values are very different and very low in most of the cases. The ship scale simulations show higher concentrations at 20 knots which reduce with increase in speed at 30 knots. This was also seen in Figures 4 and 5. The experimental data on the other hand show no such or particular pattern in the results. To investigate this further, simulations were run without any dispersion to study the background flow field differences between the model scale and ship scale.

Figure 8 shows the normalised velocity for model scale and ship scale simulations at 60º, 20 knots. The ship scale simulations show higher velocities around the deckhouse when compared to the model scale. The flow separating from the spoiler and the recirculation zone around the bridge is stronger in ship scale than the model scale. This arises due to the fundamental difference in Reynolds number. Due to higher Reynolds number in ship scale $\sim 10^8$, the velocity is much higher than the model scale velocity which is set up with Froude scaling.

Figure 9 shows the turbulent intensity for the model scale and ship scale simulations. The ship scale simulations clearly have higher turbulent energy around the regions of funnel and bridge when compared to the model scale. The energy dissipated from the tip of the spoiler is far higher for ship scale than that seen for the model scale. This shows that the behaviour of flow is different at the two Reynolds numbers. The higher energy in the flowfield will influence the amount of smoke being dispersed on the air intakes.

Figure 10 show the streak lines in the form of an oil visualisation plot for model scale and ship scale simulation at 60°, 20 knots. These plots show the formation of vortex downstream of the funnel. In the model scale, two small vortices are seen to be emerging from the funnel. On the contrary, in the ship scale, a very large vortex is seen downstream of the funnel which dominates the flow largely creating a bigger wake field around the funnel region.

This is further confirmed in Figure 11, which shows the streamlines from the exhaust pipes for the model scale and ship scale simulations. The streamlines in model scale are uniform without any interaction with the deckhouse region. On the other hand, the streamlines in the ship scale form a large vortex. This vortex is formed due to the interaction with the background flow. The flow separates from the deckhouse bridge and the funnel spoiler and interacts with the exhaust gases thereby forming the huge recirculation zone which eventually leads to a vortex. The presence of a vortex influences the flow of exhaust gases. A higher amount of exhaust gas is being carried across the deckhouse region in the ship scale, which could lead to a possibility of higher concentration deposition. It is for this reason that the SO_2 concentrations are higher for ship scale.

This vortex formation is not captured in the model scale simulations due to the scaling differences. The model scale velocities are

calculated with Froude scaling and hence the turbulence due to the Reynolds number is not accounted for accurately. This leads to inaccurate prediction or capture of flow interaction and separation.

Conclusions

To conclude, both the model scale and ship scale simulations generated SO_2 concentrations well within the limits of 2ppm. However, due to the huge difference in Reynolds numbers and the lack of accurate scaling techniques, the same level of turbulence and flow field phenomenon was not captured in the model scale results. With the scale factor being 175, the model is too small to capture the same effects of separation or circulation zones as in ship scale. Even though the model scale tests were conducted at a Reynolds number of the order of 10^5, the flow at this Reynolds number is not able to capture the turbulence and eddies that occur at full scale Reynolds number of ~10^8.

This could lead to imprecise predictions and under/over estimated results. Hence, with the current model scale set up, it is difficult to predict accurately the realistic flow features that are encountered on a full scale ship at seagoing conditions.

Without Reynolds scaling, the level of turbulence in the flow field will be very different at the two scales, explaining the large differences in the results of concentrations between ship scale and experiments.

Hence, it is important to consider Reynolds scaling in smoke dispersion predictions as the turbulence levels play a significant factor in influencing the flow behaviour and concentration deposition.

References

1. StarCCM+ v7.06.012, User guide, CD-Adapco

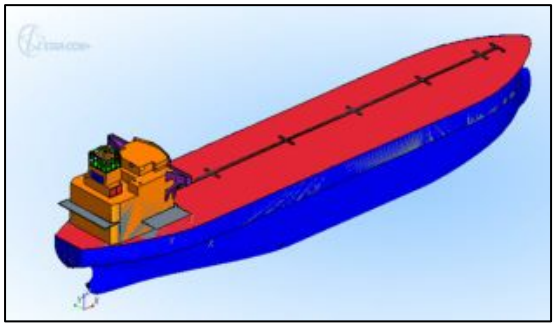

Fig 1: 3D CAD model of the Aframax tanker

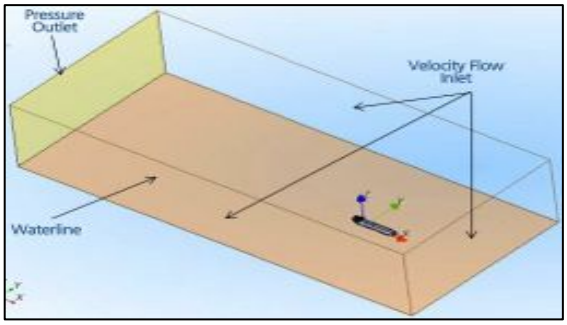

Fig 2: Flow domain around the ship

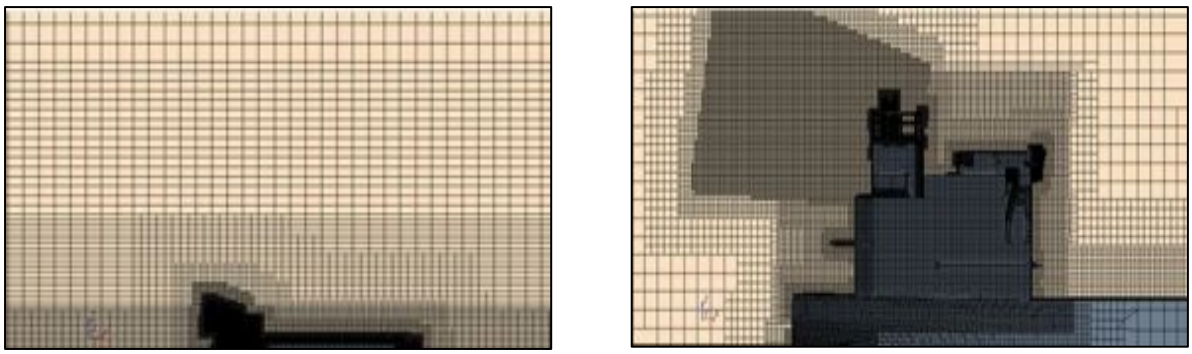

Fig 3: A view of the mesh around the ship showing the refinement regions

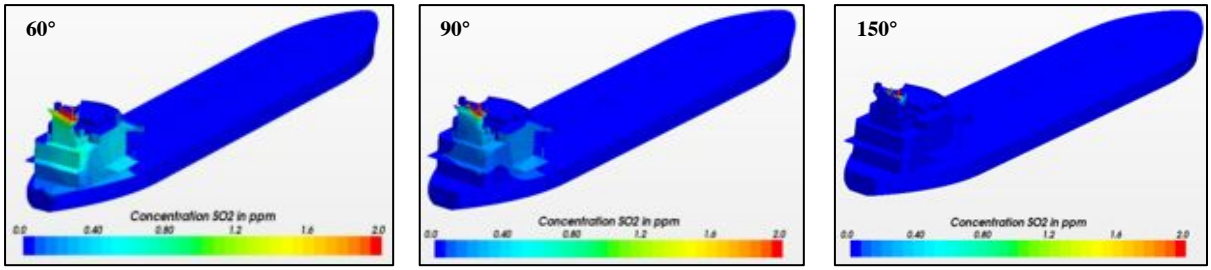

Fig 4: SO_2 concentrations for the tanker at 20 knots at wind angles 60°, 90° and 150°

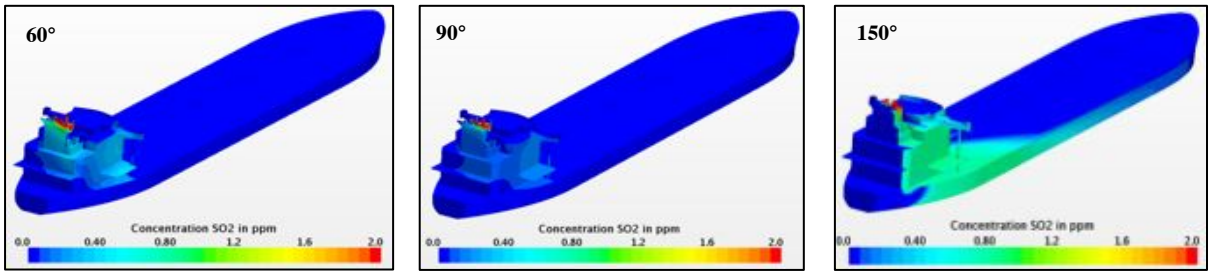

Fig 5: SO_2 concentrations for the tanker at 30 knots at wind angles 60°, 90° and 150°

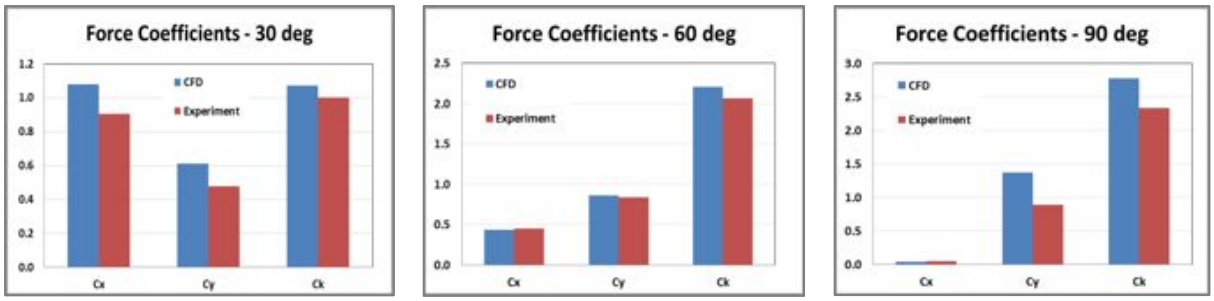

Fig 6: Comparison of force coefficients for CFD and Wind tunnel tests at 30°, 60° and 90°

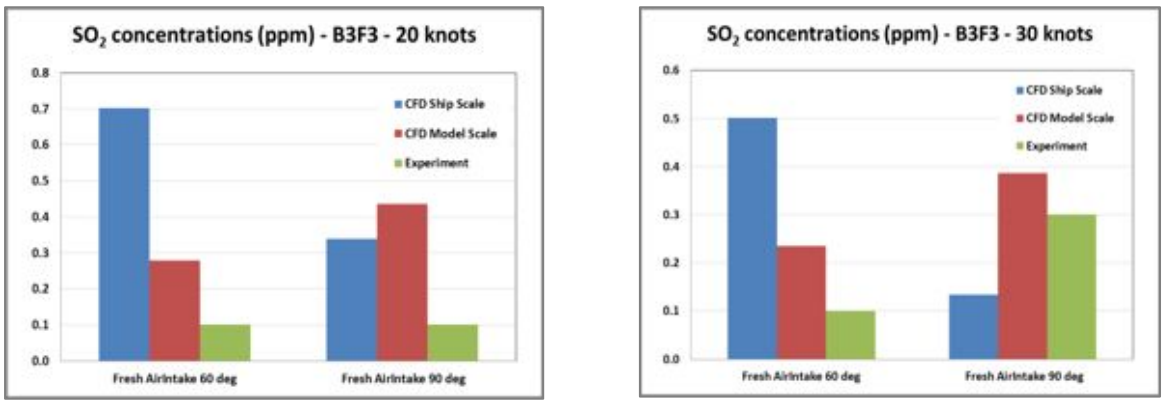

Fig 7: Comparison of SO_2 concentrations for CFD model scale, CFD ship scale and Wind tunnel tests at 60° and 90°

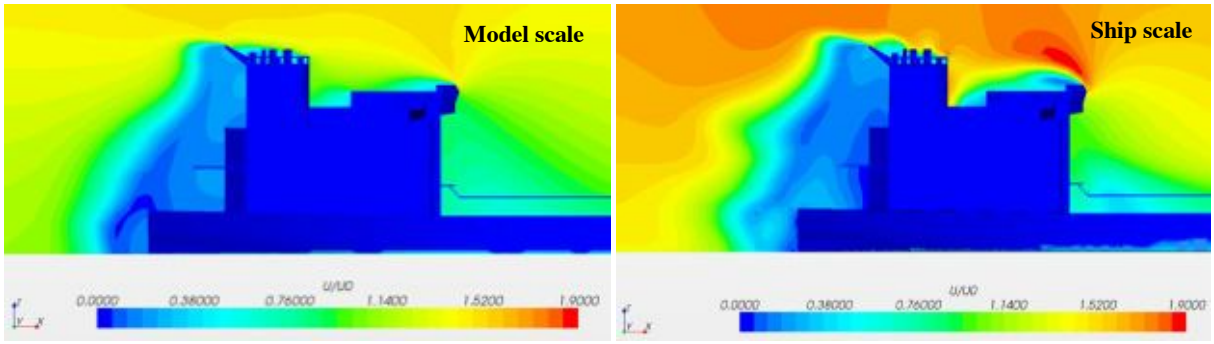

Fig 8: Normalised Velocity magnitude at Model scale and Ship scale at 20 knots, 60° wind angle

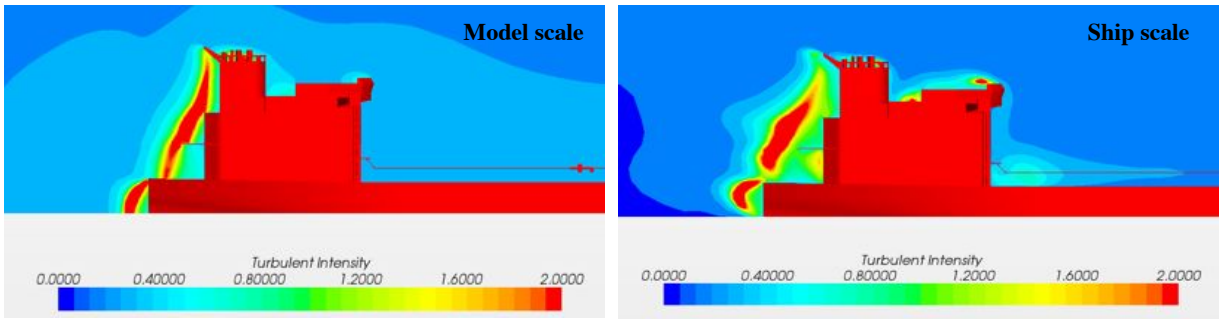

Fig 9: Turbulent Kinetic Energy at Model scale and Ship scale at 20 knots, 60° wind angle

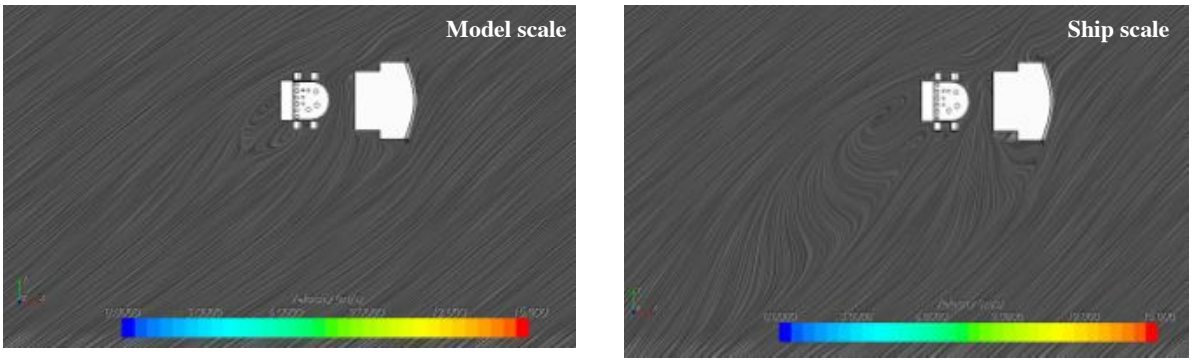

Fig 10: Oil flow image showing the vortex at Model scale and Ship scale at 20 knots, 60° wind angle

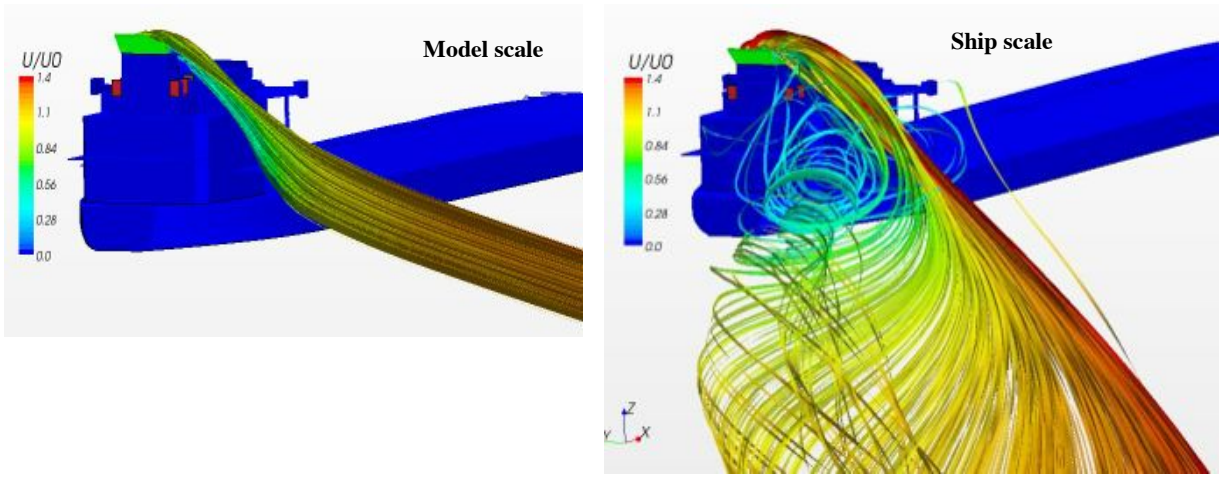

Fig 11: Streamlines at Model scale and Ship scale at 20 knots, 60° wind angle

Prediction of added resistance in waves using RANS-based analysis

Yoo-Chul Kim* (kimyc@kriso.re.kr)

Kwang-Soo Kim* (ksookim@kriso.re.kr)

Yoonsik Kim* (yoonsik@kriso.re.kr)

Jin Kim* (jkim@kriso.re.kr)

Suak-Ho Van* (shvan@kriso.re.kr)

*KRISO (Korea Research Institute of Ships & Ocean Engineering)

1. Introduction

When a ship navigates in a seaway with winds and waves, it is known that resistance is increased about 10-40% of the calm water resistance. The added resistance performance in waves is emphasized to access the powering performance of commercial ships with the index of the *EEDI_weather* in MARPOL Annex IV of IMO MEPC 64. The added resistance in waves is mainly due to wave radiation by ship motion and diffraction of incident waves on the ship hull. The added resistance caused by radiation waves due to ship motion is well predicted with potential theory (even strip theory), which is either far-field method based on momentum conservation theory (Maruo, 1960) or near field method by integrating the hydrodynamic pressure on the ship surface (Fang & Chen, 2006; Joncquez et al., 2008). On the other hand, the prediction of the added resistance caused by reflecting waves from a ship bow shows large scattered results according to the method used. The added resistance in short waves is an important factor in a large ship's performance, because the significant frequency of the sea wave spectrum coincides with this region. Ship motion in short waves is almost negligible and the added resistance in this region is primarily due to wave reflection. Several methods (Fujii and Takahashi, 1975; Faltinsen et al., 1980; Kuroda et al., 2008) are proposed to predict the added resistance in short waves. The RANS approach has been widely used in the prediction of calm water resistance and propulsion performances of a ship. Due to a large amount of computing time and resources, RANS approach to a ship motion is recently reported with the high performance computing resources (Carrica et al., 2007; Sadat-Hosseini et al., 2013).

In this study, we carried out added resistance computation for two hull forms using RANS approach. One is the original KVLCC2 and the other is the modified KVLCC2 for reduction of added resistance. The latter is called KWP-bow (KRISO Wave Piercing bow) KVLCC2 in which bow shape is sharpened by removing the bow-bulb. Test was done for thirteen different regular head-wave conditions.

2. Numerical scheme

The present study extended the RANS based WAVIS 2.2 (Kim et al. 2005, 2010 and 2011), which is widely used for the evaluation of hull form resistance and propulsion problems in Korean shipbuilding companies, to predict the ship motion and added resistance in waves. The finite volume and level-set methods are combined to solve the free surface flow based on RANS equations. The 6 DOF rigid body equations of motion are solved with forces and moments acting on a ship obtained from the unsteady RANS solver. The unsteady RANS equations are formulated in the non-inertial reference frame to use the fixed grid system instead of grid moving or re-gridding.

The governing equations are discretized based on the finite volume method. The Euler implicit scheme is used for time integration. The 3rd order MUSCL (Monotonic Upstream Centered Scheme for Conservation Laws, van Leer 1979) for convection term and central difference scheme for diffusion term are employed. The SIMPLE algorithm is used for the velocity pressure coupling with satisfaction of the continuity equation. The details of

discretization method are described in Kim et al. (2005, 2010 and 2011). The realizable k-ε model is used for turbulence closure (Shih et al., 1995). The free surface for incoming, diffraction and radiation waves (from a ship hull) is modeled by the level-set method (Sussman et al., 1998). The incoming waves are given from the linear wave theory (Newman, 1977) and super-imposed to the computational domain. The 1st order Euler method is used to solve the equations of motion with the given forces and moments from the flow solver. All the flow variables are non-dimensionalized by the ship speed and the length between perpendiculars of model ship, and water density.

3. Computational setup

The present numerical approach is applied to the KRISO VLCC Tanker (KVLCC2) model and its modified model. Table 1 shows the principal dimensions of the two hull forms. Almost same grid systems are used for two hull forms except the bow region where the hull form is modified. The generated grid distribution of the both models around the hull surface is shown in Fig. 1. The O-H type grid topology is adopted for the present computation. No-slip condition is applied to the hull surface, the symmetry condition at y=0 plane, inlet condition at x=-1.6 and outlet condition at x=1.6 in dimensionless coordinate based on ship length. The incoming wave is prescribed with the linear wave theory near inlet region of -1.6<x<-1.1 and wave damping is applied to avoid the undesirable effect of the reflected waves from the boundaries for 0.3 distance from the boundary edges. The grids are sufficiently distributed in the longitudinal direction and near free surface area to resolve the incoming and scattered waves. The number of grids in longitudinal direction per the shortest wave is set by 36 in upstream region and 58 in hull side region. Computational domain consists of 4.6 million grid cells. Only heave and pitch motions are considered in this calculation and Table 2 shows applied wave conditions based on the experimental measurement.

Table 1 Principal dimensions of the KVLCC2 and KWP-bow KVLCC2

		KVLCC2 ship	KVLCC2 model	KWP-bow KVLCC2 model
Scale ratio		1.0	1/39.44	1/39.44
Design speed	V[m/s]	7.9739	1.2697	1.2697
Froude number	Fn	0.142		
Reynolds number	Rn	2.1×10^9	9.04×10^6	9.04×10^6
Length between perpendiculars	L_{pp}[m]	320	8.1136	
Breadth	B[m]	58	1.4706	
Depth	D[m]	30	0.7606	
Draft	T[m]	20.8	0.5274	
WSA w/o rudder	S_W[m2]	27,194	17.4823	17.5736
Displacement	▽[m3]	312,622	5.0958	5.0865
Block Coeff.	C_B	0.8098	0.8098	0.7886
Longitudinal CB (from midship)	LCB[m]	$0.0348L_{pp}$	$0.0348L_{pp}$	$0.0211L_{pp}$
Pitch radius of gyration	K_{yy}	$0.25L_{pp}$		

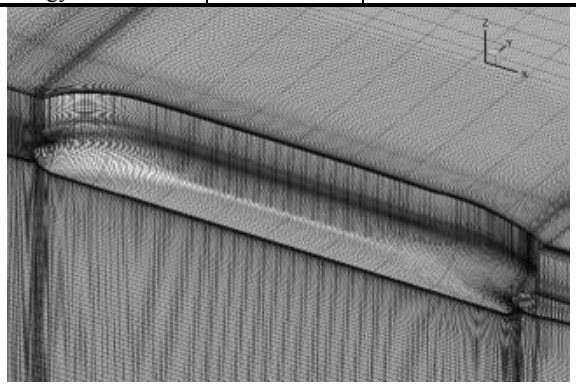

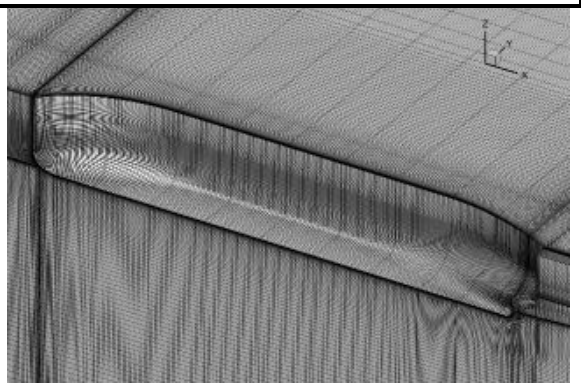

Fig. 1 Grid distribution around the hull surface (left: KVLCC2, right: KWP-bow KVLCC2)

4. Results and discussion

Figs. 2 and 3 show the 1st harmonic amplitude of heave and pitch motion responses of both hull forms at the corresponding incoming wave lengths for the present computation and the towing tank experiments. The predicted heave and pitch RAO shows a relatively good agreement with the experimental results except the case of long wave conditions. This might stem from the fact that we adopted the non-inertial reference frame in which large amplitude motion gives rise to inaccurate capturing of free surface.

Table 2 Wave conditions

Original KVLCC2		KWP-bow KVLCC2	
λ / L_{pp}	A / L_{pp}	λ / L_{pp}	A / L_{pp}
0.300	0.003660	0.300	0.003696
0.401	0.004922	0.400	0.005017
0.500	0.004821	0.500	0.005117
0.600	0.005155	0.600	0.004982
0.701	0.005035	0.700	0.004934
0.801	0.005122	0.800	0.004801
0.901	0.005001	0.900	0.004873
0.998	0.005028	1.000	0.004957
1.101	0.005183	1.100	0.005069
1.252	0.005271	1.250	0.003805
1.398	0.005187	1.400	0.003662
1.598	0.005167	1.600	0.003837
2.002	0.005014	2.000	0.003656

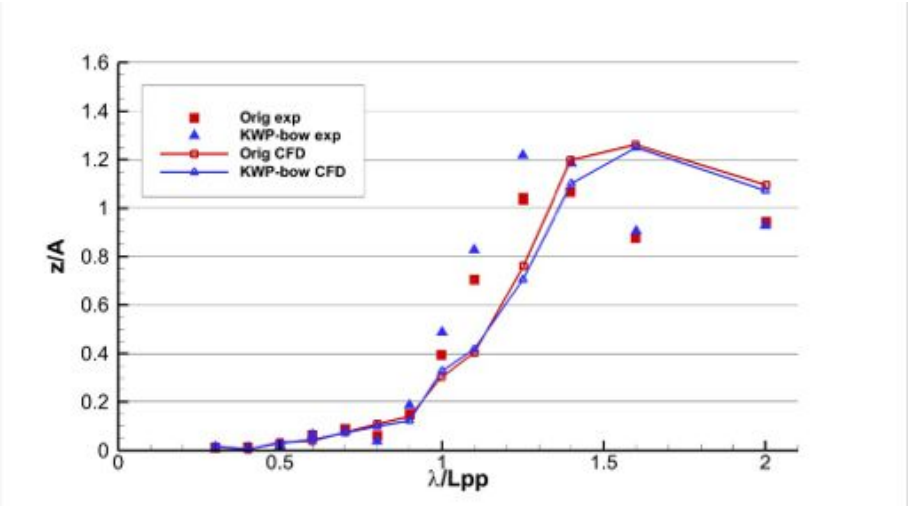

Fig. 2 Heave motion RAO

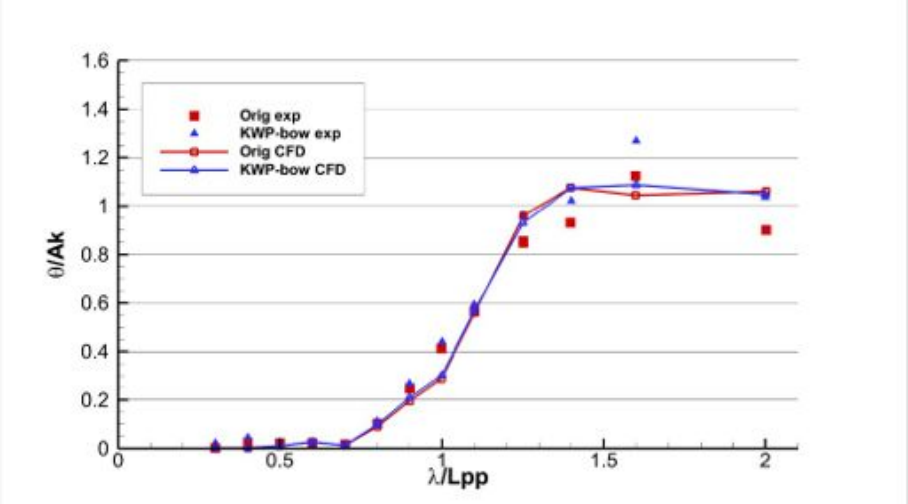

Fig. 3 Pitch motion RAO

Added resistance is defined as

$$R_{AW} = R_T - R_{SW}$$

where R_{AW} is added resistance, R_{SW} calm water resistance and R_T total resistance in waves.

Fig. 4 shows the comparison of the added resistance of KVLCC2 and KWP-bow KVLCC2 at Fn=0.142 with the experiments. The computed added resistance shows a little difference from the experiment where λ/L_{pp} is higher than 1.0. This is similar result of heave and pitch RAO. However, the unsteady RANS based method shows a good agreement with the experiment in the range of short waves in which potential based method usually needs a special treatment. It is also confirmed that newly-designed hull form for reduction of added resistance shows better performances in the range of applied wave conditions.

CFD approach in application to the problem of added resistance and ship motion has strong advantages to resolve the physics of wave diffraction without additional effort for short wave formulation while some improvements for large amplitude motions are needed.

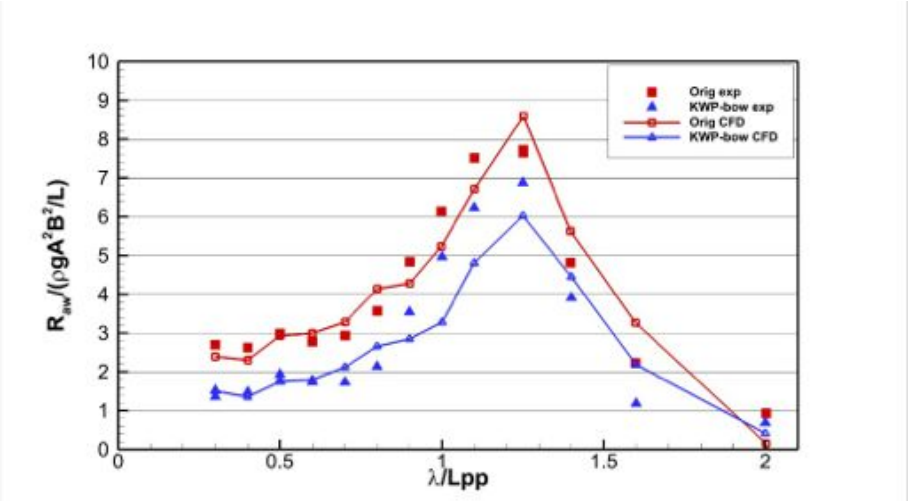

Fig. 4 Added resistance in waves

ACKNOWLEDGEMENTS

This research was sponsored by the Ministry of Trade, Industry and Energy, Korea under the project (PNS2000).

REFERENCES

Carrica, P. M., Wilson, R. V., Noack, R. W., and Stern, F. (2007). "Ship Motions using Single-Phase Level Set with Dynamic Overset Grids," *Computers & Fluids*, Vol 36, No 9, pp 1415–1433.

Faltinsen, O. M., Minsaas K. J., Liapis, N., and Skjordal, S. O. (1980). "Prediction of Resistance and Propulsion of a Ship in a Seaway," *Proc. of the 13th Symposium on Naval Hydrodynamics*, Tokyo, Japan, pp 505-529.

Fang, M. C. and Chen, G. R. (2006). "On the Nonlinear Hydrodynamic Forces for a Ship Advancing in Waves," Ocean Engineering, Vol 33, pp 2119-2134.

Fujii, H. and Takahashi, T. (1975). "Experimental Study on the Resistance Increase of a Ship in Regular Oblique Waves," *Proc. of the 14th International Towing Tank Conference*, pp 351-360.

Joncquez, S. A. G., Bingham, H., Anderson, P. (2008). "Validation of Added Resistance Computations by a Potential Flow Boundary Element Method," *Proc. of the 27th Symposium on Naval Hydrodynamics*, Seoul, Korea.

Kim, J., Park, I. R., Kim, K. S. and Van, S. H. (2005). "RANS Simulation for KRISO Container Ship and VLCC Tanker," *Journal of the Society of Naval Architects of Korea*, Vol 42, No 6, pp 593–600.

Kim, J., Kim, K. S., Park, I. R. and Van, S. H. (2010). "Numerical Simulations for High Speed Ships in Deep and Shallow Water with Sinkage and Trim," *Proc. of the 11th International Symposium on Practical Design of Ships and Other Floating Structures,* PRADS, Rio de Janeiro, Brasil, Vol 1, pp 16-24.

Kim, J., Park, I. R., Kim, K. S., Van, S. H., and Kim, Y. C. (2011). "Development of Numerical Method for the Evaluation of Ship Resistance and Self-Propulsion Performances," *Journal of the Society of Naval Architects of Korea*, Vol 48, No 2, pp 147–157.

Kuroda, M., Tsujimoto, M., and Fujiwara, T. (2008). "Investigation on Components of Added Resistance in Short Waves," Journal of the Japan Society of Naval Architects and Ocean Engineers, Vol 8, pp 171-176.

Maruo, H. (1960). "The Drift of a Body Floating on Waves," *Journal of Ship Research*, Vol 4, No 3, pp 1-10.

Newman, J. N. (1977). *Marine Hydrodynamics*, Cambridge, MIT Press.

Sadat-Hosseini, H., Wu, P. C., Carrica, P. M., Kim, H., Toda, Y., and Stern, F. (2013). "CFD Verification and Validation of Added Resistance and Motions of KVLCC2 with Fixed and Free Surge in Short and Long Head Waves," *Ocean Engineering*, Vol 59, pp 240-273.

Shih, T. H., Liou, W. W., Shabir, A., and Zhu, J. (1995). "A New k-e Eddy Viscosity Model for High Reynolds Number Turbulent Flows – Model Development and Validation," *Computers & Fluids*, Vol 24, No 3, pp 227-238.

Sussman, M. F., Fatemi, E., Smerera, P. and Osher, S. (1998). "An Improved Level-Set Method for Incompressible Two-Phase Flows," Computers & Fluids, Vol 27, No 5-6, pp 663-680.

van Leer, B. (1979). "Towards the Ultimate Conservative Difference Scheme, V: A Second Order Sequel to Godunov's Method," *Journal of Computational Physics*, Vol 32, pp 101-136.

Validation of a numerical experiment by using the non-intrusive measurement technique PIV

Tor Huse Knudsen, NTNU

Email address: graadiggrei@gmail.com

This work reports the result of an experiment measuring the wake flow behind a curved circular cylinder at Re=3900 in water. The measurement technique used was Particle Image Velocimetry (PIV), and the results are compared with a DNS experiment with similar experimental setup conducted by Gallardo et al (2014). The cylinder is a convex configuration with a quarter of a ring with a straight elongation of the cylinder in each end. The DNS experiment used free-slip-surfaces as boundary conditions for the control volume, and the PIV experiment used no-slip-surfaces.

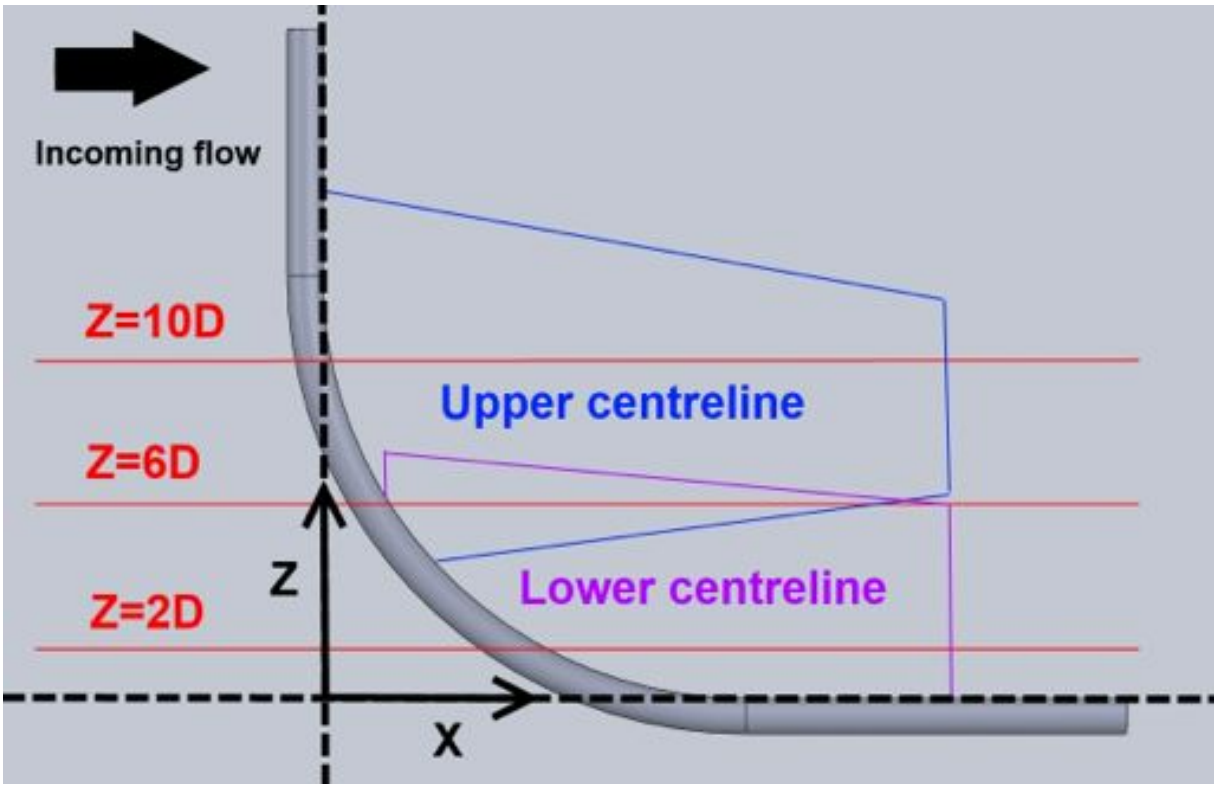

Figure 1: Experimental setup and measurement planes, quarter circle with radius 12,5 D. Measurement planes were taken at the centreplane of the cylinder, and at three different cross sections

A slight updraft was experienced downstream of the curved cylinder in an average flow field in z-direction at Z~5D-11D in Figure 2. This updraft was experienced by Gallardo et al (2014), although the strength of the measured updraft was smaller for the PIV experiment compared to the DNS measurements done by Gallardo et al (2014) (Figure 3). The difference in strength is probably due to experimental limitations such as spatial resolution and wall flare from the cylinder surface. A downdraught with a much higher amplitude compared to the updraft was also experienced behind the curved cylinder over the whole measured span. This downdraught is in good agreement with the experiment by Gallardo et al (2014), but with the peak ~0,4D downstream compared to the DNS by Gallardo et al (2014). The reason for this may be the boundary layer from the tank wall interacting with the vertical extension of the cylinder, giving an oblique inflow velocity on the vertical extension.

This may again influence the vortex shedding angle behind the curved cylinder that may be of importance for the velocity field.

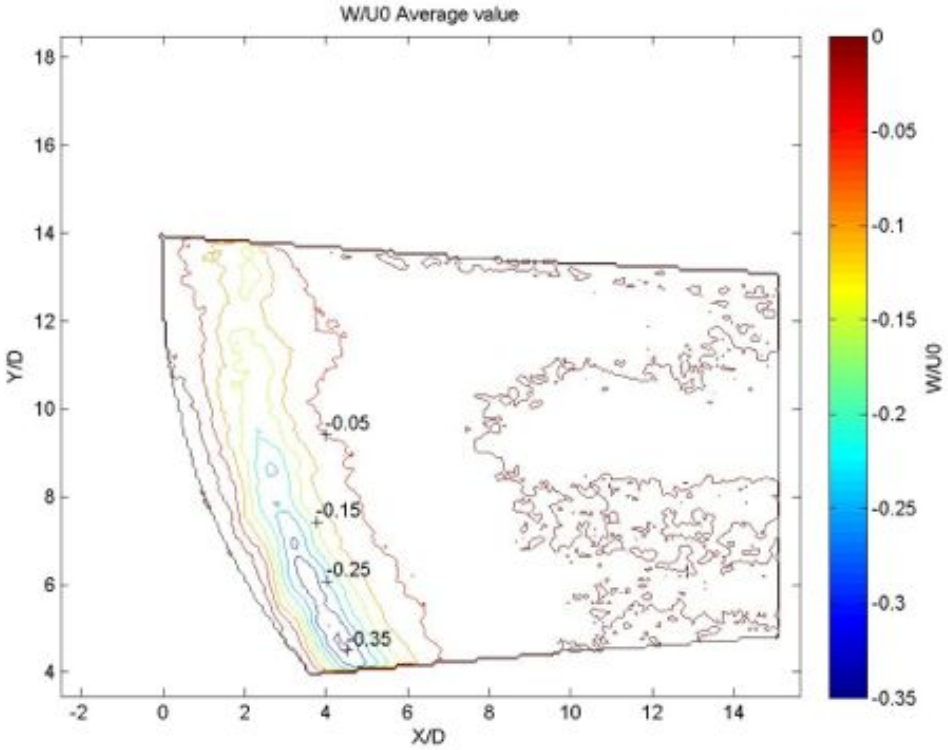

Figure 2: Average value of W/U0 at the centreline on the upper part of the cylinder.

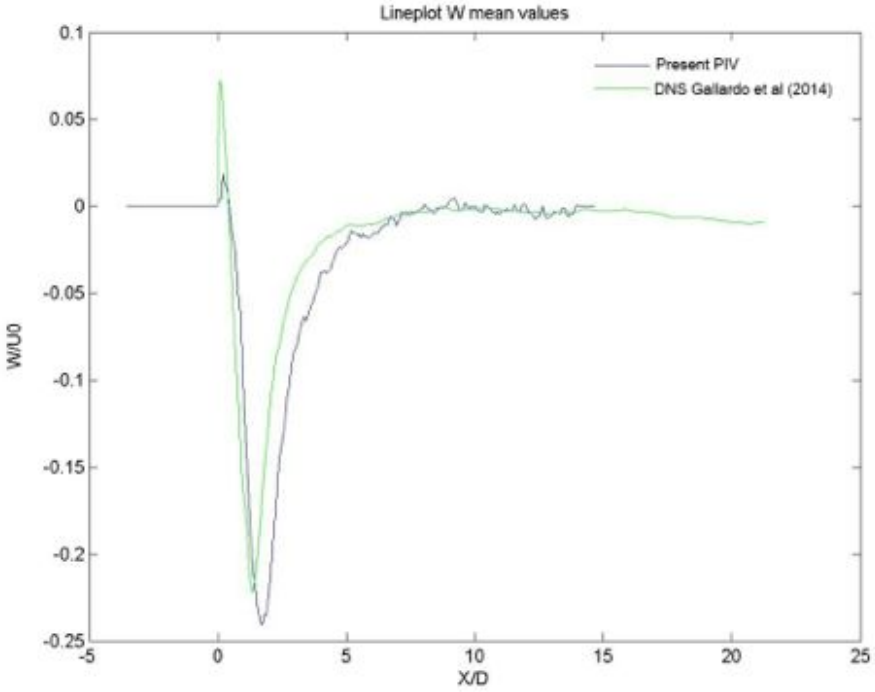

Figure 3: Comparison between the experiment by Tor (2014) and Gallardo et al (2014) [6]. Lineplot of W velocity at Z=8D.

The plots of the mean-square values of the velocity fluctuations are similar for the DNS experiment by Gallardo et al (2014) and the PIV experiment, but some differences can be seen. Figure 4 show a comparison of the mean square values of the velocity in x-direction between the numerical experiment by Gallardo et al (2014) and the PIV experiment. The bulk of the peak has the same broadness, but the characteristic double-peak seen from the DNS experiment by Gallardo et al (2014) are not present on the results from the PIV experiment. The absence of the double peak in the PIV experiment are probably due to a relatively low time and spatial resolution. This makes the PIV experiment in this case unable to measure some of the turbulent fluctuations associated with the flow. The peak obtained from the PIV experiment are also slightly lower and translated ~0,5D downstream compared to the DNS experiment. This is probably due to a boundary layer forming on the tank surface.

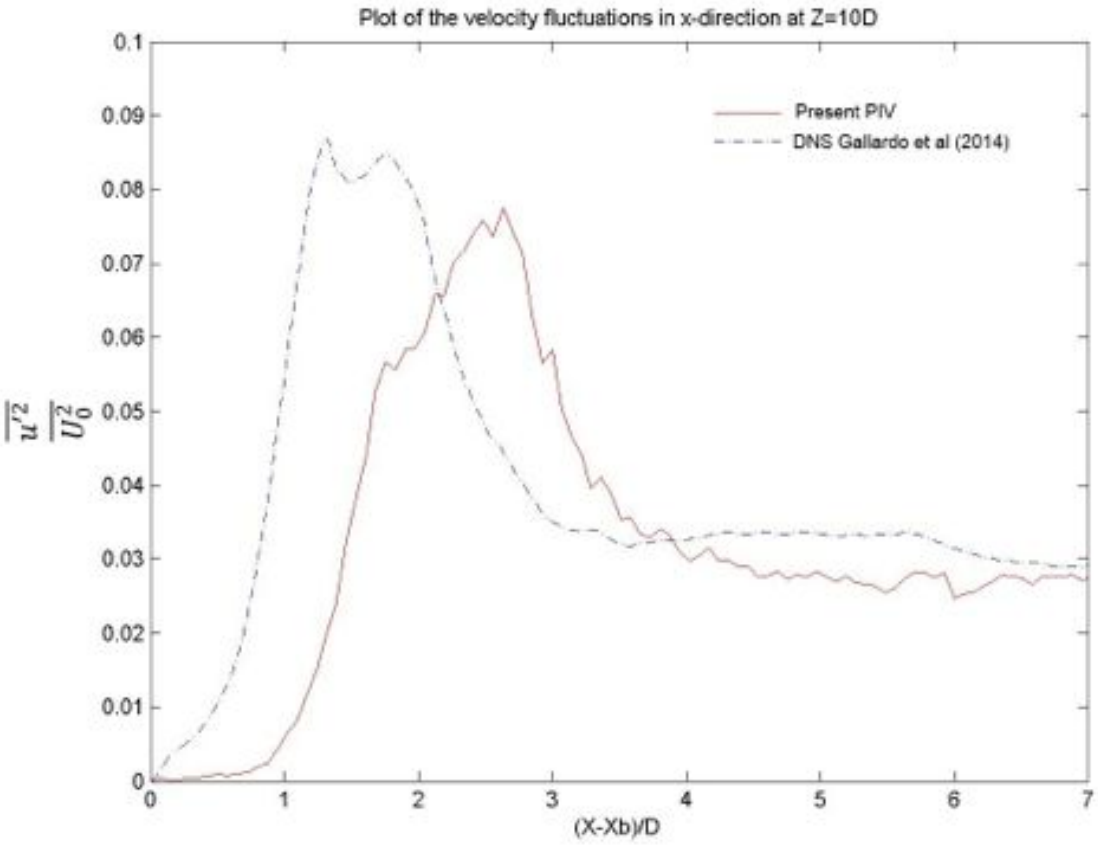

Figure 4: Lineplot of the mean square of the velocity fluctuations in x-direction at the centreline at Z=10D. The measurements are compared with data from Gallardo et al (2014) [6] with similar flow conditions. u' represent the velocity fluctuations.

The vortex shedding pattern downstream of the cylinder was measured for all time steps. Figure 5 show different vortex dislocations in the wake behind the curved cylinder for the PIV experiment. Vortex dislocations were present in the results produced by Gallardo et al (2014), but were absent in an experiment with an experimental setup without the vertical extension of the cylinder done by Gallardo et al (2011). These vortex dislocations are associated with different shedding frequencies at different depths.

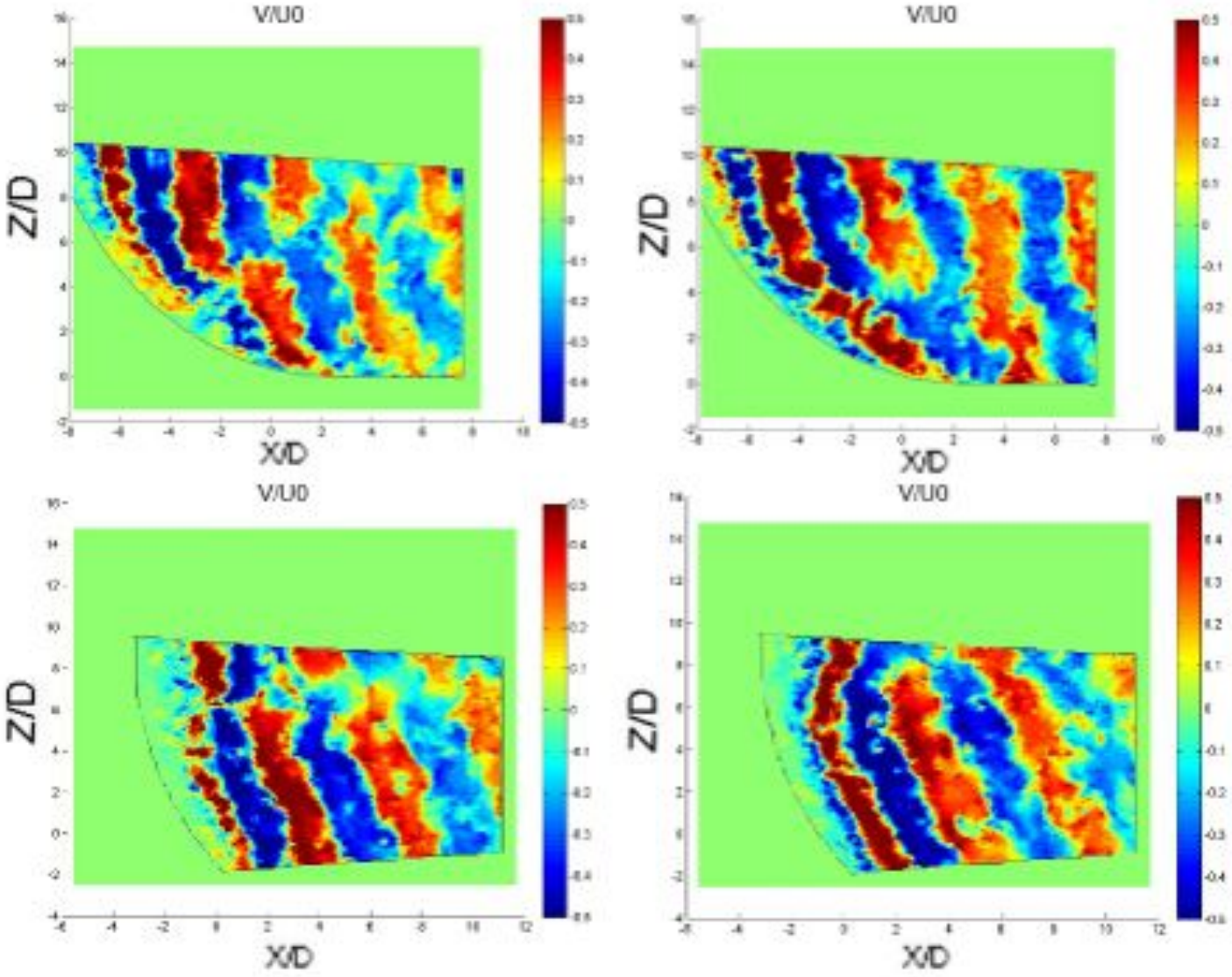

Figure 5: Vortex dislocations. Upper left: Lower part of the centreline measurements, a shift in the vortex cells. Upper right: Lower part of the

To increase the resolution in time, measurements with LDV were taken. The results for the wake flow with speeds $<0{,}3U_0$ were inaccurate, probably due to the lower speed limit of what the LDV are able to measure.

References:

Gallardo, J. P., et al. (2014). "Turbulent wake behind a curved circular cylinder." Journal of Fluid Mechanics **742**: 192-229.

Gallardo, J. P., et al. (2011). "Dynamics in the turbulent wake of a curved circular cylinder." Journal of Physics: Conference Series **318**(6): 062008.

Knudsen, Tor Huse (2014). "Wake flow behind a curved cylinder" Master thesis, NTNU

Simulation of Airflow around Wing Sails using BEM, PyOpenCL and Blender

Jarle Andre Kramer
Sverre Steen

Norwegian University of Science and Technology
jarle.a.kramer@ntnu.no

June 30, 2014

1 Introduction

Due to a project regarding design of cargo ships using wing sails as auxiliary propulsion, a fast, yet accurate, method of determining the flow around wing sails is needed. Wing sails are rigid wings used in the same way a traditional soft sail would be used. The benefit of using rigid wings, rather than soft sails, are that the control of the sail becomes much easier, as the shape of the sail is not dependent on the wind, and the amount of force the wing can extract from the wind becomes larger, at least for certain wind directions. The theory is that wing sails can provide a large amount of auxiliary propulsion for cargo ships using the wind at sea, and thereby reduce the fuel consumption and CO_2 emissions of the ship. An illustration of how a cargo ship with wing sails could look is shown in figure 1

Figure 1: Artistic illustration of how a cargo ship with wing sails could look

The physics of wing sails are such that simplified flow analysis, using potential flow and the boundary element method (BEM) for finding the velocity and pressure is expected to give accurate results. BEM is an old and well tested method that works well as long as the flow can be considered attached, and

viscous effects are secondary. Viscous effect can be modeled by connecting the BEM code with integral formulations for viscous effects.

3D BEM codes already exist in many shapes and forms, for both lifting and non-lifting shapes. The reason for developing a new code is divided in two: for one, flexibility, in terms of type of geometry and coupling with other custom codes is considered by the author to be an important feature for this project. Secondly, the author is interested in taking advantage of all the parallel computing power available in a modern computer, which hopefully will speed up BEM calculations significantly.

This extended abstract will go through two design choices that where made for the BEM code in order to implement the wanted features. Specifically, the choice of using OpenCL to access all the computing power available in a modern computer, and the use of the open source 3D software Blender as a geometry kernel and post processing tool will be discussed. The code is, for the most part, written in python, and uses the *numerical python* or *numpy* [4] package extensively. The interface between python and OpenCL is done through PyOpenCL [2]

At the time of writing this extended abstract the code is not completely done. It is lacking a few features, and contains at least one bug. However, this lack of features and buggy behavior is not directly connected to the use of OpenCL and Blender, so some general discussion about these code-design choices can still be made at this point.

2 Boundary Element Method

For incompressible, inviscid, irrotational flow, the equation of motion is the Laplace equation, which is an expression of continuity of mass. It can be shown that any solution to the Laplace equation in a domain can be represented by distributing sources and doublets along the boundaries of that domain (see for instance reference [1] chapter 3).

Sources and doublets are elementary solutions to the Laplace equation. Sources alone can model non-lifting flows, but doublets are necessary when lifting surfaces are of interest. The potential at a point (x, y, z) from one source, with constant strength σ, and one doublet with constant strength μ, smeared out over a quadrilateral polygon, located in the xy-plane, can be found from the following:

$$\phi = -\frac{\sigma}{4\pi}\iint_S \frac{d\xi d\eta}{\sqrt{(x-\xi)^2+(y-\eta)^2+z^2}} - \frac{\mu}{4\pi}\iint_S \frac{z d\xi d\eta}{((x-\xi)^2+(y-\eta)^2+z^2)^{3/2}} \tag{1}$$

Finding the solution to these integrals is not a trivial task, but possible (see for instance reference [1] for complete expressions). The geometry of the wing and the wake can then be approximated by polygon shaped panels, each polygon with an unknown value of σ and μ. Using boundary conditions, a system of equations can be built, that forces the strengths of the panels to be such that it simulates the correct potential flow.

For this code, Neumann boundary conditions has been used. That is, for every panel that represents the wing geometry, the velocity at the center of the panel, must be parallel to the panel itself. The flow is not allowed to go through a panel.

In order to get a lifting flow, a potential wake has to be modeled. This is done by letting panels extend from the trailing edge of the wing, that have the same doublet strength as the trailing edge. The geometry of the wake is not known a priori, but can be found by demanding that the wake is parallel to the local flow. This will lead to the well known *roll-up* structure of wakes (see figure 2). The actual calculation of the wake geometry is done by guessing a reasonable shape, calculate the induced velocities due to the wake and wing, and then deform the wake by integrating the velocity in time numerically. This must be done iteratively until a correct shape is found.

In order to reduce the number of unknowns, the source strength of the wing is approximated by a guess,

which is made such that each panel can induce a normal velocity on itself which is large enough to counter the normal component of the wind velocity. The only unknowns left are the values of μ on the wing, that must introduce lift, and correct the errors from the guess of σ values. That is, the total number of unknowns for the final system of equations are equal to the number of panels the wing surface consists of (n_{wing}).

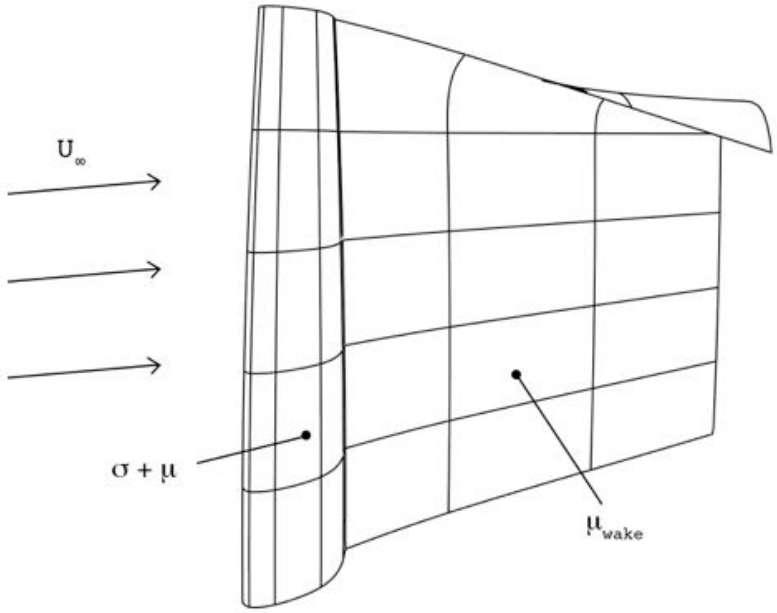

Figure 2: Illustration of the wing and wake modeled with BEM

The system of equations to be solved is determined by checking the velocity induced by all the panels, plus the free stream velocity from the wind, at each panel-center of the wing. Unlike finite volume/difference/element methods, this procedure generates a full system matrix. That is, every panel influences every point. This means that in order to build a system of equations for a wing with n_{wing} panels at the wing surface and n_{wake} panels at the wake surface, the influence from a single panel has to calculated $n_{wing} \times (n_{wing} + n_{wake})$ times.

The result of this is that building the system to be solved actually is a big challenge in terms of computational time. Functions that solves a linear system efficiently is available for many programming languages, including Python, through Numpy. The Numpy solver also take advantage of the parallel nature of the CPU. This means that the main challenge for making a custom panel code is to construct the system of equations. This has been the main focus for this project.

3 PyOpenCL

In order to speed up the calculation of the system matrix, PyOpenCL has been used. PyOpenCL is an interface between Python and the *heterogeneous platform programming framework* called "Open Computing Language" or OpenCL. PyOpenCL gives access to all of OpenCL, through python, and is also made to simplify the execution process somewhat. It is developed by Andreas Klöckner and released as open source software [2].

The greatest benefit of using OpenCL, instead of other types of parallel programming frameworks, is that OpenCL can be executed on essentially any type of computing device, such as *Central Processing Units* (CPUs), *Graphics Processing Units* (GPUs), digital signal processors and field-programmable gate arrays. Not only is the CPU of modern personal computers a many-core device, but the GPUs are getting more and more powerful as well, mainly due to the demands of the gaming industry. This computing power

is available to scientific computations using OpenCL. GPUs generally have more cores than a CPU, but at a lower clock speed. For instance, in the authors personal computer, there are one CPU (Intel Core i5), with 4 cores, each core running with a clock-speed of 3.4 GHz, while the GPU (NVIDIA GeForce 775M) have 960 cores, each running at a clock-frequency of 811 MHz. A core in a GPU is not directly comparable to a core in a CPU, but the point is that GPUs have a significant available computational power *if one can do calculations in parallel.*

In order to use OpenCL to run parallel computations, one writes a function, which is called a kernel, and tell the system to execute that kernel many times. The system will then determine how to distribute the load between the available computational cores largely by itself. As GPUs and CPUs have different memory, the data that is to be used in the calculations must be transferred to the right place. That is, in order to do computations on a GPU, input data must be transferred to the GPU memory, and when the calculations are done, the output must be transferred back so that the CPU can read it. OpenCL contains the necessary functions to do this.

In order to test the computational power of PyOpenCL, a test case was written. The test case consists of creating a number of random points, half of which is called "control points", and the rest is "source points". At each control point, the influence of all the source points are calculated, assuming the sources are point sources (which gives an expression equal to the integrand of the first integral in equation 1).

These calculations are then done in both pure Python and Python + PyOpenCL. Both PyOpenCL on the GPU and on the CPU where tested. The result can be seen in figure 3. Note that the axes are logarithmic, so the difference between pure Python and PyOpenCL is significant when the number of random points are high. The difference between the GPU and the CPU are less significant

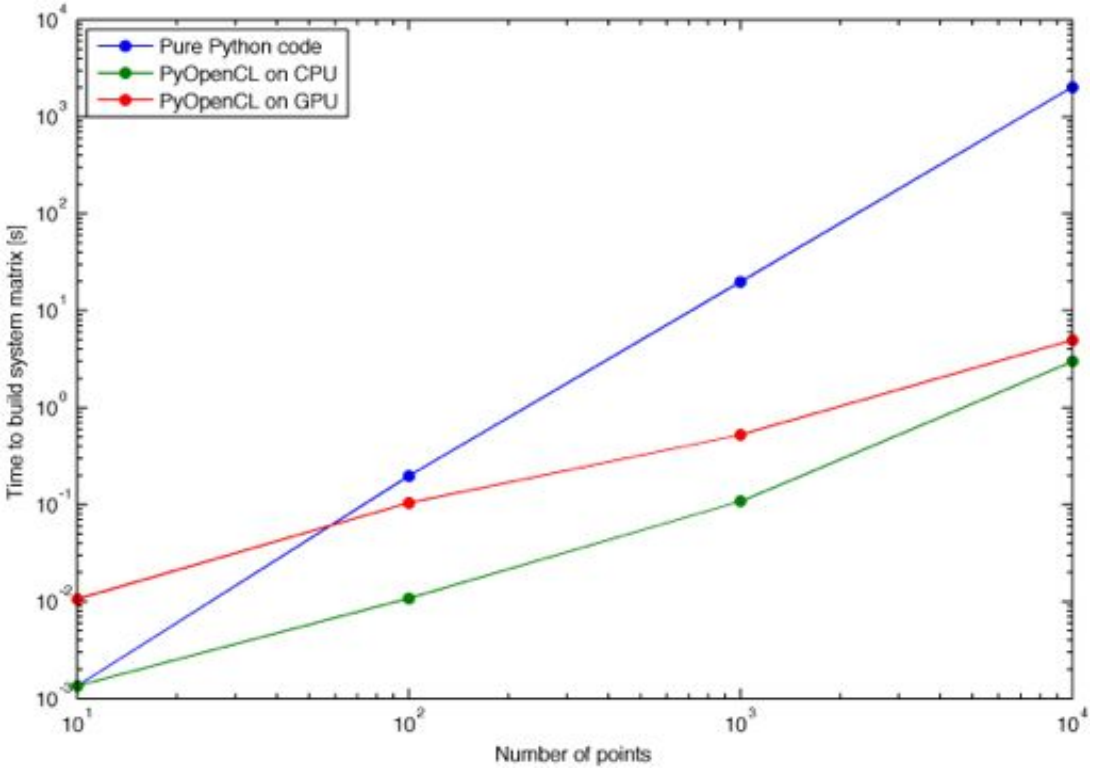

Figure 3: Time spent on building system matrix with Python and PyOpenCL

For this specific computer, the CPU is fastest, but this is not a general tendency. Other computers have different components, and in some cases the GPU might be the fastest. Coding in OpenCL allows the same code to be run on the fastest computational device in the specific computer at hand, no matter what that component is.

4 Blender

Blender is an free open source 3D software, developed by the Blender foundation. It aims at being a complete tool for everything 3D: modeling, rendering, compositing, animation, special effects, etc. It also contains many simulation features, such as rigid body simulation, cloth simulation, smoke and fire simulation, fluid simulations, a complete game engine, and much more. All of which is intended for making visually realistic images and animations, not provide accurate scientific results. That is, the main goal of Blender is to allow everyone to create stunning 3D art in the shape of movies, games and images like figure 4. The goal for this project was to see if Blender also could act as a tool to create and manage the necessary geometry for the simulations and take care of the visual post processing after the simulations are done. The hypothesis is that many of the necessary features for making visually realistic images can be used in scientific simulation as well.

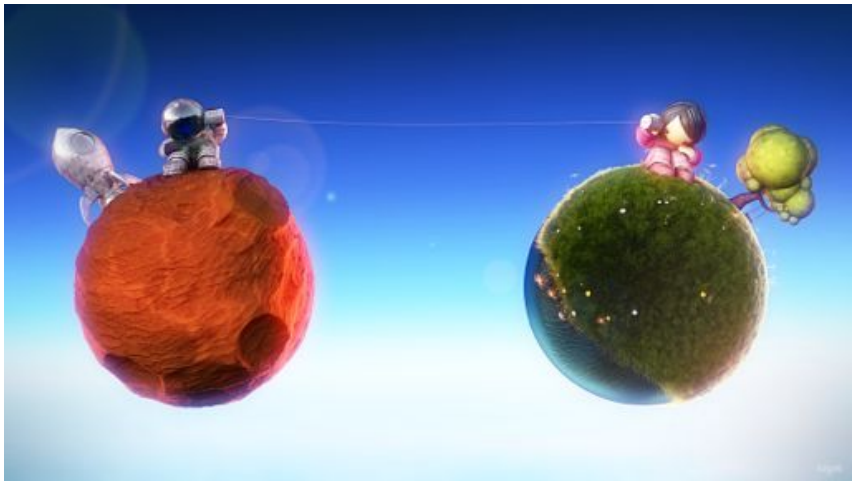

Figure 4: "Distante Worlds", made in Blender, by Reynante M. Martinez. Surce: [3]

One feature of Blender that are especially important in order to make this possible is python scripting. Most of the internal data that Blender stores in order to manage 3D models are accessible through a python console in Blender and an API. The same is true for most of the actions that are possible to do through the user interface. That is, 3D models can be created using Blender, which provides user friendly ways of modeling complex geometry, before the data that makes up these models are passed to a python function, which can do calculations based on the data, and change or add data to Blender models in order to see the result of the calculations.

This allows the BEM code to take data directly from blender, create the system of equations that need to be solved, solve the system, calculate velocity and pressure based on the solution, before the result is transferred back to blender in the shape of color maps and mesh deformation. Each vertex can get a separate color representing either pressure or velocity, and the deformation of the wake can be visualized. Everything can also be animated in time/iteration steps, as Blender provides native ways of "keying" or storing information to time steps. An example of a visualization made by the BEM code can be seen in figure 5

The visualization part of the code is planned to be extended with features that are not yet done. For instance, Blender can use "curve-objects" as geometry, which can be used to plot streamlines. Volumetric rendering is also possible, but for BEM codes this is not necessarily that useful visualization. This could however be a useful feature for plotting quantities such as vorticity in a viscous code.

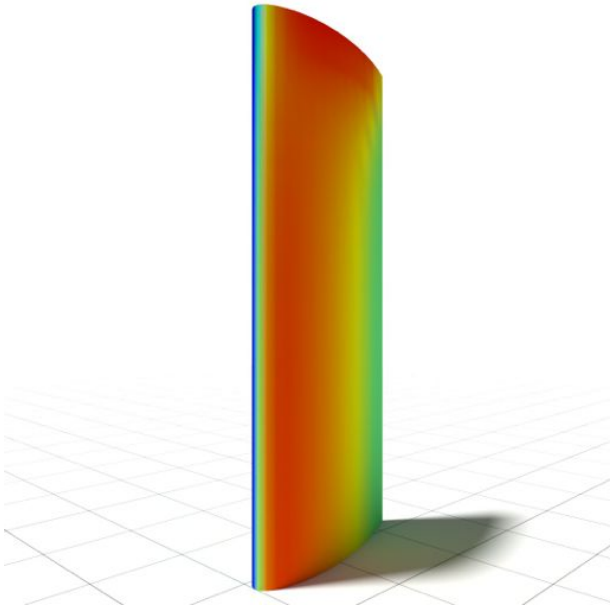

Figure 5: Color-mapping of velocity data to vertices in Blender

5 Conclusion

The main challenge of making a custom BEM code is in practice the computational time involved in making the system of equations that needs to be solved. PyOpenCL allows a code to be executed in parallel on many types of computational platforms, including many-core CPUs and GPUs. Using this parallel power can significantly reduce the time it takes to build the system matrix.

Blender provides a user friendly way to work with geometry, and through it's Python API, Blender can be extended with custom functionality such as simulation. This allows a programmer to get access to Blenders internal data to be used in the simulation, and the result of the simulations can be directly mapped back to Blender in order to create visualizations.

References

[1] Joseph Katz and Allen Plotkin. *Low-Speed Aerodynamics*. Cambridge University Press, second edition, 2001.

[2] Andreas Klöckner. Pyopencl. `http://mathema.tician.de/software/pyopencl/`.

[3] Reynante Martinez. Distant worlds. `http://www.reynantemartinez.com/distant-worlds.html`.

[4] Numpy Developers. Numpy home page. `http://www.numpy.org`.

Computations of wave loads on support structures of bottom-fixed offshore wind turbines

Marek Kraskowski, Duje Veić

Ship Design and Research Centre S.A. (CTO), Poland
marek.kraskowski@cto.gda.pl, duje.veic@cto.gda.pl

The paper presents the results of numerical computations of wave loads on supports structures of offshore wind turbines (OWTs) carried out with the use of RANSE-CFD and diffraction theory. The results are verified on the basis of experiment carried out in the towing tank equipped with wavemaker. The task of evaluating of wave loads on bottom-fixed structures may seem straightforward due to simplicity of the structure shape and lack of motion of analysed objects, however, care must be taken about correctness of simulating the wave motion in CFD computations, and the scale effect must be evaluated correctly. The computations and experiments presented here are focused on horizontal forces exerted by the wave motion on OWT support structures. Two possible approaches of evaluating the response to waves were used, i.e.:

- direct analysis of the structure at specified sea state, defined by idealised wave spectrum;
- evaluation of transfer functions (or "response amplitude operators" - RAO) for series of regular waves and computations of response at specified sea state using the formula:

$$RMS^2 = \int_0^\infty S(\omega) RAO^2(\omega) d\omega$$

where RMS is the root mean square of the response and $S(\omega)$ is the spectral density of the irregular wave.

The most common method for evaluation of wave loads on bottom-fixed structures consisting of slender cylindrical members is the Morison equation - a semi-empirical formulation using the resistance and added mass coefficients. It allows for very fast, and also sufficiently accurate computations in case when the disturbance of velocity field due to presence of structure is low. In case of OWT support structures, this is not necessarily true; for that reason, accuracy of other available computational methods was verified. Two types of support structures were investigated: a tripod and a gravity base. The models of these structures, used in experiments, are presented in Fig. 1. The scale factor is 1:40.

Fig. 1 Models of analysed structures – scale 1:40

The realized analyses include:

- measurements in the towing tank: regular (frequency domain) and irregular waves (time domain);
- RANSE computations with STAR-CCM+: regular and irregular waves (only for tripod);
- Computations based on diffraction theory (ANSYS AQWA): regular waves.

Comparison of results obtained with these three methods allows for verification of accuracy of numerical methods at model scale (i.e. accuracy of simulating the experimental conditions directly). Moreover, due to the fact that the computations with AQWA neglect the water viscosity at all, contribution of viscous forces to global forces can be evaluated, and thus the scale effect can be estimated.

The RANS computations were carried out at model scale for one wave direction in both regular and irregular waves. Symmetry of the flow was assumed, thus, only half of the model was modelled directly. This is in fact quite strong assumption in case of the flow around blunt bodies; it may result in unphysical flow on the downstream side of the analysed structure. Further studies were undertaken to check the validity of this assumption. The method of modelling the wave motion of the water consisted in applying appropriate boundary condition at the inlet of the computational domain (prescribed velocity distribution and water elevation resulting from linear wave theory) and introducing the damping zone on the opposite side of the domain, preventing the wave reflections inside the domain. In the damping zone, artificial body forces are introduced, counteracting the vertical motion of water. Using the linear wave theory for computing the boundary values at the inlet is justified by the fact that the wave motion at some distance from the inlet no longer depends of method of generating the waves. It is thus sufficient to introduce periodic oscillation of the water. Figure 2 shows the scheme of the method of modelling the wave motion.

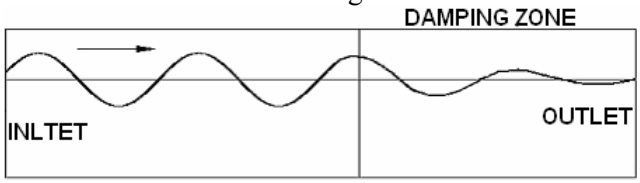

Fig. 2 Modelling the wave motion

The global view of the computational mesh is presented in Fig. 3. The depth of the domain corresponds to actual depth of the towing tank, so as the results of CFD and experiment can be compared directly. The solver setting were as follows:

– Time step: 0.005s;
– Number of iterations per time step: 5;
– Time discretization: second order.

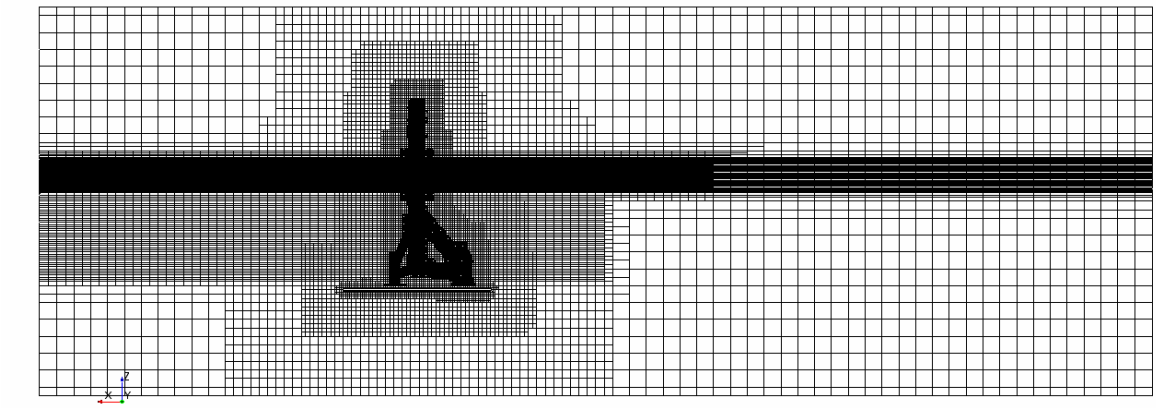

Fig. 3 Computational mesh for the tripod structure

The weather conditions of interest are storms in Baltic sea; the primary sea state to be analysed is the 50-year storm, which was approximated by JONSWAP spectrum of the following parameters:

– Significant wave height: $H_S = 9.23$ m
– Peak period: $T_P = 11.3$ s.

RANS simulations of the waves require the adaptation of the computational mesh, as insufficient density results in unphysical damping of the wave motion. The mesh density for the simulation of irregular wave of interest was adjusted in two steps by simulating the regular wave of the height corresponding to significant height of irregular wave, and period corresponding to zero-crossing

period of irregular wave. The characteristic parameter of the mesh density is the number of cells per wave height in the free surface region. The meshes with 15 and 30 cells per wave height were tested. Comparison of the results is presented in Fig. 4. For both densities of mesh, the resulting wave was lower than the wave prescribed at the inlet. For coarser mesh, reduction of wave height was observed throughout the simulation time. For fine mesh, reducing the wave height was observed at the beginning of the simulation; after some time, the wave height become stable.

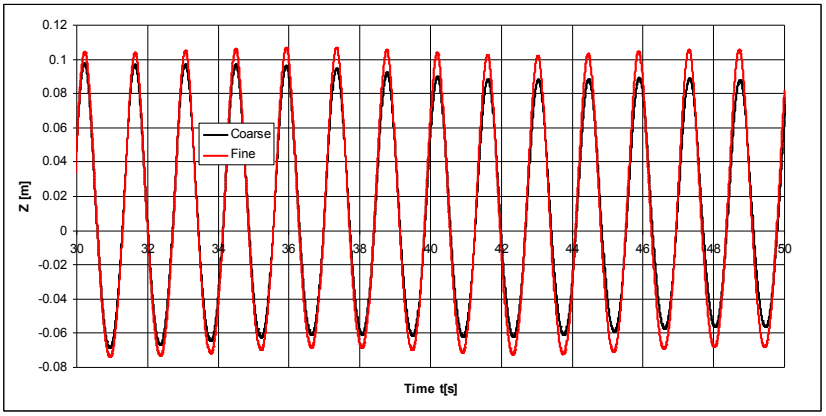

Fig. 4 Influence of the mesh density on modelling the wave motion.

After this preliminary analysis of influence of mesh density on accuracy of simulating the wave motion, the 50 year storm was simulated. Verification of accuracy of simulating the irregular wave requires spectral analysis of computed wave elevation vs. time. In few first test computations, noticeable reduction of significant wave height compared to theoretical value was observed, and subsequent attempts on improving the accuracy by refining the mesh and time step were not successful. It was then proposed to try increasing the resulting significant wave height by increasing the theoretical wave height at the inlet. This crude method turned out to be successful, i.e. the resulting wave spectrum was very close to theoretical JONSWAP spectrum (Fig. 5). A tendency to reduce the energy of shorter waves is observed; CFD also generated a second peak of spectrum for very low frequencies, which was considered to be a numerical effect, but its source was not recognized yet.

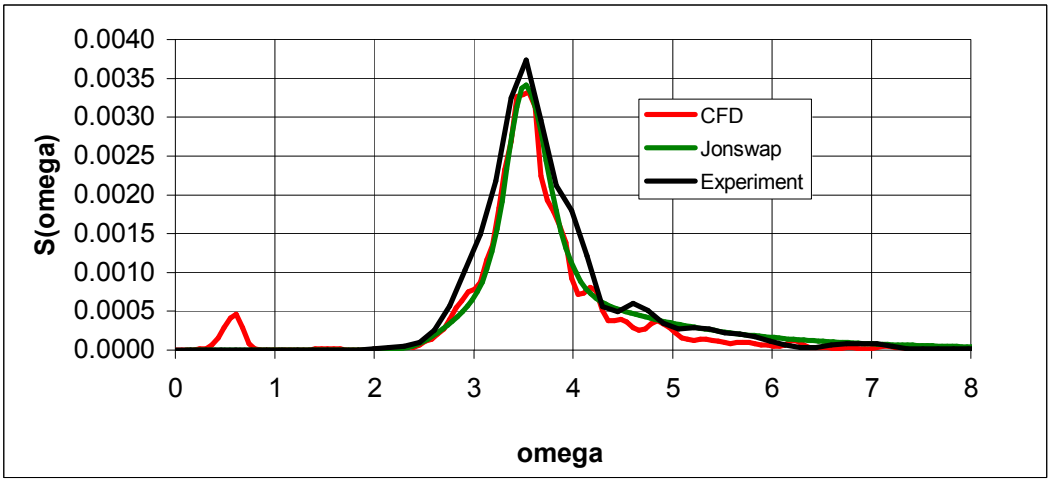

Fig. 5 Realized wave spectrum (CFD) vs. theoretical spectrum – model scale

The RANSE computations for regular waves (evaluation of transfer function) were carried out for small wave height, corresponding to the height used in the towing tank experiment, i.e. 3 cm. The comparison of mesh densities used for analyses in regular and irregular waves is presented in Fig. 6 (the width of central column of tripod is visible). Fig. 6 shows that the analysis in regular waves requires very fine mesh and thus can be inefficient in many cases.

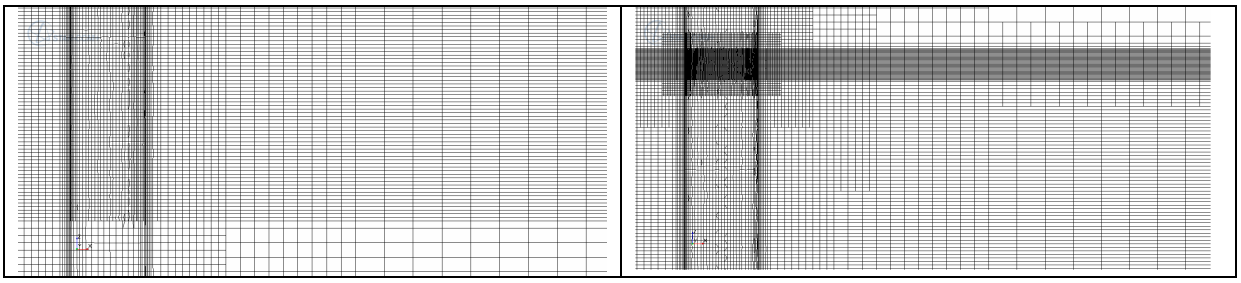

Fig. 6 Mesh density in the computations for irregular (left) and regular (right) waves

In case of regular waves, less care was taken about resulting wave height, as the computed force amplitude for each wave frequency was normalized by the actual wave height.

For the computations based on diffraction theory, carried out with ANSYS AQWA software, the surface mesh of app. 3200 faces was used. The numerical model is presented in Fig. 7. The software using the diffraction theory allows for evaluation of transfer function in entire interesting range of wave frequencies and for several wave directions in approximately one hour.

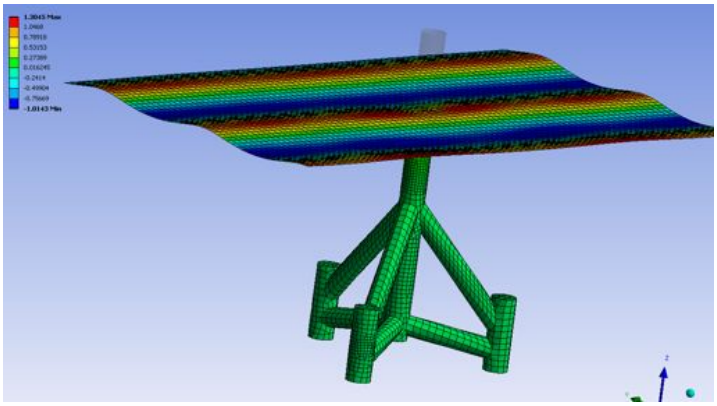

Fig. 7 Numerical model – diffraction theory

The comparison of transfer functions predicted with the use of model tests, RANSE CFD and diffraction theory is presented in Fig. 8 (tripod) and Fig.9 (gravity base).

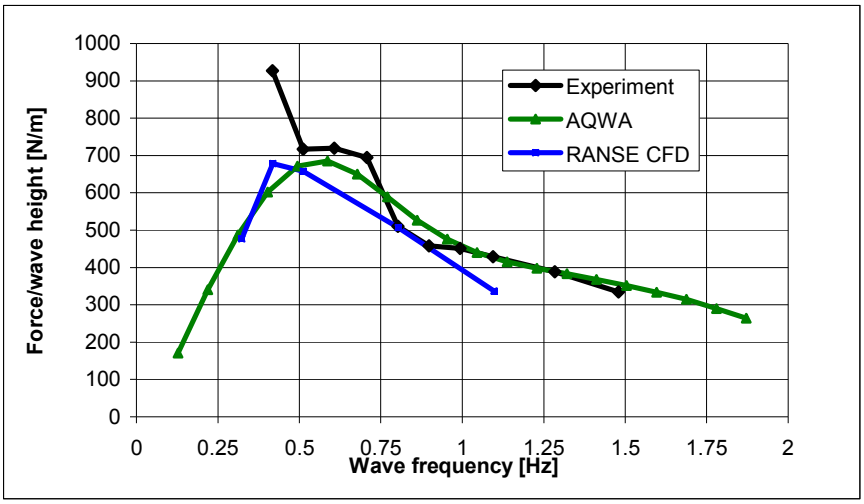

Fig. 8 Comparison of results for regular waves – tripod, model scale

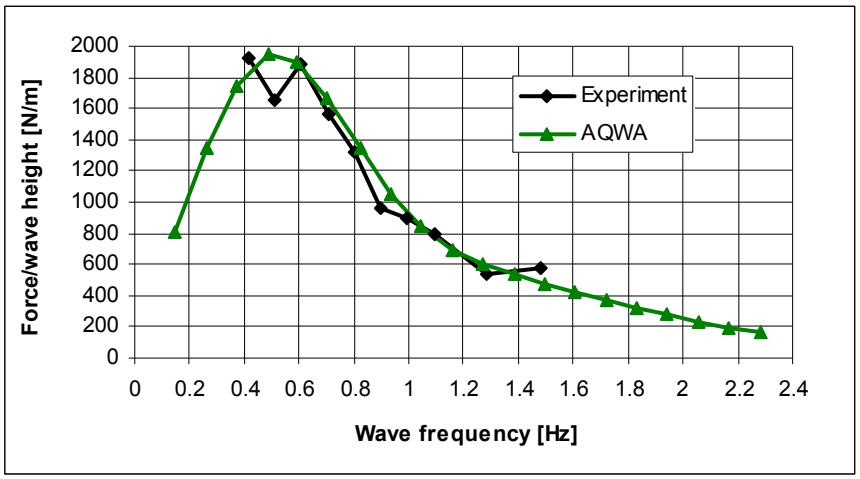

Fig. 9 Comparison of results for regular waves – gravity base, model scale

Comparison of the results of numerical computations with the results of measurements yields the following conclusions:

- The results of computations using the diffraction theory (AQWA) are in general consistent with the results of measurements, especially in case of gravity base. This allows concluding that the wave loads for analysed structures are dominated by pressure forces and the scale effect is small;
- For the tripod, large discrepancy between AQWA and the experiment is visible for lowest frequency considered in the measurements. The most important difference between the flow model used by AQWA and actual flow physics is neglecting the viscosity, but the contribution of viscous forces is expected to be much lower. There was also no resonance of the measurement stand. Thus, the cause of this phenomenon was not identified yet;
- Although the CFD computations take into account the water viscosity, the qualitative character of CFD results is closer to the results of AQWA computations than to experimental results. The results of CFD computations are underestimated in prevailing range of analysed frequencies.

The CFD computations of loads on tripod structure for irregular waves, corresponding to the wave spectrum presented in Fig.5, are presented in Fig.10. The presented curves are the spectra of horizontal force. The CFD results are close to experimental values; the discrepancies result partly from the fact that the wave height in the experiment was too large, while the wave in CFD was quite close to theoretical wave (see Fig.5).

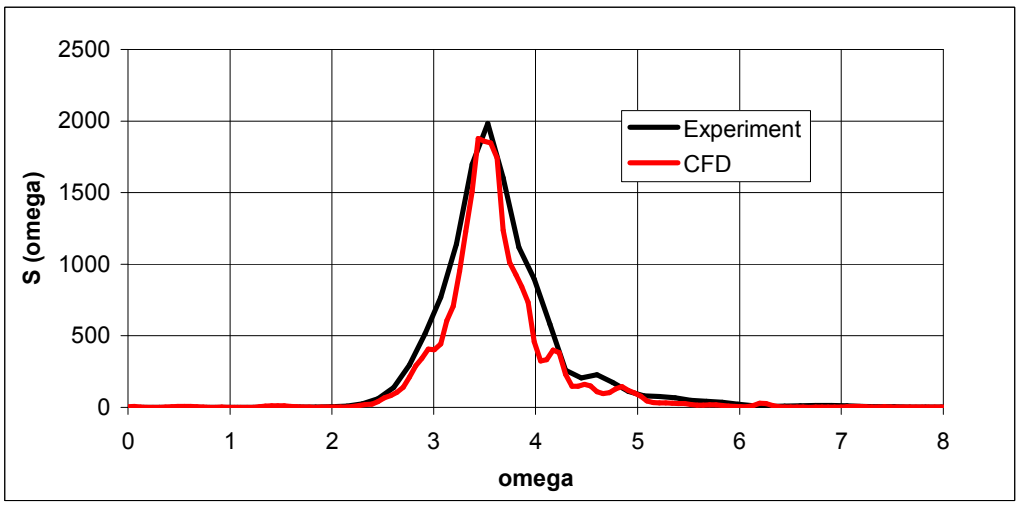

Fig. 10 Spectra of horizontal force – CFD vs. experiment

The table below show summarizes the RMS values of horizontal forces computed for the tripod structure with the use of all considered approaches.

Tab. 1 Summary of the results for tripod structure

	Force RMS [N]
Experiment – irregular wave	41.4
Experiment – regular wave	39.7
Diffraction theory - AQWA	37.0
RANSE CFD - irregular wave	38.6
RANSE CFD – regular wave	34.3

The results are quite consistent for all considered methods; only the force computed on the basis of transfer function from CFD is underestimated. The approach based on CFD computations is also not very efficient, as the evaluation of transfer function value for single wave frequency required one day of computations in presented case.

The realized work shows that both CFD and diffraction theory are suitable for evaluation of wave loads on selected types of support structures of OWTs. The presented work is in progress; further challenges include:

- Verification of CFD computations for jacket support structures, consisting of slender members, for which the scale effect is expected to be considerable;
- Evaluation of wave loads with taking into account the flexibility of the structure (especially important for the monopiles) – fluid-structure interaction;
- CFD computations of extreme events – a “freak wave”;

Acknowledgement: the work presented here was carried out within the framework of AQUILO project (agreement No. PBS1/A6/8/2012), supported by The National Centre for Research and Development.

Study of underwater noise signature from a tanker with a cavitating propeller using a DDES and acoustic analogy method

Da-Qing Li, Jan Hallander and Roger Karlsson

SSPA Sweden AB

Introduction

Shipping induced underwater radiated noise (URN) is reported to have increased significantly in the past decades, resulting in at least 15-20 dB increase in ambient ocean noise compared to pre-industrial levels. Excessive URN pollutes ocean environment and threatens marine life. International maritime organizations like IMO are paying increasing attention to many hydro-acoustic effects due to ship transportation. It is no doubt important to understand the ship generated noise and its radiation characteristics. Equally important is computational tools to predict reliably the noise level generated by ships at various operating conditions. Among the noise sources generated by a travelling ship, the propeller and hull scattering have been recognized as two dominant sources contributing to URN at the low frequency spectrum. Cavitation on propellers further enhances the radiated noise level over a wide frequency spectrum. Cavitation noise occurs when the cavity volume changes (e.g. the growth and collapse of cavitation). Collapsing cavities cause broadband noise in a frequency range up to 100 kHz. In addition, sheet cavitation produces tonal noise at harmonics of blade passing frequency (BPF), due to its volume changes with pressure variations when the propeller blade passes through the wake field.

The collaborative project AQUO (Achieve QUiter Oceans by shipping noise footprint reduction) of the 7th EU Framework Program is formed to provide support to policy makers with practical guidelines to reduce shipping noise for a quieter ocean and to investigate design improvement solutions and mitigation measures to manage ship URN and its impact on the marine fauna. Within the WP2, considerable effort is devoted to extensive experimental campaigns, improvement and validation of numerical methods to predict URN from propellers including cavitation effect and interaction with ship hull. A costal tanker and a research vessel were selected as subject of study. SSPA is engaged in the model testing, full scale measurement and numerical simulation of the coastal tanker.

The simulation is carried out with a hybrid method using a Delayed Detached Eddy Simulation (DDES) solver for flow resolution and an acoustic analogy method of Ffowcs Williams-Hawkings (FW-H) permeable surface integration for prediction of far field noise. The commercial software ANSYS FLUENT 15.0 is used. This talk presents some preliminary results of the still ongoing simulations and a comparison with the model test data.

Ship and propeller model

The coastal tanker M/T Olympus, kindly provided by Sirius Shipping (http://siriusshipping.eu/) for use in various tests in AQUO project, has a controllable pitch propeller. The main dimension and propeller characteristics are given in Table 1.

Experiment for noise measurement

Model tests carried out at SSPA include open water test, resistance, wake measurement and self-propulsion tests at design and ballast draughts. In addition, cavitation observations, pressure pulse and noise measurements were performed at 6 loading conditions. The loading condition LC2, corresponding to NCR power with 15% seamargin with design pitch setting at

ballast draught, is studied computationally. Noise measurements were made using three hydrophones (Brüel & Kjær type 8103) attached to wing-profile swords mounted in the cavitation tunnel, Figure 1 is a photo showing the hydrophone setup. The ship model is mounted on the ceiling at even keel condition but the cavitation number selected for the cavitation test is based on the ballast draught with a bow-up trim angle 0.78°. The propeller acoustical centre (AC) is defined at blade position θ=0° and a non-dimensional radius r/R=0.7, where R is the propeller radius. The distances from the hydrophones to AC are listed in Table 2. Model test results have been reported by Hallander and Lindell (2013).

Hull	Symbol	Value	Propeller	Symbol	Value
Scale factor	λ [-]	20	Scale factor	λ [-]	20
Length between perpendiculars	Lpp [m]	116.9	Diameter	[m]	4.8
Beam moulded	B [m]	18	Direction of rotation	[-]	Left
Fore draft	T_F [m]	8.12	Number of blades	[-]	4
Aft draft	T_A [m]	8.12	Blade area ratio A_E/A_O	[-]	0.45
Volume displacement	Δ [m^3]	12925	Pitch ratio P/D at r/R=0.7	[-]	0.87

Table 1 Main dimension of Olympus and her propeller characteristics

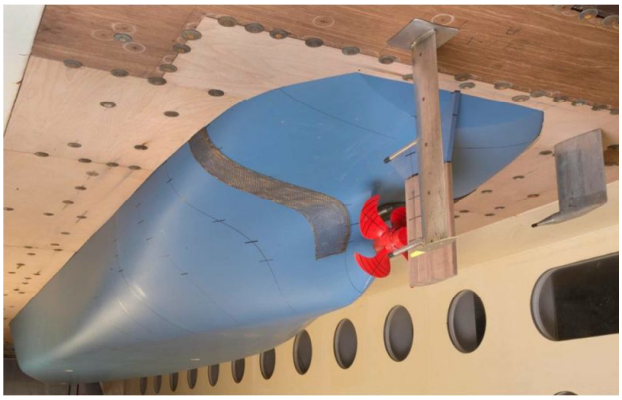

Figure 1 Hydrophone setup for noise measurement

Hydro-phone	Location	Distance to AC (mm)
K66	Traversable sword	631
K78	Port side sword	429
K79	Starboard side	460

Table 2 Hydrophone locations

Numerical methods

The numerical approach consists of two steps. First, it resolves the flow field around the ship hull with a DDES method. DDES is essentially a hybrid solution technique that switches between a RANS method and an LES (Large Eddy Simulation) method depending on grid resolution provided. With this technique, the RANS method is used to solve the flow region inside the attached boundary layer and the LES is employed in the regions of separated flow or wake where the grid is fine enough. In region farther away from the hull where the grid becomes coarse, flow field is solved by the RANS method too. For turbulent viscosity modelling, the two-equation SST k-ω turbulence model is employed. Secondly, the noise propagated from the sources to any arbitrary receiver location is determined by solving an acoustic pressure wave equation. In the present work, the solution for acoustic pressure is obtained by numerical integration of Ffowcs Williams-Hawkings (FW-H) equation over predefined permeable surfaces. As regard to cavitation prediction, the multiphase mixture flow DDES solver and Zwart's cavitation model are employed. More details can be found in ANSYS Fluent v15.0 User Manual (2013).

Computational domain, grids and BCs

A rectangular computational domain is defined around the hull (Figure 2). The inlet boundary is located at $1L_{pp}$ distance from FP and the outlet boundary $1.5L_{pp}$ aft of AP. The two sides and the bottom of the rectangular domain are placed $1L_{pp}$ away from the central line. A constant velocity, turbulence intensity and viscosity ratio are specified at inlet whereas a constant pressure is specified at outlet to ensure correct cavitation number. The free surface, side and bottom boundaries are treated as slip walls. Another rectangular surface that closely surrounds the model hull is visible in Figure 2, this surface serves as a permeable integral surface in FW-H acoustic analogy method. The meshes are of hexahedral type. The grid lines are refined not only in the wall normal direction to achieve a $y^+=1$, but also in the streamwise and girthwise direction to fulfil grid requirement for DDES method, i.e. about 10 nodes in the streamwise direction and 20 nodes in the girthwise direction per boundary layer thickness. The total number of grid cells is about 35 million.

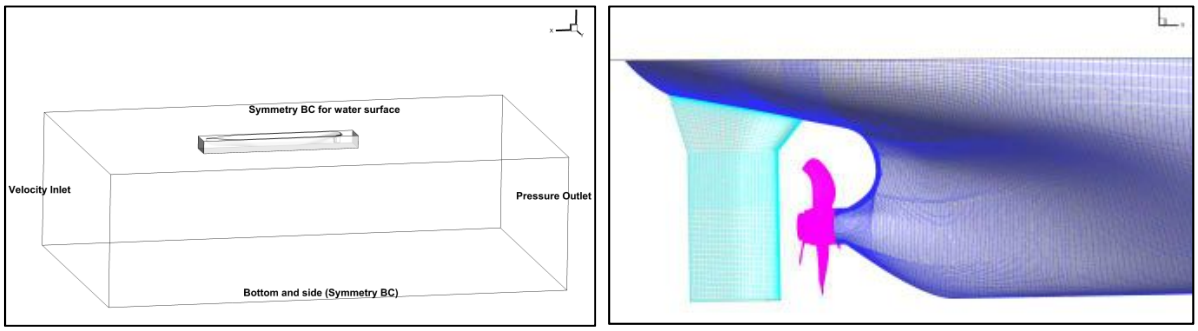

Figure 2 Computational domain (left) and surface mesh on propeller, rudder and stern (right)

Preliminary results

At loading condition LC2 the propeller is operating at a cavitation number $\sigma_n=2.9$ and a thrust coefficient $K_T=0.193$. The simulation is performed by retaining the same rotational speed as measured in the cavitation tunnel (n=23.25 rps) while adjusting the inflow speed until the computed K_T reaches about the same level as in the cavitation test, i.e. via the K_T-identity method. The predicted turbulent vortex structures at the stern are illustrated in two instantaneous sequences in Figure 3 with an iso-surface of Q=1000 (s^{-2}), where the Q-criterion is defined as $Q=\frac{1}{2}(\Omega^2-S^2)$, in which S is the strain rate and Ω the vorticity rate of the flow field. The tip vortices and the hull-rudder wake structure are well captured in the near downstream region, and they become dissipative farther downstream.

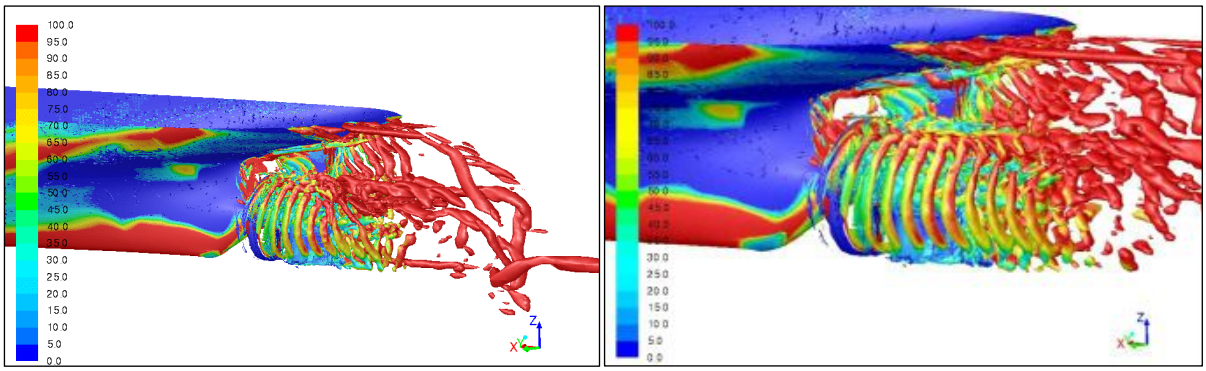

Figure 3 Vortical structure in wake and propeller slipstream represented by iso-surface of Q-criterion

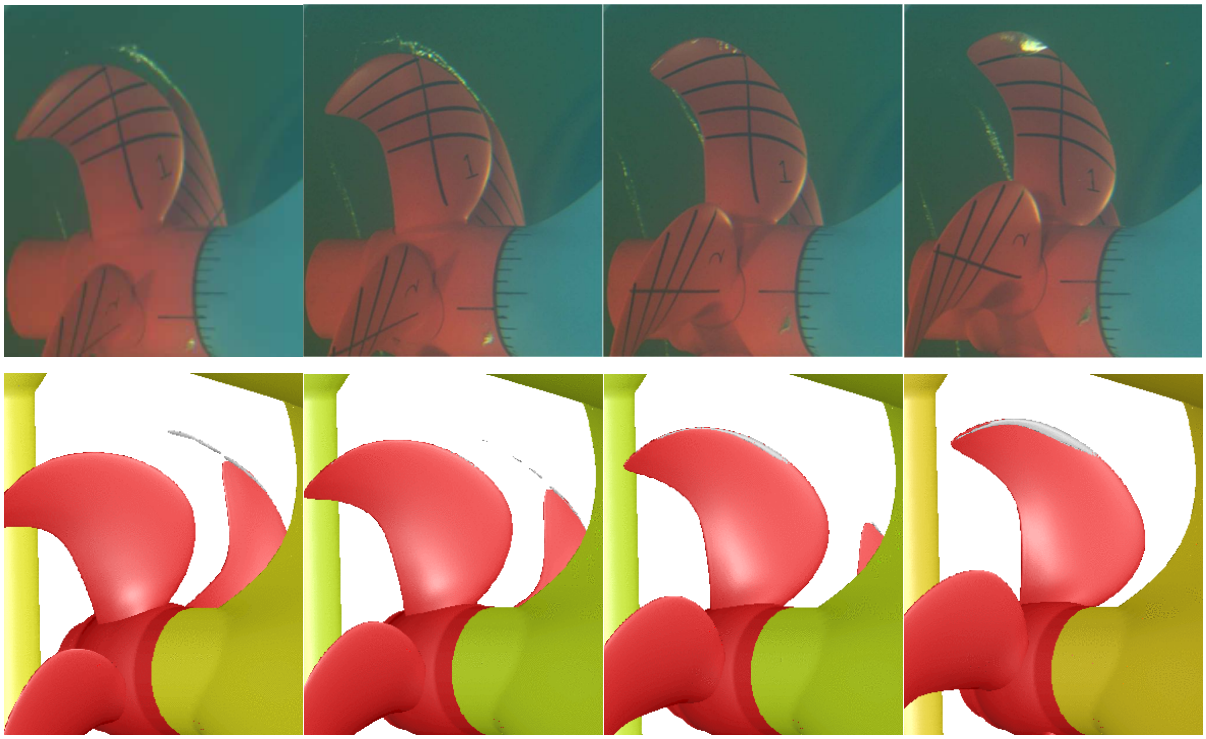

Figure 4 Cavitation pattern at θ=340°, 350°, 0°, 10°. Exp. (top) vs. DDES simulation (bottom)

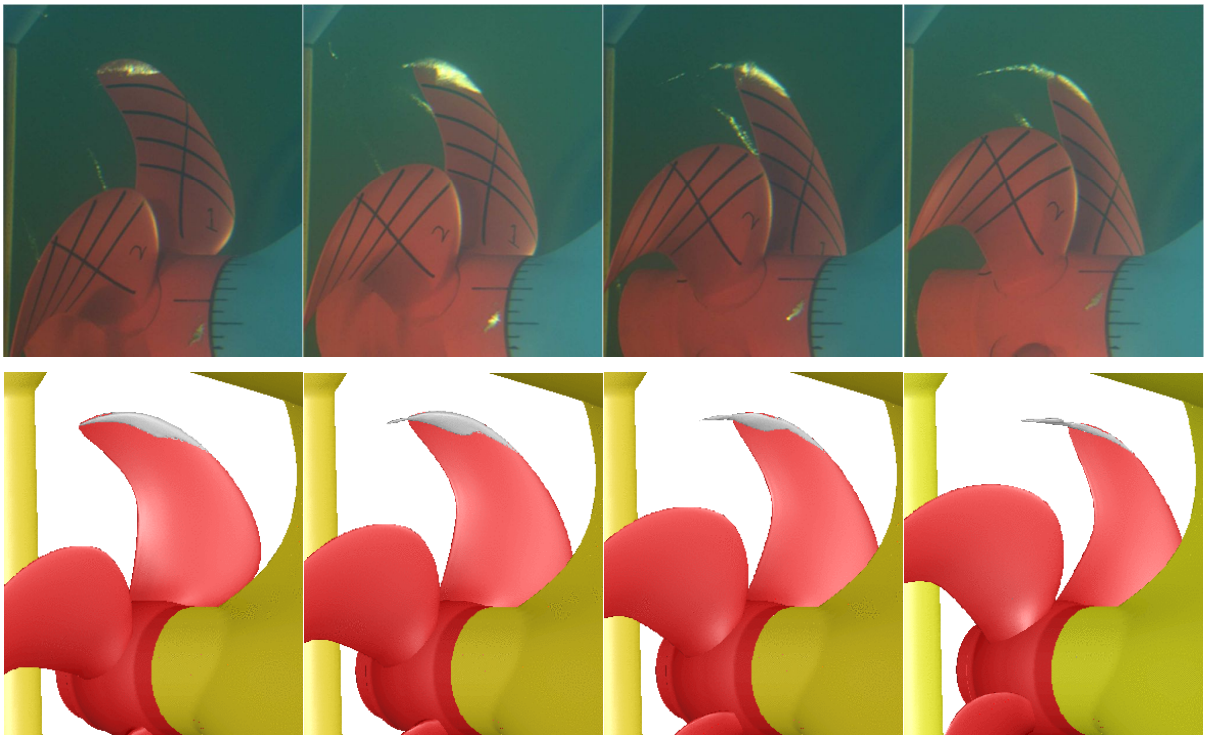

Figure 5 Cavitation pattern at θ=20°, 30°, 40°, 50°. Exp. (top) vs. DDES simulation (bottom)

In the cavitation test, a narrow and slightly unstable sheet cavity is found on suction side, starting from blade angular position θ=0° and continues up to θ=60°. As the blade exits the wake peak, the cavity rolls up into a cavitating tip vortex visible in θ=60°-70°. The predicted sheet cavity correlates quite well with the dynamic change of cavitation observed in the experiment, as shown in Figure 4 and Figure 5. Yet there are differences, the predicted cavity

starts earlier at a lower radius (at θ≈355° and 0.8R), and it seems to extend a bit more in the chordwise direction. It is however rather stable. Note also that there is a difference in the viewing angle in the simulation. The tip vortex in the experiment is a bit unstable and some bursting is observed. In the simulation, the extension of tip vortex cavity is to some extent under-predicted and no bursting is visible. It is worth noting that the model in simulation is placed at the ballast draught with exactly the trim angle at that loading (0.78°) whereas the model in the cavitation test was placed at even keel draught. This discrepancy may have a consequence on the wake field in front of propeller, thereby resulting in some discrepancy in the cavitation pattern in the simulation.

The measured sound pressure level is compared with the predicted noise signature up to 1kHz in Figure 6 at three hydrophone locations. The vertical grid lines in the diagrams are drawn at harmonics of BPF with the base harmonics of 93Hz. First, it should be pointed out that the simulation with the FW-H acoustic analogy activated was carried out for only about one and half propeller revolutions although it was started after several revolutions of cavitation simulations, therefore the statistic data for acoustic signal is far from sufficient. Comparing with measured noise signal, we see that the tonal noise, though appearing at exactly the multiples of BPF, is significantly under-predicted in frequency band lower than 186Hz and higher than 651Hz. The tones in frequency range 186-651Hz have a good correlation with the measured data. The predicted noise reveals in general a lack of broadband noise spectrum and basically only tonal noise is visible, which is not surprising recalling the limitation of available data. The increased broadband noise levels in the measurement for the range around 1000Hz are attributed to the tip vortex cavitation and its bursting as seen in Figure 4-5. The measured tones below the 1st BPF (93Hz) are the background noise, mainly caused by the cavitation tunnel impeller.

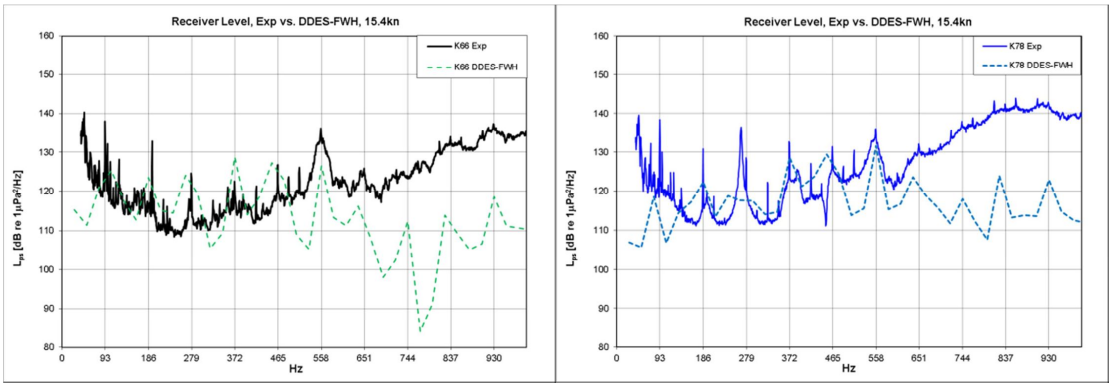

(a) Hydrophone K66 (b) Hydrophone K78

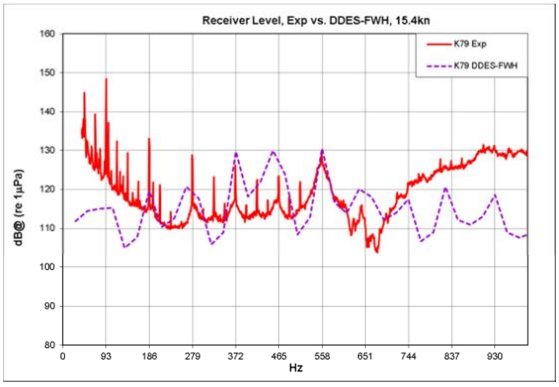

(c) Hydrophone K79

Figure 6 Noise signature at three hydrophone locations, Exp. vs. simulation

The noise signature after normalization to 1 m source level noise is shown in Figure 7 for all three hydrophones. After having been converted to source level, three measured signals still reveal some discrepancy in between, possibly an indication of directivity effect.

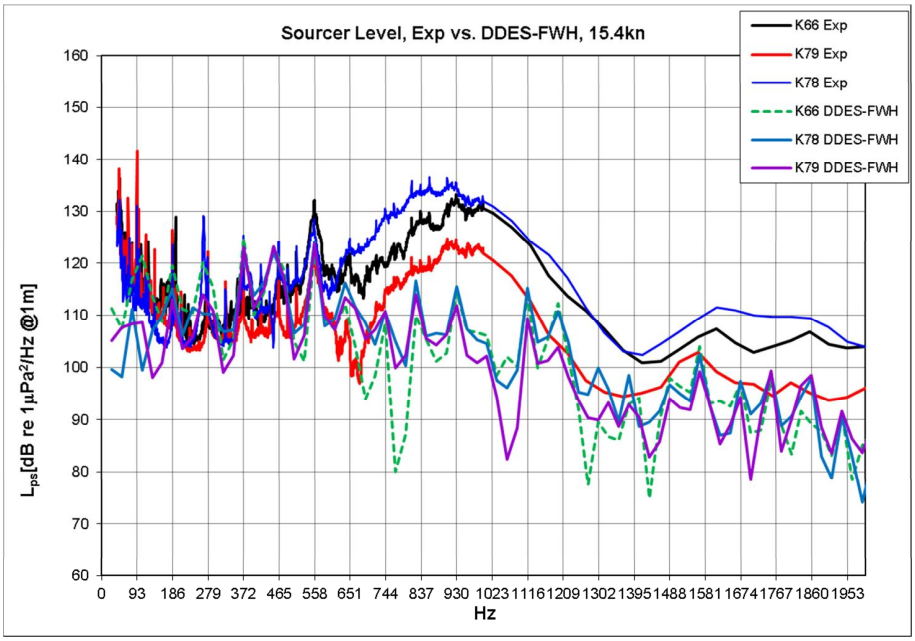

Figure 7 Overall comparison at source level, measured vs. predicted

Concluding remarks

Despite a difference in trim angle between the set-up for the simulation and the cavitation test, the predicted sheet cavitation and tip vortex cavity agree fairly well with that observed in the experiment. The predicted noise reveals a lack of broadband spectrum and primarily the tonal noise is visible, due to insufficient acoustic data available so far. Recalling our previous work using URANS-FWH method and an overall 25dB under-prediction of measured data (Hallander et al. 2012), the present DDES-FWH method seems to be promising and a step towards more reliable and accurate prediction of URN.

Acknowledgements

This work was carried out within the collaborative project AQUO (Achieve QUieter Oceans by shipping noise footprint reduction), funded by the European Commission within the Call FP7 SST.2012.1.1-1: Assessment and mitigation of noise impacts of the maritime transport on the marine environment, Grant agreement No. 314227, coordinated topic "The Ocean of Tomorrow". The content of this paper does not reflect the official opinion of the European Union. Responsibility for the information and views expressed in the paper lies entirely with the authors.

References

[1] Hallander J. and Lindell P., 2013, “Model Tests for M/T Olympus”. SSPA Report RE40116086-01-00-A, Göteborg, Sweden.

[2] Hallander, J., Li, D.Q., Allenström, B., Valdenazzi, F. and Barras, C., 2012, “Predicting underwater radiated noise due to a cavitating propeller in a ship wake”, Proceedings of 8th International Symposium on Cavitation, CAV2012, No. 151, Singapore.

[3] ANSYS FLUENT 15.0, 2013, “FLUENT User Manual”.

[4] Okeanos, 2008, “Underwater Radiated Noise of Ocean-Going Merchant Ships”, Int’l workshop on Shipping Noise nad Marine Mammals. Hamburg, Germany.

The influence of turbulence modelling techniques on the predicted cavitation behaviour on a NACA0009 foil

Artur K. Lidtke * [a], Stephen R. Turnock[a] and Victor F. Humphrey[b]

[a]Fluid-Structure Interactions Research Group, University of Southampton, SO17 1BJ, UK
[b]Institute of Sound and Vibration Research, University of Southampton, SO17 1BJ, UK

Nommenclature

α - volume fraction of fluid
$\mathbf{U}$ - velocity vector
p - pressure
$\boldsymbol{\tau}$ - subgrid stress tensor
ν_l - kinematic viscosity of water
ν_v - kinematic viscosity of vapour
ρ_l - water density
ρ_v - vapour density
R - mean cavitation nuclei radius
$\omega = |\nabla \times \mathbf{U}|$ - vorticity vector
n - number of cavitation nuclei per unit volume

1 Introduction

In recent years, the interest in limiting the input of energy and, in particular, noise into the Oceans has been getting increasingly more prominent. This resulted in, amongst others, European Union initiatives investigating the potential of reducing this component of human impact on the environment [1, 2]. While of course there are multiple sources of noise in the Oceans, natural and anthropogenic alike, shipping as a whole contributes to a large proportion of the total ambient sound level, particularly in the 10-1000 Hz frequency range [3, 4].

There exist multiple possible noise generation mechanisms for a marine propeller. First category may be attributed solely to unsteady turbulent flow and may contain both low- and high-frequency components. Most of the prominent mechanisms arise, amongst others, due to the boundary layer interacting with the trailing edge, vortices being shed, separation and impinging of vortical structures on the lifting body[5]. The second noise source category is associated with the cavitation phenomenon. This has primarily high-frequency components, due to such events as vortex cavitation, shock wave formation and cavitation sheet shedding, but may also give rise to low-frequency noise via the cavity volume fluctuations [6, 7].

This paper presents the preliminary results of a study conducted in order to establish cost-effective measures of classifying the noise levels from the propeller with the use of numerical techniques. In more detail, it discusses the influence of turbulence modelling on the predicted flow field. This is done by comparing the solutions obtained for a NACA 0009 hydrofoil case using the $k - \omega\ SST$ RANS model, implicit LES and LES with Smagorinsky model. The entire study has been conducted using open-source OpenFOAM® 2.2.2 libraries.

2 Numerical modelling

Cavitation originates from small gas nuclei present in the liquid [8]. As they are subject to low pressure their surface becomes subject to tensile stress and, depending on the local conditions and fluid properties, different types of cavitation may be observed [9]. Given the very small scale of the typical nuclei, ranging between 2 and 50 μm [10], it would be computationally prohibitive to attempt to resolve this behaviour in full detail from an engineering viewpoint. This gives rise to the use of cavitation models that attempt to capture the physics of the multiphase flow without resolving the intricate detail of this phenomenon.

A wide range of modelling approaches exist, first category of which tracks the motion of individual bubbles or macro particles by solving dedicated equations of motion. While providing detailed information about the flow these methods have been reported to be expensive due to a large amount of additional equations being solved. Moreover, careful treatment of the interactions between bubbles and solid surfaces is required which imposes further difficulties in efficient implementation [11, 12]. Another set of methods, the pressure-based models, allow both liquid and vapour phases to occupy the same physical space and their motion is solved using two sets of mass and momentum equations. The interactions between them are achieved by introducing appropriate source terms in the Navier-Stokes equations [9, 13]. The single-fluid (or density based) approaches, on the other hand, solve a single set of equations for the entire flow and the phase change needs to be accounted for otherwise. In this work the latter of the methods is used in conjunction with the volume-of-fluid (VOF) framework for modelling the cavities.

Irrespective of the underlying assumptions, a cavitation model must cope with predicting very complex and transient phenomena in order for a time- and space-accurate solution to be provided. These may include formation of re-entrant jets, non-periodic fluctuations of the cavity interface caused large amplitude variations of the angle of attack and loading, and creation of additional regions prone to cavitation due to three-dimensionality of the flow. Moreover, the turbulent mixing may force more nuclei into the boundary layer which may alter the form of cavitation present[9]. Additionally, the bubble volume change will affect the vorticity distribution and effectively the flow[14].

*Corresponding author's e-mail: akl1g09@soton.ac.uk

From a hydro-acoustic point of view, the use of a cavitation model greatly reduces the insight into the noise characteristics that may be obtained. That is because some of the main sources of cavitation induced noise are vortex cavitation, shock wave formation and sheet cavity shedding which predominantly consist of high frequency components [6, 7]. The low frequency noise due to cavity volume fluctuations, taking the form of a monopole source, may be computed even with the proposed methods [6, 7, 15, 16]. In combination with the non-cavitating noise components this will form a significant part of the entire noise spectrum but detailed information is needed about the unsteady nature of the flow for an accurate solution. For this reason the methodology considered in this work is based on Large Eddy Simulation (LES) turbulence modelling technique.

It has been reported that by considering compressibility of the flow certain advantages could be achieved. These could include a reduction in the pressure equation instabilities [17] and being able to at least partially resolve the transient phenomena associated with bubble collapse. On the other hand, the speed of sound in water (appox. 1500 ms^{-1}) is typically much larger than the flow speed considered. This implies that for a pressure wave passing through the fluid to be accurately resolved in time a very small time step would be necessary. In their work Wang and Ostoja-Starzewski successfully used a weekly compressible flow formulation which is said to overcome this limitation [18]. In this work, however, the incompressible flow assumption is used in order for the focus to be placed at other aspects of cavitation modelling.

2.1 Cavitation modelling

As already mentioned, the role of the cavitation model is to account for the mass of the fluid being transferred between the liquid and vapour phases or, in other words, predict the phase change from liquid to vapour and *vice versa*. In this work use is made of the model by Sauer and Schnerr [19] which aims to provide the required source term values by approximating the dynamics of individual bubbles present in the fluid.

The volume fraction of liquid is governed by a typical scalar transport equation, as shown in (1). The right hand side is however modified to allow for the mass to be created (condensation) or destroyed (vaporisation).

$$\frac{\partial \alpha}{\partial t} + \nabla \cdot (\alpha \mathbf{U}) = -\frac{\dot{m}}{\rho} \tag{1}$$

It should be mentioned that the pressure equation must also be modified by introduction of a source term in order to account for a velocity divergence term induced by the mass transfer, given by

$$\nabla \cdot \overline{\mathbf{U}} = \left(\frac{1}{\rho_v} - \frac{1}{\rho_l}\right)\dot{m} \tag{2}$$

The fluid properties at any one point in the domain are interpolated in accordance with the immiscible fluid mixture assumption of the VOF method, as shown in (3). It is apparent from said equation that no fluid volume is being destroyed but rather the mass is being transferred between the two phases as the volume fraction varies.

$$\begin{aligned} \rho &= \alpha\rho_v + (1-\alpha)\rho_l \\ \mu &= \alpha\mu_v + (1-\alpha)\mu_l \end{aligned} \tag{3}$$

For the system of equations to be closed an expression needs to be provided for the rate of change of mass, $\dot{m}$, term. At this point the assumptions of individual models start becoming important. In case of Schnerr-Sauer model the lacking quantity is derived from the equation of motion of an individual bubble, in its general form known as the Rayleigh-Plesset equation [8]. For simplicity, the model derivation neglects the higher-order terms, as well as the effects of surface tension and viscosity, resulting in

$$\dot{m} = \frac{\rho_\mathrm{l}\rho_\mathrm{v}}{\rho}(1-\alpha)\alpha\frac{3}{R}\sqrt{\frac{\frac{2}{3}(p-p_\mathrm{v})}{\rho_\mathrm{l}}} \tag{4}$$

where R is modelled based on the specified characteristic nuclei radius, R_0, and their volumetric density, n_0.

There have been several reasons for the Schnerr-Sauer model being used in this study. Firstly, in the presented form it is appreciably simple and introduces little overhead to the calculations apart from the need of solving the additional transport equation. It has also been demonstrated in a plethora of numerical investigations related to marine applications that it predicts the extent of cavitation appreciably well, including the unsteady cavity behaviour [9, 20, 21]. Moreover, the model is not dependent on any empirical coefficients, *per se*. The results it produces are, however, dependent on the choice of the water quality properties, namely n_0 and R_0, which makes it susceptible to prediction errors if these quantities are not chosen correctly.

2.2 Large Eddy simulation

LES is based on solving the filtered Navier-Stokes equations whereby the motions of large scales are fully resolved and the ones smaller than the grid resolution remain modelled. Filtering is done by multiplying the quantity in question with a convolution operator whose kernel is defined by the filter width related to the mesh size. Usually the speed of solution suffers when LES is used over unsteady RANS due to the increased mesh density required. However, with VOF multiphase approach a high grid resolution is necessary irrespective of the turbulence modelling technique. This implies that the increase in computational effort required will be significantly smaller and so LES may seem more appealing than for a non-cavitating flow simulation [22]. The mass and momentum equations in the incompressible form are shown in (5), with the overbar denoting a filtered quantity. These are solved using the PISO algorithm with implicit temporal schemes.

$$\begin{aligned} \frac{\partial \overline{\mathbf{U}}}{\partial t} + \nabla \cdot \left(\overline{\mathbf{U}} \otimes \overline{\mathbf{U}}\right) &= -\frac{1}{\rho}\nabla\overline{p} + \nu\nabla^2\overline{\mathbf{U}} - \nabla \cdot \boldsymbol{\tau} \\ \nabla \cdot \overline{\mathbf{U}} &= 0 \end{aligned} \tag{5}$$

In (5) $\boldsymbol{\tau}$ is the non-linear subgrid stress tensor which may be expressed as:

$$\boldsymbol{\tau} = \overline{\mathbf{U} \otimes \mathbf{U}} - \overline{\mathbf{U}} \otimes \overline{\mathbf{U}} \tag{6}$$

This may be modelled in a similar fashion to the turbulent eddy viscosity in RANS models by using the Boussinesq hypothesis. The latter assumes that the needed tensor may be described using a product of the fluid strain rate, $\mathbf{S}$, and an assumed subgrid viscosity, ν_{SGS}, yielding

$$\boldsymbol{\tau} - \frac{1}{3}\boldsymbol{\tau} \cdot \mathbf{I} = -\nu_{\mathrm{SGS}}\mathbf{S} \tag{7}$$

where $|\mathbf{S}| = (2\mathbf{S} \cdot \mathbf{S})^2$. One of the simplest available models is that by Smagorinsky, according to which the subgrid viscosity may be defined using the filter width, Δ, and a constant, C_S, as $\nu_{\mathrm{SGS}} = \left(C_S \overline{\Delta}\right)^2 |\mathbf{S}|$.

It needs to be noted that a large proportion of the turbulent kinetic energy spectrum is resolved explicitly in LES by definition. One may thus be tempted to abandon the subgrid model in lieu of an implicit modelling technique (ILES). In doing so one assumes the subgrid stress tensor to be zero and the dissipation is introduced to the flow through the grid-related discretisation error and the adoption of appropriate convective numerical schemes. Aside from simplifying the overall numerics this approach has been reported by Bensow et al. to reduce the problems associated with sharp fluid property gradients occurring at the cavity interface, as dictated by (3) [23]. As shown in the study by Lloyd, non-uniformity of grid in different directions may lead to the different velocity components being affected to a different degree when an implicit model is used [24]. This implies an additional level of care to be taken when undertaking the mesh design, especially for cases involving complex geometries such as marine propellers, potentially reducing the practical benefits of using ILES.

3 Test case

Numerical simulations have been focused on a NACA 0009 hydrofoil with the aim of replicating the conditions used for the Delft Twist 11 foil first presented by Foeth et al. [25, 26]. In said study a wing with a span-wise angle of attack variation symmetric about the mid-span was considered. Here, however, the geometry has been simplified to a fixed span-wise pitch distribution in order to allow a more in-depth study of the sheet cavity behaviour without the added complexity dictated by the complex three-dimensional flow features reported in the the original experiments.

The foil with chord of $0.15m$, angle of attack of 9° and span of $0.1\ m$ was placed in the centre of a domain which was to resemble the working section of the cavitation tunnel used by Foeth et al., as depicted in Figure 1. The densities of both fluids were taken to be 998 $kg\,m^{-3}$ and 0.023 $kg\,m^{-3}$ for water and vapour, respectively, and their corresponding kinematic viscosities were assumed to be $10^{-6}\ kg\,m^{-2}$ and $4.273 \cdot 10^{-6}\ kg\,m^{-2}$. The mean nucleation radius was assumed to be 50 μm with the corresponding distribution of $10^8\ m^{-3}$. Finally, the saturated vapour pressure of the mixture was taken to be 2970 Pa [26, 27].

The inlet was prescribed a fixed velocity of 6.97 $m\,s^{-1}$ and the simulation was carried out at the cavitation number of $\sigma = 1.07$ which was achieved by using a fixed value of pressure at the outlet of 29 kPa [26, 27]. Top and bottom of the numerical cavitation tunnel were treated as slip walls and cyclic boundary condition was prescribed to the span-wise boundaries. Convective outlet velocity conditions was used in order to limit the amount of reflections being propagated into the domain for the LES simulations [24]. The wing was treated as a no-slip surface. Wall functions were used in order to limit the cell count required in the boundary layer region, following the approach outlined by Bensow et al. [23, 28]. In order to promote convergence from the early stages of the simulations the runs were initialised from a steady-state, non-cavitating flow solution.

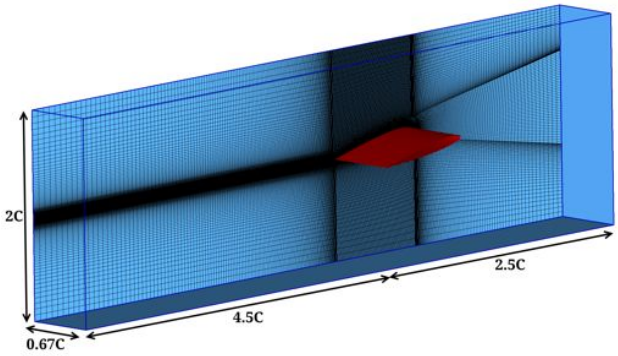

Figure 1: Overview of the domain and mesh used for all of the presented simulations. Height and width chosen so as to model the working section of the cavitation tunnel used in experiments by Foeth et al. [25, 26].

Temporal discretisation has been achieved by the use of a second-order implicit scheme which implied the maximum Courant number limit of 0.5 needed to maintain stability for LES simulations. This was kept the same for the RANS case as to allow better comparison. The volume fraction was discretised using the van Leer scheme with interface compression and a hybrid convection scheme was adopted in which upwinding is applied when required to maintain stability [24]. The velocity and volume fraction fields were solved for using the preconditioned bi-conjugate gradient (PBiCG) solver with the diagonal incomplete lower upper (DILU) preconditioner whereas the generalised algebraic multi-grid (GAMG) algorithm with the diagonal incomplete Cholesky (DIC) preconditioner was applied to the pressure equation.

Spatial discretisation of the domain has been achieved using a 480x164x80 grid with 5.1 million elements, most of which were concentrated in and near the boundary layer of the foil. Special care was taken to assure that the cavities present will not experience rapid changes in mesh density as they are formed, shed and convected downstream of the foil. The mesh was created using a set of in-house Python libraries combined with the OpenFOAM blockMesh utility.

The first wall-normal cell heigh was ensured to fall within $y^+ < 30$ everywhere on the surface of the foil except a small region close to the leading edge. For appropriate span- and chord-wise resolution of the flow the mesh was designed to be characterised by $x^+ < 200$ and $z^+ < 350$. The grid had been subject to a convergence study whereby the relative change in the predicted steady-state, non-cavitating force coefficients was investigated and found to be $< 2\%$ when compared to a mesh with 9.0 million cells.

4 Results and discussion

One of the primary low-frequency noise sources due to cavitation is the pressure variations induced by the oscillating cavity interface [10, 15, 29]. This is of particular importance when one considers the unsteady flow field a propeller operates in as it will force even more severe oscillations to occur and generate noise. Moreover, the changes in the volume of the cavities will interfere with the flow past the wing sections and alter the lift and drag characteristics. These are of course of high interest from the efficiency estimation point of view.

As a result, several aspects of the flow were studied in the presented investigation in order to provide an insight into the aspects of cavitation modelling relevant to low-frequency noise modelling. Firstly, Figure 2 presents the power spectral density of the lift coefficient recorded during the simulation. Figure 3 depicts the power spectral density of the total cavity volume, including both the attached and shed elements computed assuming the cavity interface to be described as $\alpha = 0.5$. All frequency components above 1 kHz have been removed as the sampling offset did not allow for them to be computed accurately. Similarly, the frequency bands below 4 Hz have been excluded due to limitations stemming from the total time of the simulations.

As can be seen, there are clear peaks in both spectra for all cases considered. It is interesting to notice the agreement between frequency peaks for both spectra for all cases. This immediately points out the dependence of the predicted forces on the variations of the cavity structure. However, the frequencies predicted using RANS, approximately 8 Hz, are significantly lower. This behaviour was expected as the required level of unsteadiness predicted using this method could not be achieved without any corrections being applied to the turbulence model [20]. A satisfactory agreement is observed between the implicit and explicit LES simulations, seeing 15.5 and 17.0 Hz, respectively. It is evident, though, that several higher modes have been predicted for the solution using the Smagorisnky model, whereas the implicit LES is primarily dominated by multiples of the primary shedding frequency.

An interesting observation may be made when comparing the cavity extents just after the point of maximum lift for both implicit and explicit LES simulations, shown in Figures 4 and 5, respectively. At this stage the attached sheet has been cut by the re-entrant jet close to the leading edge of the foil and starts being convected downstream to form a cloud. Both figures also show the clouds from the previous shedding event close to the trailing edge. One may immediately notice that the implicit model predicts a much more uneven surface of the cavity, inside the sheet and the cloud alike. Similar behaviour has been observed when Spalart-Almaras DDES was comapred with implicit LES in a study by Bensow [20]. Nonetheless, both models predict very similar extents for the cavity structures.

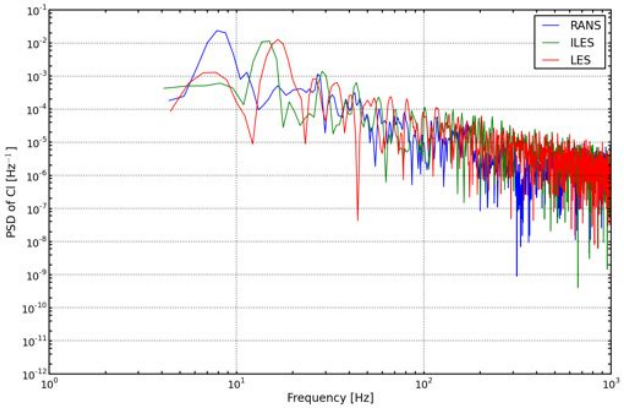

Figure 2: Power spectral density of the lift coefficient.

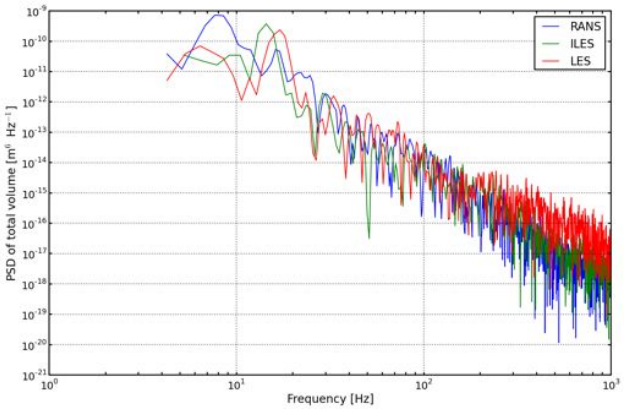

Figure 3: Power spectral density of the total cavity volume (interface assumed at $\alpha = 0.5$).

Similar observation may be made when one compares the associated iso-contours of vorticity. Clearly, the explicit model predicts much coarser and coalesced structures in the downstream part of the foil. Its counterpart, however, delivers a solution dominated by a large number of small, poorly distinguishable vortices . Close to the attached cavity both models appear to agree better by predicting elongated structures piercing through the cavity interface and likely associated with the re-entrant jet. This behaviour may be explained by a greater diffusion introduced by the subgrid model which will be particularly prominent close to the downstream cavity extent [20, 22].

A closer look at the differences between the computed cavity volumes depending on the chosen α threshold in Figure 6 points out that they are in the order of 10%. This indicates that despite a fine mesh being used the cavity interface remains blurred, which is a major disadvantage of the volume-of-fluid approach.

Comparison of the relationship between the cavitation cycle (Figure 6) and the predicted lift (Figure 7) for all the

cases reveals several interesting features. Firstly, one may clearly notice the differences in primary frequencies of all the signals, as indicated by the frequency analysis. For the RANS case one may clearly see that the peak value of the cavity volume corresponds to the maximum lift. This may be explained by the effective increase in the foil thickness caused by the presence of the cavity sheet [7, 15]. After reaching its maximum volume the sheet becomes sheared off by the re-entrant jet, convected downstream and disintegrated, at which point the minima in the lift curve occur. It should be pointed out that the drag varies in a similar fashion and its increase is dominated by the amount of separated flow in the wake of the cavity.

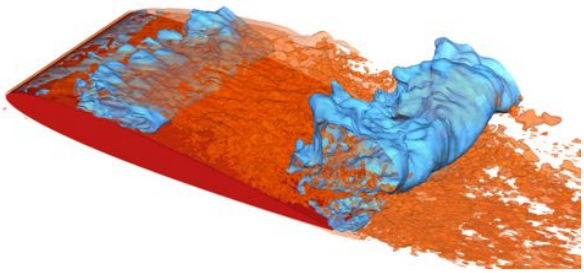

Figure 4: Iso-surfaces $\alpha = 0.5$ - light blue, $\omega = 3000\ s^{-1}$ - orange, $t = 0.34\ s$, implicit LES.

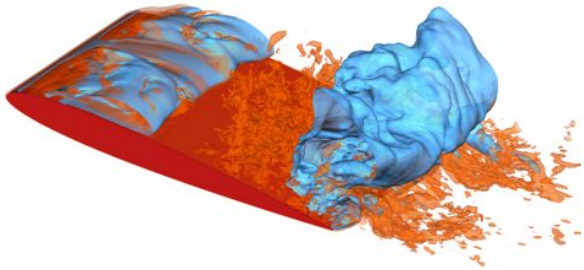

Figure 5: Iso-surfaces $\alpha = 0.5$ - light blue, $\omega = 3000\ s^{-1}$ - orange, $t = 0.40\ s$, LES with Smagorinsky model.

At the first glance the time histories for implicit and explicit LES simulations reveal a different trend whereby the peaks of the cavity volume curve correspond to the troughs of the lift time trace and *vice versa*. A more in depth analysis of the flow reveals that the same pattern is observed but the new part of the sheet starts to form before the shed cloud has been convected away from the wing surface and destroyed, as seen in Figures 8 and 9 for RANS and ILES, respectively. This also implies that the maximum volume of the cavity and the corresponding peak of the lift curve are reached while a cloud is still present in the vicinity of the foil, as seen in Figures 4 and 5. This observation also explains the higher frequency of shedding observed in the LES cases and the fact that the total volume of vapour seldom approaches zero for these simulations.

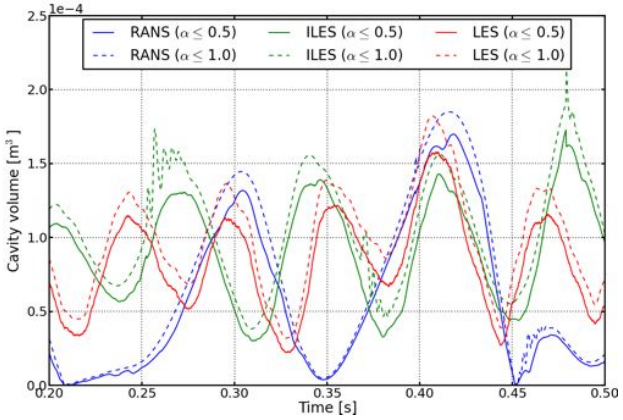

Figure 6: Fragment of the time trace of the precited cavity volume for two threshold values ($\alpha \leq 0.5$ and $\alpha \leq 1$).

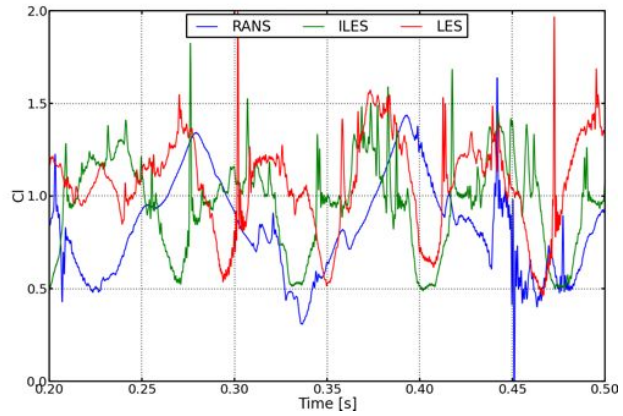

Figure 7: Fragment of the time trace of the predicted lift coefficient, frequencies above 1 kHz filtered out.

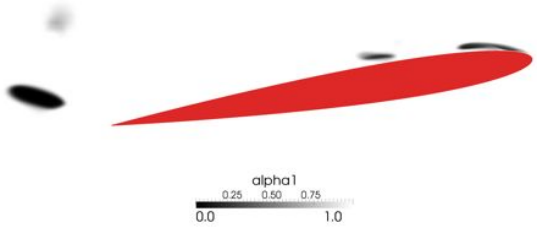

Figure 8: Isocontours of the α field at mid-span for the RANS simulation showing the beginning of the sheet cavity formation ($t = 0.34\ s$).

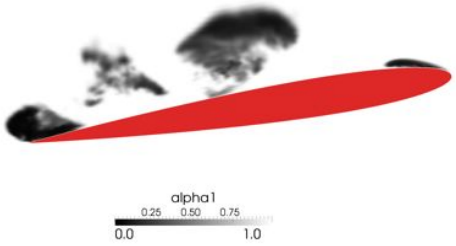

Figure 9: Isocontours of the α field at mid-span for the ILES simulation showing the beginning of the sheet cavity formation ($t = 0.25\ s$).

5 Conclusions

It has been demonstrated how three common turbulence modelling techniques may be applied to model cavitation. Clear differences have been observed in the behaviour of all the approaches. Judging from the substantial difference between the RANS and LES approaches in both the lift and cavity volume variations one may conclude that the latter should be used for this purpose whenever possible, which stands in agreement with findings by other authors [17, 22].

In particular, the slower shedding mechanism of the RANS simulation has been shown to significantly affect not only the frequency characteristics but also the time-history and correlation between the observed cavitation behaviour and the predicted forces. The analysis has shown that the formation of the cavity sheet in the RANS case is delayed until the shed cloud had collapsed which does not occur when LES is employed. This may indicate a strong dependence of the growth of the cavitation sheet on the vortical structures present in its wake and deserves further study if the understanding of the entire process is to be increased. The observed behaviour also pointed out that the snapshots of the flow remain similar between RANS and LES and so the discrepancies could not be compared against experimental data if only the extents of cavitation were compared against high-speed camera photos. Instead, a more detailed time- and frequency-based analysis would be required.

Noticeable discrepancies have been observed in the predicted vortical and cavitation structures for the implicit and explicit subgrid modelling techniques, although the overall trends proved to be in agreement. This illustrates an important challenge in the field of high-fidelity cavitation modelling where limited experimental data is available in the form which would allow direct, in-depth comparison and validation.It may be expected on the basis of published results that if accurate noise prediction of the cavitation behaviour is to be achieved then further work is required to enable more advanced subgrid modelling techniques to be used without adversely affecting the predicted cavitation behaviour. It is therefore evident that said subject remains open, both from experimental and computational point of view, and deserves further study.

6 Acknowledgements

The authors would like to acknowledge the use of the Iridis 4 supercomputer of University of Southampton, UK, on which the discussed simulations have been conducted.

References

[1] A. Van der Graaf, M. Ainslie, M. André, K. Brensing, J. Dalen, R. Dekeling, S. Robinson, M. Tasker, F. Thomsen, and S. Werner, "European Marine Strategy Framework Directive Good Environmental Status (MSFD-GES)," Tech. Rep. February, 2012.

[2] M. L. Tasker, M. Amundin, M. Andre, A. Hawkins, W. Lang, and T. Merck, "MARINE STRATEGY FRAMEWORK - Task Group 11 Report and other forms of energy Underwater noise," Tech. Rep. 31210, 2010.

[3] J. Hildebrand, "Anthropogenic and natural sources of ambient noise in the ocean," *Marine Ecology Progress Series*, vol. 395, pp. 5–20, Dec. 2009.

[4] R. J. Urik, "AMBIENT NOISE IN THE SEA," tech. rep., 1984.

[5] T. Brooks, D. Pope, and M. Marcolini, *Airfoil self-noise and prediction*. NASA, 1989.

[6] C. Park, H. Seol, K. Kim, and W. Seong, "A study on propeller noise source localization in a cavitation tunnel," *Ocean Engineering*, vol. 36, pp. 754–762, July 2009.

[7] H. Seol, J.-C. Suh, and S. Lee, "Development of hybrid method for the prediction of underwater propeller noise," *Journal of Sound and Vibration*, vol. 288, pp. 345–360, Nov. 2005.

[8] M. S. Plesset and A. Prosperetti, "Bubble dynamics and cavitation," *Annual Review of Fluid Mechanics*, 1977.

[9] A. Vallier, *Simulations of cavitation-from the large vapour structures to the small bubble dynamics*. PhD thesis, Lund University, 2013.

[10] K. Woo Shin, *Cavitation simulation on marine propellers*. PhD thesis, Technical University of Denmark, 2010.

[11] A. Vallier, J. Revstedt, and H. Nilsson, "A multi-scale approach for modelling cavitation on hydrofoils , implemented in OpenFOAM," in *8th International OpenFOAM Workshop*, (Jeju, Korea), 2013.

[12] G. Chahine, "Nuclei effects on cavitation inception and noise," in *5th Symposium on Naval Hydrodynamics*, no. August, (St. John's, Newfoundland and Labrador, Canada), pp. 8–13, 2004.

[13] D.-m. Liu, S.-h. Liu, Y.-l. Wu, and H.-y. Xu, "LES numerical simulation of cavitation Bubble shedding on ALE 25 and ALE 15 hydrofoils," *Journal of Hydrodynamics, Ser. B*, vol. 21, pp. 807–813, Dec. 2009.

[14] J. Choi, C.-T. Hsiao, G. Chahine, and S. Ceccio, "Growth, oscillation and collapse of vortex cavitation bubbles," *Journal of Fluid Mechanics*, vol. 624, p. 255, Mar. 2009.

[15] F. Salvatore and S. Ianniello, "Preliminary results on acoustic modelling of cavitating propellers," in *IABEM 2002, International Association for Boundary Element Methods*, (UT Austin, TX, USA), 2002.

[16] S. Ianniello, R. Muscari, and a. Mascio, "Ship underwater noise assessment by the acoustic analogy. Part I: nonlinear analysis of a marine propeller in a uniform flow," *Journal of Marine Science and Technology*, vol. 18, pp. 547–570, July 2013.

[17] T. Huuva, *Large eddy simulation of cavitating and non-cavitating flow*. PhD thesis, Chalmers University of Technology, 2008.

[18] G. Wang and M. Ostoja-Starzewski, "Large eddy simulation of a sheet/cloud cavitation on a NACA0015 hydrofoil," *Applied Mathematical Modelling*, vol. 31, pp. 417–447, Mar. 2007.

[19] J. Sauer and G. H. Schnerr, "Development of a new cavitation model based on bubble dynamics," *Zeitschrift für Angewandte Mathematik und Mechanik*, vol. 81, pp. 561–562, 2001.

[20] R. Bensow, "Simulation of the unsteady cavitation on the the Delft Twist11 foil using RANS, DES and LES," in *2nd International Symposium on Marine Propulsors*, no. June, (Hamburg, Germany), 2011.

[21] A. H. Koop, *Numerical simulation of unsteady three-dimensional sheet cavitation*. PhD thesis, University of Twente, Enschede, The Netherlands, Sept. 2008.

[22] M. Wikstrom, *Approaching Large eddy simulation of cavitating flows for marine applications*. PhD thesis, Chalmers University of Technology, 2006.

[23] R. Bensow and G. Bark, "Implicit LES predictions of the cavitating flow on a propeller," *Journal of fluids engineering*, vol. 132, no. 4, p. 041302, 2010.

[24] T. P. Lloyd, *Large eddy simulations of inflow turbulence noise: application to tidal turbines*. PhD thesis, University of Southampton, 2013.

[25] E. J. Foeth, C. W. H. Doorne, T. van Terwisga, and B. Wieneke, "Time resolved PIV and flow visualization of 3D sheet cavitation," *Experiments in Fluids*, vol. 40, pp. 503–513, Feb. 2006.

[26] E. Foeth, *The structure of three-dimensional sheet cavitation*. PhD thesis, TU Delft, 2008.

[27] M. Hoekstra, T. van Terwisga, and E. J. Foeth, "SMP11 Workshop - Case 1: DelftFoil," in *Second International Symposium on Marine Propulsors*, (Hamburg, Germany), 2011.

[28] R. Bensow and M. Liefvendahl, "Implicit and explicit subgrid modeling in les applied to a marine propeller," *38th Fluid Dynamics Conference and ...*, pp. 1–12, 2008.

[29] R. E. Bensow and G. Bark, "SIMULATING CAVITATING FLOWS WITH LES IN OPENFOAM," in *European Conference on Computational Fluid Dynamics*, no. June, (Lisbon, Portugal), pp. 14–17, 2010.

Implementing the Ffowcs Williams-Hawkings acoustic analogy into a viscous CFD solver.

Thomas P. Lloyd[a*], Douwe Rijpkema[b] and Erik van Wijngaarden[b]

[a]MARIN Academy; [b]Research and Development Department; MARIN, Wageningen, NL.

1 Introduction

Whilst predicting the underwater radiated noise from naval vessels has long been of interest, recent attention has shifted towards the environmental impact of commercial vessels (Merchant *et al.*, 2012). Concurrently, within the field of hydroacoustics, propeller-induced hull vibrations remain an important design consideration (van Wijngaarden, 2011). Studies in these areas may be made using measurements, at both model- or full-scale, or computational tools.

Simulations negate some of the difficulties inherent in performing acoustic measurements in hydrodynamic testing facilities such as cavitation tunnels. To date, the relatively few publications on this subject (*e.g.* see Testa *et al.*, 2008) have focussed on using 'acoustic analogies', methods which separate the sound generation and propagation processes. An acoustic analogy for bodies undergoing arbitrary motion was first derived by Ffowcs Williams and Hawkings (1969). These authors made no stipulation that the surface used to describe the source should be impermeable; they did however comment that they generally expected an impermeable surface to be used. In this case, ignoring the non-linear volume source, the source terms consist of 'thickness' and 'loading' components; these assumptions lead to a form of the FW-H equation commonly known as 'Farassat 1A' (Brentner and Farassat, 1998), which is arguably the most commonly used FW-H formulation in the aeroacoustics community.

For maritime problems, two major differences from aeroacoustic problems make the 'Farssat 1A' formulation less attractive. Firstly, simulating unsteady cavitation is typically important, since this is often the dominant noise source of a propeller (Carlton, 2007). In addition, justification for neglecting the role of the non-linear terms in the sound generation process has recently been called into question for hydroacoustics (Ianniello *et al.*, 2013). Accordingly, the 'porous' formulation of the FW-H, formally derived by Di Francescantonio and DiFrancescantonio (1997), is preferable. Then, the propeller is surrounded by a porous data surface (PDS) upon which velocity, pressure and density fluctuations are extracted from the computational fluid dynamics (CFD) simulation.

Note that the PDS approach is similar to that taken in the Kirchhoff acoustic analogy; a comparison of these two methods may be found in, for example, Brentner and Farassat (1998). The Kirchhoff method, however, assumes the PDS to be located in the linear (acoustic) flow region. Hence error will be introduced into the solution if the PDS is moved too close to the propeller. For the prediction of hull pressures close to the propeller, the Kirchhoff method has been shown to be sufficient (van Wijngaarden, 2011); the accuracy of the method for far-field pressure prediction is less clear however.

This paper details the verification of an FW-H equation implementation within the CFD code, *ReFRESCO*®, as well as comparing results obtained with those from an existing Kirchhoff equation solver, *EXCALIBUR*.

2 Theoretical Background

The porous FW-H equation takes the form

$$4\pi p'(\boldsymbol{x},t)H(f) = \int_S \frac{\rho_0 \dot{U}_n}{r} dS(\boldsymbol{y}) + \int_S \frac{\dot{L}_r}{c_0 r} dS(\boldsymbol{y}) + \int_S \frac{L_r}{r^2} dS(\boldsymbol{y}), \tag{1}$$

where p' is the pressure fluctuation, $H(f)$ the Heaviside function for the data surface f, r the source-receiver distance and c_0 the sound speed; $U_n = u_n + (\rho/\rho_0 - 1)(u_n - v_n)$ and $L_i = p\hat{\boldsymbol{n}} + \rho u_i(u_n - v_n)$, where and u and v are the fluid and porous surface velocities. The subscripts n and r denote a dot product with the unit normal ($\hat{\boldsymbol{n}}$) and unit vector in the radiation direction ($\hat{\boldsymbol{r}}$) respectively. We assume density fluctuations are negligible, and the data surface to be stationary, hence $\rho = \rho_0$ and $v_n = 0$. Thus, re-writing the loading terms into linear and non-linear contributions, Equation 1 becomes

$$4\pi p'(\boldsymbol{x},t)H(f) = \underbrace{\int_S \frac{\rho_0 \dot{u}_n}{r} dS(\boldsymbol{y})}_{\text{thickness, } p'_T} + \underbrace{\int_S \frac{\dot{p}\hat{\boldsymbol{n}}\cdot\hat{\boldsymbol{r}}}{c_0 r} dS(\boldsymbol{y}) + \int_S \frac{\rho_0 (u_n \dot{u}_r)}{c_0 r} dS(\boldsymbol{y})}_{\text{unsteady loading, } p'_{L1}} + \underbrace{\int_S \frac{p\hat{\boldsymbol{n}}\cdot\hat{\boldsymbol{r}}}{r^2} dS(\boldsymbol{y}) + \int_S \frac{\rho_0 u_n u_r}{r^2} dS(\boldsymbol{y})}_{\text{steady loading, } p'_{L2}}. \tag{2}$$

* *corresponding author's e-mail*: T.Lloyd@marin.nl

For comparison, we also write the Kirchhoff formulation, which is based on the Helmholtz equation, and therefore assumes the acoustic data surface to be in the linear region. In this work we only consider free-field radiation, meaning the solution to the Kirchhoff-Helmholtz equation may be written as

$$4\pi p'(\boldsymbol{x},t)H(f) = -\int_S \frac{\boldsymbol{n}\cdot\nabla p'}{r}dS(\boldsymbol{y}) + \int_S \frac{\dot{p}'\hat{\boldsymbol{n}}\cdot\hat{\boldsymbol{r}}}{c_0 r}dS(\boldsymbol{y}) + \int_S \frac{p'\hat{\boldsymbol{n}}\cdot\hat{\boldsymbol{r}}}{r^2}dS(\boldsymbol{y}). \tag{3}$$

Strictly speaking, Equations 2-3 should be evaluated at the retarded time. This means the contribution to the far-field pressure signal from each source point is corrected for the propagation time r/c_0. However, since the Mach number is generally low underwater, it has been shown that these retarded time differences may be neglected (Ianniello *et al.*, 2013).

3 Numerical Framework

To solve the hydrodynamic problem, we used *ReFRESCO*, a dedicated maritime CFD code that has previously been applied to propulsor calculations by MARIN (Rijpkema and Vaz, 2011). *ReFRESCO* is a finite-volume Navier-Stokes equations solver, which uses cell-centred collocated variables. In this application we used a segregated solution approach, and solved the steady Reynolds-averaged Navier-Stokes equations, with the $k-\omega$ SST turbulence model (Menter *et al.*, 2003). A SIMPLE-type algorithm was used for velocity-pressure coupling. The grid is of multi-block structured type, created using *GridPro*®.

For the acoustic problem, we adopted two methods. Firstly, the FW-H equation was solved in the time domain; this has been implemented as a run-time post-processing module within *ReFRESCO*. At each time step of an unsteady hydrodynamic computation, the relevant data are interpolated onto a cylindrical PDS encompassing the propeller. In the steady case, the final converged solution is used, with the PDS data artifically revolved around one blade passage. The pressure time traces are then Fourier transformed to give the pressure harmonics.

Results using the Kirchhoff equation were obtained using *EXCALIBUR*, an existing frequency-domain, Helmholtz equation solver (van Wijngaarden, 2011), which has previously been coupled to *ReFRESCO* (van Wijngaarden and Rijpkema, 2012). *EXCALIBUR* can be used to compute both free-field and hull pressures, as well as propeller source strengths based on measured hull-scattered pressure fluctuations. In this case, we provided the time domain information on the same PDS to *EXCALIBUR*, which directly returns the pressure harmonics. Note that in the future, the FW-H method will be implemented into *EXCALIBUR*, allowing multi-body scattering problems to be computed.

4 Propeller Test Case

4.1 Case description

A suitable test case is provided by the two-bladed S6666 propeller, for which experimental measurement data exists. A full description of the experiments is given by van Wijngaarden (2011), with previous computations using the *ReFRESCO-EXCALIBUR* coupling reported in van Wijngaarden and Rijpkema (2012). Computations represent a bollard pull condition, using zero-pitch blades. The relevant parameters are: propeller diameter $D_P = 0.34\ m$; rotation rate $n = 10\ rps$; inflow speed $U_0 = 0.01\ ms^{-1}$; and turbulence intensity $\mathcal{I} = 1\%$. The measured thrust coefficient is $K_T = 0.023$.

Since the current FW-H implementation can only simulate free-field conditions, the measured data have been corrected to reflect this. This was accomplished using *EXCALIBUR*, by computing the pressures both on a representative hull aftbody model and at equivalent free-field locations. The ratio of these two results gives the *solid boundary factor* (SBF), which is then applied to the measured data. A summary of the probes used here is given in Table 1, along with the computed solid boundary factors.

A propeller grid of 8.5×10^5 cells was used; the domain consists of a cylinder of diameter $6D_P$ and length $6D_P$, with the propeller located at the domain centre, on an infinite hub of diameter $D_H = 0.3D_P$. An overview of the structured grid is given in Figure 1. The baseline PDS has dimensions $D_{PDS} = 1.15D_P$ and $L_{PDS} = D_H$, and a grid density in the tangential, radial and axial directions of $(N_\theta, N_R, N_x) = (91, 28, 28)$. These parameters have been chosen based on the sensitivity studies reported by van Wijngaarden and Rijpkema (2012).

4.2 Flow solution

Since only free-field acoustic predictions can be made with the FW-H method currently implemented, the propeller flow was also solved for open water conditions. This considerably reduces the complexity of the hydrodynamic simulation. In addition, computation time is reduced by first performing a steady simulation, and then solving the acoustic problem as a post-processing step. In order to do this, the converged steady

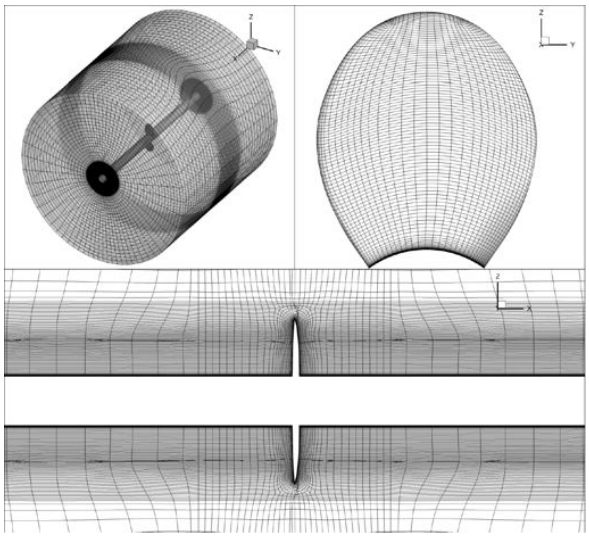

Figure 1: Coarse grid views (van Wijngaarden and Rijpkema, 2012)

ID	x	y	z	SBF
1	-0.0752	-0.180	0.2475	2.01
2	-0.0752	-0.090	0.2385	1.97
8	0.000	0.000	1.834	1.83
14	0.1048	0.090	0.2405	2.04
16	0.2098	-0.135	0.1905	2.44

Table 1: Probe locations (in metres) and solid boundary factors

solution is used as restart data for a modified solver which computes the FW-H equation based on one iteration of the solution. The flow field data (velocity and pressure) are interpolated onto the PDS using a first order scheme. One view of the flow solution is provided in Figure 2a, where a slice of axial velocity is shown. A visualisation of the baseline PDS is also included. Figure 2b confirms that the velocity components have converged (in the L_2 norm) to approximately 10^{-5} while the other quantities reach 10^{-7}.

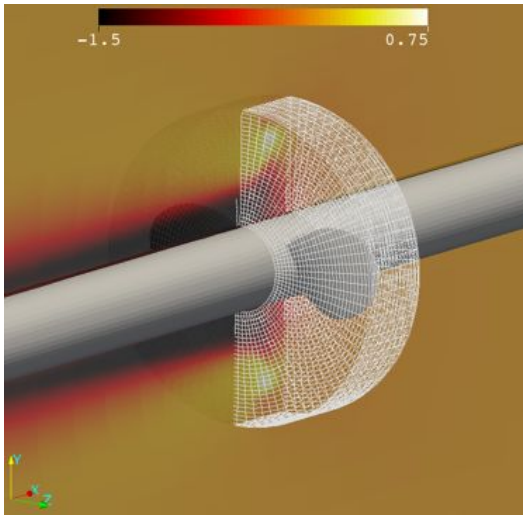

(a) Axial velocity (in metres per second) on a slice, and PDS visualisation. Flow in $-ve$ x-direction.

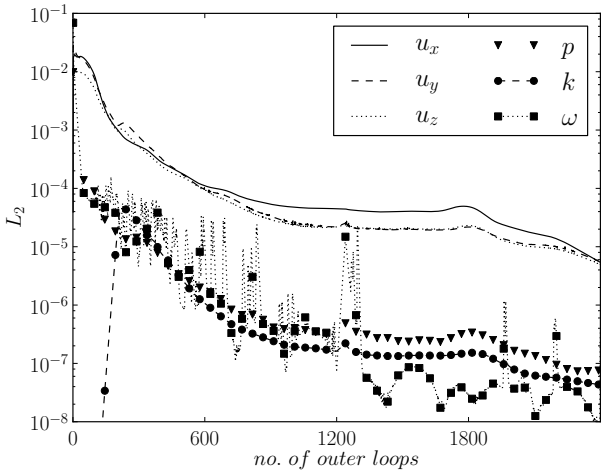

(b) Residuals

Figure 2: Flow field results for S6666 propeller

4.3 Acoustic results

A selection of acoustic results is presented, aiming to verify the FW-H implementation and study the behaviour of the PDS. Figure 3 shows the frequency components computed from the FW-H and Kirchhoff pressure time traces, compared to *EXCALIBUR* results using the same (baseline) PDS, and the corrected measurement data. The FW-H results show a good agreement with the measurement data, although the first harmonic is generally under-predicted. At all probe locations the Kirchhoff results are in slightly better agreement (for this PDS) with the measurements than the FW-H predictions.

One advantage of the present implementation is the ability to separate the contributions of the various FW-H source terms; this is currently not possible in *EXCALIBUR*. Therefore we also computed the Kirchhoff equation within *ReFRESCO* to further examine the difference between the two formulations. Only the thickness (p'_T) and loading (p'_L) are plotted. While one might expect the acoustic pressure to be dominated by the thickness component, since the probe locations are all within one diameter of the propeller, there is a large

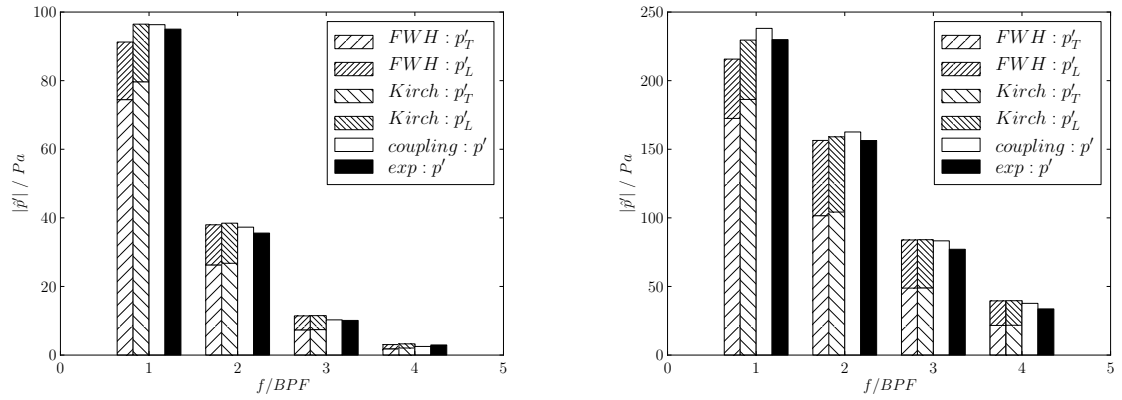

(a) probe 2

(b) probe 8

(c) probe 14

(d) probe 16

Figure 3: Harmonic analysis of FW-H results for probes 2, 8, 14 and 16 (using baseline PDS), compared to Kirchhoff and corrected measurement data: hatched bars are FW-H (and Kirchhoff) terms (p'_T the thickness, and p'_L the loading); '*coupling*' refers to frequency domain Kirchoff method.

length	L_x / D_H	N_x
short	0.5	14
baseline	1.0	28
medium	2.0	56
long	4.0	112

Table 2: Summary of porous data surface geometry variations.

contribution from the steady loading. Due to the fact that the loading term is the same between both formulations, the difference between the FW-H and Kirchhoff methods comes from the prediction of the thickness term.

One way to test the FW-H method is to vary the size and grid density of the control surface. This was performed by van Wijngaarden and Rijpkema (2012), but only for probe 8, which shows the best agreement. For this study the axial grid density was kept constant and the length of the control surface successively varied by a factor of two. Table 2 summarises these variations.

Results are presented for probes 1 and 8. The frequency components predicted for each of the four porous data surfaces are plotted in Figures 4 and 5. Clearly the 'short' PDS gives the largest under-prediction of the first harmonic at both probe locations. In addition, the thickness component dominates the pressure signal. For the 'baseline' case, the amplitude of the thickness component reduces, while the steady loading contribution has increased; overall the prediction is improved. The 'medium' and 'long' surfaces show small improvements in the pressure amplitudes compared to the 'baseline' case.

Note the dramatic increase in the magnitude of the loading contribution as the length of the surface is increased. This could be caused by the change in the distance between the PDS faces and the probe. The sensitivity of the magnitude of the 'thickness' and ''loading' terms when using the PDS highlights the fact that these terms can no longer be thought of as directly relating to the displacement and loading effect at the blade surface. Predictions made using *EXCALIBUR* are generally higher than the measured values for

the short surfaces and reduce as the length is increased; the magnitudes of the separate contributions cannot currently be extracted however.

Overall, the results are encouraging from the point of view that simple free-field acoustic predictions can be made inside a single code.

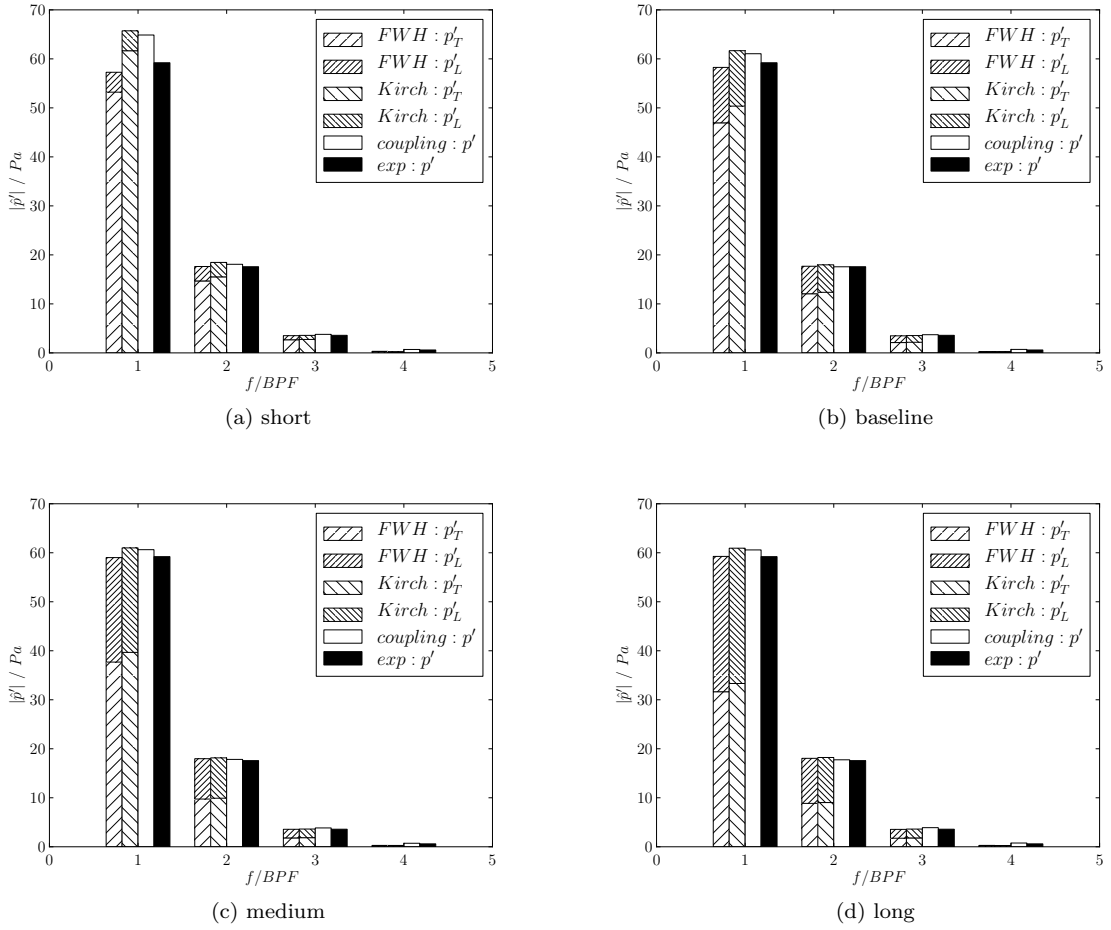

(a) short (b) baseline

(c) medium (d) long

Figure 4: Harmonic analysis of FW-H results at probe 1, for varying length of porous data surface.

5 Outlook

An assessment of a simplified FW-H implementation into the viscous CFD solver *ReFRESCO* has been presented. The results for the chosen test case are encouraging, and will be extended to propellers with higher loading. The dependence of the relative magnitude of the thickness and loading terms on the length of the PDS highlights the importance of choosing an appropriate PDS as well as the conceptual separation between the physical and numerical source terms in the porous formulation. It is also important to emphasise that the measurement locations for this case lie close to the propeller and therefore the pressure signals include large near-field contributions. This would typically not be the case for radiated noise predictions, although in such cases reliable measurement data becomes more difficult to obtain.

In the future, the same FW-H method will be implemented into *EXCALIBUR*, which will allow direct comparison between FW-H and Kirchhoff methods in the frequency domain, and may be extended to allow predictions involving scattering bodies to be made (Gennaretti and Testa, 2008). These methods will then be used for more complex hull-propeller interaction scenarios.

References

Brentner, K.S. and Farassat, F. (1998), An analytical comparison of the acoustic analogy and Kirchoff formulation for moving surfaces. *AIAA Journal*, **36**(8): pp. 1–17, doi:10.2514/2.558.

Carlton, J. (2007), *Marine propellers and propulsion*. 2nd edn., Oxford: Butterworth-Heinemann, pp. 247–260, ISBN 978-0750681506.

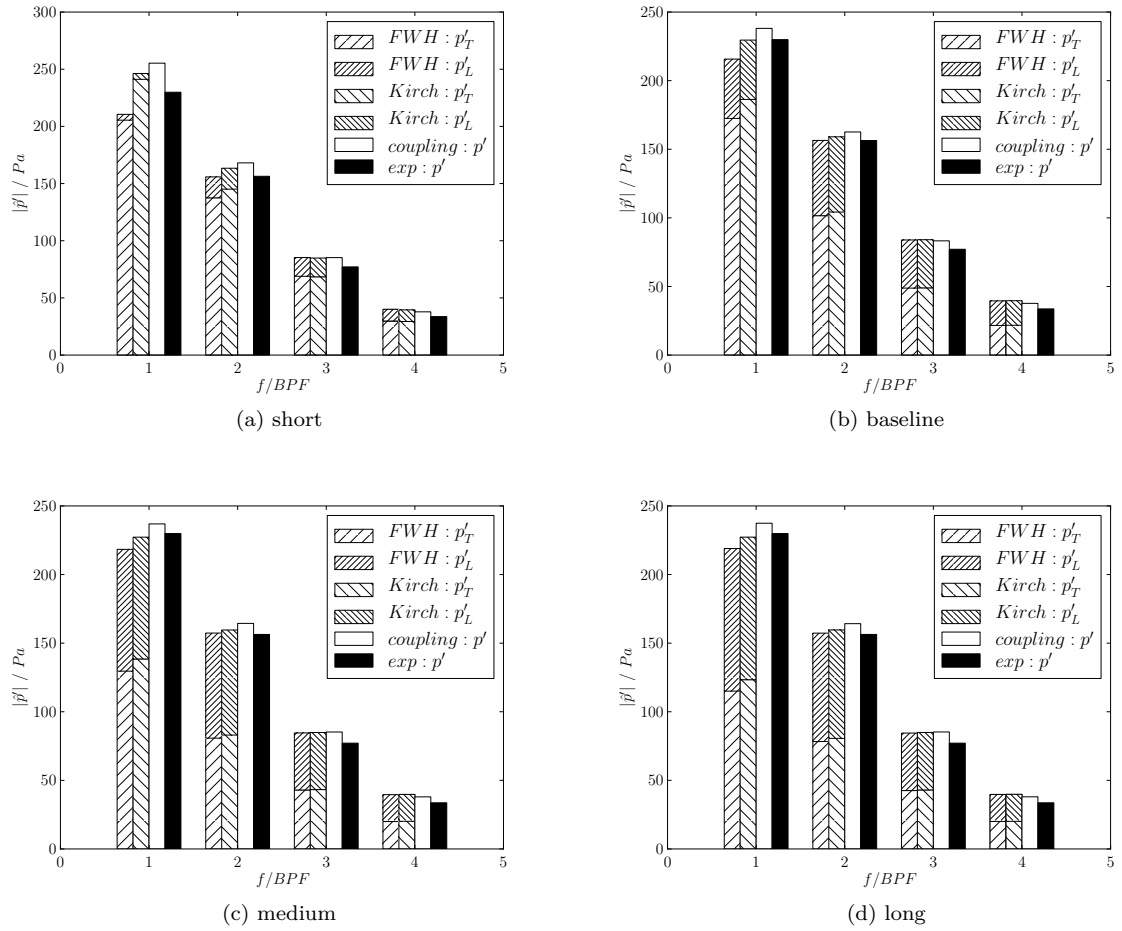

(a) short (b) baseline

(c) medium (d) long

Figure 5: Harmonic analysis of FW-H results at probe 8, for varying length of porous data surface.

Di Francescantonio, P. and DiFrancescantonio, P. (1997), A new boundary integral formulation for the prediction of sound radiation. *Journal of Sound and Vibration*, **202**(4): pp. 491–509, doi:10.1006/jsvi.1996.0843.

Ffowcs Williams, J.E. and Hawkings, D.L. (1969), Sound generation by turbulence and surfaces in arbitrary motion. *Philosophical Transactions of the Royal Society A: Mathematical, Physical and Engineering Sciences*, **264**(1151): pp. 321–342, doi:10.1098/rsta.1969.0031.

Gennaretti, M. and Testa, C. (2008), A boundary integral formulation for sound scattered by elastic moving bodies. *Journal of Sound and Vibration*, **314**(3-5): pp. 712–737, doi:10.1016/j.jsv.2008.01.028.

Ianniello, S., Muscari, R. and Mascio, A. (2013), Ship underwater noise assessment by the acoustic analogy. Part II: hydroacoustic analysis of a ship scaled model. *Journal of Marine Science and Technology*, **18**(4): pp. 547–570, doi:10.1007/s00773-013-0227-0.

Menter, F.R., Kuntz, M. and Langtry, R. (2003), Ten years of industrial experience with the SST turbulence model. In: K. Hanjalic, Y. Nagano and M. Tummers (eds.), *Turbulence, Heat and Mass Transfer 4*, pp. 625–632.

Merchant, N.D., Blondel, P., Dakin, D.T. and Dorocicz, J. (2012), Averaging underwater noise levels for environmental assessment of shipping. *The Journal of the Acoustical Society of America*, **132**(4): pp. EL343–EL349, doi:10.1121/1.4754429.

Rijpkema, D. and Vaz, G. (2011), Viscous flow computations on propulsors: verification, validation and scale effects. In: *Proceedings of Marine CFD*, London: RINA.

Testa, C., Ianniello, S., Salvatore, F. and Gennaretti, M. (2008), Numerical approaches for hydroacoustic analysis of marine propellers. *Journal of Ship Research*, **52**(1): pp. 57–70.

van Wijngaarden, E. (2011), *Prediction of propeller-induced hull-pressure fluctuations*. Ph.D. thesis, Maritime Research Institute Netherlands.

van Wijngaarden, E. and Rijpkema, D. (2012), Coupling a Helmholtz-equation hydroacoustic model and CFD solvers. *Tech. rep.*, MARIN.

SIMULATION OF SEAKEEPING TESTS USING OPENFOAM

Jan Löhrmann*
Technical University of Berlin
Department of Dynamics of Maritime Systems
Berlin, Germany
Email: jan-patrick.loehrmann@tu-berlin.de

Andrés Cura Hochbaum
Technical University of Berlin
Department of Dynamics of Maritime Systems
Berlin, Germany

INTRODUCTION

In the past, seakeeping analysis has almost solely been done using potential theory based methods. As long as pressure dominated effects are analysed, these methods yield good accuracies with very low computational effort. However, if viscous effects can't be neglected these methods can no longer be applied. As the development of viscous flow solvers took place rapidly and computational resources became cheaper, the application of RANS solvers onto difficult unsteady situations became more and more practicable.

This study has been done to validate the open source code *OpenFoam* for such cases. The benchmark ship DTMB 5415 was used for this purpose, which has been investigated for many years e.g. in the CFD Workshop Tokyo 2005 [1]. The model's dimensions are listed in table 1. Validation was done for two test cases, namely calm water and head waves. Afterwards, further simulations were performed for a sea spectrum analysis. The conditions for the two test cases are listed in table 2.

TABLE 1. MAIN PARTICULARS OF THE DTMB 5415

L_{PP}	5.72 m	Length btw. perp.
B	0.768 m	Breadth
T	0.248 m	Draught
S_0	4.861 m^2	Wetted surface
t_{FP}	-0.017732 m	Trim fwd. perp.
t_{AP}	-0.004 m	Trim aft. perp.

NUMERICAL METHOD

Two solvers were used for the simulations.*interFoam* was used to simulate the calm water condition. *interFoam* is a standard solver within *OpenFoam* for incompressible multiphase flows, where the interface is being solved by using the Volume of Fluid method. The equations which are solved are the Reynolds averaged Navier-Stokes equations (RANSE) in combination with the continuity equation for incompressible fluids. Coupling of pressure and velocity is done using the PISO algorithm. The turbulence has been modelled using the k-ω-SST model based on [2]. Since a fixed trim has been prescribed, no ship movements had to be investigated.

TABLE 2. TEST CASE CONDITIONS

Test case "Calm Water"		
v	2.1 m/s	Ship velocity
Fr	0.28	Froudenumber
Re	1.201E+07	Reynoldsnumber
Test case "Head Waves"		
v	2.1 m/s	Ship velocity
$\lambda = 1,5 \cdot L_{PP}$	8.58 m	Wave length
$A_k = 2 \cdot \pi \cdot \zeta / \lambda$	0.025	Wavesteepness
ζ_a	0.034 m	Amplitude
ω_e	4.2179 rad/s	Encountering freq.

waveFoam was the second solver used for the simulations of the ship in waves. This solver is based on *interFoam* with several additions to e.g. generate different wave types. Furthermore, relaxation zones have been implemented to generate and absorb the waves and avoid reflections. This relaxation technique is achieved by applying a relaxation function (Eqn. (1)) in the defined zones to influence the computation of the velocity field and the phase fraction (Eqn. (2)).

$$w = 1 - \frac{exp(\sigma^p) - 1}{exp(1) - 1} \quad \text{for} \quad \sigma \in [0;1] \tag{1}$$

$$\phi = (1 - w)\phi_{target} + w \cdot \phi_{computed} \tag{2}$$

where σ is 0 in the free computational domain (around the ship) and increases linearly to 1 at the do-

*Address all correspondence to this author.

main boundaries at the inlet and outlet. The exponent p can be chosen and is set to 3.5 as default value. Full descriptions of the solver can be found in [3].

Grid Dependency

Grid generation has been done using the commercial software *Hexpress*, which produces unstructured, full-hexahedral meshes. The dynamic trim of the ship has already been considered while generating the grid. Four different grids were generated using a grid refinement ratio of $r_G = 2$ to perform a grid analysis. The grid size as well as the cells per wave length λ and height H are shown in table 3. The x-axis of the grid is directed along the untrimmed longitudinal axis of the ship, the y-axis is directed positive to starboard and the z-axis is directed positive upwards. Grid dependency has been investigated on both test cases. Symmetry was assumed at the central-longitudinal plane. The non-dimensional wall distance y^+ has been chosen to be about 80 combined with using wall functions [4]. Table 4 shows the total resistance and its frictional and pressure components for the four grids at a time step of $\Delta t = 0.001$. The results show an acceptable convergence with the exception of a slight increase of the resistance at grid 1. The convergence ratio for the total resistance F_x for the grids 1-3 and grids 2-4 are defined according to [5]:

TABLE 3. NUMERICAL GRIDS

Grid #	Cells	z/H	x/λ
1	11.650.000	11	294
2	1.600.000	10	146
3	300.000	8	73
4	73.000	6	37

TABLE 4. GRID DEPENDENCY FOR CALM WATER

Grid #	F_x [N]	F_F [N]	F_P [N]
1	23,97	16,44	7,53
2	22,30	15,83	6,47
3	26,79	15,69	10,83
4	35,81	13,62	22,18

$$R_{i,1-3} = \frac{\varepsilon_{i,21}}{\varepsilon_{i,32}} = \frac{\hat{S}_{i,2} - \hat{S}_{i,1}}{\hat{S}_{i,3} - \hat{S}_{i,2}} = -0,37 \qquad (3)$$

$$R_{i,2-4} = \frac{\varepsilon_{i,32}}{\varepsilon_{i,43}} = \frac{\hat{S}_{i,3} - \hat{S}_{i,2}}{\hat{S}_{i,4} - \hat{S}_{i,3}} = 0,50 \qquad (4)$$

with $\hat{S}_i$ being the solution of the respective grids. The convergence ratio shows a monotone convergence for grids 2-4, while grids 1-3 only achieve an oscillatory convergence. The frictional resistance in grid 1 increases compared to grid 2 which leads to a divergence of the frictional resistance for grids 1-3.

Similar results were achieved for the test case of head waves with the addition that the wave amplitude ratio ζ_a/ζ shows a monotone convergence from 0.83 on grid 4, to 0.97 on grid 1, with ζ_a being the generated amplitude and ζ the target amplitude. Grid 2 already achieves 0.96. The generated amplitude has been determined through Fourier analysis of the free-surface elevation in the far field of the ship and averaging between the fore and aft perpendicular. All calculations were made with only one PISO iteration.

The residuals and the convergence of the resistance on grid 2 show a satisfactory behaviour while having a reasonable resolution with approximately 1.6 million cells. That was the reason why it was decided to use this grid for the further investigations.

Timestep Dependency

A time step dependency analysis has been performed for both test cases to determine the influence of the chosen time step on selected results. Time steps from $\Delta t = 5 \cdot 10^{-5}$ up to $1 \cdot 10^{-2}$ have been investigated.

Although grid 2 was selected in the previous section, it was decided to use grid 3 for the time step analysis, as the computational time was wanted to be kept reasonable even at very small time steps of up to $5 \cdot 10^{-5}$. Therefore, this analysis can only indicate qualitative but not quantitative trends. It has to be mentioned, that with the release of OpenFoam-2.3.0, a significant enhancement of the applicable time step due to an implementation of a semi-implicit solver for the phase fraction has been achieved. Simulations with the previous explicit version of the phase solver where restricted to Courant numbers < 1, which resulted in extremely high computational times. During the time step dependency analysis, a maximum Courant number, time-averaged between 10s - 20s simulation time of up to 30 was achieved without affecting the convergence.

Figure 1 shows the resistance coefficient c_T over the investigated time steps. It can be seen that there is a strong dependency on the time step. The resis-

tance coefficient increases dramatically with decreasing time step. The resistance coefficient is almost constant from $\Delta t = 0.001$ on towards bigger time steps.

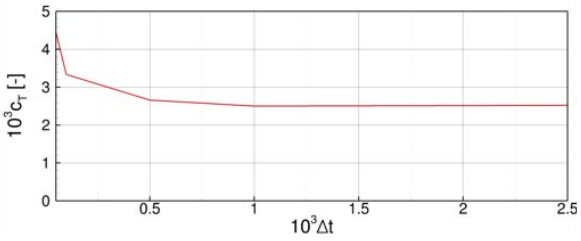

FIGURE 1. TIME STEP DEPENDENCY FOR CALM WATER CONDITION

Only three time steps have been investigated for the test case with head waves, as very high and very low time steps lead to divergence of the solution. Nevertheless, the time step dependency is similar to the calm water condition. This confirms that for each case considered a certain lower limit of Δt should be kept. In addition to the resistance, the generated wave amplitude has been investigated as well. The wave amplitude ratio ζ_a/ζ increases from 0.88 up to 0.94 when decreasing the time step one order of magnitude from $\Delta t = 0.005$ to $\Delta t = 0.0005$. Only small changes from $\Delta t = 0.001$ to $\Delta t = 0.0005$ could be seen, which is why it was decided to choose the time step $\Delta t = 0.001$ for all further calculations.

Influence of PISO Iterations

All calculations for the calm water test casewere done with only one PISO iteration, as this is a pseudo unsteady flow. One and four PISO iterations were tested for the test case with head waves. The resulting forces barely change when increasing the number of iterations. Nevertheless, more iterations strongly influence the quality of the achieved wave amplitude. The wave amplitude ratio ζ_a/ζ can be enhanced on grid 3 from 0.93 to 0.97 using four instead of one iteration. It has to be mentioned that stability problems occurred when starting with a higher number of PISO iteration.

RESULTS OF VALIDATION

Calm Water

The simulation was done using grid 2 at a time step of $\Delta t = 0.001$ and one PISO iteration. This resulted in a computational time of 103 hrs for 20s simulation time on 4 processors (Intel Xeon E5607 2.27GHz).

Figure 2 shows the total resistance (red) and its pressure (blue) and frictional component (green). The dotted line indicates the experimental value for the total resistance. The computed resistance is in a good agreement with the experimental data. The error E defined according to [5] is about 1.7%D. The free-

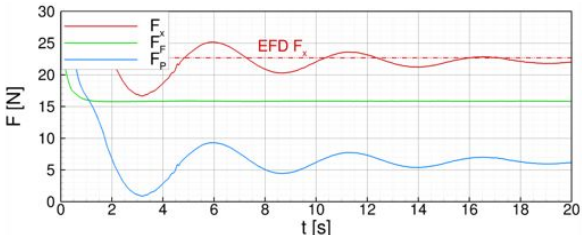

FIGURE 2. RESISTANCE FORCES FOR CALM WATER CONDITION

surface elevation can be seen in fig. 3. Compared to the experimental data shown on the top side, the simulation has a satisfactory agreement with slightly smaller amplitudes. This is due to numerical damping caused by a rather unfortunate strong expansion of the cell size in transverse direction. Further grid refinement, especially in regions further away from the hull, would lead to an enhancement of the achieved wave amplitude. However, this has not been considered in this investigation, since the focus lays on the simulation of seakeeping tests. The results of the calm water test have been considered as sufficiently satisfactory for this purpose.

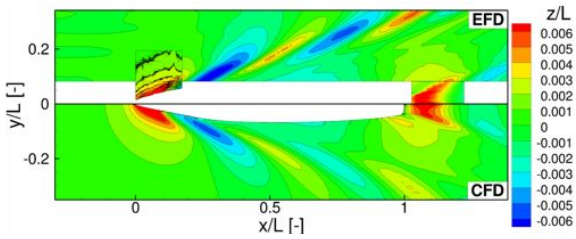

FIGURE 3. COMPARISON OF EXPERIMENTAL AND NUMERCIAL FREE-SURFACE ELEVATION FOR CALM WATER CONDITION

Head Waves

The simulation was done using grid 2 with a time step of $\Delta t = 0.001$. Only one PISO iteration has been done, as a wave amplitude ratio of 0.96 has already been achieved which is seen as sufficient. Further increasing of the PISO iterations would have lead to longer computational time but only fewer improvements as shown above. The computational time and time averaged maximum Courant number are very similar to the calm water test case.

Figure 4 shows the surface elevation at $x = 0$ (FP) in the far field, where no influence of the ship wave system occurs. The generated wave has a good agreement with the analytical solution with less than 5%

deviation in the wave amplitude. Furthermore, fig. 5

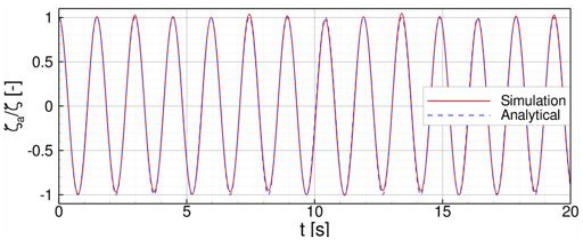

FIGURE 4. WAVE AMPLITUDE AT $x = 0$ (FP) IN THE FAR FIELD OF THE SHIP

shows the elevation of the wave amplitude over the domain at four instants namely $\frac{t}{T_e} = 0$, $\frac{1}{4}$, $\frac{2}{4}$ and $\frac{3}{4}$, with T_e being the encountering period of the wave which is defined to have a non-dimensional elevation of 1 at $x = t = 0$. It can be seen that the wave amplitude ratio resumes at a good level of around 1 and waves are being damped effectively by the relaxation zone at the outlet, which starts at $x/L \approx 1.9$. To analyse the resistance, the signal of the total force

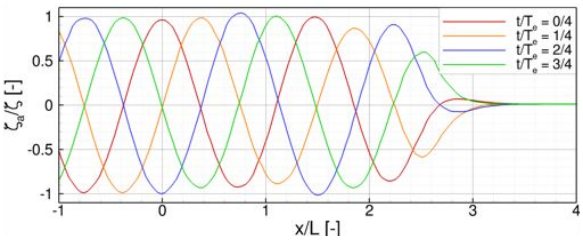

FIGURE 5. WAVE AMPLITUDE IN THE FAR FIELD OF THE SHIP AT FOUR DIFFERENT INSTANTS

component in longitudinal direction has been Fourier analysed (fig. 6). The plot visualises the 0th and 1st harmonics. The 0th harmonic has an amplitude of $\frac{a_0}{2} = 23.533N$ and represents the mean resistance in head waves. The 1st harmonic has an amplitude of 37.879 N and is the first order force due to the head waves of $f_e = 0.6713Hz$. The frequency of the signal has a good agreement with the generated encountering frequency of the wave. At $f/f_e = 2$ a multiple of the encountering frequency can be seen with a very low amplitude. Additionally, a local maximum at $f/f_e = 0.251$ with an amplitude of 1.02 N occurs. This local maximum can be explained by reflections of the waves at the domain boundaries. Nevertheless, the influence of these reflections is small compared to the amplitude of the 1st harmonic.

The resistance, dynamic buoyancy and pitching moment were made non-dimensional using equations 5. The comparison of the determined forces/moment (red) with the results of the flow code *Neptun*, which also participated in the CFD Workshop

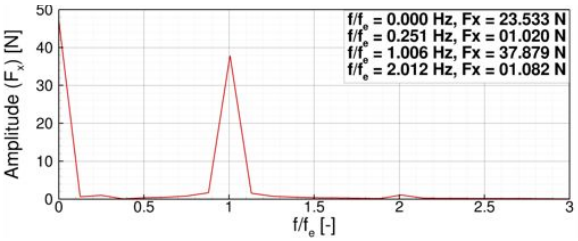

FIGURE 6. COMPONENTS OF THE FOURIER ANALYSIS OF THE TOTAL RESISTANCE OVER NON-DIMENSIONAL FREQUENCY

Tokyo 2005 [6] and the experimental data (blue) are shown in fig. 7. At first, a good agreement can be seen between the results of *OpenFoam* and *Neptun*. In both cases, the peak values don't always match the experimental data but are within a good correspondence. Moreover, a difference in the phase between the experimental data and both numerical data can be seen, which already occurred in the mentioned workshop and is most probably caused by a time lag in the experimental data.

$$c_T = \frac{F_x(t)}{\frac{\rho}{2} \cdot v^2 \cdot S_0}, \quad c_H = \frac{F_z(t)}{\frac{\rho}{2} \cdot v^2 \cdot S_0}, \quad c_M = \frac{M_y(t)}{\frac{\rho}{2} \cdot v^2 \cdot S_0 \cdot L_{PP}} \tag{5}$$

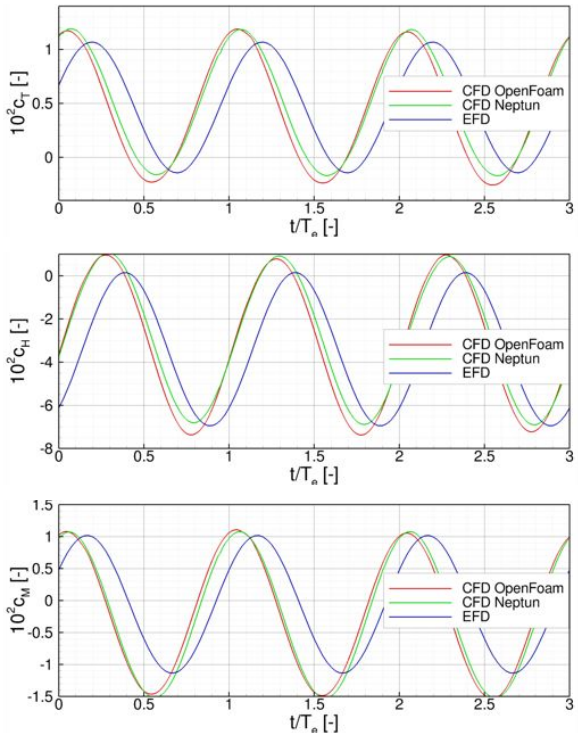

FIGURE 7. COMPARISON OF OPENFOAM, NEPTUN AND EXPERIMENTAL RESULTS FOR c_T, c_H AND c_M

SEA SPECTRUM ANALYSIS

After having validated the generation of regular waves, a sea spectrum was tested. The generation of sea spectra is already included in *waveFoam* but limited to standard spectra for ships at zero speed. A limitation of $0.5 \cdot f_P \leq f \leq 2 \cdot f_P$ was applied to exclude higher and lower frequencies (standard setting is $0.3 \cdot f_P \leq f \leq 3 \cdot f_P$). The same grid as before was used to generate a JONSWAP spectrum with the parameters, as shown in table 5. This leads to a surface elevation at $x = 0$ in the far field as shown in fig. 8.

TABLE 5. PARAMETERS OF THE JONSWAP SPECTRUM

H_S	0.2 m	Significant wave height
T_P	2.3441 s^{-1}	Peak period
γ	3.3	Peak enhancement factor
μ_0	180 °	Encountering angle
N	10	Number of frequencies

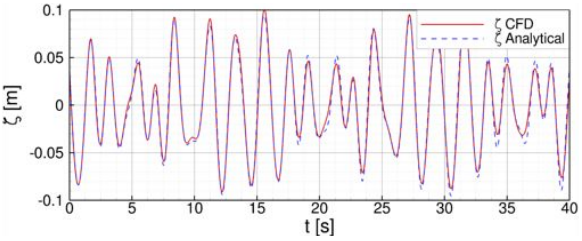

FIGURE 8. WAVE AMPLITUDE OF THE GENERATED WAVE SPECTRUM AT $x = 0$ (FP)

As with the regular waves, there is a good agreement between the analytical solution of the wave train and the generated waves. The deviation of the wave amplitude is less than 5% in the peaks for the first 20s of simulation time. This is increasing slightly to maximal 10% up to 40s simulation time.

Afterwards, the individual wave components, which were used to generate the spectrum, where simulated separately. Those waves are listed in table 6 with their respective non-dimensional amplitude $2 \cdot \zeta / H_S$, frequency f/f_P, the random chosen phase ε and the steepness $A_k = 2\pi \cdot \zeta / \lambda$. The accuracy of the individual wave amplitudes is shown in fig. 9 for 3 out of 10 wave components. The generated wave amplitudes are in general in a good agreement with the respective analytical solution from the 3rd wave onwards. Only waves number 1 and 2 are not very accurate in their amplitude and period. This can be explained by their low wave height, long wave length and consequently low steepness. Waves 3-10 have an average deviation of their wave amplitude of only 0.7%. Finally, the total resistance and wave amplitude of the single wave components have been superposed, as shown in figure 10. Not only the superposition of the wave amplitudes but also of the resistance of the single components agrees well with the corresponding signal of the wave spectrum simulation. This indicates that higher order forces are of less importance considering this particular spectrum. On the other hand, this indicates that the resistance of the ship due to several individual waves can be determined by generating a wave spectrum and analysing the resistance signal through Fourier analysis to determine the

TABLE 6. INDIVIDUAL WAVE COMPONENTS OF THE GENERATED SPECTRUM

Wave #	$2 \cdot \zeta / H_S$	f/f_P	ε	A_k
1	0.031005	0.575001	0.76095	0.0008
2	0.137892	0.725000	2.16132	0.0054
3	0.322803	0.875001	6.16261	0.0181
4	0.384560	1.025000	1.30606	0.0296
5	0.293996	1.175000	1.92987	0.0297
6	0.202895	1.325000	1.29352	0.0261
7	0.165854	1.475000	5.32802	0.0264
8	0.135921	1.625000	0.69639	0.0263
9	0.111905	1.775000	4.06245	0.0258
10	0.092901	1.925001	2.41405	0.0252

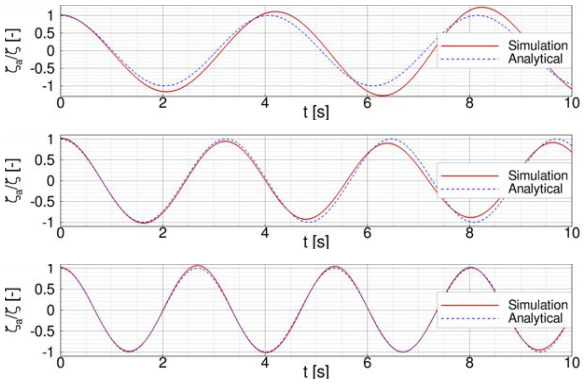

FIGURE 9. FIRST THREE WAVE AMPLITUDES OF THE INDIVIDUAL COMPONENTS OF THE SPECTRUM AT $x = 0$ (FP)

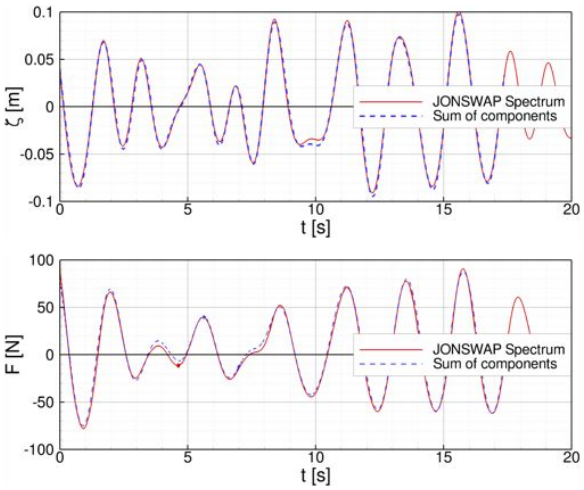

FIGURE 10. COMPARISON OF THE WAVE AMPLITUDE (TOP) AND RESISTANCE (BOTTOM) OF THE WAVE SPECTRUM SIGNAL (RED) AND THE SUPERPOSITION OF THE WAVE COMPONENTS (BLUE)

respective resistance for each wave. Fourier analysis has been done for the wave spectrum signal and all individual waves . Tab. 7 contains the determined first harmonics of each individual wave component as listed in tab. 6 as well as of the spectrum signal. The error E indicates the deviation of the force amplitudes at the respective frequencies in the spectrum from the force amplitudes of the individual wave components. The magnitude of the force amplitudes of the wave spectrum differs up to 49% from the force amplitudes of the individual wave components. This concerns mainly the frequencies at the boundaries of the spectrum, which are having small amplitudes. However, the amplitudes of the wave components with the highest energy of the spectrum can be predicted with $\pm$17%. It has to be noted, that a signal with 40s simulation time has been used for the Fourier analysis of the spectrum, instead of the shown signal of 20s simulation time (see fig. 10). This yields a much better agreement with the Fourier analysis of the single wave components as with the signal with only 20s simulation time.

CONCLUSION

It has been shown, that *OpenFoam* in combination with *waveFoam* is capable of producing good results regarding the accuracy of wave amplitude and length of regular and irregular seas. Waves with a low steepness are of less accuracy, which is due to numerical damping. The influence of wave reflections is low and the efficiency of the absorbing zones is good. The comparison of the resulting forces with experimental data shows a good agreement, although some peak values differ slightly. The calm water resistance and free-surface elevation are also of sufficient accuracy.

Attention must be paid not only to the chosen grid

TABLE 7. 1st HARMONICS OF THE SIGNAL OF THE SINGLE WAVE COMPONENTS AND THE SPECTRUM

f [Hz]	F_x [N] Single wave	F_x [N] Spectrum	E [%D]
0.245297	1.847	2.745	-49 %
0.309287	11.895	13.913	-17 %
0.373278	29.211	24.257	+17 %
0.437268	36.193	31.700	+12 %
0.501258	22.603	21.416	+5%
0.565249	9.696	10.765	-11%
0.629239	3.287	4.463	-36%
0.693230	2.284	2.913	-22%
0.757220	1.996	2.113	-6%
0.821211	0.940	0.963	-2%

but also to the time step which can have a significant influence on the resulting forces and the accuracy of the generated wave amplitude if chosen smaller than a certain limit.

Performing sea spectrum analysis to determine individual wave forces has its limits, since the magnitude of the force amplitudes partially differ from the individually determined force amplitudes. Nevertheless, a satisfactory agreement of the predicted force amplitudes for the individual waves can be achieved. Attention must be paid though to the accuracy of the Fourier analysis, as this has a strong influence on the results.

REFERENCES

[1] Hino, T., ed., 2005. The Proceedings of CFD Workshop Tokyo 2005.

[2] Menter, F. R., 1993. " Zonal Two Equation k-ω Turbulence Models for Areodynamic Flows ". *24th Fluid Dynamics Conference*.

[3] Jacobsen, N. G., Fuhrman, D. R., and Fredsøe, J., 2012. " A Wave Generation Toolbox for the Open-Source CFD Library: OpenFoam® ". *Int. J. Numerl. Meth. Fluids,* ***70***(9), pp. 1073–1088.

[4] Wilcox, D. C., 1993. *Turbulence Modeling for CFD*. DCW Industries, La Cañada, California, USA.

[5] ITTC, 2008. Uncertainty Analysis in CFD Verification and Validation - Methodology and Procedures. Tech. rep., International Towing Tank Comference.

[6] Cura Hochbaum, A., and Pierzynski, M., 2005. "Flow Simulation for a Combatant in Head Waves". *The Proceedings of CFD Workshop Tokyo 2005*.

Numerical Prediction of Resistance and Squat for a Containership in Shallow Water

Philipp Mucha and Bettar el Moctar*

1 INTRODUCTION

The prediction of ship resistance has been brought to a renewed attention in the context of energy efficient shipping and minimum power requirement estimation for ship operation in adverse conditions, IMO (2012.) In shallow water ship resistance increases significantly and its dependence on foward speed is even stronger than in the open sea. Besides, waterway administrations are increasingly interested in the prediction of ship squat as vessels entering ports and channel systems are getting larger in size. In doing so, the application of Computational Fluid Dynamics (CFD) is getting more frequent. This work deals with the numerical prediction of ship resistance for the Panmax class Kriso containership (KCS) taking into account the shallow water effect and dynamic squat. The capabilities of a field method drawing upon the solution of the Navier-Stokes equations and a 3D boundary element method using Rankine sources are explored through comparison with experimental data.

2 METHODOLOGY

Model Tests. Towed resistance tests for the KCS were carried out at the Development Centre for Ship Technology and Transport Systems (DST) in Duisburg, Germany, in the course of a Planar Motion Mechanism (PMM) test programme in shallow water, DST (2009.) The model was tested at scale λ=40 and without appendages (Table 1.) The geometry of KCS is publicly available, e.g. SIMMAN (2014.) No full-scale ship exists. Various water depths were investigated ranging from tank depth to draft ratio h/T of 1.7 to 1.15. Four different foward speeds U were considered corresponding to depth Froude numbers $F_{nh} = U/\sqrt{hg}$ from 0.27 to 0.68, where g is the gravitational acceleration. The model was free to heave and trim, but otherwise constrained. Sinkage was measured with laser plates at positions 1.44 m and -1.33 m with respect to the midship position at $L_{pp}/2$. Sinkage is given positive down at the midship position throughout this paper. Trim is given positive aft-down and in arc minutes corresponding to 1/60 of degree. The static trim of the model was zero.

Numerical Methods. The field method draws upon the solution of the Navier-Stokes equations which describe the dynamics of a viscous and incompressible flow. Forces acting upon the ship hull are obtained by integrating the pressure and shear stresses over the ship's surface allowing for a separate analysis of pressure and friction resistance. The boundary element method stems from potential flow theory. Rankine sources are used to model the ship flow and appropriate boundary conditions are satisfied to define the strengths of the point sources. To arrive at a prediction of the total resistance, friction resistance is found from the ITTC-1957 frictional correlation line (ITTC, 2002) taking into account local Reynolds numbers at each panel along the ship hull.

In the field method, mass and momentum conservation equations are formulated in integral notation reading

$$\frac{\partial}{\partial t}\int_V \rho \,\mathrm{d}V + \int_S \rho \mathbf{v}\cdot\mathbf{n}\,\mathrm{d}S = 0 \qquad (1)$$

Table 1: Main particulars: length between perpendiculars L_{pp} , beam at waterline B_{wl}, draft T and longitudinal position of the centre of gravity with respect to amidships x_G in [m]. Nondimensional block coefficient c_B and wetted surface area S_w in [m^2].

L_{pp}	B_{wl}	T	c_B	x_G	S_w
229.20	32.20	10.00	0.64	-2.18	8992.00

*Philipp Mucha is with the Institute of Ship Technology, Ocean Engineering and Transport Systems (ISMT, University of Duisburg-Essen) and the German Federal Waterways Engineering and Reserach Institute (BAW.) Bettar el Moctar is with ISMT. Email: philipp.mucha@uni-due.de, ould.el-moctar@uni-due.de

$$\frac{\partial}{\partial t}\int_V \rho \mathbf{v}\,\mathrm{d}V + \int_S \rho(\mathbf{vv})\cdot\mathbf{n}\,\mathrm{d}S = \int_S \mathbf{T}\cdot\mathbf{n}dS + \int_V \rho\mathbf{b}\,\mathrm{d}V \tag{2}$$

where $\mathbf{v}$ denotes the fluid velocity vector, $\mathbf{n}$ is the normal vector of S, which represents the area of the surface of the control volume V, $\mathbf{T}$ denotes the stress tensor and $\mathbf{b}$ a vector describing a force per unit mass. The transport of turbulent momentum is considered introducing time average and fluctuating terms of the flow quantities to the equations. These are closed by turbulence models. The flow equations are discretized using the Finite Volume (FV) method and solved in a segregated fashion based on the Semi-Implicit Method for Pressure-Linked Equations (SIMPLE) algorithm, Patankar and Spalding (1972). Trim and sinkage are modelled with transient mesh deformations (mesh morphing) taking into account the rigid body motions in heave and pitch which are found from coupling the flow equations with Newton's equations of motion. The free surface is modelled using the Volume of Fluid (VoF) method, e.g. Ferziger and Peric (2002). Numerical uncertainty analysis follows the ITTC recommendations (2008.) The commerical solver STARCCM+ (Cd-Adapco, 2014) is used.

The boundary element method GL Rankine (Söding, 2012) predicts steady ship flows using nonlinear boundary conditions. Following the assumption of inviscid, incompressible and irrotational flow, a velocity potential ϕ exists, which has to satisfy the Laplacian

$$\Delta\phi = 0 \tag{3}$$

in the fluid domain and the boundary conditions

$$(\nabla\phi - \mathbf{U})\,\mathbf{n} = 0 \tag{4}$$

on the body boundary and free surface,

$$\nabla\phi\mathbf{n} = 0 \tag{5}$$

on the channel bottom and walls and

$$\frac{\zeta}{g} = \mathbf{U}\nabla\phi - \frac{1}{2}|\nabla\phi|^2 \tag{6}$$

on the free surface. In (4-6) $\mathbf{U}$ is the ship velocity vector and ζ the free surface elevation. An unstructured triangular grid is used on the submerged ship surface and a block-structured quadrilateral grid is employed on the free surface. Rankine sources are distributed following the desingularization method. Channel boundaries can be modelled either directly, using triangular panels, or employing image sources for rectangular channel cross sections. The Laplacian is satisfied by the formulation of the potential

$$\phi = \phi(\mathbf{x}) = \sum_{j=1}^{n} q_j G\left(\mathbf{x}, \xi_j\right) \tag{7}$$

where $G\left(\mathbf{x}, \xi_j\right)$ is a Rankine source of strength q_j and ξ_j denotes the source location points. A detailed formulation of the method can be found in the given reference. Upon the determination of the potential ϕ and the pressure at each panel found from Bernoulli's equation forces acting on the ship hull are available through integration and used to determine iteratively the dynamic trim and sinkage from hydrostatic balancing. Related literature contains applications of the method to the determination of ship squat in shallow water, von Graefe et al. (2011.)

3 RESULTS

Application of the Numerical Methods. In the field method the solution domain is composed of hexahedral control volumes which are arranged in an unstructured fashion. The discretization scheme is of second order using central differences. On the surface of the ship prismatic cells are used to achieve better resolution of the near-wall flow and boundary layer. The amount and density of these cells is chosen in accordance with the targeted nondimensional wall distance $y^+ = u^* y/\nu$, where y is the distance from the wall to the first interpolation point and ν the kinematic fluid viscosity. u^* is defined as $\sqrt{\tau/\rho}$, where τ is the wall shear stress. In case of applying a Low-Reynolds number turbulence model y^+ is targeted to 1. If a wall function approach is employed, y^+ is between 30 and 60. The turbulence model is kω-SST, Menter (1994.) One ship length upstream from the bow a velocity inlet boundary condition is set, three ship lengths downstream a pressure outlet condition holds. The width of the numerical tank equals the width of the tank from the model test facility (W=10m.) Free slip conditions are chosen for the tank walls and the bottom. The numerical grid is locally refined in the stern region, between the ship and the tank bottom and around the free surface. Near the outlet boundary the grid is coarsened to provide damping of the downstream propagating ship waves. Due to port-starboard symmetry only half of the fluid domain is modelled and a symmetry condition maps the solution onto the image of the domain. In the initial simulation phase the ship remains fixed until

a prescribed release time to initialize the solution and avoid large cell deformations. The time step is chosen as to accurately resolve the rigid body dynamics. Within each time step ten iterations are performed to update the velocity and pressure. After approximately 150s simulation time the longitudinal force X, sinkage z and trim θ show a converged trend in slightly oscillating around a mean value, which is shown in Figure 1. The absolute normalized residuals of momentum, continuity and the turbulence quantities decrease by two to three orders. All simulations are performed on a High Performance Computing (HPC) system using the Message Passing Interface (MPI) technique for job parallelization. These are run on four Intel(R) Sandy Bridge nodes (16 cores each) and for the medium grid take about six hours until the time series show a converged trend. The simulation of one case with GLR takes between 2 and 3 hours on an ordinary desktop computer at 2.4GHz with 4GB RAM.

Sensitivity Analysis. In the field method resistance, sinkage and trim are determined on three different grids of various resolution to investigate the sensitivity of the solution to spatial discretization. Where possible, the order of the discretization error p is assesed following ITTC (2008.) In Tables 2 and 3 the error ratio $E\%=100(D-S)/D$ compares the experimental data D and the simulation result S. Following the ITTC approach the numerical value S is corrected to provide a numerical benchmark $S_C = S - \delta^*$, where δ^* is found from generalized Richardson extrapolation of the results from the different grids. A crossed field indicates that the convergence condition is not met.

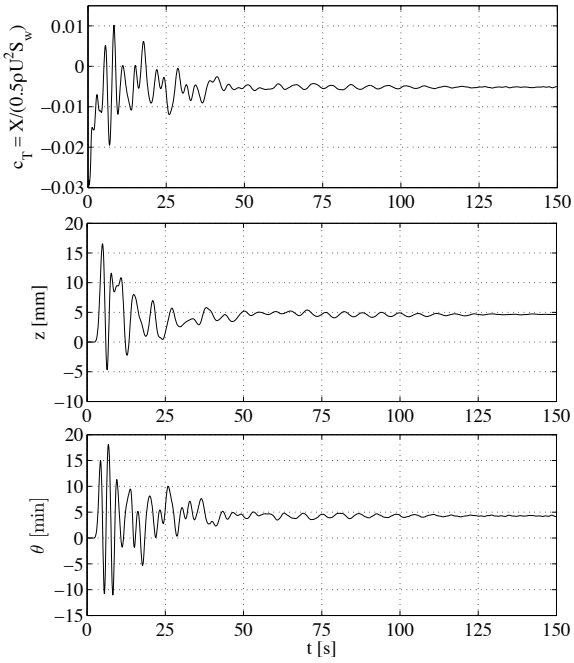

Figure 1: Convergence histories of the resistance coefficient (top), sinkage and trim (bottom) found from the field method, $h/T=1.6$ and $U=0.73$ m/s

Table 2: Grid sensitivity study - $h/T=1.6$, $U=0.73$ m/s, $F_{nh}=0.37$

CVs/10^6	X [N]	X_s [N]	z [mm]	θ [min]
0.6	-8.156	-6.025	4.632	4.026
1.4	-7.633	-6.017	4.790	3.977
2.0	-7.685	-6.064	4.603	4.279
Experiment	-7.088		4.474	-1.111
δ^*	x	-	x	x
p	x	-	x	x
E%	-8.420	-	-2.880	-
Panels/10^3				
14.85	-7.537	-6.343	5.090	-0.296
E%	-6.330	-	-13.770	-

Table 3: Grid sensitivity study - $h/T=1.3$, $U=0.73$ m/s, $F_{nh}=0.41$

CVs/10^6	X [N]	X_s [N]	z [mm]	θ [min]
0.5	-8.641	-6.271	6.293	4.238
1.2	-7.918	-6.201	7.084	3.739
1.8	-8.588	-6.294	6.431	4.283
Experiment	-8.317	-	6.160	-1.343
δ^*	x	-	x	x
p	x	-	x	x
E%	-3.250	-	-4.400	-
Panels/10^3				
14.85	-7.659	-6.512	6.050	-0.578
E%	11.170	-	1.180	-

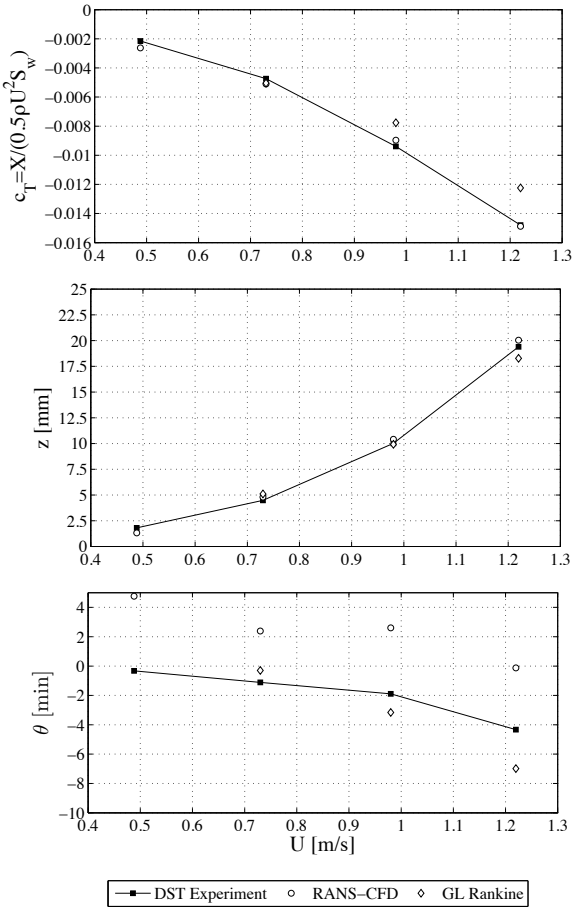

Figure 2: Comparison of the predictions for the resistance coefficient (top), sinkage and trim (bottom) against forward speed for h/T=1.6 by experiment, a field method (wall function approach, medium size grid) and a boundary element method

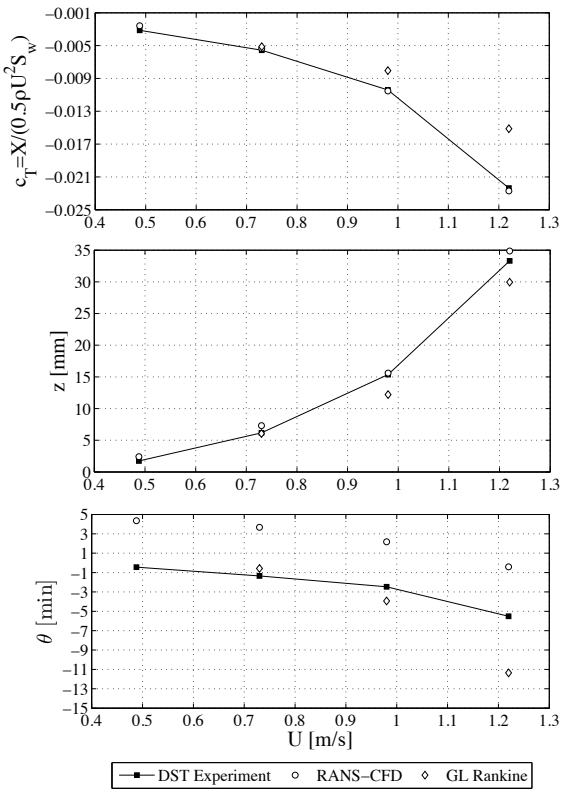

Figure 3: Comparison of the predictions for the resistance coefficient (top), sinkage and trim (bottom) against forward speed for h/T=1.3 by experiment, a field method (wall function approach, medium size grid) and a boundary element method

4 DISCUSSION

Tables 2 and 3 present the results from the sensitivity studies for the two water depths corresponding to F_{nh}=0.37 and F_{nh}=0.41. Unless stated differently, in these studies the wall function approach is used. The observations from these studies read:

- For the case F_{nh}=0.37 (Table 2) the total resistance coefficient c_T found from the field method with the finest grid deviates by 8.42% from the experiment. With 6.33% GLR provides a result of similar magnitude than the RANS simulation. In the field method the convergence character is not monotonic and no numerical benchmark S_C can be determined. The friction resistance prediction made by GLR is around 5% higher than the result from the RANS simulation. Simulations for the deep water case show that the numerically predicted friction resistance deviates less than 2% from the value found from the ITTC-1957 formula with both methods.

- For the case F_{nh}=0.37 (Table 2) the deviation of the midship sinkage prediction from the experimental data is 2.88% for the field method and 13.77% for GLR. The RANS simulation predicts a stern-down trim, the experiment and GLR a trim to bow. As typical for the subcritical speed range $U \leq \sqrt{gh}$ the sinkage dominates compared to the trim, i.e. it is an order of magnitude greater than the difference between the sinkage at the fore and aft body. As for the the longitudinal force, trim and midship sinkage do not allow for a generalized Richardson extrapolation and an assessment of the discretization error for the field method.

- For the case F_{nh}=0.41 (Table 3) with lower underkeel clearance (UKC) the deviation between experiment and RANS simulation for

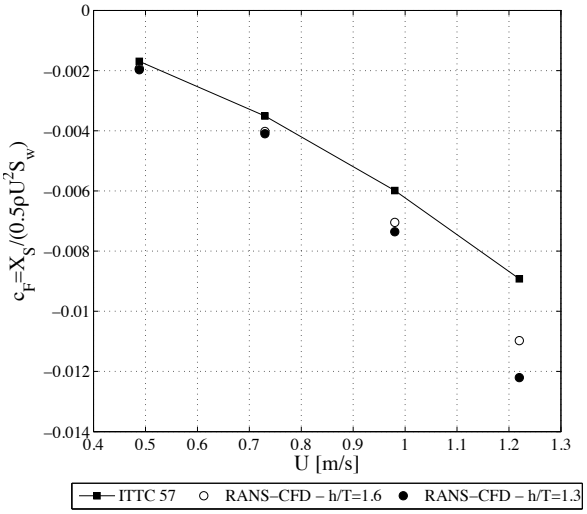

Figure 4: Overview of the friction resistance coefficient prediction for h/T=1.3 and 1.6 and the ITTC-1957 formula for deep water

the total resistance yields 3.25%. GLR's result is 11.17% lower than the experiment. With 4.4% the deviation of midship sinkage is predicted by the field method with a magnitude similar to the case for the higher depth Froude number. GLR's prediction is less than 2% lower than the EFD result. The observations for the trim are encountered again, too. In general, all quantities show a considerable increase compared to the case with higher UKC.

- The non-monotonic convergence character of the results from the spatial discretization studies is assumed to emerge from local grid quality and the consideration of the free surface. When the free surface is refined the resolved wave pattern in close vicinity to the hull differs from the one obtained with coarser grids, affecting the wetted surface and wave resistance, too.

The investigation of the entire speed range with the field method is performed with the medium size grid and presented in Figures 2 and 3. It is observed that for higher speeds the agreement between the field method and experiment is fairly good for c_T and z. Besides, the trim takes a similar trend, i.e. trimming to bow as the speed increases, albeit the prediction of the trim in the RANS simulation is stern-down in the lower speed range. Due to numerical difficulties in the computation of the wave profile and steady potential for slow forward speeds with the presented method, there is no result from GLR for the case with the lowest speed in Figures 2 and 3. However, to obtain a result for X it would be possible to run a double-body simulation instead.
Figure 4 compares the friction resistance coefficient c_F found from the RANS simulations with the prediction by the ITTC-1957 formula, where X_S is the longitudinal force contribution resulting from the shear stresses. The following conclusions are drawn from the observations:

- The general agreement between the resistance prediction by experiment and both numerical simulations is satisfactory. The greater deviations for the RANS simulations in the lower speed range might be associated with the grid resolution of the free surface, which remained unchanged during the speed variation tests. Yet, for lower speeds it would be necessary to adapt the resolution to account for the generally shorter waves than those being present at higher speeds. An additional simulation for the case h/T=1.3 and U=0.49 m/s using a Low-Reynolds turbulence number modelling approach and a no-slip boundary condition on the tank bottom showed a slight increase by 2.8% in c_T. A more extensive investigation is needed to verify if this trend is systematic.

- The agreement for the midship squat prediction is satisfactory. The midship sinkage is dominated by the local pressure along the midship body which can be well captured by both numerical methods. Trim is influenced by the local pressure at the fore and aft shoulders. The stern-down trim predicted by the RANS method compared to the bow-down trim predicted by GLR arises from lower local pressures in the aft body. Here, local flow analysis show that the streamlines detach from the body shortly behind the aft shoulders. A more elaborate uncertainty analysis for the experiment is desirable with respect to repeatability of the model test runs.

- It is seen that friction resistance shows a marked dependence on the water depth, especially in the upper speed range. Next to the identified flow separation in the aft body this trend brings to the attention the role of scale effects involved in extrapolation procedures based on model testing, since viscous effects are more dominant than for the full-scale ship

flow due to the violation of Reynolds similarity. An advantage of numerical methods in hydrodynamics is that they offer the possibility to investigate both model and ship flows.

- The presented work investigates the bare hull flow around KCS. The consideration of the propeller action in both model testing and the field method is of interest for further investigations.

5 ACKNOWLEDGMENTS

The authors would like to thank the Federal Waterways Engineering and Research Institute (BAW) for use of computational resources and the financial support of this work. Andreas Gronarz of DST kindly provided the EFD results. Alexander von Graefe and Vladimir Shigunov (both DNVGL) consulted in running GL Rankine. The authors appreciate their support.

6 REFERENCES

Cd adapco, 2014, *STARCCM+-User-Guide 9.02.007*

Ferziger, J., Peric, M., 2002, *Computational Methods for Fluid Dynamics*, Springer

Gronarz, A., Broß, H., Müller-Sampaio, C., Jiang, T., Thill, C., 2009, *SIMUBIN - Modellierung und Simulation der realitätsnahen Schiffsbewegungen auf Binnenwasserstraßen*, Report 1939 B, Development Centre for Ship Technology and Transport Systems (DST)

Menter, F.R., 1994, *Two-Equation Eddy-Viscosity Turbulence Models for Engineering Applications*, AIAA Journal, 32:8, 1598-1605

Patankar, S., Spalding, D., 1972, *A calculation procedure for heat, mass and momentum transfer in three-dimensional parabolic flows*, Int. J. of Heat and Mass Transfer, 15:10, 1787-1806

SIMMAN 2014 - Workshop on Verification and Validation of Ship Manoeuvring Simulation Methods, called 06/01/2014, `http://www.simman2014.dk`

Söding, H., 2012, *Rankine source method for seakeeping predictions*, Proceedings of the 31st International Conference on Ocean, Offshore and Arctic Engineering, OMAE Paper-No. 83450

The International Maritime Organization, 2012, *Air Pollution and Energy Efficiency - Consideration of the Energy Efficiency Design Index for New Ships - Minimum Propulsion Power to Maintain the Manoeuvrability in Adverse Conditions*, Document MEPC 64/4/13

The International Towing Tank Conference, 2002, *Resistance, Uncertainty Analysis, Example for Resistance Test*, Recommended Procedures and Guidelines 7.5-02-02-02

The International Towing Tank Conference, 2008, *Uncertainty Analysis in CFD - Verification and Validation Methodology and Procedures*, Recommended Procedures and Guidelines 7.5-03-01-01

Von Graefe, A., el Moctar, O., Shigunov, V., Söding, H., Zorn, T., 2011, *Squat Computations for Containerships in Restricted Waterways*, Proceedings of the 2nd International Conference on Ship Manoeuvring in Shallow and Confined Water: Ship-to-Ship Interaction

Multi-objective extensions of the deterministic particle swarm algorithm for RBRDO in ship design: a parametric study

Riccardo Pellegrini[1,2], Andrea Serani[1,2], Matteo Diez[1], Umberto Iemma[2], Emilio F. Campana[1]

[1]CNR-INSEAN, Natl. Research Council-Marine Technology Research Inst., Rome, Italy (matteo.diez@cnr.it)

[2]Roma Tre University, Dept. of Engineering, Rome, Italy

1 Introduction

Simulation-based design (SBD) optimization assists the designer in the design process of complex engineering systems. In this context, real-world problems are affected by different sources of uncertainties (operational, environmental, geometrical or numerical) and require reliability-based robust design optimization (RBRDO) formulations to identify the optimal solution. RBRDO is usually computationally very costly (especially if high-fidelity simulations are used) and may be achieved by means of metamodels, with efficient optimization algorithms. Herein, a RBRDO for ship design is solved, for real ocean environment including stochastic sea state and speed. The problem is taken from [1] and is formulated as an unconstrained multi-objective optimization problem aimed at (a) the reduction of the expected value of the resistance in wave at sea state 5, varying the speed and (b) the increase of the ship operability, with respect to a set of motion-related constraints. The design space used is a four-dimensional representation of shape modifications, based on the Karhunen-Loève expansion of free-form deformations of the original hull [2]. A metamodel based on stochastic radial basis function [3] is used, trained by URANS simulations. The ship considered is a 100m Delft catamaran, sailing in head waves in the North Pacific ocean.

The objective of the present work is the assessment of deterministic derivative-free multi-objective optimization algorithms for the solution of the RBRDO problem, with focus on multi-objective extensions of the deterministic particle swarm optimization (DPSO) algorithm [4].

Five approaches for multi-objective deterministic PSO (MODPSO) are addressed and include generalizations of the single-objective algorithm by: (a) distance from personal and social Pareto fronts, evaluated in the design variables and objective functions space respectively, (b) personal aggregated objective and distance from social Pareto front, evaluated in the design variables and objective functions space respectively, and (c) vector evaluated particle swarm optimization. Three performance metrics are used, providing the assessment of the proximity of the solutions to the reference Pareto front along with their wideness. The algorithms and their parametric implementation are evaluated by 66 test problems from literature, and applied to the catamaran RBRDO problem, varying the number of analysis-tool calls (evaluation budget) required.

2 Multi-objective extensions of deterministic PSO

The following single-objective deterministic PSO (DPSO) iteration [4] is used in the current work for extension to multi-objective optimization:

$$\begin{aligned} v_i^{t+1} &= \chi \left[v_i^t + c_1 \left(p_i - x_i^t \right) + c_2 \left(g - x_i^t \right) \right] \\ x_i^{t+1} &= x_i^t + v_i^{t+1} \end{aligned} \tag{1}$$

where x_i^t and v_i^t are the (vector-valued) position and velocity of the particle i ($i = 1,\ldots,N_p$) at iteration t, χ is a damping factor, c_1 and c_2 are coefficients controlling the personal and social behavior of the particle swarm, p_i is the best position ever visited by the i-th particle, whereas g is the best position ever visited by all the particles.

When the number of objective functions, N_{of}, is greater than one, the definition of personal best position, p_i, and global best position, g, should reflect the multi-objective nature of the problem. The DPSO iteration is rewritten as

$$\begin{aligned} v_i^{t+1} &= \chi \left[v_i^t + c_1 \left(p_i - x_i^t \right) + c_2 \left(g_i - x_i^t \right) \right] \\ x_i^{t+1} &= x_i^t + v_i^{t+1} \end{aligned} \tag{2}$$

where the personal best position p_i takes into account multiple objectives, as well as the global term g_i, which is based on the knowledge shared by all the particles and may vary from particle to particle.

Pareto-front based MODPSO. The idea behind this variant of the algorithm is that of generalizing the single-objective DPSO, in the Pareto-optimality sense [1]. Specifically, p_i and g_i are defined as follows:

- p_i is the closest point to the i-th particle of the personal Pareto front of all positions ever visited by the i-th particle;
- g_i is the closest point to the i-th particle of the global Pareto front of all positions ever visited by all the particles.

Distances are evaluated in the design variables space (MODPSO1) and in the objective functions space (MODPSO2).

Pareto-front and aggregate-objective-function based MODPSO. This variant has been presented in [5] and makes use of an aggregate objective function for the personal term. Accordingly:

- p_i is the personal optimum of all positions ever visited by the i-th particle, with respect to the aggregate objective function, $f_{\text{AOF}} = \sum_{j=1}^{k} w_j f_j$, where $w_j = 1/N_{of}$;
- g_i is the closest point to the i-th particle of the global Pareto front of all positions ever visited by all the particles evaluated in the design variables space (MODPSO3) and in the objective functions space (MODPSO4).

Vector evaluated DPSO. This variant makes use of a number of sub-swarms equal to the number of objective functions [6]:

- p_i is the personal optimum of all positions ever visited by the i-th particle of the j-th swarm, with respect to the j-th objective function;
- g_i is the global optimum of all positions ever visited by the all the particles of the k-th swarm ($k \neq j$), with respect to the k-th objective function.

If $N_{of} > 2$, the exchange of information among sub-swarms follows a ring connection. Herein, this algorithm is referred to as MODPSO5.

3 Implementation and evaluation metrics

The PSO coefficient sets are taken from literature and included in Tab. 1. The swarm size is set to $N_p = 2^n N_{dv} N_{of}$ with $n \in \mathbb{N}[1,6]$, where N_{dv} is the number of design variables. The swarm initialization is based on the Hammersley distribution [7], which is applied respectively to (A) the whole domain, (B) the domain boundaries, and (C) the domain and the boundaries in even amount. The initial particles location is combined with null and non-null initial velocity, following [4]. Finally, a semi-elastic wall type approach is used for the box constraints [4].

Table 1: Coefficient sets

Reference	χ	c_1	c_2
Shi and Eberhart (1998)	0.729	2.050	2.050
Trelea (2003)	0.600	1.700	1.700
Clerc (2006)	0.721	1.655	1.655
Campana and Pinto (2005)	1.000	0.400	1.300
Diez et al. (2013)	0.990	0.330	0.660

Generational Distance (GD) and Inverse Generational Distance (IGD) are chosen as performance indicators, providing a measure of the proximity of the solutions to the reference Pareto front, along with their wideness, respectively [8]. An overall performance metric is given, as a Generational Merit Factor (GMF), combining GD and IGD as $\text{GMF} = \sqrt{(\text{GD}^2 + \text{IGD}^2)/2}$.

4 Numerical Results

The evaluation metrics GD, IGD and GMF are evaluated as a function of the number of objective-functions calls (No. of f_{eval}). The reference Pareto front (used by GD and IGD) is defined as the set of non-dominated solutions among all optimizations (obtained by varying the algorithms' parameters), with a number of function evaluations

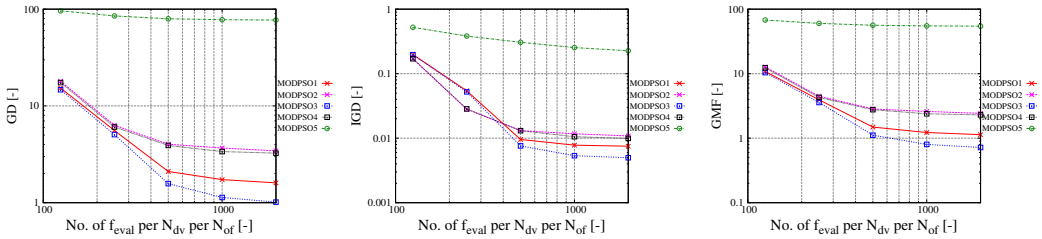

Figure 1: Test problems, average GD, IGD and GMF, conditional to the algorithm used

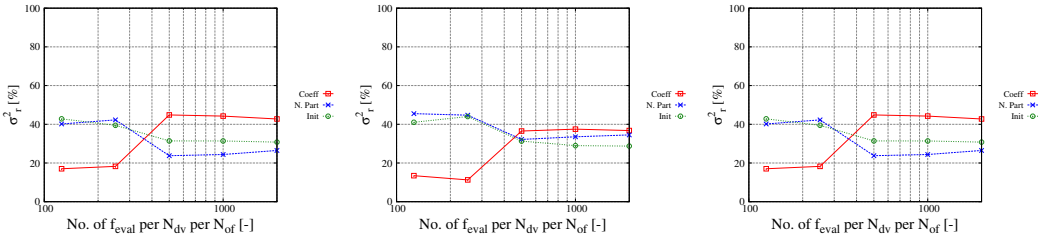

Figure 2: Test problems, relative variance for GD, IGD and GMF (from left to right) for MODPSO1

equal to No. of $f_{eval} = 2{,}000 N_{dv} N_{of}$. MODPSO algorithms are assessed using 66 test problems. The number of design variables N_{dv} ranges from two to eight, whereas the number of objective functions N_{of} ranges from two to three. Figure 1 shows the average GD, IGD and GMF values obtained by the MODPSO algorithms, over all test problems, coefficient sets, swarm sizes and initializations. MODPSO1 and MODPSO3 have a similar performance; also MODPSO2 and MODPSO4 a have similar performance; MODPSO3 has the best performance overall, whereas MODPSO5 is found the least effective. Figures 2, 3, 4, 5 and 6 show the relative variance of GD, IGD and GMF, retained by each of the MODPSO parameter (coefficient set, swarm size, initialization), for MODPSO1, MODPSO2, MODPSO3, MODPSO4 and MODPSO5, respectively. All parameters affect significantly the algorithms' performance, and therefore deserve a careful investigation. Specifically, the best average performance for MODPSO1 is found using the coefficient set from [9], a swarm size equal to $32 N_{dv} N_{of}$ and initialization of particles over the domain, with non-null velocity. The best-performing implementation for MODPSO2 is given by the coefficients from [10], with $16 N_{of} N_{dv}$ particles initially distributed over the domain, with non-null velocity. The best performance for MODPSO3 is provided by the coefficient set from [9], a swarm size equal to $64 N_{dv} N_{of}$ and initialization of particles over the whole domain, with non-null velocity. MODPSO4 presents its best performance with the same parameters of MODPSO2. Finally, the best-performing MODPSO5 is given by the coefficient set from [1], a swarm size equal to $64 N_{dv} N_{of}$, with particles initialized over domain and boundaries, with non-null velocity.

Figure 7 shows the average GD, IGD and GMF values obtained by the MODPSO algorithms for the catamaran RBRDO problem. GD, IGD and GMF have similar trends. As for the test problems, the choice of the algorithm is found a significant issue. MODPSO1, MODPSO2, MODPSO3 and MODPSO4 show close performances, and are more effective than MODPSO5. Figures 8, 9, 10, 11, and 12 show the relative variance of GD, IGD and GMF, retained by each of the MODPSO parameter (coefficient set, swarm size, initialization), for MODPSO1, MODPSO2, MODPSO3, MODPSO4 and MODPSO5, respectively. The best implementation for MODPSO1 is found using the coefficient set by [1], with $64 N_{of} N_{dv}$ particles, initialized over domain and boundaries, with null velocity. The best implementation for MODPSO2 is found using the coefficient set from [10], with $4 N_{of} N_{dv}$ particles, initialized over the domain, with non-null velocity. The best-performing implementation for MODPSO3 is given by the coefficients from [11], with $16 N_{of} N_{dv}$ particles initially distributed over domain and boundaries, with null velocity. MODPSO4 gives its best results when implemented with the same coefficients and number of particles of MODPSO2, but initialized over domain and boundaries, with non-null velocity. The best implementation for MODPSO5 is found using the coefficient set from [1], with $32 N_{of} N_{dv}$ particles, initialized over domain and boundaries, with non-null velocity. The best-performing implementation overall is provided by MODPSO3. Finally, Figure 13 shows the best Pareto fronts for each of the algorithm (with No. of $f_{eval} = 2{,}000 N_{dv} N_{of}$), with comparison with the reference.

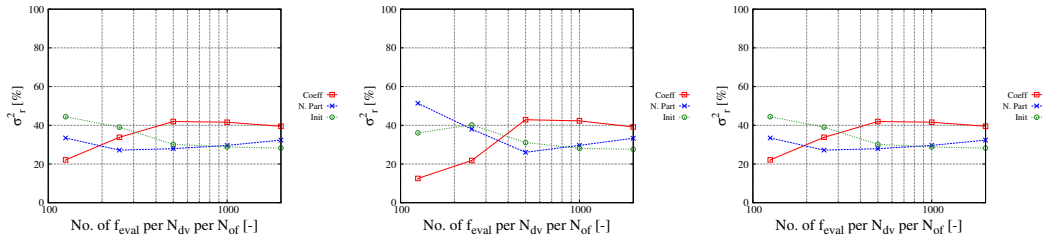

Figure 3: Test problems, relative variance for GD, IGD and GMF (from left to right) for MODPSO2

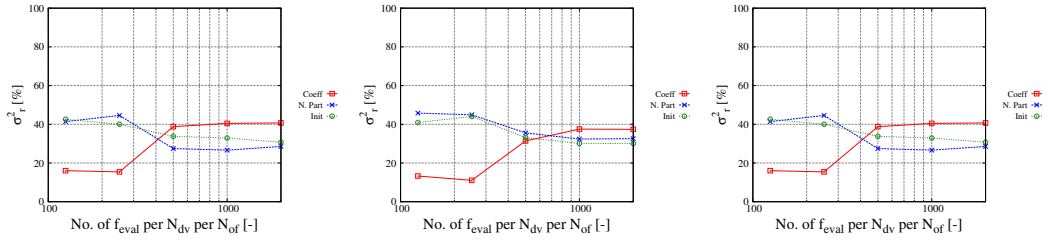

Figure 4: Test problems, relative variance for GD, IGD and GMF (from left to right) for MODPSO3

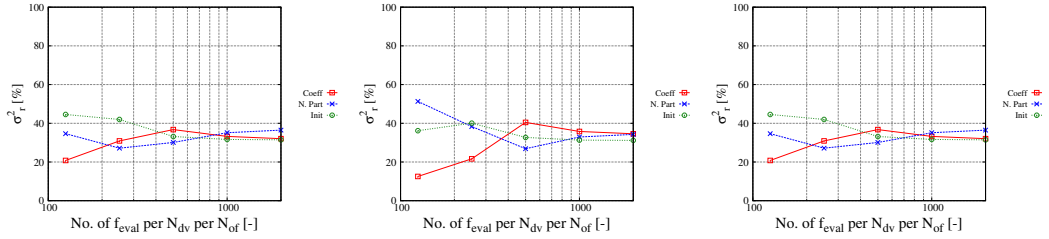

Figure 5: Test problems, relative variance for GD, IGD and GMF (from left to right) for MODPSO4

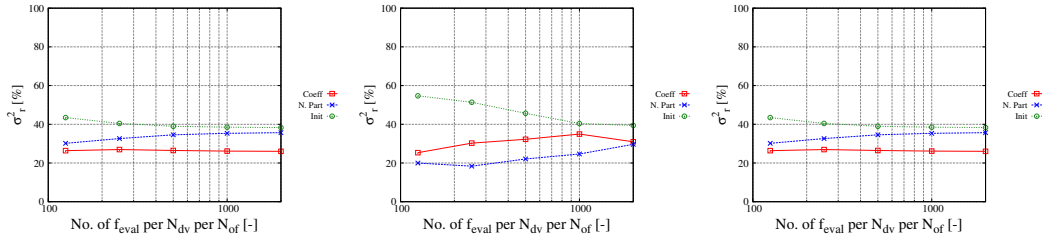

Figure 6: Test problems, relative variance for GD, IGD and GMF (from left to right) for MODPSO5

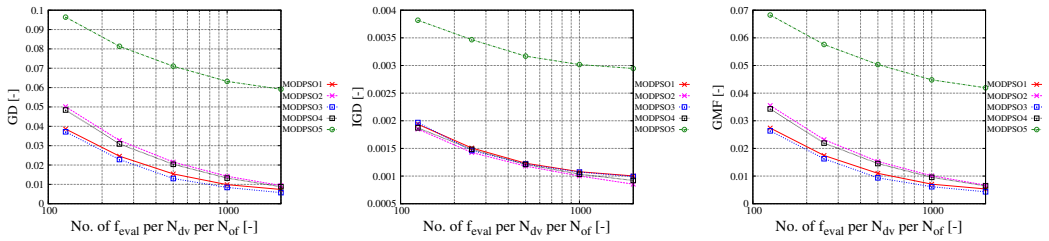

Figure 7: Catamaran RBRDO, average GD, IGD and GMF, conditional to the algorithm used

5 Conclusions

A parametric analysis of five MODPSO variants' performance has been given, varying the coefficient set, the swarm size and the initialization of the particles. The algorithms are extension to multi-objective problems of the single-objective DPSO. Three evaluation metrics have been used, namely the generational distance, the inverse generational distance and an overall generational merit factor. Results have been shown for 66 test problems and

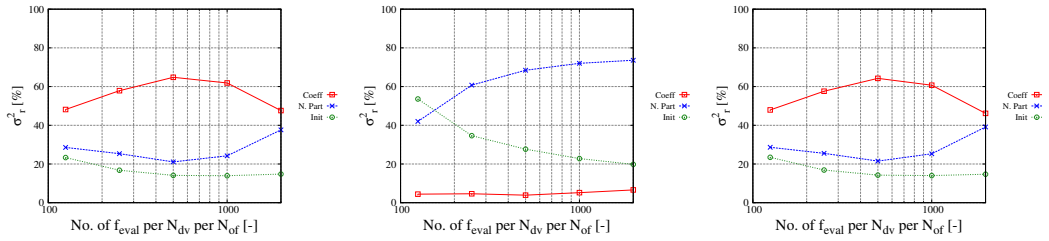

Figure 8: Catamaran RBRDO, relative variance for GD, IGD and GMF (from left to right) for MODPSO1

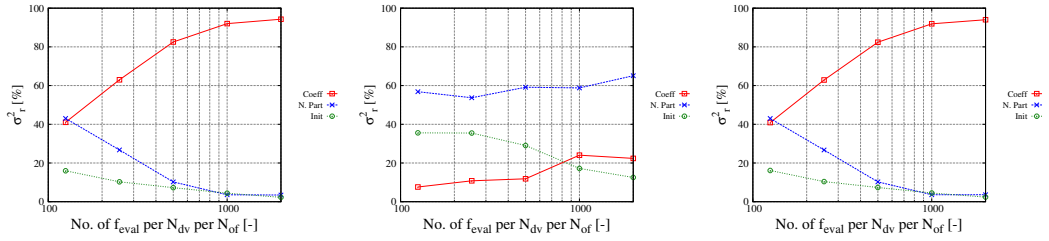

Figure 9: Catamaran RBRDO, relative variance for GD, IGD and GMF (from left to right) for MODPSO2

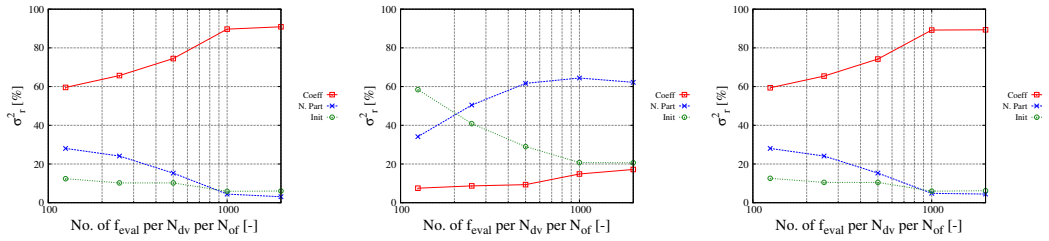

Figure 10: Catamaran RBRDO, relative variance for GD, IGD and GMF (from left to right) for MODPSO3

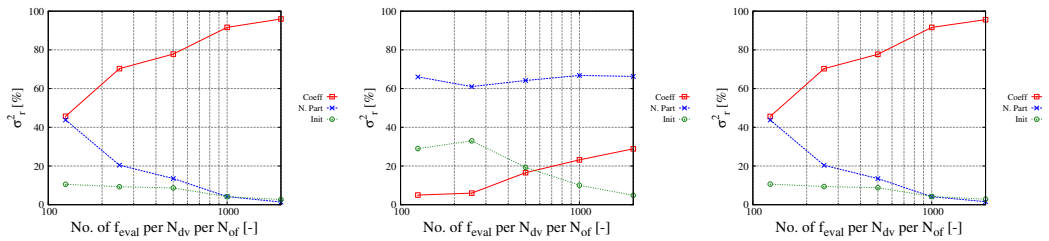

Figure 11: Catamaran RBRDO, relative variance for GD, IGD and GMF (from left to right) for MODPSO4

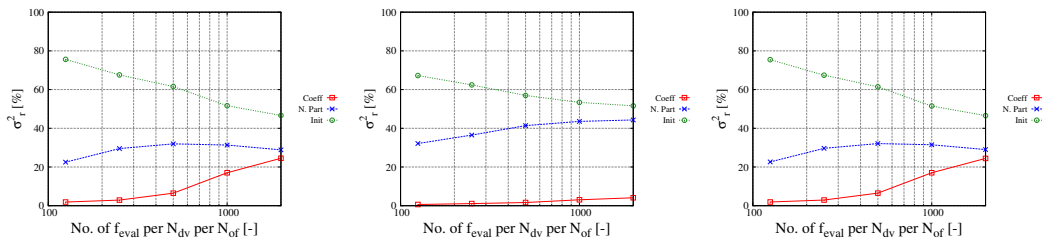

Figure 12: Catamaran RBRDO, relative variance for GD, IGD and GMF (from left to right) for MODPSO5

for a metamodel-based RBRDO of a high-speed catamaran in real ocean environment.

The choice of the algorithm has been found the most significant issue in order for the MODPSO to be effective and efficient. Coefficient set, swarm size, particles initialization also affect the optimization performance (at least for the Pareto-front based algoritms). Overall, MODPSO3 is found the most effective for both the test problems and the catamaran RBRDO.

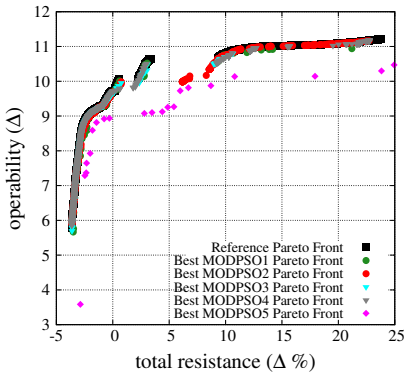

Figure 13: Comparison of Pareto fronts

Acknowledgements

The present research is supported by the US Navy Office of Naval Research, NICOP Grant N62909-11-1-7011, under the administration of Dr. Ki-Han Kim and Dr. Woei-Min Lin, and by the Italian Flagship Project RITMARE, coordinated by the Italian National Research Council and funded by the Italian Ministry of Education, Research Program 2011-2013.

References

[1] M. Diez, X. Chen, E. F. Campana, and F. Stern, "Reliability-based robust design optimization for ships in real ocean environment," in *12th International Conference on Fast Sea Transportation, FAST2013, Amsterdam, The Netherlands*, 2013.

[2] X. Chen, M. Diez, M. Kandasamy, Z. Zhang, E. F. Campana, and F. Stern, "High-fidelity global optimization of shape design by dimensionality reduction, metamodels and deterministic particle swarm," *Engineering Optimization,*, in press, 2014. DOI:10.1080/0305215X.2014.895340.

[3] S. Volpi, M. Diez, N. J. Gaul, H. Song, U. Iemma, K. K. Choi, E. F. Campana, and F. Stern, "Development and validation of a dynamic metamodel based on stochastic radial basis functions and uncertainty quantification," *Structural Multidisciplinary Optimization,*, in press, 2014. DOI 10.1007/s00158-014-1128-5.

[4] A. Serani, M. Diez, C. Leotardi, D. Peri, G. Fasano, U. Iemma, and E. Campana, "On the use of synchronous and asynchronous single-objective deterministic particle swarm optimization in ship design problems," in *International Conference on Engineering and Applied Sciences Optimization, OPT-i 2014, Kos Island, Greece, 4-6 June*, 2014.

[5] E. Campana and A. Pinto, "A multiobjective particle swarm optimization algorithm based on sub-swarms search," Tech. Rep. CNR–INSEAN, 2005.

[6] K. Parsopoulos, D. Tasoulis, M. Vrahatis, *et al.*, "Multiobjective optimization using parallel vector evaluated particle swarm optimization," in *Proceedings of the IASTED International Conference on Artificial Intelligence and Applications, AIA 2004*, vol. 2, pp. 823–828, 2004.

[7] T. Wong, W. Luk, and P. Heng, "Sampling with Hammersley and Halton points," *Journal of Graphics Tools*, vol. 2, no. 2, pp. 9–24, 1997.

[8] J. Cabrera and C. C. Coello, "Micro-MOPSO: a multi-objective particle swarm optimizer that uses a very small population size," in *Multi-Objective Swarm Intelligent Systems*, pp. 83–104, Springer, 2010.

[9] I. C. Trelea, "The particle swarm optimization algorithm: convergence analysis and parameter selection," *Information Processing Letters*, vol. 85, no. 6, pp. 317–325, 2003.

[10] M. Clerc, "Stagnation analysis in particle swarm optimisation or what happens when nothing happens," Tech. Rep. CSM–460, Department of Computer Science, University of Essex, 2006.

[11] Y. Shi and R. C. Eberhart, "Parameter selection in particle swarm optimization," in *Evolutionary Programming VII*, pp. 591–600, Springer, 1998.

On the use of Hybrid Turbulence Models

Filipe S. Pereira[1,3], Guilherme Vaz[2], and Luís Eça[3]

[1] *Maritime Research Institute of Netherlands (MARIN) Academy, Wageningen, The Netherlands, f.pereira@academy.marin.nl;*
[2] *Maritime Research Institute of Netherlands (MARIN), Wageningen, The Netherlands;*
[3] *Instituto Superior Técnico (IST), Lisbon, Portugal.*

1 Introduction

In many engineering applications, the quantities of interest are only time or ensemble averaged values and so the Reynolds-Averaged Navier Stokes equations (RANS for time-averaging and URANS for ensemble averaging) play a dominant role. In these equations, the effect of the turbulent field is represented by the Reynolds stresses that require a closure model, the so-called turbulence model. Unfortunately, experience has shown that the turbulence models available nowadays are not able to make reliable predictions of many complex flows, especially when the flow is not statistically steady. The significant increase in computing power led to the appearance of mathematical models that aim at determining the instantaneous flow quantities. However, the Reynolds numbers of many engineering applications only allow the solution of the large scales of turbulence and so models as for example Large Eddy Simulation (LES) still require a closure model due to the filtering applied to the equations. However, in these formulations the closure model represents only the small scales of turbulence and so they should be easier to develop than those applied in RANS/URANS.

In many hydrodynamic applications we have wall bounded flows at very high Reynolds numbers. Such conditions make LES extremely expensive and so alternative formulations have been proposed in the open literature: one of the alternatives is to use the so-called Hybrid methods [1–4]

The aim of this work is to assess the numerical requirements and prediction capabilities of three Hybrid formulations: Scale Adaptive Simulations (SAS) [1, 2], Delayed Detached-Eddy Simulations (DDES) [3], and Partially-Averaged Navier Stokes (PANS) equations [4, 5] based on an adapted $k-\omega$ SST model [6]. The selected test case is the flow over a backward-facing step at a Reynolds number based on the step height, h, of 37500. This choice is motivated by the existence of experimental data [7], the simplicity of the geometry and the complexity of the flow that exhibits separation, a free shear layer and reattachment. On the other hand, a statistically steady internal flow is not the easiest choice for hybrid methods because a large percentage of the turbulence production occurs in the near-wall region. RANS and URANS solutions using the SST $k-\omega$ model [6] are also determined for comparison purposes. All simulations are carried out with the finite volume solver ReFRESCO [8].

The paper is organized as follows: section 2 provides a description of the turbulence models applied in the present work. The numerical simulations details are given in section 3. Section 4 presents the results, while section 5 summarizes final remarks.

2 Turbulence Models

Turbulence is characterized by the wide range of scales present in the fluctuations around a mean value. Therefore, filtered/averaged formulations of the NSE are required for practical applications,

$$\frac{\partial \langle V_i \rangle}{\partial t} + \frac{\partial \langle V_i \rangle \langle V_j \rangle}{\partial x_j} = -\frac{\partial \langle p \rangle}{\partial x_i} + \nu \frac{\partial^2 \langle V_i \rangle}{\partial^2 x_j} - \frac{\partial \tau\left(V_i, V_j\right)}{\partial x_j}. \tag{1}$$

In equation 1, τ is the generalized central second moment, Sub-Filter Stresses (SFS) or Reynolds stresses. In the former equations, the instantaneous velocity field (and pressure) was decomposed into resolved/averaged, $\langle V \rangle$, and unresolved/fluctuations components, v, such that $V = \langle V \rangle + v$. Thereby, the effect of the unresolved components on the resolved/averaged ones is represented by the SFS/Reynolds term, which requires modelling. In this work, the SFS/Reynolds is approximated using the Boussinesq approximation,

$$\tau\left(V_i, V_j\right) = -\nu_u \left(\frac{\partial \langle V_i \rangle}{\partial x_j} + \frac{\partial \langle V_j \rangle}{\partial x_i} \right) + \frac{2}{3} k_u \delta_{ij}, \tag{2}$$

where the subscript u stands for unresolved in formulations that attempt to partially simulate turbulence and is normally replaced by t for the RANS/URANS approach. Therefore, all the formulations tested in this work have the same basic

form of the governing equations, but different closure models to obtain the unknown ν_u/ν_t. However, as mentioned above, there is a fundamental difference between the RANS/URANS approach and all the others: in RANS/URANS the unknowns of the partial differential equations are globally averaged quantities, whereas the other approaches propose to determine part of the turbulence fluctuations.

2.1 Reynolds-Averaged Navier-Stokes

The RANS/URANS dominant role in engineering results from its satisfactory accuracy for statistically steady flows and relatively low computational cost. All the computations performed used the Menter's two-equations $k-\omega$ SST closure model [6]. This model blends the $k-\varepsilon$ and $k-\omega$ in order to combine their main advantages and accounts for the effect of the principal turbulent shear stress which is especially important for flows with adverse pressure gradient [6]. The $k-\omega$ SST methodology defines the eddy-viscosity as,

$$\nu_t = \rho\mu_t = \rho\frac{a_1 k}{\max\left(a_1\omega, SF_2\right)}, \tag{3}$$

where S is the magnitude of the strain-rate tensor, and k and ω are the turbulent kinetic energy and specific dissipation, respectively. These turbulent quantities are calculated using transport equations,

$$\begin{aligned}\frac{\partial\rho k}{\partial t} + \frac{\partial\rho k V_j}{\partial x_j} &= P_k - \beta^* k\omega \\ &+ \frac{\partial}{\partial x_j}\left[\left(\mu + \mu_t\sigma_k\right)\frac{\partial k}{\partial x_j}\right],\end{aligned} \tag{4}$$

$$\begin{aligned}\frac{\partial\rho\omega}{\partial t} + \frac{\partial\rho\omega V_j}{\partial x_j} &= \frac{\alpha\rho}{\mu_t}P_k + \frac{\partial}{\partial x_j}\left[\left(\mu + \mu_t\sigma_\omega\right)\frac{\partial\omega}{\partial x_j}\right] \\ &- \beta^*\omega^2 + \frac{2\rho\sigma_{\omega_2}}{\omega}\left(1-F_1\right)\frac{\partial\omega}{\partial x_j}\frac{\partial k}{\partial x_j},\end{aligned} \tag{5}$$

where P_k stands for the kinetic energy production, $P_k = \min(\mu_t S^2, 10\beta^* k\omega)$. The blending functions, F_1 and F_2, and constants a_1, β^*, σ_k, σ_ω, α and σ_{ω_2} (equations 3, 4, 5) are given in [6]. The $k-\omega$ SST is used as basis for all other approaches tested in this work. Therefore, the following subsections only present the main modifications required for each formulation.

2.2 Scale-Adaptive Simulations

In many statiscally unsteady flows, RANS/URANS turbulence models tend to produce too high levels of eddy-viscosity, producing too diffusive predictions. In order to deal with this shortcoming, Menter et al. [1, 2] proposed a new version of the $k-\omega$ SST closure model. To this end, Menter et al. added an extra term to the ω equation (proportional to $\alpha\rho P_k/\mu_t$) in an attempt to adjust the eddy-viscosity level to the local characteristics of the flow. The modified ω equation has the form,

$$\begin{aligned}\frac{\partial\rho\omega}{\partial t} + \frac{\partial\rho\omega V_j}{\partial x_j} &= \frac{\alpha\rho}{\mu_t}P_k + \frac{\partial}{\partial x_j}\left[\left(\mu + \mu_t\sigma_\omega\right)\frac{\partial\omega}{\partial x_j}\right] \\ &- \beta^*\omega^2 + \frac{2\rho\sigma_{\omega_2}}{\omega}\left(1-F_1\right)\frac{\partial\omega}{\partial x_j}\frac{\partial k}{\partial x_j} + Q_{SAS},\end{aligned} \tag{6}$$

where the extra term, Q_{SAS}, is defined by,

$$\begin{aligned}Q_{SAS} = \rho\max\Bigg[&\rho\xi_2 S^2\left(\frac{L}{L_{vK}}\right)^2 - C_{SAS}\frac{2\rho k}{\sigma_\phi} \\ &\times\max\left(\frac{1}{k^2}\frac{\partial k}{\partial x_j}\frac{\partial k}{\partial x_j}, \frac{1}{\omega^2}\frac{\partial\omega}{\partial x_j}\frac{\partial\omega}{\partial x_j}\right), 0\Bigg].\end{aligned} \tag{7}$$

In equation 7, L is the length scale of the largest non-resolved scales (integral length scale in RANS mode, $Q_{SAS}=0$), $L = \sqrt{k}/(\omega C_\mu^{0.25})$, and L_{vK} the von Kárman length scale, $L_{vK} = \kappa\left(S^2/(\nabla S)^2\right)^{0.5}$ (C_μ and κ are constants with values 0.09 and 0.41). Thus, the presence of unsteadiness tends to decrease L_{vK}, leading to an increase of Q_{SAS}, and respective ω increase and ν_t decrease. As a result, the model has the ability to operate in scale-resolving simulation mode, *i.e.* it can resolve *part* of the turbulence spectrum in certain areas of the domain. This is termed Scale-Adaptive Simulations.

2.3 Delayed Detached-Eddy Simulations

The Detached-Eddy Simulations (DES) model blends LES and RANS models. The idea behind it, is to use RANS in near-wall regions, and LES to capture the outer detached-eddies. To accomplish such goal, the dissipation term in the k equation is modified in order to reduce the eddy-viscosity in LES regions. In this work, we used the second generation of this approach, Delayed Detached-Eddy Simulations (DDES), since it executes a smoother transition between RANS and LES, and it is resistant to grid induced separation (see, for instance, [3]). The k transport equation takes the form [3],

$$\begin{aligned}\frac{\partial\rho k}{\partial t} + \frac{\partial\rho k V_j}{\partial x_j} &= P_k - \frac{\rho\sqrt{k^3}}{l_{DDES}} \\ &+ \frac{\partial}{\partial x_j}\left[\left(\mu + \mu_t\sigma_k\right)\frac{\partial k}{\partial x_j}\right],\end{aligned} \tag{8}$$

where l_{DDES} is the DDES length scale defined as,

$$l_{DDES} = l_{RANS} - f_d\max\left(0, l_{RANS} - l_{LES}\right). \tag{9}$$

In equation 9 l_{RANS} is the RANS length scale, $l_{RANS} = \sqrt{k}/\left(C_\mu\omega\right)$ (in contrast to SAS, $L =$

$\sqrt{k}/(\omega C_\mu^{0.25})$), l_{LES} the LES length scale, $l_{LES} = C_{DES} l_{max}$ (C_{DES} and l_{max} are a local constant depending on F_1 and the maximum cell length), and f_d is an empiric blending function [3]. As a result of the previous modification, k (unresolved/modelled) decreases as a function of the grid resolution (l_{LES}), reducing the eddy-viscosity.

2.4 Partially-Averaged Navier-Stokes

PANS has a different modelling philosophy than DDES. Instead of being a "zonal approach", the initial version of PANS proposes a formulation for the complete domain that includes two parameters, f_k and f_ε, that define the percentage of kinetic energy and dissipation that is supposed to be modelled, *i.e.* when these parameters are one, PANS is equal to RANS, and when they are set to zero it becomes DNS. To this end, two constant coefficients, $f_k = k_u/k$ and $f_\omega = f_\varepsilon/f_k = \omega_u/\omega$, are introduced in k and ω equations to define the percentage of total kinetic energy and specific dissipation that should be modelled/unresolved. Thus [4, 9],

$$\begin{aligned}\frac{\partial \rho k_u}{\partial t} + \frac{\partial \rho k_u \langle V_j \rangle}{\partial x_j} &= P_k - \beta^* k \omega_u \\ &+ \frac{\partial}{\partial x_j}\left[\left(\mu + \mu_u \sigma_k \frac{f_k^2}{f_\omega}\right)\frac{\partial k_u}{\partial x_j}\right],\end{aligned} \tag{10}$$

$$\begin{aligned}\frac{\partial \rho \omega_u}{\partial t} + \frac{\partial \rho \omega_u \langle V_j \rangle}{\partial x_j} &= \frac{\alpha \rho}{\mu_t} P_k - \left(\alpha \beta^* - \beta^* \frac{\alpha}{f_\omega}\right. \\ &\left. + \frac{\beta}{f_\omega}\right)\omega_u^2 + \frac{\partial}{\partial x_j}\left[\left(\mu + \mu_u \sigma_\omega \frac{f_k^2}{f_\omega}\right)\frac{\partial \omega_u}{\partial x_j}\right] \\ &+ \frac{2\rho\sigma_{\omega_2}}{\omega_u}(1 - F_1)\frac{f_k}{f_\omega}\frac{\partial \omega_u}{\partial x_j}\frac{\partial k_u}{\partial x_j}.\end{aligned} \tag{11}$$

Note that the influence of the resolved velocity scales on the transport of k_u and ω_u was neglected (see [4, 9]). Regarding to the blending functions of the $k-\omega$ SST closure model, since F_1 was initially tunned for RANS models, and it is part of the transport of equations, we decided to modified it to use k and ω instead of k_u and ω_u. This is a different formulation than that used in [9], and it will be assessed in the future. Moreover, the Prandtl number was also not modified. On the other hand, F_2 was kept unchanged since it is not included in the transport equations. PANS relies on two parameters, f_k and f_ε, to define the resolved and unresolved scales. Therefore, a question arises: how to specify these parameters? Regarding to f_ε, considering the high Reynolds' number and the grids used, it was set as unity, $0 \leq f_k \leq f_\varepsilon \leq 1$. For f_k, the following expression to estimate the lowest value supported by a certain grid, *i.e.* the maximum resolved kinectic energy, was used (see [5]),

$$(f_k)_{min} = \frac{1}{C_\mu^{\frac{1}{2}}}\left(\frac{h_{max}}{l_{RANS}}\right)^{\frac{2}{3}}, \tag{12}$$

being l_{RANS} defined in section 2.2. Equation 12 uses the maximum cell length instead of the minimum one [5]. This issue is addressed in section 4.

3 Numerical Simulations

3.1 ReFRESCO

The numerical simulations are performed with ReFRESCO. It is a viscous-flow CFD code that solves multiphase incompressible flows with RANS equations. ReFRESCO is complemented with turbulence closure models, cavitation models and volume-fraction transport equations for different phases. Several turbulence RANS closure models are available. The equations are discretised in a strong-conservation form using a finite-volume approach with cell-centered collocated variables. ReFRESCO is parallelized using MPI and sub-domain decomposition. It is currently being developed, verified and validated at MARIN (the Netherlands) [8], in collaboration with IST (Portugal), USP-TPN (Brazil), TUDelft (the Netherlands), RuG (the Netherlands) and UoS (United Kingdom).

3.2 Case Study, Domain and Grids

The different approaches tested in this work are assessed predicting the flow past a backward-facing step for a Reynolds' number of 37500 (based on the step height, h). The computational domain is as follows: while in the upstream region the domain has $4h \times 8h \times 3h$ (stream-wise, vertical and span-wise directions, respectively), the downstream re-

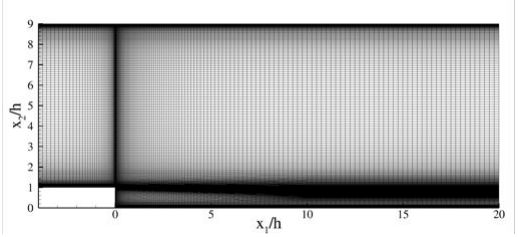

(a) T_1- structured grid (1.7M cells)

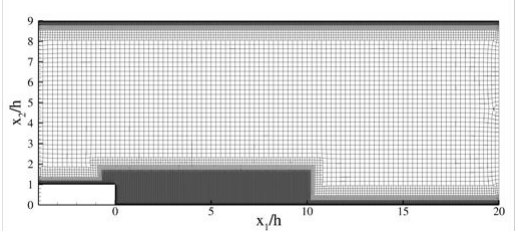

(b) T_2 - unstructured grid (4.6M cells)

Figure 1: Grid types (2D view).

gion has $20h \times 9h \times 3h$. The computations are carried out with two types of grids: T_1 and T_2. The first is a structured grid and has a smooth variation of the cells size, figure 1a, the second is unstructured and with very fine cells at boundary layers and free-shear regions, figure 1b. For T_1, the coarsest grid of a set covering a grid refinement of two is used (the remaining grids will be used in future computations). This set ranges from 1.6M to 13.0M cells. This leads to $x^+_{max} \approx 170 - 340$, $y^+_{max} \approx 0.7 - 1.4$ and $z^+_{max} \approx 60 - 120$. Moreover, 16 2D grids with a number of cells up to 2.5M are used to perform RANS solution verification. On the other hand, T_2 is tested with a single grid with 4.6M cells ($x^+_{max} \approx 50$, $y^+_{max} \approx 1$ and $z^+_{max} \approx 50$).

3.3 Numerical Settings

In order to solve the momentum, pressure and turbulent transport equations, a segregated approach is used. The QUICK is applied to discretise the convective terms of all transport equations (including turbulence). To ensure a negligible contribution to the numerical error from the round-off and iterative error, when compared to the discretisation error, the calculations are executed with double precision and an iterative convergence criterion (L_∞) of, at least, $c_{it} \leq 10^{-6}$, for mean flow and turbulence quantities normalized residuals at each time step. The time step is set such that the Courant number is kept lower than unity. However for T_1, this value raises to 4 at $x_1/h = 0$ (with a global average value of 0.3). The unsteady simulations started from a converged RANS solution and predicted 300s, being the first 150s discarded. Regarding to boundary conditions, these followed [10]. Synthetic perturbations were not, initially, prescribed at the inflow, but their role on the predictions quality is currently being analyzed. Cyclic boundary conditions at the span-wise direction will be applied in future predictions.

4 Numerical Results

4.1 RANS Solution Verification

As mentioned in section 1, one of the goals of the present work is to assess the trade-off between gain of accuracy and computational demands of the new methodologies when compared with common RANS models. Therefore, the initial step of this work is to perform a solution Verification exercise for a simple 2D RANS case. This exercise followed the procedure described in [11]. The results for the friction and pressure forces, F_f and F_p, at the bottom wall downstream of the step ($0 \leq x_1/h \leq 20$) are shown in figure 2. Although figure 2 shows relatively small differences between the values obtained with the coarsest and finest grids (10% for F_f and 1% for F_p), it also indicates the requirement of grids with more than 1M cells to attain the asymptotic region. Such type of behaviour was also observed for different solvers in the Lisbon Workshop [10].

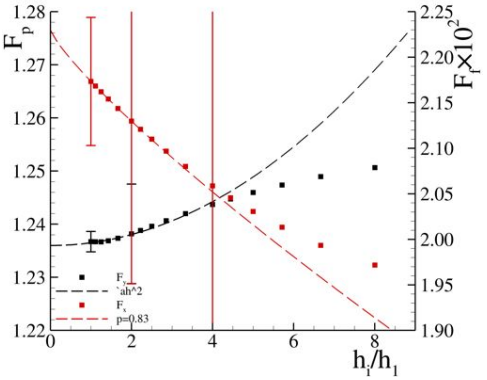

Figure 2: Order of grid convergence, p, and numerical uncertainty for a RANS solution using 2D grids (up to 2.5M cells).

4.2 Resolved Turbulent Kinetic Energy

In order to get some insight over the maximum level of resolved turbulence kinetic energy achievable by a certain grid, the PANS f_k parameter is estimated applying equation 12 to the results of 3D RANS computations. The results for each type of grid used during the unsteady computations

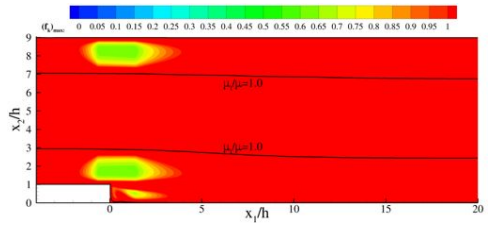

(a) f_k using h_{max} (T_1 - 1.7M cells).

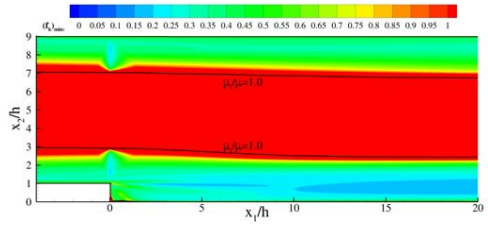

(b) f_k using h_{min} (T_1 - 1.7M cells).

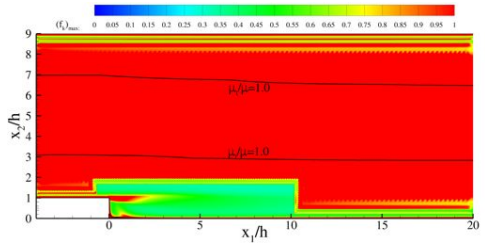

(c) f_k using h_{max} (T_2 - 4.6M cells).

Figure 3: Estimation of f_k for grids T_1 and T_2.

are presented in figure 3. It is visible, when using h_{max}, that the current T_1 grid is still quite coarse to reach levels of resolved turbulence close to LES ($f_k \leq 0.3 - 0.4$). Regarding to T_2, the values of f_k reach 0.5 in most of turbulent regions. On the other hand, when h_{min} is used, the average values for the T_1 grid are close to 0.3. This suggests, at least for flows over walls (stretched cells), an under-prediction of $(f_k)_{min}$ with h_{min}. Although the estimated values for f_k are far from LES (especially for T_1), this exercise showed that the former grids have enough resolution to resolve *part* of the turbulent energy spectrum. However, one must be careful with the time step and simulation solution time required to capture turbulence fluctuations.

4.3 Velocity Field

The velocity field obtained with RANS and DDES models with grid T_2 are depicted in figure 4. As expected, the DDES model can capture some turbulent structures since it solves part of the turbulent energy spectrum. Therefore, and considering that the statistics are not applied *a-priori*, the DDES leads to a highly unsteady velocity field instead of a constant averaged velocity, figure 5 (the steadiness of hybrid methods using grid T_1 is discussed in section 4.4). Nevertheless, velocity fluctuations and turbulent structures are not itself a guarantee of the numerical predictions quality. To that end, analysis using energy spectrum's, and auto and two-point correlations should be carried out. Figure 6 depicts a frequency power spectrum of the axial velocity at $\vec{x} = (6.0, 0.75, 0.0)$. It confirms the ability of DDES to resolve part of the turbulent energy spectrum, and shows that the simulation (DDES, T_2) reached to the inertial range (where the turbulent kinectic energy decays with -5/3). Furthermore, for frequencies larger than 10^0, it is observed a larger decay of turbulent kinetic energy. This results from the lower spatial than time resolution in this region.

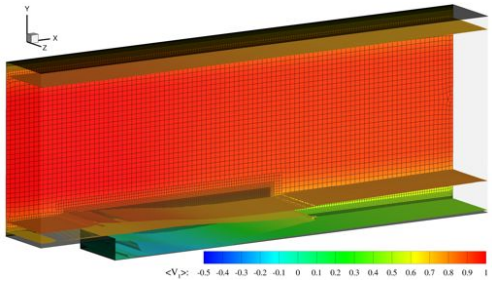

(a) RANS/URANS

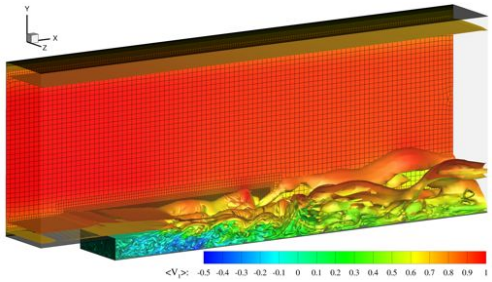

(b) DDES.

Figure 4: Axial velocity, $\langle V_1 \rangle$, flow field and vorticity (x_3 component) iso-surfaces using grid T2.

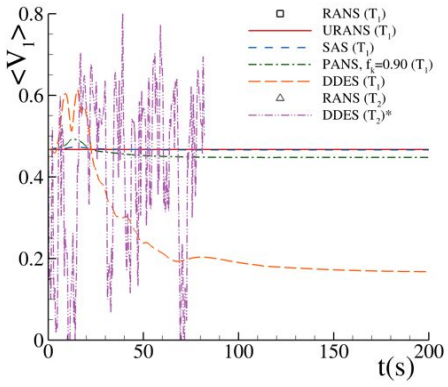

Figure 5: Time evolution of the stream-wise velocity, $< V_1 >$, at $\vec{x} = (6.0, 0.75, 0.0)$. *final 82s of simulation.

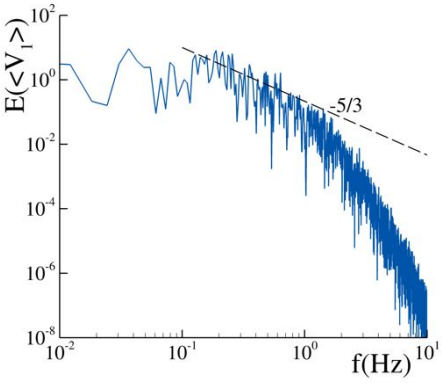

Figure 6: Frequency power spectrum of the stream-wise velocity, $< V_1 >$, at $\vec{x} = (6.0, 0.75, 0.0)$.

4.4 Friction Coefficient Profile

In order to asses the quality of the numerical results obtained with the different turbulence models, the friction coefficient profile along the lower downstream wall is compared with experimental data [7]. The results for T_1 and T_2 grids (T_2 is only used with DDES) are plotted in figure 7. These show a good agreement of RANS/URANS, SAS and DDES (T_2) models. However, for T_1, the hybrid models lead to large recirculation regions, $C_f < 0$. Furthermore, this trend tends to increase with the "theoretical" level of resolved scales (PANS $f_k = 0.95$, PANS $f_k = 0.90$ and DDES). Therefore, the results may indicate an equations "triggering" problem due to the non-use of inflow perturbations, leading to a flow "laminarization" effect. This issue does not occur in grid T_2 results. Thus, considering the topol-

ogy of grid T_2, the refinement level and the type of grid cells (isotropic) may favour the equations "triggering". Table 1 summarizes the obtained reattachment lengths, L_r/h, with RANS, URANS, SAS and DDES (T_2). The DDES method got the best agreement with the experiments. Finally, figure 8 depicts the evolution of the friction force at the bottom wall downstream the step. As for the velocity, the DDES led to a highly unsteady friction force evolution, with the fluctuations reaching 25% of the mean value. Furthermore, note that the time-step set for the DDES (T_2) computations was $0.01s$ (Courant<1) and $170s$ of simulation is, clearly, not sufficient to obtain statistical convergence.

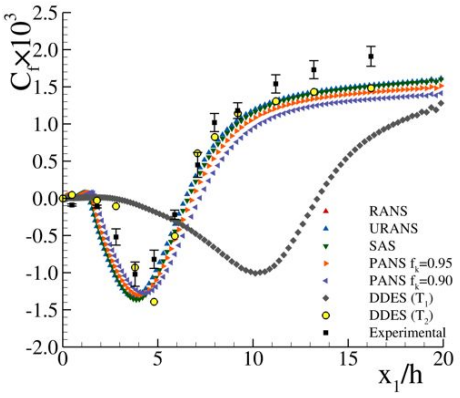

Figure 7: Friction coefficient, C_f, profile at the bottom wall downstream the step.

Table 1: Reattachment length, L_r/h. DDES result obtained with T_2

RANS	URANS	SAS	DDES	Exp
6.44	6.44	6.58	6.35	6.26 ± 0.1

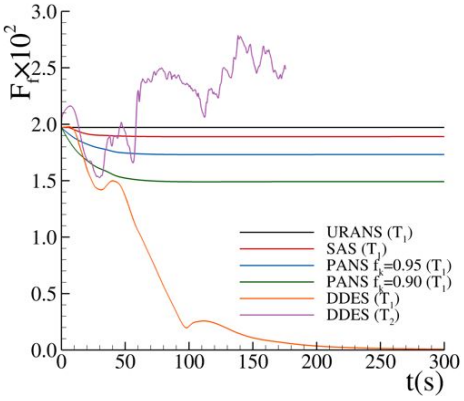

Figure 8: Time evolution of the friction force, F_f, at the bottom wall downstream the step.

5 Conclusions

The present work analyzed three different concepts to improve the accuracy of turbulent flows predictions: SAS, DDES and PANS. To this end, simulations with these models were carried out to predict the flow over a backward-facing step for a Reynolds' number of 37500. For comparison, RANS/URANS simulations were also executed.

This work started with the execution of a solution verification study with RANS (2D). It showed that for a 2D solution, the solution requires more than 1M cells to reach into the asymptotic region. Adding the estimates executed to find $(f_k)_{min}$ achievable by each grid, the correct usage of hybrid models suggests a substantial increase of the grid requirements. This is in agreement with the results obtained with these models. Although they showed their capabilities to capture turbulent structures and improve the results quality, the simulations carried out with grid T_1 (1.6M cells) show the importance of setting velocity perturbations (synthetic turbulence) at the inflow boundary. Issues as the magnitude of these perturbations, self-sustainability or synthetic methods are, currently, being addressed.

References

[1] F.R. Menter, M. Kuntz, and R. Bender. A Scale-Adaptive Simulation Model for Turbulent Flow Predictions. In *AIAA 41st Aerospace Science Meeting & Exhibit*, January 2003.

[2] F.R. Menter and Y. Egorov. The Scale-Adaptive Simulation Method for Unsteady Turbulent Flow Predictions. Part 1: Theory and Model Description. *Flow Turbulence Combust*, 85:113–138, 2010.

[3] M.S. Gritskevich, A.V. Garbaruk, J. Schütze, and F.R. Menter. Development of DDES and IDDES Formulations for the $k-\omega$ Shear Stress Transport Model. *Flow Turbulence Combust*, 88:431–449, 2012.

[4] S.S. Girimaji. Partially-Averaged Navier-Stokes Model for Turbulence: A Reynolds-Averaged Navier-Stokes to Direct Numerical Simulation Bridging Method. *Journal of Applied Mechanics*, 73:413–421, 2006.

[5] S.S. Girimaji and K.S. Abdul-Hamid. Partially-Averaged Navier-Stokes Model for Turbulence: Implementation and Validation. In *43rd AIAA Aerospace Sciences Meeting and Exhibit*, Reno, Nevada, January 2005.

[6] F.R. Menter, M. Kuntz, and R. Langtry. Ten Years of Industrial Experience with the SST Turbulence Model. *Turbulence, Heat and Mass Transfer*, 4:625–632, 2003.

[7] D.M. Driver and H.L. Seegmiller. Features of Reattaching Turbulent Shear Layer in Divergent Channel Flow. *AIAA Journal*, 23(2), 1985.

[8] G. Vaz, F. Jaouen, and M. Hoekstra. Free-Surface Viscous Flow Computations: Validation of URANS code FRESCO. In *OMAE 2009*, Hawai, USA, May 2009.

[9] S. Lakshmipathy and V. Togiti. Assessment of Alternative Formulations for the Specific-Dissipation Rate in RANS and Variable-Resolution Turbulence Models. In *20th AIAA Computational Fluid Dynamics Conference*, June 2011.

[10] 3rd Workshop on CFD Uncertainty Analysis. Lisbon, October 2008. Instituto Superior Tecnico.

[11] L. Eça and M. Hoekstra. A Procedure for the Estimation of the Numerical Uncertainty of CFD Calculations Based on Grid Refinement Studies. *Journal of Computational Physics*, 262:104–130, 2014.

Optimization of the STREAMLINE tanker using RANS/FS computations

Auke van der Ploeg, A.v.d.Ploeg@MARIN.NL

1. Introduction

In the 7th-Framework EU project "STREAMLINE" one work package was entirely devoted to the optimization of state-of-the-art propulsion. Part of the work consisted of the optimization of the aft part of the hull form and propeller of a chemical tanker that will be referred to as the 'STREAMLINE tanker'. The ship's speed is 14 knots, L_{pp}=*94m*, *B=15.4m*, the design draft is *6m* and the block coefficient is *0.786*. The Froude number is 0.237 and the full-scale Reynolds number is $6x10^8$. In this paper, we will focus on the automatic optimization of the hull form only. To mimic the constraints of a typical practical design project, the displacement was not allowed to decrease and the propeller location as well as the ship's main dimensions were fixed. Constraints to guarantee sufficient room for machinery were that section 2 (the blue line shown in Figure 1) and all sections more upstream should stay outside a box indicated by the red lines.

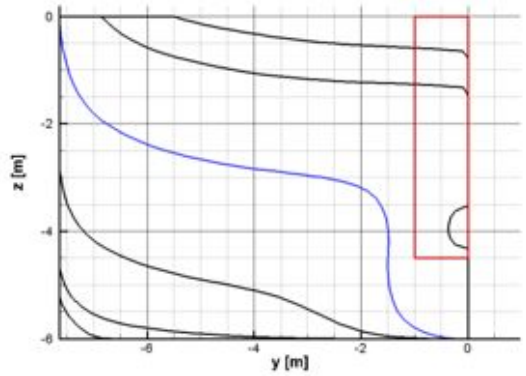

Figure 1 Body plan of the original vessel, together with the box indicating the required room for machinery.

For the aft part of ships, where the flow is often dominated by viscous effects, potential-flow solvers cannot be used, since friction and scale effects are not taken into account. Therefore, viscous flow solvers have to be used. The optimization of the STREAMLINE was done using RANS computations for full-scale Reynolds-number. The rudder was not taken into account in these computations.

During the STREAMLINE project, the RANS solver used in the automatic optimization procedures could not yet include free surface effects, and therefore, the optimization was done using double body RANS computations. In van der Ploeg, Starke and Veldhuis (2013) the ship's wave making was taken into account in a first systematic variation for the STREAMLINE tanker and the differences in the trends due to the free surface effects were studied. The main difference compared to optimization using double body computations was an extra decrease in the required power, which could be explained by a combination of an extra decrease in the nominal resistance and an extra increase in the open water efficiency. However, since the search space was the same as used in the double body optimization, the basis hull forms had relatively small changes compared to the original hull form near the water line. In this paper we describe some results that can be obtained by extending the search space with hull forms with larger changes near the water line.

2. Deformation of hull forms

The first step is to create a number of so-called basis hull forms that 'span' the design space. In our case, we have used our CAD system GMS to create these. Any design experience, for example, based on an analysis of a CFD computation for the original vessel, can be used in this step.

As a next step, parametric deformations of the geometry are obtained with the GMS-Merge tool (Hoekstra and Raven, 2003). It interpolates between the basis hull forms described above. If the basis hull forms satisfy the geometric constraints and are well chosen all variations in the design space do so, although this is not guaranteed.

The next step is to perform RANS computations for each variant. As soon as an initial optimization has been performed the parameter range can be narrowed, adapted or enlarged, based on the evaluation of all variations. The process typically proceeds in a number of consecutive steps, providing large freedom and insights in possibilities for further improvement.

3. RANS/FS method

The RANS code used is PARNASSOS, a code developed & applied by MARIN and IST (Hoekstra, 1999). It computes the steady, turbulent flow around ship hulls by solving the discretised Reynolds-averaged Navier-Stokes equations for steady, incompressible flow.

For the optimization of the STREAMLINE tanker we used Menter's one-equation turbulence model (Menter, 1997) with the Dacles-Mariani correction (Dacles-Mariani, 1995).

The inflow boundary is located $0.5L_{pp}$ in front of the bow, and the outflow boundary at $1.5L_{pp}$ behind the transom. Due to symmetry considerations, only the starboard side is taken into account. In a *(x,y,z)*-co-ordinate system fixed to the ship, with *x* positive

aft and z upward, the lateral outer boundary is a quarter of a cylinder with axis $y=z=0$ and radius $1.0L_{pp}$. At this boundary tangential velocities and pressure found from a potential-flow computation are imposed. Since that computation gives good results already for much of the wave pattern, these boundary conditions (although of Dirichlet type for the pressure) hardly cause any wave reflection.

PARNASSOS uses block-structured grids. In our case, we use a special block topology that can handle both wetted and dry transoms, and even transoms that are partly dry and partly wetted. This topology consists of four blocks (Figure 2). The block upstream of the transom contains an HO-type body-fitted grid with the usual strong contraction in wall-normal direction towards the hull in order to have y^+-values below 1 near the wall, even for full-scale computations. It has a non-conformal matching with three blocks downstream of the transom, containing HH-type grids. The grid nodes in the block immediately behind the transom are contracted towards both the symmetry plane and the free surface to get sufficient resolution near the transom. The grid consists of 3.8 million cells for all four blocks together. In (van der Ploeg and Starke, 2011) it is shown for several hull forms that with this grid density the grid dependence in the computed flow and free surface is small, and that good agreement with available measurements can be obtained.

A finite-difference discretization is used with second and third-order schemes for the various terms. The resulting system of non-linear equations is solved very efficiently with respect to both CPU-time and memory usage (van der Ploeg et al, 2000), which makes it very well suited for doing systematic variations or in combination with an optimization strategy.

3.1 Free-Surface treatment

The method is of a free-surface fitting type; the upper boundary of the computational domain coincides with (an approximation of) the wave surface all the time, and therefore needs to be updated repeatedly. Free-surface boundary conditions (FSBC's) are imposed here. If we denote the velocity components by u,v,w, the wave height by $\zeta(x,y)$, and non-dimensionalise all quantities using the ship's speed U, a reference length L_{pp}, and gravity acceleration g, the free-surface boundary conditions are:

- a kinematic condition,
$$\zeta_t + u\zeta_x + v\zeta_y - w = 0 \text{ at } z = \zeta \qquad (1)$$
- a normal component of the dynamic condition, requiring that at the surface the pressure is atmospheric ($p=0$); neglecting surface tension and viscous contributions this takes the form
$$Fn^2\psi - \zeta = 0 \quad \text{at} \quad z = \zeta \qquad (2)$$
in which $\psi=(p+\rho gz)/(\rho U^2)$ is the non-dimensional hydrodynamic pressure.

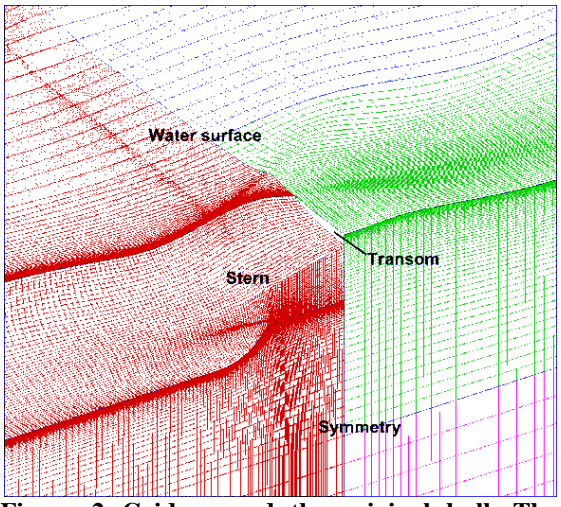

Figure 2 Grid around the original hull. The upper boundary matches the converged free surface.

- Two tangential components of the dynamic condition, requiring that no shear stress is exerted on the water surface.

By substituting the wave elevation from the dynamic condition into the kinematic condition one obtains

$$Fn^2\left(u\psi_x + v\psi_y + w\psi_z\right) - w = 0 \quad \text{at} \quad z = \zeta \qquad (3)$$

Together with the dynamic condition it describes exactly the same problem as the original set of conditions; but it has the advantage of permitting an iterative procedure solving directly the steady wave pattern without having to take into account any time dependent terms. We start with a grid of which the upper boundary matches a first estimate of the wavy surface, for example, estimated from a panel code, or simply an undisturbed water surface. Next, the following iterative method is used:

- Solve the RANS equations in which the combined condition (3) and the tangential dynamic conditions are imposed at the current estimate for the wave surface; this gives a new estimate for the wave surface.
- The new wave surface and grid are updated using the normal dynamic condition (2).

Each time after the RANS equations have been solved, corrections of trim and sinkage can be computed from the imbalance in forces and moments, and these corrections can be taken into account in the next grid update. Upon convergence the pressure deviation, normal velocity and shear stress vanish at the wave surface and the solution of the steady RANS/FS problem has been obtained.

In the present applications, the 'balanced discretization' (Raven et al, 2004) has been used, which reduces the numerical damping of the waves to 5th order in the longitudinal step size Δx, and the numerical dispersion to 3rd order in the vertical spacing Δz. This contributes to a good accuracy of the wave pattern even at a distance from the hull.

3.2 Automatic grid generation

Grids need to be generated around each variant and a fully automatic grid generation procedure is therefore required. To minimize the effect of discretization errors on the computed trends, these grids have to be as similar as possible. As a first step in the construction of the grid for a hull form variant, the wall grid for the original hull form is projected on the variant. Next, the 3D-grid is obtained using the usual grid-generation techniques: for this we use in-house developed elliptic grid generation software, which solves a Poisson equation to have maximal orthogonality of the gridlines in the interior of the computational domain. Near the boundaries, orthogonality can be controlled by the user. These settings are chosen the same for all hull forms.

4. Object functions

The choice of object functions is of crucial importance in hull form optimization projects. We use two object functions, decreasing the first minimizes fuel consumption and minimizing the second object function reduces the risk of erosive cavitation or vibration hindrance.

4.1 Object function for the required power

Minimizing the resistance only is not the best way to reduce fuel consumption, since a decrease of the resistance is often accompanied by a relatively strong decrease of the nominal wake fraction (van der Ploeg and Hoekstra, 2009), changing the point of operation of the propeller. Instead, we use an estimate of the power delivered to the propulsor:

$$P_D = \frac{R_T \times (1-w)}{1-t} \times \frac{V_S}{\eta_R \times \eta_0} \qquad (4)$$

in which R_T is the towing resistance, w the estimated effective wake fraction, V_S the ship speed, t the thrust deduction fraction, η_o the propeller efficiency in open water, and η_R the relative rotative efficiency, approximated by 1. The behind efficiency of the propeller is defined as $\eta_B = \eta_0 \times \eta_R$. It is essential to estimate η_B, as this efficiency can vary significantly between design variations. The behind efficiency could be evaluated by a coupling with a panel code for the propeller or by incorporating the propeller in the RANS computation. However, this would mean that one optimizes the hull form for the particular propeller chosen, instead of optimising both in combination. In order to estimate better the achievable performance, η_B is obtained from the B-series of propellers (Kuiper, 1992). The thrust, wake fraction, number of blades, propeller diameter and revolution rate were fixed, while the blade area ratio and pitch ratio for each hull form were found from the B-series.

The effective wake is estimated from the nominal wake using the NOMEFF tool (Gent and Hoekstra, 1985). NOMEFF calculates the change from nominal to effective wake field from the effect of an assumed axisymmetric force distribution on a nonuniform velocity field. Linearized Euler equations for unbounded flow are used, and the induction of the force field, defined as the velocities it induces in a uniform flow with an inflow speed equal to the average of the nominal field is subtracted.

To compute the thrust deduction fraction we perform a second RANS computation including a force distribution representing the propeller with an imposed thrust T_0. This imposed thrust should be a reasonable estimate of the thrust T required for self propulsion. Assuming a linear behaviour between the resistance force on the hull and T_0, the thrust deduction coefficient can then be computed from $t=(R_0-R_T)/T_0$ with R_0 the resistance force from the second RANS computation. Since the rudder is not taken into account in the RANS computations, for all hull forms the thrust deduction fractions thus obtained are increased by a fixed value.

4.2 Object function for the wake

In case of danger of erosive cavitation, one would like to prevent strong variations of the wake in circumferential direction, especially in the top half of the propeller plane. We will use the L_1-norm of the variation of

$$\beta = \tan^{-1}\left(V_x \Big/ \left(\omega \tfrac{r}{R} - V_\theta\right)\right)$$

with V_x and V_θ the axial and tangential velocity components respectively, θ the angular position in rad. and ω the propeller rotation rate in rad/s. β is the undisturbed propeller inflow angle and its variation in circumferential direction as the propeller rotates is $\partial\beta/\partial\theta$. The Wake Object Function (WOF) is determined from integration in circumferential direction and over a range of radii from the hub to the tip and the propeller radius:

$$WOF \equiv \frac{\int_{r=hub}^{r=tip} \oint_\theta \left|\frac{\partial\beta}{\partial\theta}\right| f(\theta,r)\, d\theta dr dr}{\int_{r=hub}^{r=tip} \oint_\theta f(\theta,r)\, d\theta dr dr} \qquad (5)$$

Herein f is a weighting function that can be used to make the outer region and/or the top region of the propeller more important, here defined as

$$f(\theta,r) = re^{-2(\theta-\theta_{top})^2}.$$

5. Results

The RANS/FS-study in (van der Ploeg, Starke and Veldhuis, 2013) was restricted to the same design space used in combination with RANS/DB computations and the basis hull forms had relatively small changes compared to the original

hull form near the water line. However, significant effects of taking into account the free surface can already be seen. This is illustrated in Figure 3 in which each symbol corresponds with an evaluated hull form. The more 'optimal' hull forms are closer to the lower-left corner of the chart. As can be seen from the figure, there is a set of hull forms (the Pareto front) that show the best compromise between decreasing the required power and the wake object function.

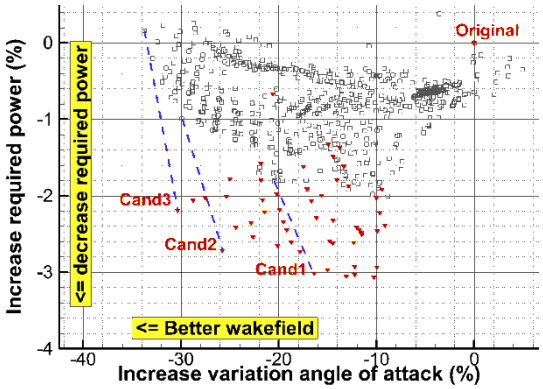

Figure 3 Pareto fronts computed both with and without wavy surface using the same design space. Grey squares: DB. Red triangles: FS.

Without taking the wavy surface into account (grey squares), the optimal hull form (Cand2) combines a 1% decrease of the required power with a decrease of 30% in the wake object function given by equation (5). When the wave making is included (red triangles), the same decrease in the wake object function can be combined with a 2.2% decrease in required power by Cand3.

Figure 4 shows the pressure on the hull for the original vessel. It appears that there is an area with low pressure near the water line just in front of the propeller plane, which causes a relatively deep wave trough. Therefore, we enlarge the design space with new hull forms, allowing larger changes near the water line

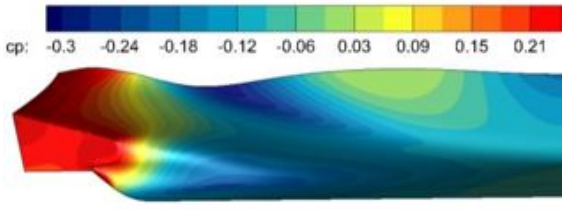

Figure 4 Pressure coefficient on the original hull form.

We have constructed two new basis hull forms that aim to reduce the wave resistance, by reducing the curvature in the geometry at this location. Those two extra basis hull forms are shown in Figure 5.

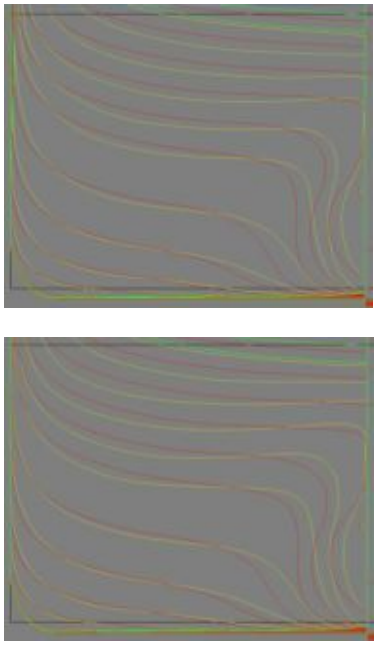

Figure 5 New basis hull forms with reduced curvature (yellow) compared to the original hull form (red).

The hull form shown in the top picture reduces the curvature in main stream direction; the one shown in the bottom picture reduces the curvature in girth wise direction. In addition, one extra basis hull form aims to increase the wetted part of the transom. A systematic variation in a four-dimensional design space was performed. Together with the three extra basis hull forms described above, one extra basis hull form was used in which the gondola was made more slender. This last basis hull form was used in the RANS/DB optimization as well. From the computed Pareto fronts shown in Figure 6 it appears that a significant extra decrease in required power can be obtained with this extension of the design space. The hull form Cand4 is the hull form on the Pareto front that shows the lowest required power and still a (slight) improvement of the wake quality.

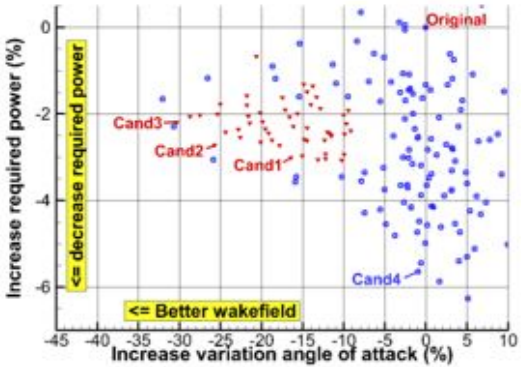

Figure 6 Pareto fronts obtained with RANS/FS. Red triangles: same design space as used for RANS/DB. Blue squares: extended design space including hull forms with larger changes near the water line.

This hull form is compared with the original hull form in Figure 7. It shows a combination of less curvature near the water line at the wave trough, a larger wetted part of the transom and a more slender gondola. Figure 8 shows that at the position near the waterline at the wave trough, indeed the pressure has increased, and Figure 9 shows that this results in a decrease of the wave trough. This figure also shows that closer to the transom, the reduced curvature along the waterline results in a significant decrease of the wave top. Along the wetted part of the transom of the Cand4 hull form, the pressure is lower compared to that of the original hull form as shown in Figure 11. A lower pressure level in itself here results in an increase of the resistance. However, the fact that the wetted area of the transom has increased compared to that of the original vessel combined with a positive pressure results in a decrease of the resistance. Overall, the (nominal) resistance R_T of the Cand4 hull form has decreased with 4.5%. Together with a decrease of the product of efficiencies $\eta_0 \times \eta_H$ this results in a decrease of the estimate of the required power of 5.6%.

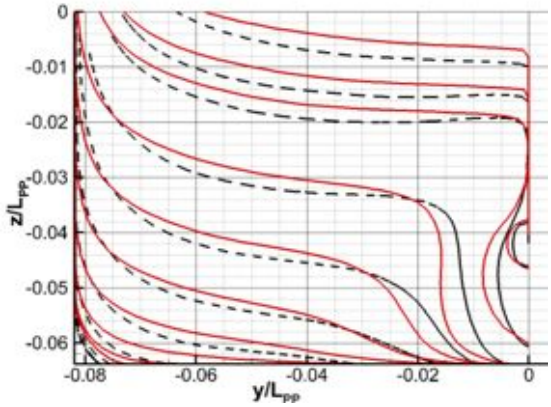

Figure 7 Hull form Cand4 (black) compared with the original hull form (red).

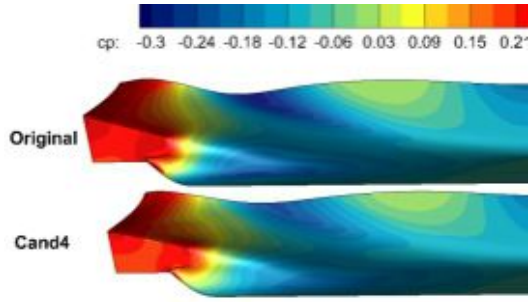

Figure 8 Pressure coefficient on the hull.

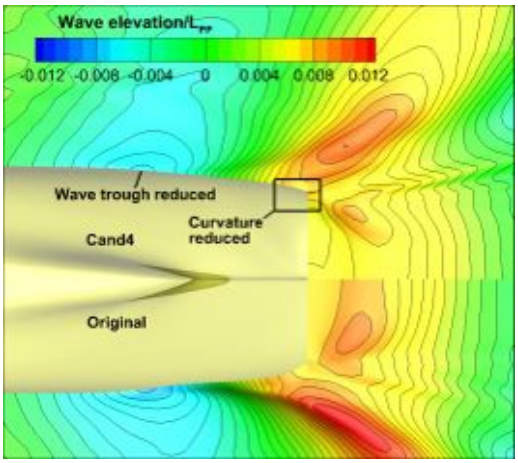

Figure 9 Stern wave systems: Top: for Cand4. Bottom: for the original vessel.

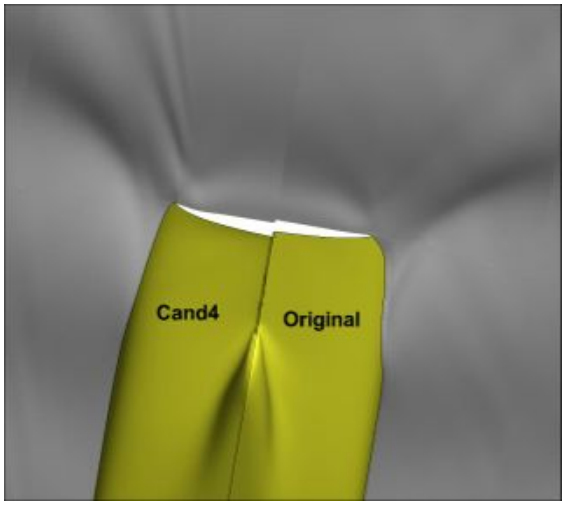

Figure 10 Fish-eye view of computed stern wave system.

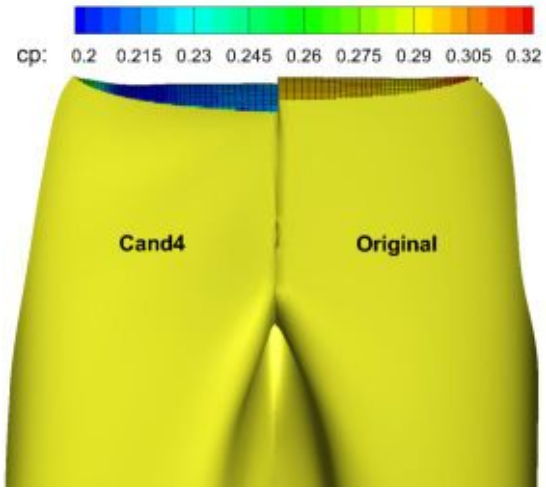

Figure 11 Pressure coefficient at the wetted part of the transom. Note that the range for the pressure only includes positive values.

6. Conclusions

We have described a procedure for doing systematic hull form variations, and evaluating each hull form with two RANS computations at full scale including the ship's wave making. In this way, we can compute trends in an estimate for the required power and in the wake quality.

The hull form variation technique described in Section 2 is defined by only a few, physically relevant, and ship-specific parameters. Hence the dimension of the search space is relatively low, which allows doing systematic variations of all parameters. The steady iterative approach described in Section 3 ensures that only a limited number of free surface updates are required, which helps to keep the required computational effort within reasonable bounds.

The computational effort for computing the data indicated by the blue symbols in Figure 6 is about one weekend on a cluster of PCs. For practical ship design projects, it is desirable to reduce this to about one night. Of course, one can always use coarser grids instead of the 3.8M-grids used in this paper. However, this is a dangerous route, as it is important that for all ingredients required for the power estimate (resistances, efficiencies, and thrust deduction fraction) computed trends are not affected by grid dependence. Therefore, in the near future we will study alternative ways to accelerate the computation: a more efficient implementation of the RANS computations by exploiting graphical processors (GPU's) present in many of today's modern PCs, and reducing the required number of hull form evaluations by using response surfaces.

For the STREAMLINE test case, we performed a first systematic variation in which we used the same design space as was used in the RANS/DB optimization. We found that if the ship's wave making is taken into account, the decrease in required power that can be obtained by hull form variation is larger than in case of evaluation with RANS/DB.

In a second systematic variation, in which the design space was enlarged with three hull forms with larger differences near the water line, it appeared that an additional decrease in required power can be obtained. A 5.6% decrease in required power was achieved, without decreasing the wake quality. We expect that using the experience from these systematic variations, other basis hull forms can be designed in such a way that a further improvement can be obtained.

References

Van Brummelen, E.H., Raven, H.C. and Koren,B., (2001), "Efficient numerical solution of steady Free-surface Navier-Stokes flow", Jnl. Computational Physics, Vol. 174, pp. 120-137.

Dacles-Mariani, J., Zilliac, G.G., Chow, J.S., and Bradshaw, P., (1995), "Numerical/ experimental study of a wingtip vortex in the near field", AIAA Jnl, Vol. 33-9, pp. 1561-1568.

Gent W. van and Hoekstra M., (1985), "Force field approach for propeller-wake interaction", MARIN Report No. 44303-7-SR.

Hoekstra M., (1999), "Numerical simulation of ship stern flows with a space-marching Navier Stokes method", Thesis, Technical University of Delft.

Hoekstra M. and Raven H.C., (2003), "A practical system for hydrodynamic optimization of ship hull forms", NAV 2003 Conference, Palermo, Italy.

Kuiper, G., (1992), "The Wageningen Propeller Series" MARIN publication 92-001. Published on the occasion of its 60th anniversary.

Menter, F.R., (1997), "Eddy-viscosity transport equations and their relation to the k-ε model", Journal of Fluids Engineering,Vol. 119, pp. 876-884.

Ploeg A. van der, Hoekstra M., and Eça L., (2000), "Combining accuracy and efficiency with robustness in ship stern flow computation", Proc. 23rd Symp. Naval Hydrodynamics, Val de Reuil, France.

Ploeg A. van der and Hoekstra M., (2009), "Multi-objective optimization of a tanker after body using PARNASSOS", Proceedings 12th NuTTs-symposium, Cortona.

Ploeg A. van der and Raven H.C., (2010), "CFD-based Optimization for Minimal Power and Wake Field Quality", Proceedings 11th International Symposium on Practical Design of Ships and other Floating Structures, Rio de Janeiro, pp. 92-101.

Ploeg A. van der and Starke, A.R., (2011), "Prediction of the transom flow regime with viscous free surface computations", International Conference on Computational Methods in Marine Engineering" Barcelona.

Ploeg A. van der, Starke, A.R and Veldhuis, C., (2013), "Optimization of a chemical tanker with free-surface viscous flow computations", Proceedings 12th International Symposium on Practical Design of Ships and other Floating Structures, Changwon City, Korea, pp. 716-723.

Raven, H.C., Van der Ploeg, A., and Starke, A.R. (2004), "Computation of free-surface viscous flows at model and full scale by a steady iterative approach", 25th Symp. Naval Hydrodynamics, St.John's, Canada.

Numerical Studies of Hydrodynamic Interactions of Two Bodies in Waves

W. Qiu, P. Wen, M. Liu and H. Peng
Faculty of Engineering and Applied Science
Memorial University, Canada

It is important to predict the hydrodynamic interaction of bodies in waves since it concerns the safe operation of vessels and offshore platforms in close proximity, such as ship replenishment and side-by-side offloading operations. There are still challenges in the prediction of low-frequency load and especially the resonant free surface elevation between two bodies. Most of the linear potential-flow based seakeeping programs currently used by the industry over-predict the free surface elevation between the vessels/bodies and hence the low-frequency loadings on the hull. This leads to problems in the design of the fenders, hawsers and loading arms and causes unsafe operations. To overcome the problems, the lid technique, in which the free surface in the gap is replaced by a flexible plate, has been developed to suppress the unrealistic values of low-frequency forces. A linear dissipation term has also been proposed to modify the free-surface equation. However, these methods would require artificial coefficients related to the flexibility of plate and the dissipation term as input in order to give reasonable predictions. Without the experimental data, it is challenging to specify the coefficients.

This paper presents the results of CFD computations for the free surface elevation with an objective to quantify the contribution of viscosity. A commercial software package, Star-CCM+, was applied to simulate the hydrodynamic interaction of the two identical box-like bodies with round corner in waves. The computed motions and wave elevations between the two bodies were compared with experimental data and the solutions by the potential-flow codes. The effect of viscosity on the free surface elevations was discussed.

17th Numerical Towing Tank Symposium (NuTTs'14), 2014.09.28-09.30, Marstrand, SWEDEN.

Development of URaNS Maneuvering Simulator and its Application to ESSO OSAKA

Nobuaki SAKAMOTO and Kunihide OHASHI
†National Maritime Research Institute (NMRI), Mitaka, Tokyo JAPAN
sakamoto@nmri.go.jp k-ohashi@nmri.go.jp

1. INTRODUCTION

Accurate prediction in maneuverability of a ship is quite important in terms of her navigational safety. International Maritime Organization (IMO) revised the standards for ship maneuverability on 2002, and it has been applied to ships in 100m in length and over, and chemical tankers and gas carriers regardless of the length[1]. On 2013, IMO has adopted guidelines for determining minimum propulsion power to maintain the maneuverability of ships in adverse conditions[2] influenced by slow steaming in order to accomplish energy saving. These standards and guidelines indicate that not only resistance and propulsion but also maneuvering characteristics must be taken into consideration at the initial design stage of a ship.

Systems-based approach has widely been utilized to estimate the maneuvering characteristics of a ship[3]. In this method, mathematical models are developed in order to represent hydrodynamic forces and moments acting on the hull and rudder, propeller thrust, propeller/rudder inflow and necessary interaction coefficients, e.g. coefficient of flow straightening, coefficient of increasing rudder force and so on[4]. Although systems-based approach is practical and easily-used, it usually requires dozens of captive and/or dynamic planer motion mechanism (PMM) tests to determine hydrodynamic derivatives of a target ship. Empirical, in other words, database method may contribute to reduce the number of PMM tests, yet its accuracy is questionable when the database is not sufficient enough to cover the dimensions of a target ship. Viscous Computational Fluid Dynamics (CFD) may able to alternate PMM tests[5] and to contribute estimating necessary interaction coefficients, but dozens of simulations are still necessary to obtain input data for systems-based approach.

Direct maneuvering simulations using viscous CFD greatly reduce these experimental/computational costs as well as assumptions for developing mathematical models. Once the equations of motions (EoMs) for a ship utilize time-accurate hydrodynamic forces and moments obtained from Navier-Stokes (NS) equation, it is not necessary to calculate hydrodynamic derivatives. As long as the propeller is numerically represented (e.g. body force or fully discretized), rudder inflow is also a solution from NS equation and thus its modeling and estimations of interaction coefficients are unnecessary. Such approach has been reported by Broglia et al. (2012)[6] and Carrica et al. (2013)[7], both adopt overset grid for computation, and show encouraging results although CPU hours are longish.

Based on these backgrounds, the present research aims to develop simple (but still direct) maneuvering simulator based on unsteady Reynolds-averaged NS (URaNS) solver. Hull and rudder motions are treated by moving grid technique instead of overset grid. The code is applied to estimate turn and zig-zag maneuvers of ESSO OSAKA tanker, and the results are compared with the available sea trial data.

2. COMPUTATIONAL METHOD

2.1 Governing equation and discretization

The viscous CFD solver utilized in the present study is SURF, the finite volume and unstructured grid based URaNS/Detached Eddy Simulation (DES) solver for ship hydrodynamics developed by CFD research group at NMRI[8]. The governing equations are the continuity and URaNS equations. These are non-dimensionalized by the fluid density ρ, the fluid kinematic viscosity ν, the characteristic length L_{pp}, and the characteristic velocity U_0. For the use of artificial compressibility approach in the velocity-pressure coupling in unsteady flow calculations, pseudo time step τ is utilized in order to satisfy divergence-free condition at each physical time step t. In consequence, the equations to be solved are

$$\frac{\partial}{\partial t}\iiint_{V_i}\mathbf{q}dV+\frac{\partial}{\partial \tau}\iiint_{V_i}\mathbf{q}^*dV + \oint_{\partial V_i}\left\{\left(\mathbf{e}-\mathbf{e}^v\right)n_x+\left(\mathbf{f}-\mathbf{f}^v\right)n_y+\left(\mathbf{g}-\mathbf{g}^v\right)n_z\right\}dS=0 \tag{1}$$

where V_i is a control volume (=cell i), $[n_x, n_y, n_z]^T$ is the unit normal vector for each faces of cell i, **q** and **q*** are the flow variable vectors, **e**, **f**, **g** are the inviscid flux vectors and $\mathbf{e}^v$, $\mathbf{f}^v$, $\mathbf{g}^v$ are the viscous flux vectors. Inviscid flux vectors are described as

$$\begin{aligned}
&\mathbf{q}=[0,u,v,w]^T,\mathbf{q}^*=[p,u,v,w]^T\\
&\mathbf{e}=\left[\beta u,u\left(u-u_g\right)+p,u\left(v-v_g\right),u\left(w-w_g\right)\right]^T\\
&\mathbf{f}=\left[\beta v,v\left(u-u_g\right),v\left(v-v_g\right)+p,v\left(w-w_g\right)\right]^T\\
&\mathbf{g}=\left[\beta w,w\left(u-u_g\right),w\left(v-v_g\right),w\left(w-w_g\right)+p\right]^T
\end{aligned} \tag{2}$$

where β is the artificial compressibility parameter and $[u_g, v_g, w_g]^T$ is the grid velocity vector which accounts for motions of the grid during a simulation. Turbulence is modeled by Spalart-Allmaras model, and free surface is modeled by single-phase level-set method although free surface is not taken into account in the present study. The effect of propeller is represented by body force model based on infinite-bladed propeller theory.

Inviscid fluxes in momentum and turbulence transport equations are evaluated by the 2nd-order upwinding scheme based on the flux-difference splitting of Roe, and 1st-order upwinding scheme, respectively. Viscous fluxes appeared in momentum and turbulence transport equations are evaluated by the 2nd-order central differencing scheme. Temporal discretization is accomplished using 2nd-order Euler backward differencing scheme with fully implicit manner.

2.2 Treatment of rudder motion

Rudder motion is treated in such a way that the grid deformation due to steering is restricted in the rudder vicinity. In practice a certain deformation region is determined as the input data to the simulation where longitudinal center of rudder rotation is located at aft perpendicular (AP). Inside the deformation region, each cell node has a certain weight varying from 0 to 1, and local grid morphing is carried out accordingly. Figure 1 presents the typical example of the region for local grid morphing around a rudder.

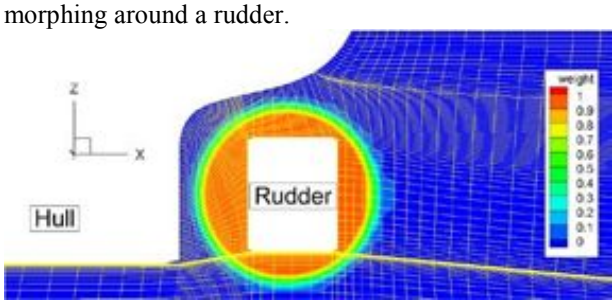

Fig. 1 Example of the region for local grid morphing around a rudder

2.3 Treatment of ship motion

Different from the treatment of rudder motion, the whole computational domain moves following ship motions. This means that the boundary condition (BC) in terms of velocity at body surface is the same as the motion velocity of the hull, in the meantime, the velocity BC at inflow is zero. Figure 2 shows the computational procedure by taking both rudder and ship motions into account.

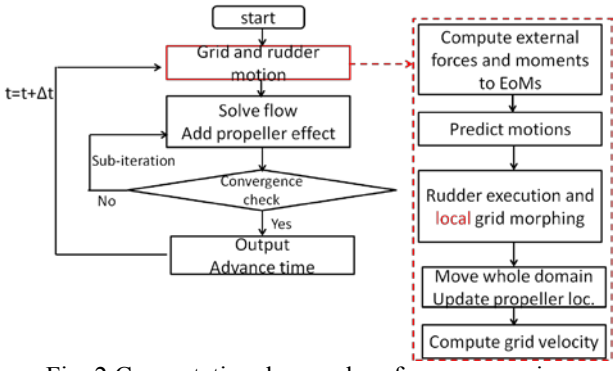

Fig. 2 Computational procedure for maneuvering simulation (EoMs are weakly coupled with RaNS.)

The ship is allowed to have 3 degrees of freedom (DOF), i.e. surge, sway and yaw. The non-dimensional forms of their EoMs are

$$\ddot{x} = \frac{1}{\nabla}\left(Ctx + Ctx_{prop.} - SFC\right)$$
$$\ddot{y} = \frac{1}{\nabla}\left(Cty + Cty_{prop.}\right) \quad (3)$$
$$\ddot{r} = \frac{1}{I_{zz}}\left(Cnz + Cnz_{prop.}\right)$$

where ∇ is the non-dimensional volume of the hull, I_{zz} is the non-dimensional moment of inertia around z-axis, [Ctx, Cty, Cnz] are the coefficients of hydrodynamic forces (surge and sway) and moment (yaw) acting on hull and rudder, [$Ctx_{prop.}$, $Cty_{prop.}$, $Cnz_{prop.}$] are the coefficients of hydrodynamic forces (surge and sway) and moment (yaw) due to propeller thrust, and SFC is the skin friction correction in case that the self-propulsion point is set to ship point. Notice that the present simulations are all carried out at model-point, and thus the SFC is set to zero.

Equations of motions are weakly coupled with URaNS equations and solved numerically using 2nd-order Adams-Bashforth scheme.

3. SIMULATION DESIGN

3. 1 Geometry and test cases

Figure 3 shows the overview of the hull and rudder of ESSO OSAKA as well as its major dimension (Simonsen and Stern 2005[9]; Skejic and Faltinsen 2008[10]). This hull has been recognized as one of the most popular benchmark cases for maneuvering prediction since its geometry and several sea trial data are open to public (ITTC 2002)[11]. Among all accessible sea trial data, two of them are of the interest in the present study: 1) Turning circle maneuver and 2) 10°/10° and 20°/20° zig-zag maneuvers.

Due to the limitation of the present grid morphing scheme to handle steering, it is necessary to cordon a certain gap between overhang part of the stern and rudder top. In order to make this gap, the original rudder is slightly shrunk in z-direction and translated in x-z plane maintaining the sectional geometry of the rudder. This results in 19% of decrease in rudder area and the amount of translation in x and z directions are +0.3%L_{pp} and -0.2%L_{pp}, respectively, as shown in Fig. 3.

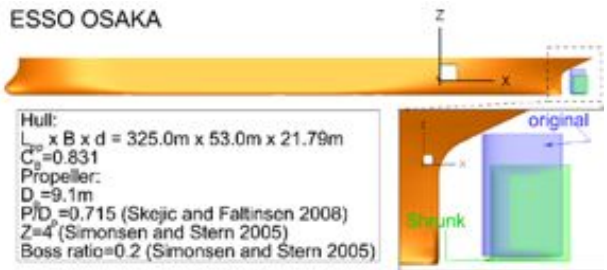

Fig. 3 Geometry of ESSO OSAKA

3. 2 Computational set up

Table 1 summarizes the common input parameters among the present simulations. All the simulations are carried out in model-scale. The propeller rotation speed is non-dimensionalized by L_{pp} and U_0, and is kept constant during the simulation. The same characteristics

length and velocity are utilized to non-dimensionalize helm rate. The non-dimensional time step Δt for time advancement in RaNS and EoMs is set to 0.01.

Table 1 Common input parameters

Parameter	Value	Reference
Rn	3.609E+06	Simonsen and Stern (2005)
Prop. rev.	54.077[-]	
Helm rate	1.723[rad]	Skejic and Faltinsen (2008)
Δt	0.01[-]	-

Figure 4 shows the coordinate system used for the present CFD simulations. All the transport equations and ship motions in the code are based on the inertial earth-fixed coordinate system x_E-y_E-z_E (termed earth-system hereafter). The coordinate is right-handed side, e.g. x positive from forward perpendicular (FP) to aft perpendicular (AP), y positive from port to starboard and z positive from keel to deck. The positive direction of rotation in x_Ey_E-plane is counter-clockwise observing from deck. Non-inertial ship-fixed coordinate system x_s-y_s-z_s (termed ship-system hereafter) is attached to the center of gravity (CoG) of the ship (x_G, y_G, z_G) whose positive directions of translation and rotation are coincident with earth-system. Figure 5 presents the computational grid in the hull vicinity. The grid has HO topology and consists of structured cells for which the total number of cells is approximately 0.88M.

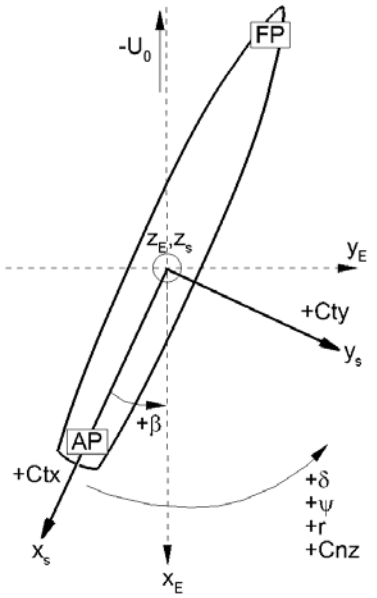

Fig. 4 Coordinate system for the present CFD simulations

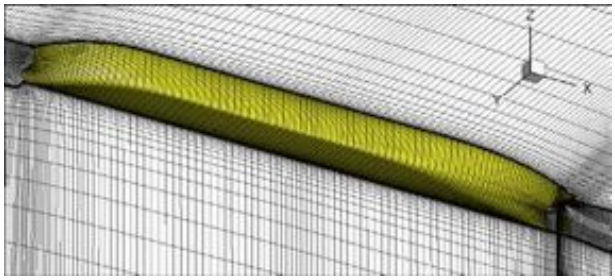

Fig. 5 Computational grid in the vicinity of the hull

4. RESULTS AND DISCUSSIONS

4. 1 ±20° turning circle maneuver

Due to difficulty in grid deformation with 35° of rudder deflection, the steering angle for the turning circle simulation is set to ±20°. Since the rudder angle is set to 35° in the sea trial data, the computational results cannot directly be compared with them and only qualitative discussions can be made. Table 2 summarizes the computational results of turning ability, e.g. advance (A_D) and the tactical diameter (D_T) non-dimensionalized by L_{pp}. Figure 6 shows the computational results of the time history of Ctx, Cty and Cnz. Figures 7 and 8 summarize the computational and sea trial results of trajectory, speed loss and rate of turn which are all non-dimensionalized by L_{pp} and U_0.

For port side turning (PT), A_D and D_T are approximately 12% and 14% smaller, respectively, compared to those of starboard side turning (ST) which is well known trend for a ship with single-screw and single-rudder[12]. In Fig. 7, longitudinal center of turning is similar between ST and PT while lateral center of turning is larger for ST than PT. These are reasonable physics in connection to Fig. 6 in a sense that the mean value of Ctx is almost the same between ST and PT while the mean value of Cty is slightly larger for ST than PT.

Table 2 Summary of turning ability: CFD only, δ=±20deg.

	A_D/L_{pp}	D_T/L_{pp}
Starb.turn (δ=+20deg.)	3.98	4.77
Port turn (δ=-20deg.)	3.52	4.08

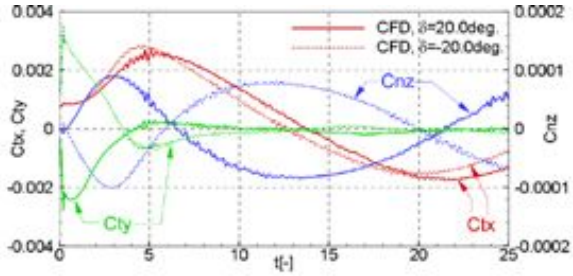

Fig. 6 Computational results of the time history of hydrodynamic forces and moment coefficients for 20° turning circle maneuver

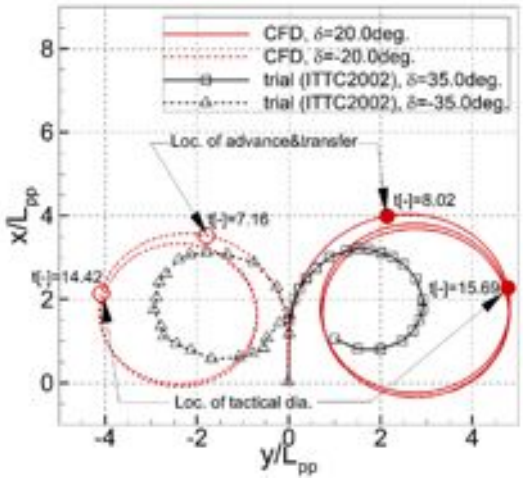

Fig. 7 Trajectory of turning circle maneuver: CFD (δ=±20deg.) vs Sea trial (δ=±35deg.)

The speed loss becomes constant as Cty becomes constant at t~11.0. The computational results show that the speed loss is 1% larger for PT than that of ST since the turning radius is smaller for PT than that of ST. In the sea trial data such difference cannot be observed since the turning radius is likely to be the same between PT and ST. The rate of turn somewhat converges to the same value (~±0.2) between computational results and sea trial data although the δ is different between the two.

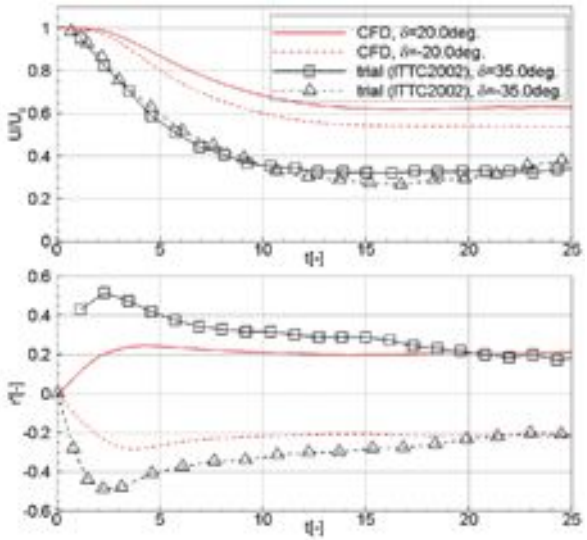

Fig. 8 Speed loss (top) and rate of turn (bottom) of turning circle maneuver:
CFD (δ=±20deg.) vs Sea trial (δ=±35deg.)

4. 2 10°/10° and 20°/20° zig-zag maneuvers

Table 3 summarizes the yaw checking ability, e.g. 1st and 2nd overshoot angles (OSA) and non-dimensional time to reach 1st and 2nd OSAs, between the computational results and sea trial data. Figure 9 shows the computational result of the time histories of Ctx, Cty and Cnz for 10°/10° zig-zag maneuver. Figures 10a, 10b, 10c and 10d present the computational and sea trial results of yaw angle, rate of turn, speed loss and drift angle for 10°/10° zig-zag maneuver. Notice that only the computational result is shown for the time history of rudder motion. Figure 11 shows the computational results of time series of vortical structure in the stern vicinity during 2nd execution of the rudder for 10°/10° zig-zag maneuver depicted by the 2nd invariant of the rate of deformation tensor (termed **Q** hereafter). Figures 12, 13 and 14 are the same as Figs. 9, 10 and 11 but the condition of maneuver is 20°/20° zig-zag.

In the yaw checking ability the computational results generally agree well with the sea trial data for 10°/10° zig-zag maneuver, although the 2nd OSA is underestimated in comparison to the sea trial data. For 20°/20° zig-zag maneuver, both 1st and 2nd OSAs are very well predicted in comparison to the sea trial data, yet $T_1{}^{st}{}_{OS}$ and $T_2{}^{nd}{}_{OS}$ show phase lag to the sea trial data. There are two possible reasons to cause such discrepancy; 1) the rudder area used for the computation is 19% smaller than that of the prototype which yields less yaw moment and thus results in the delay of response in ship motion to the steering and 2) the grid resolution in the stern vicinity is not fine enough to capture the complex flow physics corresponding to the large helm which causes inaccurate estimation in forces and moments acting on rudder (and possibly on the stern region). In terms of rate of turn, computational results are satisfactory for both zig-zag maneuvers compared to the sea trial data, but the phase lag is still apparent in 20°/20°. For the speed loss, computational results are also satisfactory for both zig-zag maneuvers yet the simulation takes more time than the sea trial to reach final speed. The computational results of drift angle tends to follow the trend of the sea trial data, but the phase lag relative to the sea trial data becomes apparent in connection to the phase lag of the yaw angle especially at 20°/20°. The time series of vortical structure in the stern vicinity show two major vortex systems; one is at stern region above the rudder (V1), and the other is at the downstream of starboard side rudder (V2) as shown in Figs. 11 and 14. The V1 is likely to be generated by the ship motion and moves together with the hull, while the V2 is due to steering and resultant massive flow separation. Comparing between Fig. 11 and Fig. 14, the V2 tends to merge the V1 as the steering angle becomes larger. In terms of accurate prediction in forces and moments acting on hull and rudder, it would be crucial to resolve both V1 and V2 and its unsteady behavior.

5. CONCLUDING REMARKS

Maneuvering simulator is developed based on URaNS solver SURF with moving grid technique. The steering is treated by local grid morphing while the whole computational domain moves for the treatment of ship motions. The code is applied to solve turn (δ=±20°) and 10°/10° and 20°/20° zig-zag maneuvers for ESSO OSAKA, then the results are compared with the available sea trial data.

The computational results of turning circle maneuver qualitatively capture the trend of difference between starboard side turning and port side turning. Instead of present grid morphing technique around a rudder, the use of spring network method[13] or overset grid will accurately reproduce rudder area which will make it possible to estimate turning ability of the present ship without limitation in steering angle.

The computational results of 10°/10° zig-zag maneuver generally agree well with the sea trial data. Once the steering angle becomes 20°/20°, the phase lag becomes apparent in yaw angle, rate of turn and drift angle. Two possible reasons for this discrepancy are the lack of rudder area and grid resolution in the rudder/stern vicinity to capture vortices originated from hull and steering motions. These will be improved by changing the treatment of rudder motion as previously mentioned, and by selecting appropriate turbulence models with much finer grids.

ACKNOWLEDGMENT

This work is supported by MEXT Grant-in-Aid for

Young Scientist (B) #24760680. The hull and rudder geometries are provided by Dr. Simonsen at FORCE TECHNOLOGY which is greatly appreciated.

REFERENCES

1) Standards for ship manoeuvrability, 2002, Resolution MSC. 137(76), IMO.
2) 2013 Interim guidelines for determining minimum propulsion power to maintain the manoeuvrability of ships in adverse conditions, ANNEX 16, Resolution MEPC.232(65), IMO.
3) Stern, F., Agdrup, K., Kim, S.Y., Hochbaum, A.C., Rhee, K.P., Quadvlieg, F., Perdon, P., Hino, T., Broglia, R. and Gorski, J., 2011, Experience from SIMMAN 2008-The First Workshop on Verification and Validation of Ship Maneuvering Simulation Methods, Journal of Ship Research, Vol. 55, No. 2., pp.135-147.
4) Japan Society of Naval Architects and Ocean Engineers (JASNAOE), 2012, Final Report of the Research Committee on Standardization of Mathematical Model for Ship Maneuvering Predictions(In-Japanese), http://www.jasnaoe.or.jp/research/p_committee_end.html
5) Sakamoto, N., Carrica, P.M. and Stern, F., 2012, URANS simulations of static and dynamic maneuvering for surface combatant: part 1. Verification and validation for forces, moment and hydrodynamic derivatives, Journal of Marine Science and Technology, Vol. 17, 4, pp. 422-445.
6) Broglia, R., Dubbioso, G., Durante, D. and Di Mascio, A., 2012, Simulation of turning circle by CFD: Analysis of different propeller models and effect on manoeuvring prediction, Applied Occean Research, Vol. 39, pp. 1-10.
7) Carrica, P.M., Ismail, F., Hyman, M., Bhushan, S. and Stern, F., 2013, Turn and zigzag maneuvers of a surface combatant using a URANS approacj with dynamic overset grids, Journal of Marine Science and Technology, Vol. 18, 2, pp. 166-181.
8) Hino T., 1997, "A 3D unstructured grid method for incompressible viscous flows", Journal of the Society of Naval Architects of Japan, Vol. 182, pp.9-15.
9) Simonsen, C.D. and Stern, F., 2005, RANS Maneuvering Simulation of Esso Osaka With Rudder and a Body-Force Propeller, Journal of Ship Research, Vol. 49, No. 2, pp. 98-120.
10) Skejic, R. and Faltinsen, O.M., 2008, A unified seakeeping and maneuvering analysis of ships in regular waves, Journal of Marine Science and Technology, Vol. 13, pp. 371-394.
11) The Specialist Committee on Esso Osaka, 2002, Final Report and Recommendations to the 23rd ITTC, Proc. 23rd ITTC Vol. II, pp. 581-743.
12) Yasukawa, H., and Yoshimura, Y., 2012, Ship Motions -Maneuvering Characteristics- (in Japanese), Seizando Publisher, ISBN978-4-425-71451-3.
13) Jacquin, E., Guillerm, P.E., Drouet, A., Perdon, P. and Alessandrini, B., 2006, Simulation of unsteady ship maneuvering using free-surface RANS solver, Proc. 26th Symposium on Naval Hydrodynamics, Rome, Italy.

Table 3 Summary of yaw checking ability: CFD vs Sea trial

10°/10° zig-zag				
	1st OSA	$T_1{}^{st}{}_{OS}$[-]	2nd OSA	$T_2{}^{nd}{}_{OS}$[-]
Sea trial	4.21°	3.40	13.34°	8.61
CFD	3.13°	3.94	8.19°	8.67
20°/20° zig-zag				
Sea trial	8.93°	3.26	13.25°	8.02
CFD	9.36°	4.29	13.66°	10.62

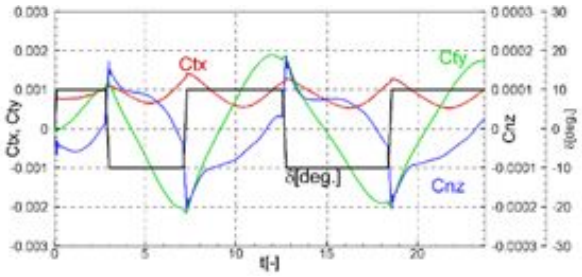

Fig. 9 Computational result of the time histories of hydrodynamic forces and moment coefficients and rudder motion for 10°/10° zig-zag maneuver

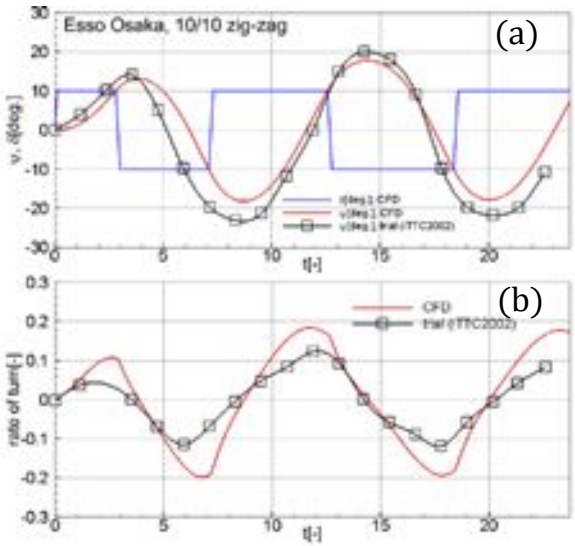

Fig. 10 Computational and sea trial results of 10°/10° zig-zag maneuver: a) yaw and rudder angles, b) rate of turn

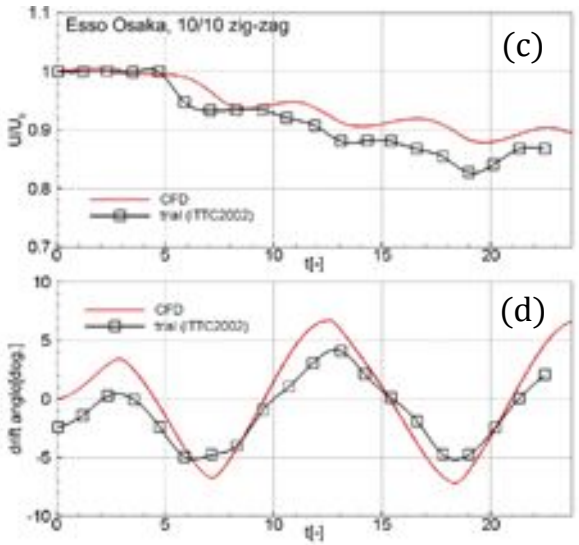

Fig. 10 Cont., c) speed loss and d) drift angle

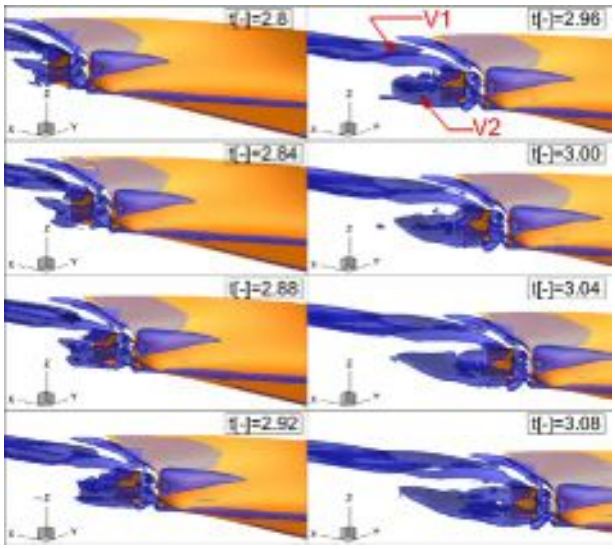

Fig. 11 Time series of vortical structure in the stern vicinity at 2nd execution of rudder for 10°/10° zig-zag maneuver (2.8<t[-]<3.08) depicted by Q=30 iso surface

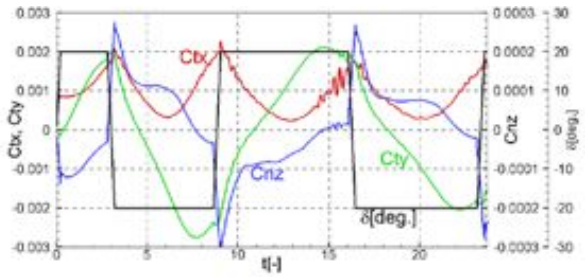

Fig. 12 Computational results of the time history of hydrodynamic forces and moment and rudder motion for 20°/20° zig-zag maneuver

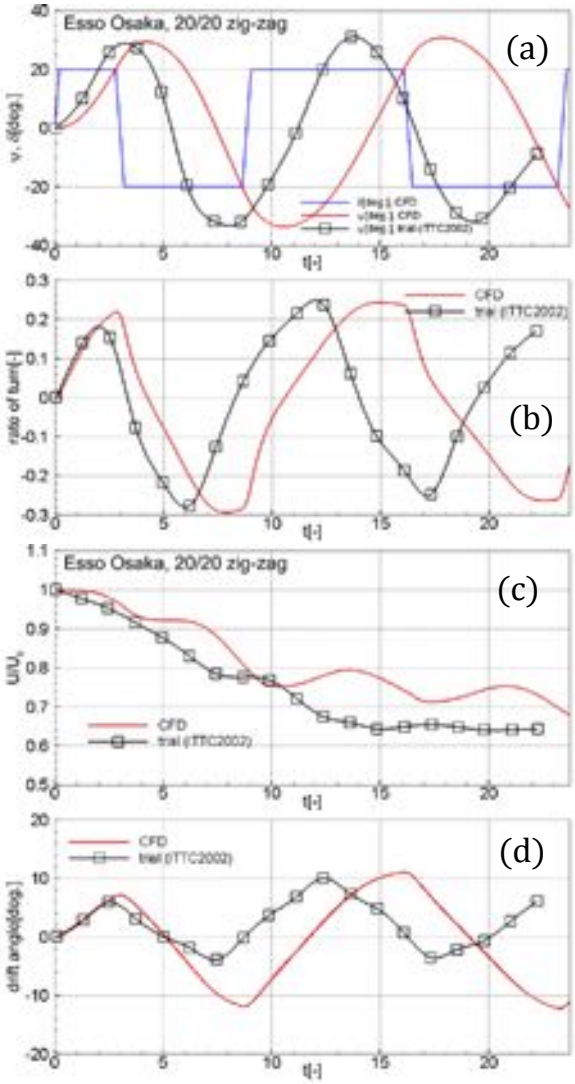

Fig. 13 Computational and sea trial results of 20°/20° zig-zag maneuver: a) yaw and rudder angles, b) rate of turn, c) speed loss and d) drift angle

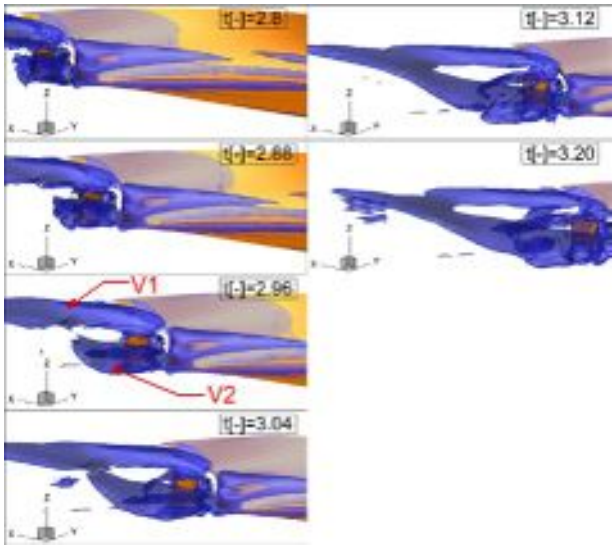

Fig. 14 Time series of vortical structure in the stern vicinity at 2nd execution of rudder for 20°/20° zig-zag maneuver (2.8<t[-]<3.36) depicted by Q=30 iso surface

ADJOINT-BASED SHAPE OPTIMISATION APPLIED TO THE BOW OF A BULK CARRIER

Lars-Uve Schrader[1]
HSVA Hamburg Ship Model Basin, Hamburg, GERMANY

Introduction. When sailing at design speed and draught, full-form ships (e.g. bulk carriers) create waves with a high crest at the bow followed by a deep trough at the forward shoulders of the ship hull (Fig. 1). This wave formation accounts for most of the wave drag of such vessels. Therefore, hydrodynamic optimisation studies for blunt vessels often focus on the shape of the bulbous bow and the forward shoulders. Numerical investigations are usually based on an efficient flow solver (e.g. a potential-flow method) along with a certain design search procedure (e.g. a genetic algorithm). Several hundred different hull forms may be compared to each other by this approach so as to find an 'optimal' hull shape w.r.t. a certain design objective (e.g. minimum drag). However, in conjunction with more refined and costly flow simulations (e.g. RANS computations), this approach is no longer feasible. In such cases adjoint optimisation methods represent an attractive alternative.

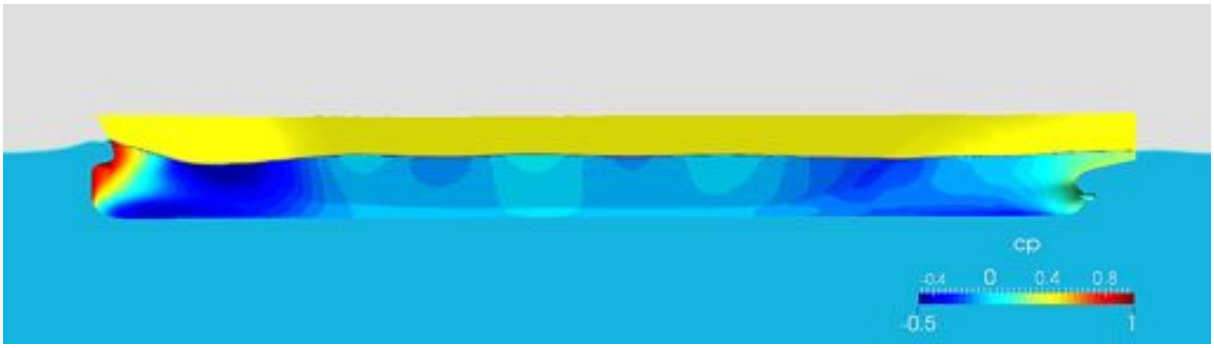

Figure 1. Pressure distribution and wave profile along the hull of a Handysize bulk carrier sailing at 14 knots in calm waters

Adjoint-based shape optimisation. Hydrodynamic form optimisation of ship hulls deals with finding appropriate shape deformations δn in order to drive a certain cost function J (e.g. the hull resistance) towards a local optimum where $\delta J = 0$. Adjoint methods offer an efficient way to establish the relationship between δJ and δn, expressed in terms of the shape sensitivity gradient G as $\delta J = (G, \delta n)_{\Gamma_{hull}}$. Γ_{hull} is herein the hull surface, and the notation $(a, b)_C = \int_C a \cdot b \, \mathrm{d}c$ is used. Since the velocity and pressure perturbations v_i' and p' induced by the hull surface shifts δn are required to satisfy the equations of fluid motion, the optimisation task is stated as a constrained problem (Lagrange multiplier method), with L being the augmented cost function (Lagrangian),

$$\delta L = 0 = \delta J + \left(v_i^*, R_i'\right)_\Omega + \left(p^*, \partial v_i'/\partial x_i\right)_\Omega . \tag{1}$$

δJ and δL are the variations of the cost function and the Lagrangian, x_i denote the three spatial directions in the flow domain Ω, and R_i' are the residuals of the linearised RANS equations governing the flow perturbations v_i' and p'. The quantities v_i^* and p^* play the role of the Lagrange multipliers associated with the constraints (second and third terms on the r.h.s. of Eq. 1), where v_i^* and p^* represent the adjoint counterparts of v_i' and p'. The constraints in (1) ensure that the shift-induced flow perturbations constitute a divergence-free solution to the linearised flow equations.

[1]Schrader@hsva.de

Next, $\delta L = \delta L(v_i', p', v_i^*, p^*) = 0$ is written out,

$$\delta L = 0 = \left(\frac{\partial L}{\partial v_i'}, \delta v_i'\right)_\Omega + \left(\frac{\partial L}{\partial p'}, \delta p'\right)_\Omega + \left(\frac{\partial L}{\partial v_i^*}, \delta v_i^*\right)_\Omega + \left(\frac{\partial L}{\partial p^*}, \delta p^*\right)_\Omega . \tag{2}$$

Eq. (2) is in general fulfilled only if all terms on the r.h.s. vanish independently. The third and fourth terms become zero by virtue of the linearised RANS equations and the continuity condition, $R_i' = 0$ and $\partial v_i'/\partial x_i = 0$. Integrating Eq. (1) by parts,

$$\delta L = \delta J + \left(v_i', R_i^*\right)_\Omega + \left(p', \partial v_i^*/\partial x_i\right)_\Omega + (\text{boundary terms}),$$

reveals that the first two terms on the r.h.s. of (2) can be eliminated by satisfying the adjoint RANS equations and the adjoint continuity condition, $R_i^* = 0$ and $\partial v_i^*/\partial x_i = 0$, along with appropriate boundary conditions (see Ref. [1] for the detailed form of the adjoint system). Moreover, a relation for the shape sensitivity G is obtained [1],

$$G = -(\mu + \mu_T)\frac{\partial V_t}{\partial n}\frac{\partial v_t^*}{\partial n}\left(t_i t_i^*\right), \tag{3}$$

where μ and μ_T are the molecular and turbulent viscosities. The components V_t and v_t^* of the mean velocity and the adjoint perturbation act along the surface-tangential unit vectors t_i and t_i^*, defined as $t_i = n_j \bar{S}_{ij}$ and $t_i^* = n_j \bar{S}_{ij}^*$ with $\bar{S}_{ij}$ and $\bar{S}_{ij}^*$ denoting the normalised strain tensor and its adjoint counterpart [2]. The cost function J appears either as a boundary condition or as a volumetric forcing term of the adjoint system [1] – depending on whether J is defined on a boundary (e.g. drag force) or in the interior of the flow domain (e.g. wave energy).

In summary, the constrained shape optimisation problem stated in Eq. (1) is equivalent to (i) solving the mean-flow equations, (ii) evaluating the cost function, (iii) solving the adjoint flow equations, (iv) computing the shape sensitivity and (v) executing normal hull-surface shifts in proportion to the local sensitivity gradient (Fig. 2). These shifts need to be small to justify the linearisation in the derivation of the adjoint system. Steps (i)-(v) are repeated iteratively until a local optimum of the cost function has been found. The free water surface is kept unchanged during the adjoint simulations, i.e. its variation is neglected within one iteration of the optimisation procedure ('frozen free-surface treatment'). After executing the hull deformations, the free interface is allowed to adjust to the new flow conditions in the next iteration. This approach is analogous to the 'frozen-turbulence treatment' commonly used in the context of adjoint RANS methods [2].

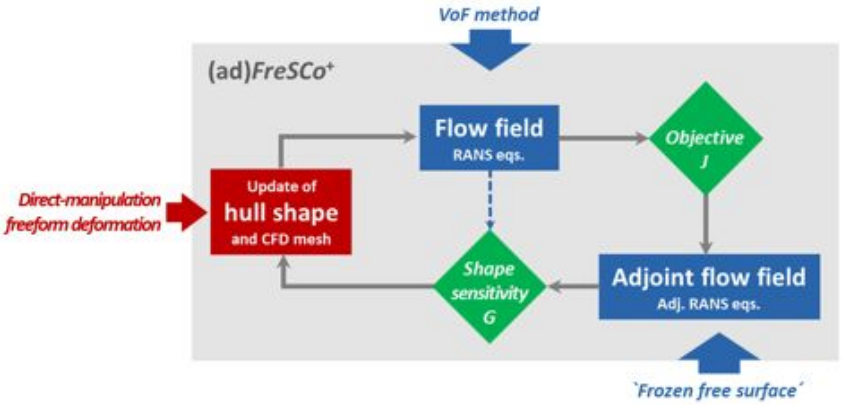

Figure 2. Hydrodynamic shape optimisation using an iterative adjoint procedure. The implementation (ad)$FreSCo^+$ developed by Hamburg University of Technology (TUHH) and HSVA is used here (see Ref. [1] for details of (ad)$FreSCo^+$ and Refs. [2, 3] for applications to ship hulls). The shape of the free surface is 'frozen' in the adjoint simulation and adjusted to the updated hull shape in the subsequent forward simulation.

Table 1. Length, breadth, draught, speed and Froude number of the Handysize bulk carrier considered

L_{pp} [m]	B [m]	T_m [m]	V_S [kts]	Fr [-]
172.0	30.0	10.5	14.0	0.175

Application. An adjoint-based shape optimisation study of a Handysize bulk carrier (Tab. 1) is reported, using the implementation (ad)$FreSCo^+$ by Hamburg University of Technology (TUHH) [1] and HSVA. The package (ad)$FreSCo^+$ consists of the viscous free-surface flow solver $FreSCo^+$ based on the RANS equations and a VoF method, the adjoint RANS equation solver ad$FreSCo^+$ and a freeform deformation module for the execution of the hull shape modifications (see Fig. 2). The study aims to reduce the wave resistance of the bulk carrier through a modification of the fore ship. The following cost function is considered,

$$J_w = \frac{1}{W_{ref}^2 \Omega_{wet}} \int_{\Omega_f} c_w W^2 \, \mathrm{d}\Omega, \tag{4}$$

where $$\Omega_{wet} = \int_{\Omega_f} c_w \, \mathrm{d}\Omega \qquad \text{and} \qquad W_{ref} = U_{ship} \tan(\alpha_{bw})$$

are used for normalisation. W is the vertical mean flow component, and W_{ref} serves as a reference based on the ship speed U_{ship} and the bow-wave angle α_{bw}. Ω_f is an upstream localised volume encompassing the free surface (shown in white in Fig. 3a), with Ω_{wet} being the wet portion of Ω_f, and c_w denotes the water concentration. The cost function J_w measures the vertical kinetic energy in the wet flow region stretching from the wave crest at the bow to the wave trough at the forward shoulders. The optimisation task consists in minimising J_w so as to reduce the free-surface elevation, leading to diminished wave drag. Since J_w is solely defined in the fore-ship region, the shape modifications will affect the bow wave and the wave trough at the fore shoulders only. Note that J_w is volume-based and therefore appears as a volumetric forcing term of the vertical adjoint momentum equation (Fig. 3b).

(a) (b)

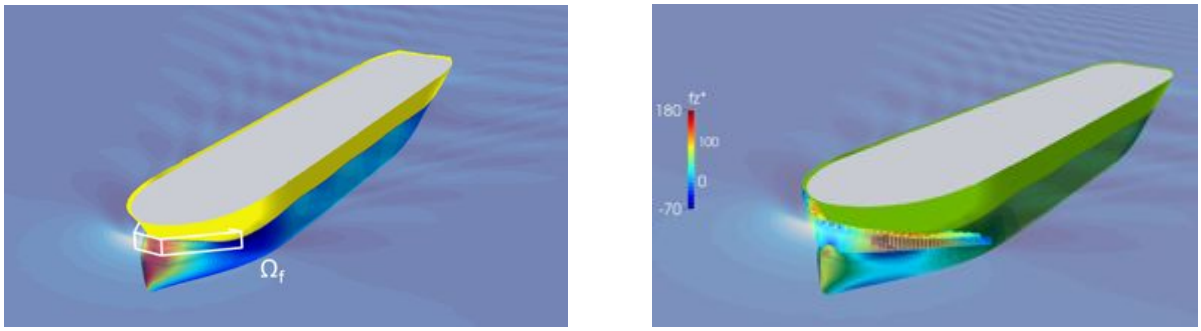

Figure 3. (a) Localised region in the flow field around the fore ship of the bulk carrier (white volume Ω_f), used for the evaluation of the cost function J_w (cf. Eq. 4). (b) Volumetric forcing of the adjoint system associated with the cost function J_w

The shape sensitivity gradient G w.r.t. J_w is calculated from the hull shear stress and its adjoint counterpart (cf. Eq. 3). G can be viewed as a detailed map of favourable normal shifts at the nodes of the hull surface mesh, eventually leading to a local minimum of the cost function J_w. Here, G suggests an upward extension of the bulbous bow (blue patch in Fig. 4) along with a decrease in volume near the fore shoulders (red region). After seven optimisation loops, the slope of the wave between the bow and the forward shoulders is somewhat flatter, and the trough moves a bit downstream and is less pronounced (Fig. 5). This leads to a downstream shift of

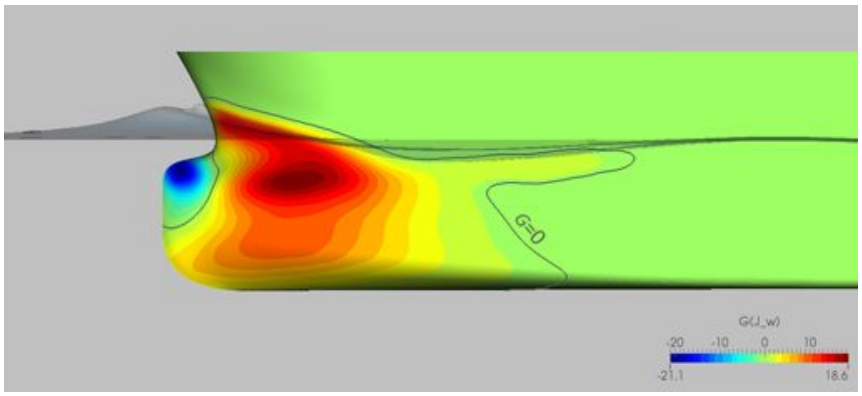

Figure 4. Shape sensitivity gradient G (Eq. 3) w.r.t. the cost function J_w (Eq. 4) of the original hull design

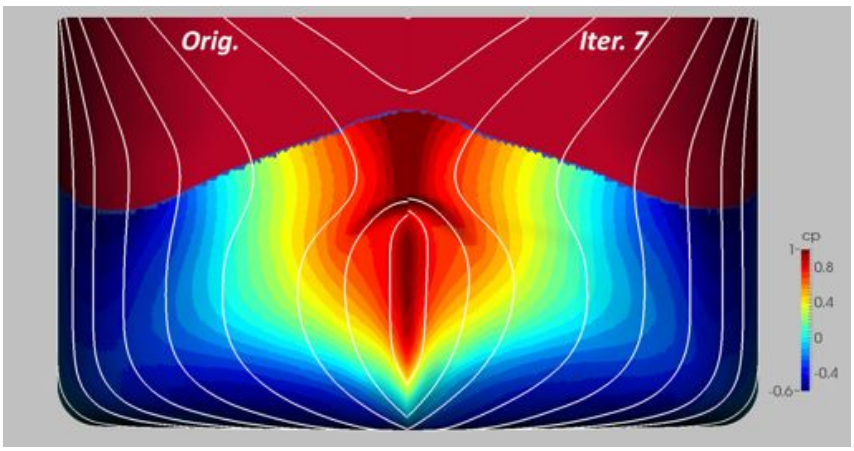

Figure 5. Comparison of the frame sections and the pressure distribution of the original hull (on the left) and the design variant obtained after seven optimisation loops (on the right)

the wave pattern with slightly weaker secondary waves in the near field of the ship (e.g. dashed ellipse in Fig. 6). Thanks to the bow modifications, the cost function J_w drops by almost 14% after seven iterations, while the wave drag is some 3% smaller than that of the original bulk carrier. However, the total ship resistance is hardly diminished as the wave drag accounts for only 4.2% of the hull resistance for this vessel. Moreover, the wave resistance of later design stages (from the eighth iteration on) turns out to increase again. This behaviour is accounted to the onset of unfavourable wave interference at the aft shoulders and the stern. It comes as no surprise that local modifications of the bow-wave system can easily create unwanted effects in the downstream parts of the wave field.

Discussion. The adjoint framework realised in (ad)$FreSCo^+$ proves to be a robust and efficient tool for the computation of the shape sensitivity gradient – the main quantity of interest in shape optimisation. Adjoint methods provide the shape sensitivity at a computational cost of only two flow simulations in total (one forward and one adjoint simulation), whereas direct methods require one simulation per nodal shift in order to construct the shape sensitivity, rendering them prohibitively expensive when a large number of local hull deformations is considered. Herein lies the strength and attractiveness of the adjoint methodology. The shape optimisation study for the bulk carrier reported here shows that the success of the design process strongly hinges on the choice of cost function. In the future, additional cost functions and optimisation constraints will be developed and tested in order to arrive at hull designs with small wave drag and low total resistance. Ship types operating at much larger Froude numbers such as small container

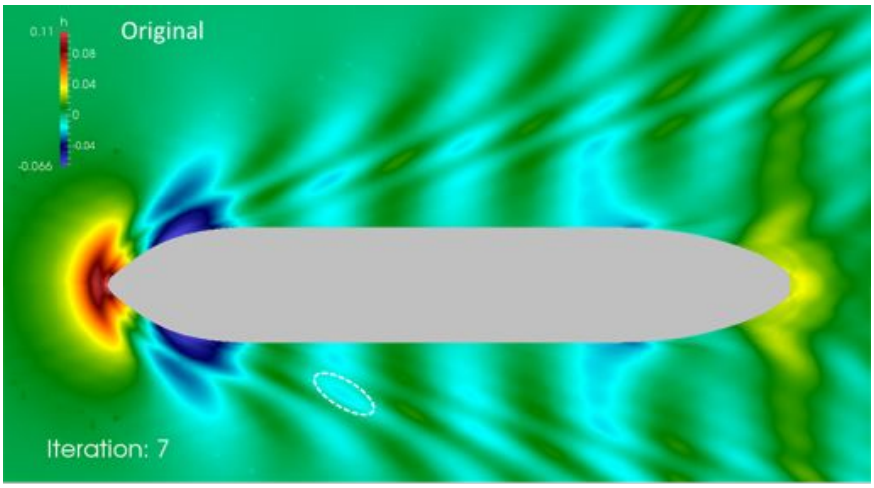

Figure 6. Comparison of the wave pattern created by the original hull (upper half) and by the design variant obtained after seven optimisation loops (lower half)

carriers and offshore support vessels will be considered. Moreover, the adjoint methodology will be refined and enhanced by a fully adjoint treatment of the free interface. This will be realised through the implementation of an adjoint VoF equation in (ad)$FreSCo^{+}$.

Acknowledgments. The work presented at the Numerical Towing Tank Symposium is part of the research project "No-Welle" conducted in collaboration with Hamburg University of Technology (TUHH), FRIENDSHIP SYSTEMS GmbH and Voith Turbo Schneider Propulsion GmbH & Co. KG. Funding by the Federal Ministry for Economic Affairs and Energy of Germany (BMWi) is gratefully acknowledged.

References

[1] A. Stück. Adjoint Navier-Stokes methods for hydrodynamic shape optimisation. *Tech. Report Hamburg University of Technology*, 661, 2012.

[2] A. Stück, J. Kröger, and T. Rung. Adjoint-based hull design for wake optimisation. *Ship Technology Research*, 58(1):34–44, 2011.

[3] M. Brenner, S. Harries, S. Wunderlich, J. Kröger, A. Stück, T. Rung, S. Gatchell, L.-U. Schrader, and J. Marzi. FORM-PRO. Hydrodynamische Optimierung von Schiffen mit aktiver Propulsion. *Tech. Report Projektträger Jülich, Schifffahrt und Meerestechnik (in German)*, 65–83, 2012.

Extended dynamic controller for quick and accurate CFD calculations of self-propelled ships at imposed power

Ivan Schrooyen, Ulstein, Ulsteinvik/Norway, ivan.schrooyen@ulstein.com
Karl Randle, Ulstein, Ulsteinvik/Norway, karl.randle@ulstein.com
Lucie Clous, ENSEIRB-MATMECA, Bordeaux/France, lclous@enseirb-matmeca.fr
Benjamin Herry, NUMECA Int., Brussels/Belgium, benjamin.herry@numeca.be
Benoit Mallol, NUMECA Int., Brussels/Belgium, benoit.mallol@numeca.be

Abstract

Accurate prediction for a self-propelled ship is a challenging task for computational methods. It is even more complicated when these results should be provided rapidly for industrial purposes. Advanced numerical techniques are then required together with a smart approach to reduce human and computation time. A commercial CFD RANSE chain has then been used to define a methodology to create such a project, in which the mesh generation plays a crucial role for the accuracy, and a dynamic controller for the rapidity of the simulation, which has been developed to automatically modify the ship speed for an imposed RPM of the propeller, or the ship speed and the RPM for an imposed power on the propeller shaft during the simulation. This paper is devoted to the presentation of the methodology and the validation of the approach. This validation is based on the relative comparison between full scale CFD calculations and recent sea trials of an offshore vessel (Ulstein PX121 equipped with Rolls-Royce AZP100). Finally, the numerical method is compared to classical model testing at different points of view, such as human effort, total cost, reliability and total time between order and results.

Cavitation simulation on Kappel propeller with a hull wake field

Keun Woo Shin (keun.shin@man.eu)

MAN Diesel & Turbo, Frederikshavn, Denmark

INTRODUCTION

Up-to-date marine propellers are designed to accompany a certain extent of cavitation for optimum propulsive efficiency, but excessive extent and certain types of cavitation have the risk of high hull pressure pulse, blade surface erosion and thrust breakdown. Propeller cavitation becomes unsteady and complex due to the interaction of the propeller flow and the non-uniform wake field behind the hull.

Unsteady caviation simulations by LES for a ship propeller with a non-uniform wake inflow have showed good accuracy (Bensow & Bark 2010). Cavitation simulations by DES for a propeller on a ship hull have also showed a good agreement with a cavitation test (Boorsma & Whitworth 2011). Cavitation simulations by RANS for two propellers on a ship hull have been well validated against cavitation tests (Paik et al. 2013). RANS cavitation simulations show a general agreement in sheet cavitation variations, but such small-length scale characteristics as tip vortex cavitation and fluctuating cavitation interface are not captured well by RANS unlikely LES and DES. On the other hand, RANS has an advantage in computational effort, compared to LES and DES. In our study, both RANS and DES are applied to cavitation simulations and the results are compared. Accuracy in unsteady cavitation variations is evaluated to assess whether CFD is a practical tool for the ship propeller design.

The Kappel propeller is an innovative tip-modified propeller, which shows higher propulsive efficiency and lower hull pressure pulse than conventional propellers. Lifting surface method and boundary element method can be less accurate in estimating the thrust, efficiency and cavitation due to the complex blade geometry of Kappel propeller. Hence CFD can be an important complementary tool in the innovative propeller design. Unsteady cavitation simulations on a Kappel propeller by RANS and DES are validated against model test results from a cavitation tunnel.

1. HULL WAKE FIELD MODEL

Non-cavitating flow simulations for a Kappel propeller have been validated against open-water and self-propulsion test results (Shin et al. 2013). A measured hull wake field has been applied as an inlet flow instead of modelling a ship hull. The same case for a 5.8m (D=0.25m in model scale) Kappel propeller on a 35,000 DWT tanker is handled for cavitation simulations.

Fig. 1: *Kappel model propeller handled in cavitation simulations*

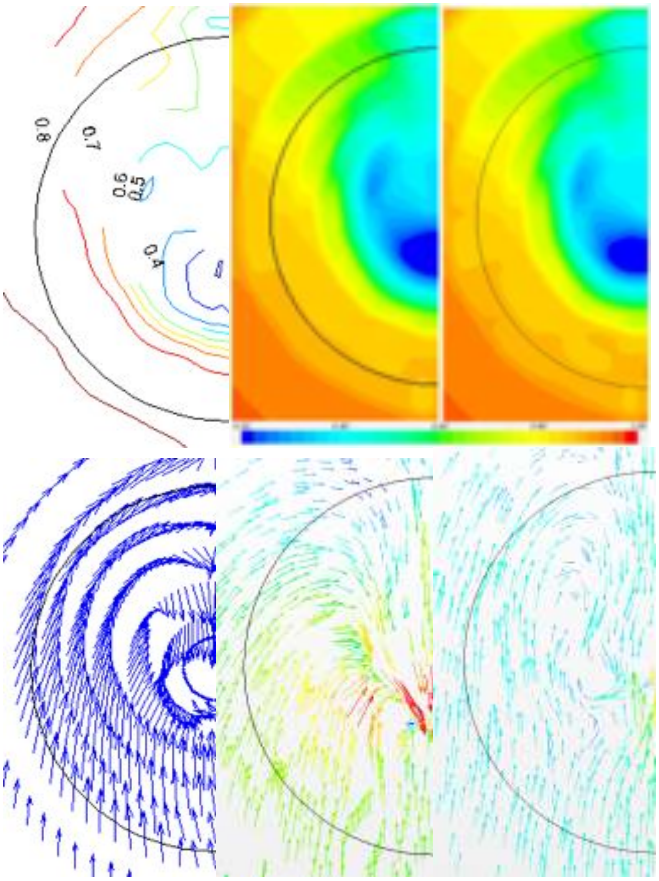

Fig. 2: *Axial component (top) and transverse components (bottom) of hull wake field on the propeller plane: measurement (left), CFD wake models only with an upward flow (center) and with both upward and horizontally centered flows (right)*

The axial wake field at the inlet is prepared by scaling the measured axial wake field with a ratio of the effective wake fraction to the nominal one. A uniform upward flow has been added to the axial wake field previously for the non-cavitating flow simulations. A horizontally centered flow is also added together with an upward flow in order to reproduce the bilge vortex in the transverse flow more accurately. The horizontally centered and upward flows can be explained by the wedge shape and upward slope of the aftship.

The wake model is simulated without a propeller and the flow field on the propeller plane is compared with the wake field measurement. In the wake model test, the axial wake is not scaled for the direct comparison with the measurement. Since the wake measurement from the target ship in the cavitation simulations is confidential, a dummy wake field from another single-screw low-speed ship is handled.

The propeller plane is located 3D downstream from the inlet. When the distance between the propeller plane and inlet is increased, the wake flow can be more diffused. When it is reduced, a numerical error can occur in case of highly-loaded propellers, because the inlet flow can be disturbed by the propeller flow.

Both wake models show a good agreement with the measurement in the distribution and magnitude of the axial wake. The wake with a horizontally centered flow shows that the high-wake region at inner radii is concentrated inside a circle with a slightly smaller radius by the effect of the horizontally centered flow. While the bilge vortex is not formed along the upper part of the propeller disk without a horizontally centered flow, the direction of the bilge vortex becomes closer to that in the measurement by adding it.

2. COMPUTATIONAL MODEL AND SETUP FOR CAVITATION SIMULATIONS

Non-cavitating flow simulations have been made at Vs=1.66m/s, N=9.64rps in model scale corresponding toVs=15.5kn, N=120rpm in full scale according to the condition in the self-propulsion test. Cavitation simulations are made at Vs=5.07m/s, N=30.0rps in model scale corresponding to Vs=16.0kn, N=125.9rpm in full scale. While Vs and N are scaled complying with Froude's law in self-propulsion tests, N is higher to avoid scale effects in cavitation tests. As a part of EU Project Kapriccio, cavitation tests for the Kappel propeller installed on the ship model have been carried out in a large cavitation tunnel in HSVA.

In the cavitation test, N is fixed and the tunnel flow speed corresponding the ship speed Vs is adjusted to reach KT=0.164, which is obtained from the self-propulsion test. With N=30rps fixed, Vs is adjusted in the same way as in the cavitation test. The effective wake fraction w=0.33 is kept constant. It is important to check whether KT is for the model scale, because KT in the cavitation test report is often for the full-scale trial condition, if not indicated. The model-scale KT is scaled to the full-scale trial one by Reynolds number correction, wake fraction correction and model-ship correlation factors (ITTC 1978).

All CFD simulations are made by StarCCM+. RANS computations are made with the Gamma ReTheta transition model and the k-ω SST turbulence model. SST-DES (Menter & Kuntz 2002) computations are also performed. In SST-DES, LES is applied to separated flow regions and RANS with the k-ω SST turbulence model works in the rest of the flow domain. A zonal DES limiter is adopted to avoid grid dependency in distinguishing between LES and RANS regions.

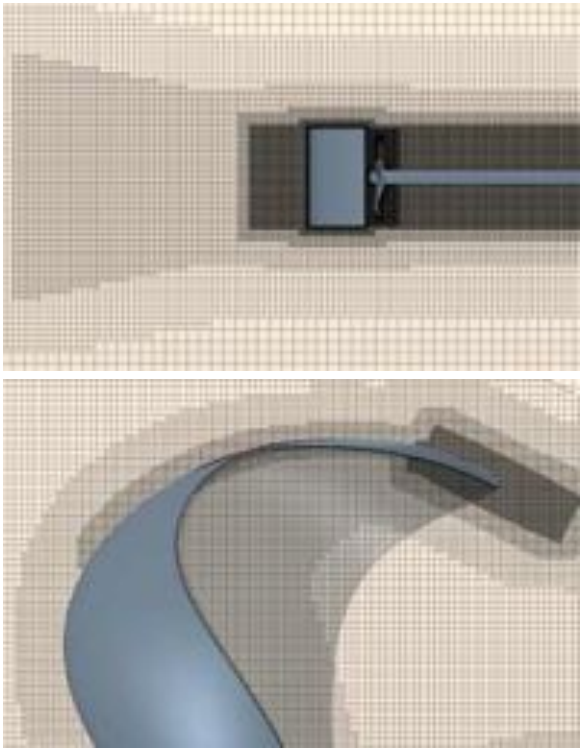

Fig. 3: *Volume mesh on a longitudinal section (top) and on a transverse section at the propeller plane (bottom)*

The surface of the blade, hub and rudder has a grid size of Δx=0.5-1.0mm. The blade edges has a finer grid of Δx=0.25-0.5mm. Even a finer grid of Δx=0.12-0.25mm is applied to the blade tip. All wall surfaces have 6-12 Prism layers with a thickness of 0.12-0.25mm. The volume mesh is hexahedral and tetrahedral. The volume mesh around the propeller and rudder has 8 cell layers with the same grid size as the surface mesh. The finest volume mesh is applied to the region around the blade tip and along the tip vortex trace.

Unsteady-state simulations are made with $\Delta t=9.3\cdot10^{-5}$s corresponding to 1° rotation per Δt. A second-order temporal scheme is adopted. The convective term is discretized by blending the second-order upwind and central differencing schemes. The diffusion term is discretized based on the gradients from the element shape functions.

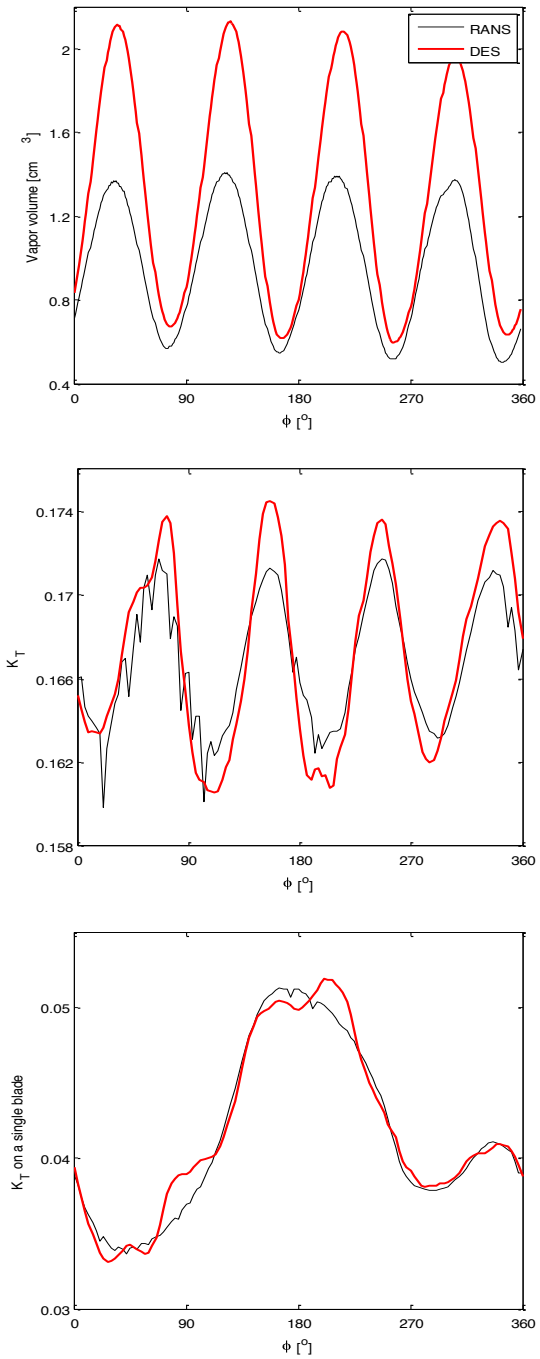

Fig. 4: *Vapor volume (top), K_T on the whole propeller (middle) and on a single blade (bottom) as functions of the blade angle φ*

The built-in cavitation model in StarCCM+ is an eulerian multiphase model consisting of VOF and a vapor transport equation based on the Rayleigh-Plesset equation. The ambient pressure is obtained from the cavitation number $\sigma_n=0.22$ corresponding to a shaft depth of 6.7m in the design draft. The hydrostatic pressure is applied by the gravity force and the reference altitude is on the shaft depth.

3. CAVITATION SIMULATION RESULT

When the thrust is time-averaged over the last revolution, K_T from the RANS simulation is near K_T =0.164 from the cavitation test. K_T from DES is about 1.0% higher than K_T from RANS. The K_T variation from RANS has some spikes, which may be related to the irregular cavitation at the collapsing part. But the vapor volume variation has a smooth curve. It can be inferred that small cavitation fluctuations have considerable effects on the thrust variation.

The variations of K_T and the total vapor volume are periodic every 90°. The vapor volume peak comes about 30° after the thrust peak. The vapor volume variation is about 30° shifted from the K_T variation. It implies that it takes a certain time for the cavity to be formed over the blade, after the leading edge enters the high-wake region. The thrust on a single blade is the highest at the upright position, because the wake peak is formed in this region. The vapor volume on a single blade is not calculated, because the rotating domain needs to be sub-divided into 4 parts for each blade and cavitation simulations need to be performed again. A cavitation simulation takes 60-70 hours for 10 revolutions with 32 nodes of 3.06 GHz processor and infiniband. The cavitation variation images show that the maximum extent is at φ=200-220°. The maximum vapor volume on a single blade is also about 30° after the highest thrust.

In Fig. 5, the cavitation distributions from RANS and DES are compared with that from the experiment. In CFD, the cavitation ineterface is for the 50% vapor-fraction iso-surface. While the sheet cavitation starts at r/R=0.7-0.8 at φ=150° in the experiment, it starts at r/R=0.9-1.0 at φ=120° in both RANS and DES. At φ=160°, the sheet cavitation appears slightly at the leading edge of r/R=0.7-0.9 in the experiment, it is extended from r/R=0.7 to the tip and the chordwise extent is larger in CFD. At φ=180°, the experiment also shows a radial extent from r/R=0.7 to the tip, but CFD shows that the chordwise extent is less at r/R=0.75-0.9 and more at r/R=0.9-1.0. At φ=200°, the sheet cavitation is extended over the whole chord at r/R=0.9-1.0 in both the experiment and CFD, but CFD shows leading-edge cavitation at r/R=0.8-0.9, whereas the cavitation is aft of the mid chord in the experiment.

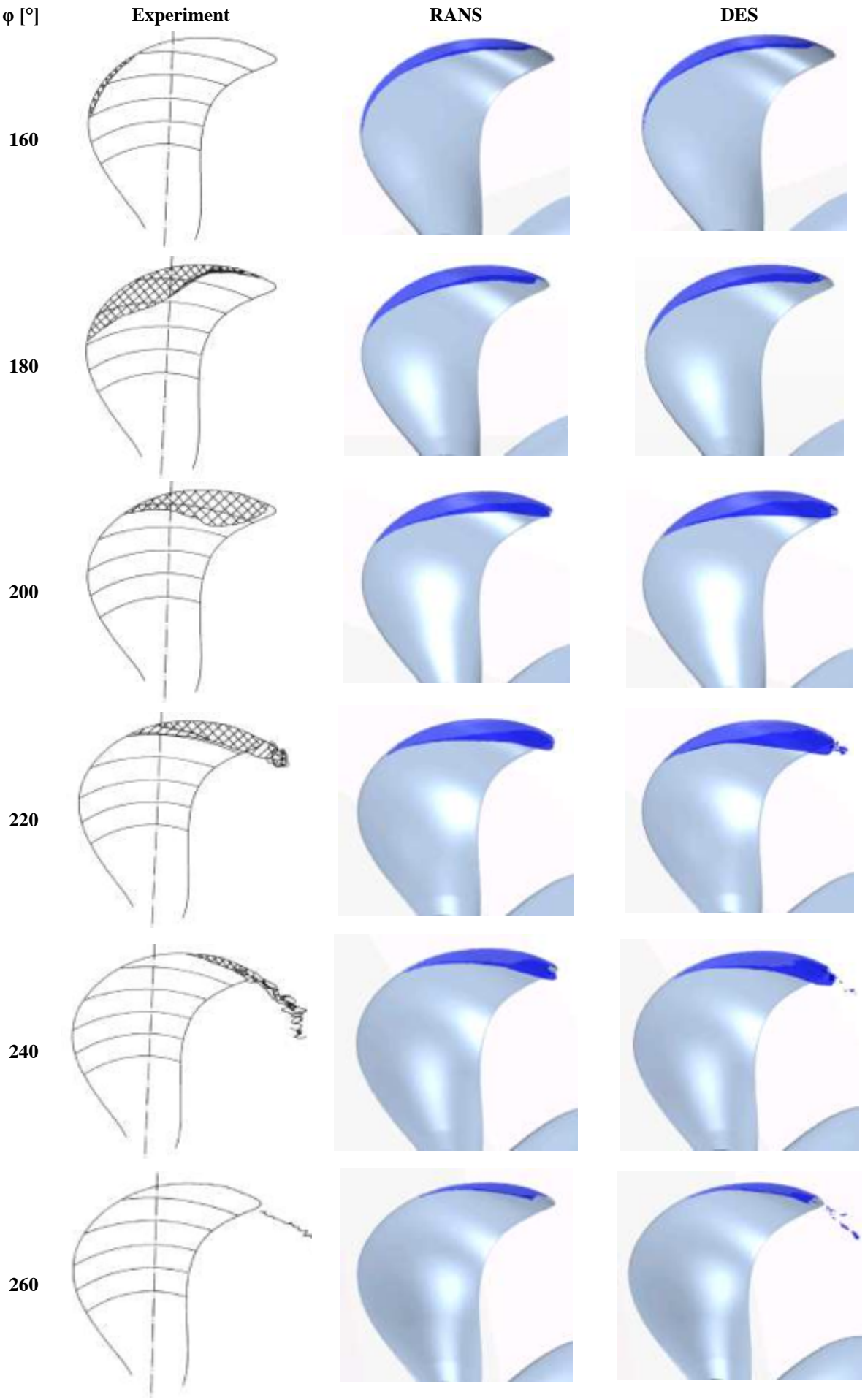

Fig. 5: *Cavitation distributions at different blade angles φ from the experiment and CFD*

At φ=220°, super-cavitation appears at r/R=0.9-1.0 in both the experiment and CFD. DES shows an unstable detachment at the end of the sheet cavitation, which has a similarity with the experiment. At φ=240°, the sheet cavitation is suppressed and unstable tip cavitation appears in the experiment, whereas the cavitation is slightly reduced and the most portion remains in CFD. DES shows scattered vapors along the tip vortex trace. While slight sheet cavitation still remains in CFD, it disappears completely at φ=260° in the experiment.

The sheet cavitation is more extended at r/R=0.9-1.0 and it starts earlier and lasts longer in CFD, whereas it is more developed at r/R=0.75-0.9 at φ=180° in the experiment. Such differences indicate that the high hull wake is more concentrated within a smaller radius in the cavitation test than the measurement. Wake measurements are made at a ship speed scaled by Froude's law in a towing tank, but cavitation tests are made at a higher ship speed and hence the boundary layer is thinner and the hull wake can be more narrowly distributed in the upper propeller disk.

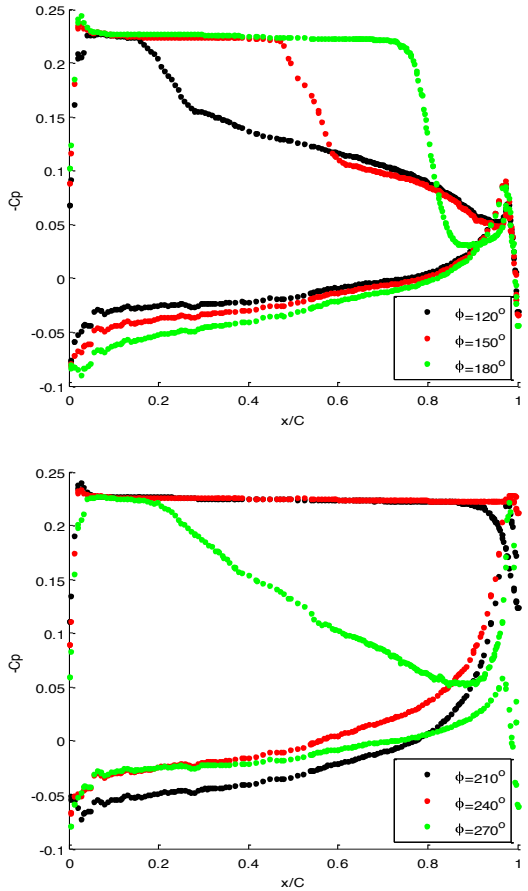

Fig. 6: *C_P on 0.95R section at different blade angles*

Since the turbulence model in RANS generally underestimates the turbulent stresses in separated flow regions, the cavitation detachment is not reproduced in RANS, but DES improves the vortex shedding to show cavitation detachment. When the tip vortex is strong, the vortex cavitation is extended to a long distance in a stable form. The vortex cavitation is unstable and short in this case, because the tip vortex is weakened by the tip bending.

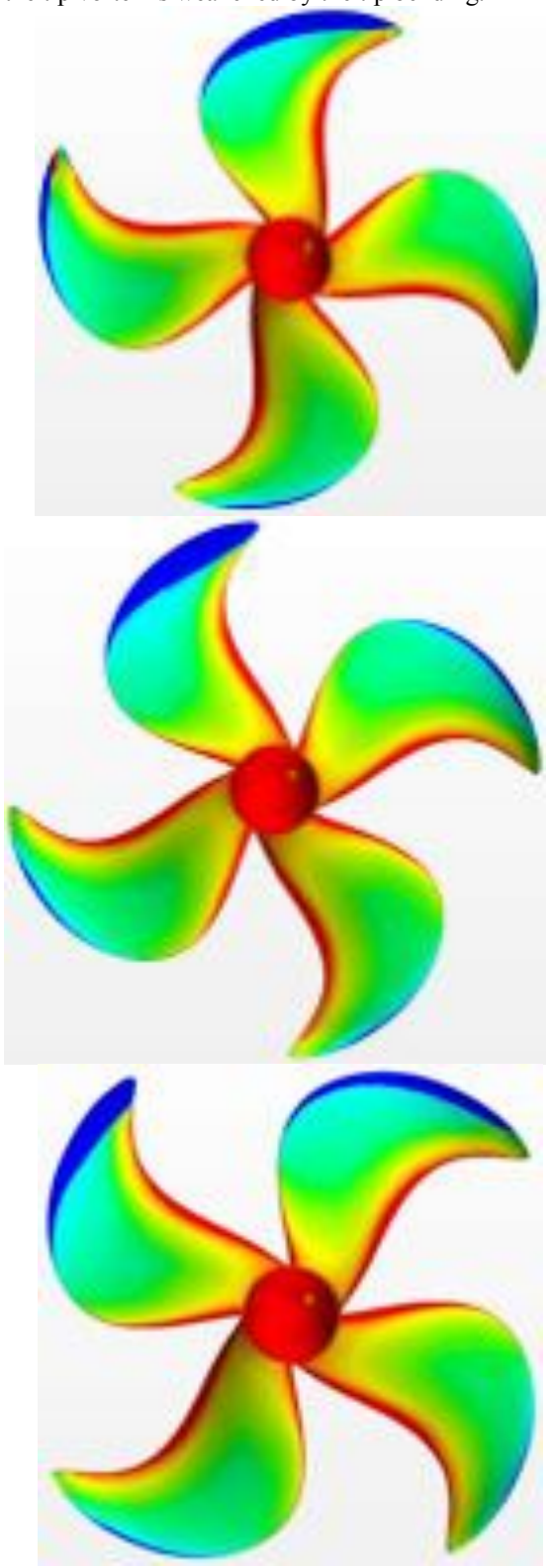

Fig. 7: *C_P on the suction side of the blade at different blade angles*

C_P on the 0.95R section and the blade surface from DES are presented in Fig 6. and Fig. 7. Since the

pressure at the cavity interface is close to the vapor pressure P_V, the blade surface under the cavitation has a constant pressure close to P_V i.e. – $C_P \approx \sigma_n$. The reference velocity in C_P and σ_n is the angular velocity of the blade tip. The constant pressure on the sectional C_P indicates a chordwise cavitation extent. As the blade enters the high-wake region, the pressure difference between the face and back sides gets larger and the sheet cavitation is extended at φ=120°-180°. The constant pressure encloses almost the whole section with the super-cavitation at φ=210°-240°. As the blade get out of the high-wake region, the cavitation is suppressed at φ=270°.
The suction drop aft of the constant pressure is steeper at φ=180° than those at φ=120°-150°. It may explain how the thrust breakdown occurs when the cavitation is extensive. At φ=270°, the suction peak at the end of the section is caused by scattered vapors.

While the lowest pressure on the back side of the blade drops without a lower limit in non-cavitating flow simulations, the cavitation occurs in low-pressure regions under P_V in cavitation simulations and the cavitation interface has a constant pressure. Since the vapor is convected by the propeller flow, the low-pressure region under P_V is more extended in cavitation simulations. The variation of the constant pressure along the blade angle corresponds to the cavitation variation.
At φ=270°, the pressure fluctuation at the end of the sheet cavitation indicates a flow separation. The sheet cavitation is detached in a form of scattered vapors by vortex shedding accompanying the flow separation.

4. CONCLUSION

Cavitation simulations on a Kappel propeller by RANS and DES are compared with experimental results from a cavitation test. Both RANS and DES show acceptable accuracy in simulating unsteady sheet cavitation. The sheet cavitation from CFD is overestimated in the region at the tip, but it is underestimated at slightly inner radii from the tip. Such deviations are likely to be due to the difference in the hull wakes from the towing tank and the cavitation test. It can be investigated by cavitation simulations with including a hull model in future.
DES shows improvement in simulating the detached cavitation related to the flow separation and vortex shedding. The case handled in our study does not include the cloud cavitation and intensive vortex cavitation, but DES is expected to have an advantage in simulating those types of cavitaton leading to material erosion. Both RANS and DES can be used as a complementary tool for the Kappel propeller design. When the sheet cavitation is extensive, DES is recommended for an assessment of the erosive cavitation risk.

REFERENCES

1. Andersen P., Friesch J., Lundegaard L., Patience G., 2005, Development of a marine propeller with nonplanar lifting surfaces, Marine Technology, Vol. 42, No. 3
2. Bensow R. E. and Bark G., 2010, Simulating cavitating flows with LES in Openfoam, ECCOMAS CFD, Lisbon, Portugal
3. Boorsma A. and Whitworth S., 2011, Understanding details of cavitation, SMP'11, Hamburg, Germany
4. ITTC, 1978, ITTC- Recommended procedures and guidelines: 1978 ITTC performance prediction method
5. Menter F. R., Kuntz M., 2003, Adaptation of eddy-viscosity turbulence models to unsteady separated flow behind vehicles, Pro. Conf. The Aerodynamics of Heavy Vehicles: Trucks, Busses and Trains, Asilomar, CA, Springer
6. Paik K., Park, H., Seo J., 2013, URANS simulations of cavitation and hull pressure fluctuation for marine propeller with hull interaction, SMP'13, Tasmania, Australia
7. Shin K. W., Andersen P., Bering R. M., 2013, CFD simulation on Kappel propeller with a hull wake field, 16th NuTTS, Mulheim, Germany

Numerical Simulation of Free Surface Break-up and Re-attachment Inside an Air Cavity

Abolfazl Shiri * and Michael Leer-Andersen
SSPA AB, Götebory, Sweden

Rickard E. Bensow
Chalmers University of Technology

Jacob Norrby
STENA Rederi AB, Götebory, Sweden

1 Introduction

Marine vessels with relatively large wetted surface area are suitable for the implementation of pressurized air cavity. Air cavity on the hull FOB (flat of bottom) is one method for air lubrication in especially for displacement ships. Other types of air lubrication can be implemented for decreasing the viscous drag of the hull surface. Foeth [1] gives a description of different air lubrication methods and argues the importance of the hull design and geometry for the optimum performance of the air cavity system. Different formation of the air cavity wave system behind a wedge under the hull was studied by Matveev [2]. He describes the behavior of the free surface as an important parameter for drag reduction which is controlled by the air cavity pressure and shape of the hull adjacent to the cavity. The study by Thill et al. [3] observes the speed dependence of the air cavity system due to the variation in the wavelength of the free surface disturbance.

An analytical investigation by Schmidth [4] provides a family of curves for hull shape to decrease the wave amplitude in different water speed inside the cavity. The study by Shiri et al. [5] discusses the importance of the air-water interface inside the cavity and the relation between the drag reduction and smoothness of the interface. They also show that the angle and position of re-attachment to the cavity's aft surface are an important factor for the pressure forces exerted on the cavity. Also the amount of air release in form of bubbles and/or air layer has a role in lubricating the stern.

The goal of the present study is to simulate the behavior of the interface at the re-attachment position and possible free-surface breaking on the inclined surface (beach), similar to the experimental condition. The experimental observation in Shiri et al. [5] for a simplified air cavity describes the re-attachment process as the breaking wave. For the resistance measurement in the model test with air cavity system, we need the information on force scaling at the aft plate of the cavity to provide the correct estimation of forces on the full scale cavity and hull.

2 Air Cavity Concept and Principle

The viscous resistance due to the skin friction on a submerged surface is calculated using *wall shear stress*:

$$\tau_w = \mu_{water} \left(\frac{\partial u}{\partial y} \right)_{wall} \tag{1}$$

*abolfazl.shiri@sspa.se ; Tel: +46 31 772 90 69

The dynamic viscosity (μ) of water is approximately 60 times more than of the air at ambient temperature, hence the shear force on a solid surface, moving adjacent to water, is a lot more than the skin friction resistance exerted by air at the same speed. Figure 1 shows a schematic drawing of an air cavity where a section of the wetted surface have been replaced with an air filled cavity. Water detaches from the solid surface and forms a free-surface under the air-filled cavity section and the solid to water no-slip boundary layer is replaced by air-water interface. The free-surface flow re-attaches to the solid surface at the aft section of the cavity. With a proper design of the air cavity at FOB in a displacement ship, the viscous resistance reduction can reach 15–20% without releasing air.

As discussed in Matveev 2007 [6], the shear force between air and water at the separation point, and the air pressure difference inside the cavity with the adjacent hydrodynamic pressure, cause a pressure disturbance on the free surface. Therefore, an immediate problem with using an air cavity as shown in Figure 1 is how to keep the pressure disturbances as small as possible to generate a flat free surface. This will both decrease air release and resistance. In the design used here the air pressure inside the cavity is adjusted by regulating the pressurized air inlet in the cavity. The entire concept aims at creating air circulation in the cavity without releasing air, thus transferring the shear stress from solid-water to solid-air boundary layer. The cavity's parts are described as (I) the cavity's dry ceiling, (II) inclined surface called *"Beach"* to allow the smooth re-attachment and the (III) aft surface where the water boundary layer restarts again.

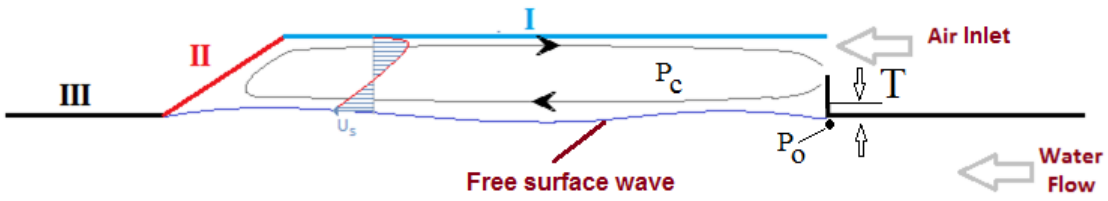

Figure 1: Schematic of the free surface wave system and cavity parts: (I) Cavity ceiling, (II) Beach and (III) Aft surface. **T** is *cavity static submersion*.

The longitudinal wave system caused by pressure disturbance in front edge of the cavity has the wave length of $\lambda = 2\pi U^2/g$ which only depends on the water speed U. The wave elevation inside cavity is proportional to the cavity pressure difference $\Delta P = P_c - P_o$. In a submerged cavity, the hydrostatic pressure of the water at the bottom of the hull is $P_o = \rho_w g\, d$; where d is hull draft and ρ_w is water density. Therefore the *cavity static submersion* is defined as a length scale of the wave system as

$$T = \frac{P_o - P_c}{\rho_w g} \tag{2}$$

Two dimensionless parameters, defined to characterize the cavity, are Froude number based on the static submersion

$$Fn_T = \frac{U}{\sqrt{gT}} \tag{3}$$

and the Euler number based on the cavity pressure difference:

$$En = \frac{P_o - P_c}{\rho_w U^2} \tag{4}$$

Adding the equations 2, 3 and 4 together provides the scaling relation of $Fn_T^2 = En^{-1}$. We use these equations to scale the cavity pressure and static submersion from model scale to full scale hull, in which the geometry and speed is scaled with the Froude number based on the hull

length L, ($Fn_L = U/\sqrt{gL}$). If the pressure difference goes toward zero, Fn_T yields to infinity. This means in theory, there shouldn't be any disturbance to create a wavy free surface. The assumption obviously ignores the shear stress exerted by the air inside cavity.

3 Single Cavity Experiment

The experiment described in Shiri et al. [5] provides force measurements in a single cavity, placed in the pressurized test section of SSPA's cavitation tunnel. Figure 2 shows the schematic of the test section and a picture of beach surface in the aft section of cavity. The detail of experiment and the result are presented in Shiri et al. [5].

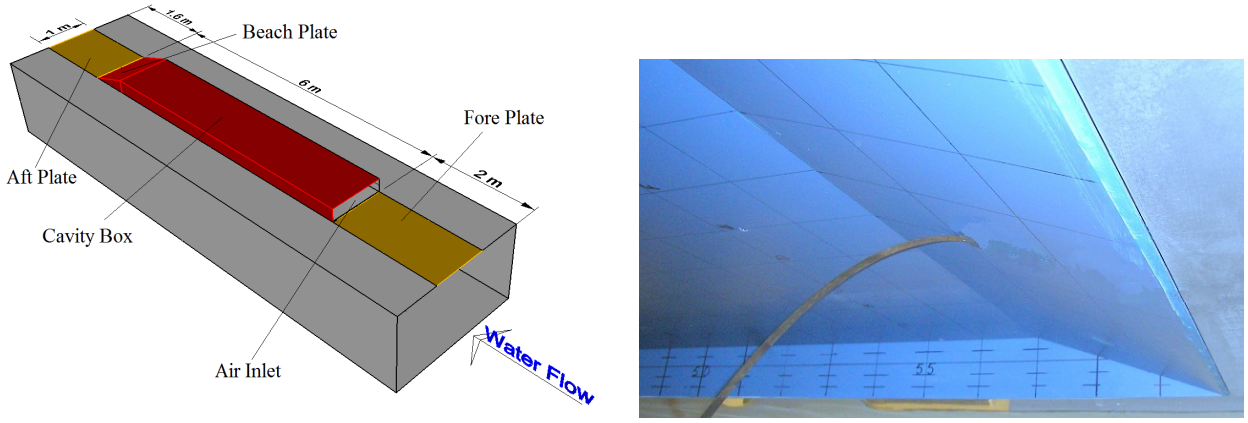

Figure 2: Left: Schematic of the test section. Right: Beach surface view from underneath of cavity.

The wave amplitude increases with larger static submersion depth. The combination of different cavity pressures ($\Delta P = 5, 100, 200, 300pa$), beach inclination angles ($18.4^o, 11.3^o, 8.1^o$) and different water velocity results on the force variation measured on the cavity. Higher pressure in cavity (smaller ΔP) decreases the wetted surface area on the beach wall, hence lowering the pressure force on the cavity. The wavy free surface length scale with different speed and the position of re-attachment shifts on the beach surface. Since wavelength is proportional to the square of the velocity, any minor change in velocity results in a large change of the position.

The process of re-attachment for the water speed lower than $1m/s$ is smooth. Figure 3 shows the beach view for two speeds of $1m/s$ and $1.5m/s$. There is no surface breaking or bubble making in the left picture while the bubbles start to form at higher speeds. The bubble in the water indicates the local surface wave breaking and is due to combined angle of attachment and higher Weber number. Weber number is defined as the ratio of the inertia to the surface tension:

$$We = \frac{\rho U^2 L}{\lambda} \tag{5}$$

where U is the velocity, L is length scale and λ is the surface tension. Higher Weber number diminishes the effect of surface tension and allows the ripples on the surface to break and entrap packages of air as bubbles. Aerated water has different properties and lubricate the surface aft of the beach. Scaling the resistance force of the model scale without considering the Weber number effect introduces uncertainty into a full scale estimation.

4 Computational Study

To simulate the behavior of free surface re-attachment and air bubble and air film formation, a series of CFD simulation was carried out with two different settings. First setting includes

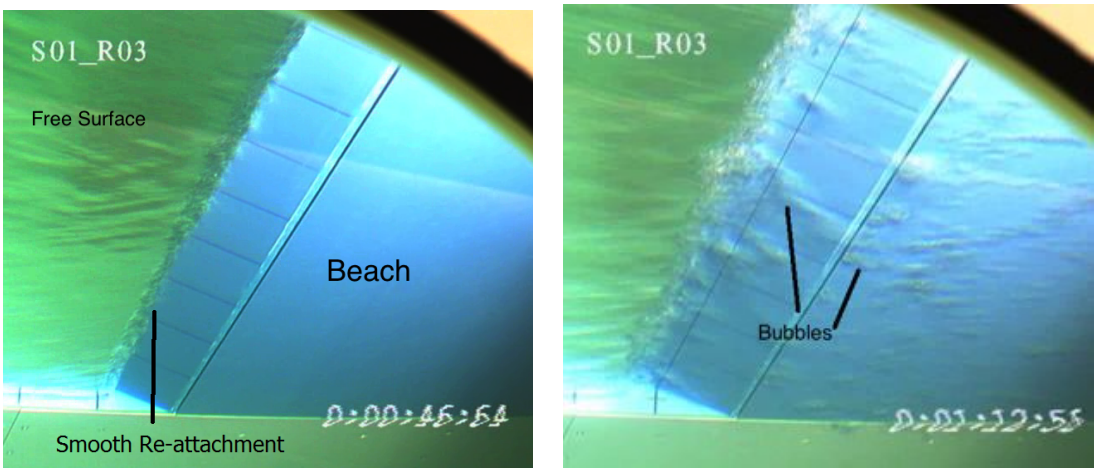

Figure 3: Re-attachment of the free surface at (Left) water speed approx. $1m/s$ and (Right) water speed approx. $1.5m/s$. Beach angle=18.4^o.

the entire air cavity, simulating the free surface wave system and the beach re-attachment. The other setup excluded the starting section of the cavity, hence allowing the free surface to approach the beach horizontally. This way the variation in speed does not have any effect on the re-attachment angle and position. Figure 4 shows the schematic of the computational domain and the boundary conditions used in the simulation.

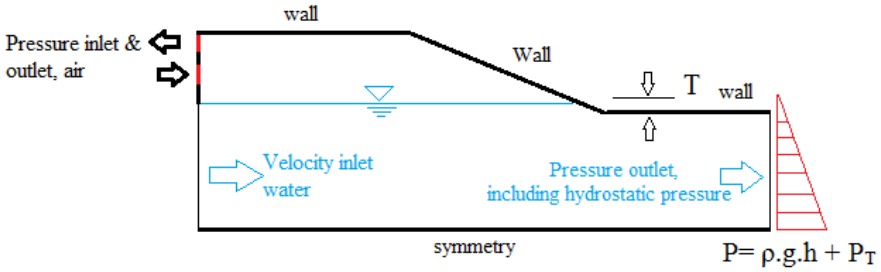

Figure 4: Boundary conditions in computational domain of the second setting.

The computational study was carried out using two-phase Fluent RANS solver. The solver employed Volume of Fluid (VOF) method to simulate a two-dimensional unsteady water-air interface inside the cavity. The initial *static submersion depth*, T is calculated based on the pressure difference $\Delta P = 200pa$ in the experiment. A constant velocity inlet is selected for the water entrance section, while two pressure inlet/outlet boundary conditions (BC) allow the air to regulate the cavity's air pressure. Outlet BC is selected as pressure outlet, including hydrostatic pressure variation with water depth. walls are considered as hydraulically smooth with no-slip BC, except at the bottom with symmetry BC. The wall adhesion is turned off as Fluent 15.0 solver has difficulty measuring viscous force while using the wall adhesion option. The surface tension coefficient is equal to 0.072 N/m for air-water interface. The viscous model $\kappa - \Omega$ SST with low Reynolds correction is used for turbulence closure and y^+ value for the first cells adjacent to the beach surface is less than 1. The observation in the experiment showed the bubble sizes vary from very small up to few centimeters. The use of fine mesh in the attachment region is necessary to capture bubble formation correctly.

5 Results and Discussion

In 2-dimensional simulation of the entire cavity, free-surface wave amplitude increases by decreasing the cavity pressure due to higher pressure jump at inlet, causing a larger pressure disturbance. Variation in speed does not have considerable effect on the wave amplitude as shown in Figure 5. The cavity pressure difference ($\Delta P = P_c - P_o$) on the other hand, correlates with the wave elevation. For the speed of $V \leq 1m/s$ simulation shows a different wave amplitude compare to the higher speeds. Although the free surface elevation increases immediately after cavity's edge but the pressure disturbance creates smaller wave amplitudes. In experiment the same pattern was also observed. Looking at the re-attachment behavior at the beach in Figure 6, the water surface braking in higher water velocities.

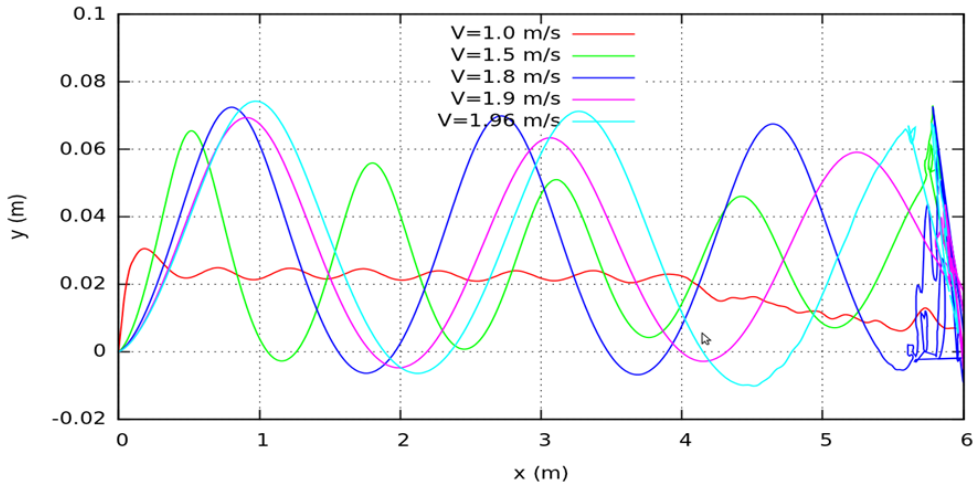

Figure 5: Water free surface inside the cavity in different water speeds.

Figure 6: 2D simulation of the entire cavity in different water speed.

It is difficult to run the case of zero pressure difference in the cavity as air releases at the beach in shape of air layer with high flow rate which makes the cavity unstable. Viscous force measurement shows a drag reduction in simulations with high flow rate of air release. This is unlike the experimental result in which the bubbles were convected away from the aft section and did not help the drag reduction process. This might be partly due to mesh resolution at

the aft plate in simulation or the three-dimensional flow in the experiment.

Simulation with horizontal free surface reveals the importance of the air circulation inside the cavity. The air motion caused by the shear force exerted from water surface, creates a large circulation over the entire cavity, but is broken up closer to the beach due to high pressure gradient at the beach. The size of these local re-circulations cells depends on the water velocity. Figure 7 shows the velocity contour in air cavity for water speed of $U = 2.5m/s$. The local air circulation can cause disturbances on the water surface which is mostly confined to the region close to the beach. Since in model scale experiment speeds are lower than full scale cavity, more study on the effect of air recirculation on scaling of the free surface is required.

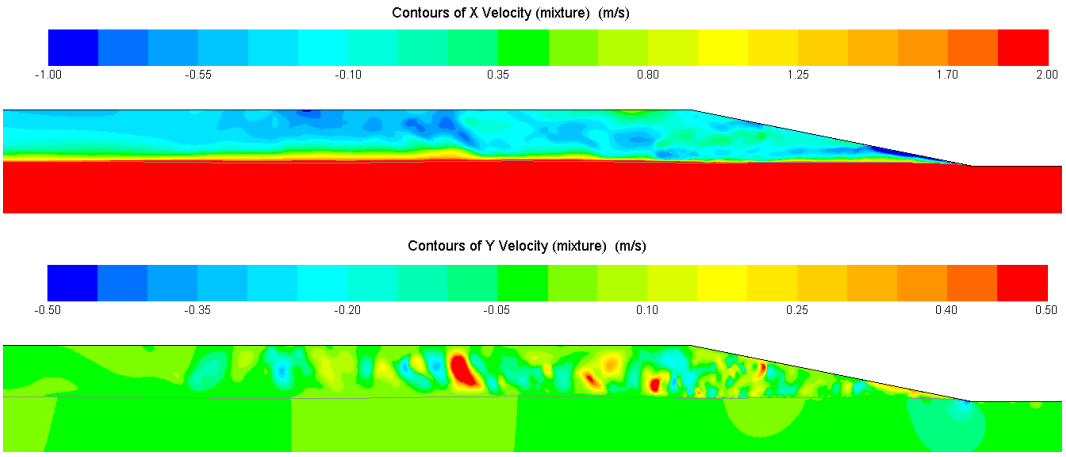

Figure 7: 2D simulation of the half cavity. $U = 2m/s$.

Acknowledgments

The study is supported by STENA Rederi AB and the Swedish Energy Agency, grant 37936-1. The authors would like to thank the technical staff in SSPA Sweden AB for their support.

References

[1] Foeth, E. J., "Decreasing frictional resistance by air lubrication," *Proceedings of the* 21^{th} *International Hisawa Symposium on Yacht Design and Yacht Construction*, 2010.

[2] Matveev, K. I., "On the limiting parameters of artificial cavitation," *Ocean Engineering*, Vol. 30, No. 9, 2003, pp. 1179–1190.

[3] Thill, C., Toxopeus, S., and van Walree, F., "Project Energy-saving Air-lubricated ships (PELS)," *Proceedings of the* 2^{nd} *International Symposium on Seawater Drag Reduction*, May 2005, Busan, Korea.

[4] Schmidth, G., "Linearized stern flow of a two-dimensional shallow-draft ship." *Journal of Ship Research*, Vol. 25, No. 4, 1981, pp. 236–424.

[5] Shiri, A., M., L.-A., Bensow, R. E., and J., N., "Decreasing frictional resistance by air lubrication," *Proceedings of the* 29^{th} *Symposium on Naval Hydrodynamics*, August 2012, Gothenburg, Sweden.

[6] Matveev, K. I., "Three-dimensional wave patterns in long air cavities on a horizontal plane," *Ocean Engineering*, Vol. 34, No. 13, 2007, pp. 1882–1891.

Comparison of LES and DNS for the flow past a circular cylinder with fairings

Håkon Strandenes*, José P. Gallardo*, Bjørnar Pettersen* and Helge I. Andersson**

*Department of Marine Technology
**Department of Energy and Process Engineering

Norwegian University of Science and Technology, Trondheim, Norway
E-mail: {hakon.strandenes, jose.p.gallardo, bjornar.pettersen, helge.i.andersson}@ntnu.no

1 Introduction

The flow past different kinds of cylinders are a key problem in many areas of industry and nature. The simplest configuration is the flow around a smooth, circular cylinder. Even though the problem description is very simple, the flow solution is highly complex and a challenge to calculate numerically. The behaviour of the flow is highly dependent on the Reynolds number $Re = U_\infty D/\nu$ (where U_∞ is the inflow velocity, D is the cylinder diameter and ν is the kinematic viscosity of the fluid), and already for very low Reynolds number, the flow becomes unstable and vortex shedding is observed. For higher Reynolds number, approximately $Re > 200$, the vortex shedding and wake region becomes three-dimensional, and transition to a turbulent wake begins.

One of the main challenges in this flow problem is caused by the separation of the flow. Since the cylinder is smooth, we have no *a priori* knowledge about the point of flow separation. Capturing this point is vital to determine the forces on the cylinder, since the pressure distribution around the cylinder is highly sensitive to the location of this point.

This abstract will focus on a circular cylinder with fairings as shown in figure 1. The purpose of these fairings is to reduce the oscillating forces caused by the vortex shedding process, and hence reduce the VIV (Vortex Induced Vibrations) motions of for example offshore risers. For the present study, we use $Re = 5000$.

Our aim at the current stage of this project is to compare the results from DNS (Direct Numerical Simulations) and LES (Large Eddy Simulations) to enhance our experience with LES in particular. We are able to do fully resolved DNS for this flow configuration and believe that these results are very accurate, however they are costly. We hope that LES can be used as an alternative approach, and that this could be used in conjunction with DNS and experiments to do complementary simulations of cases that we previously could not afford to study.

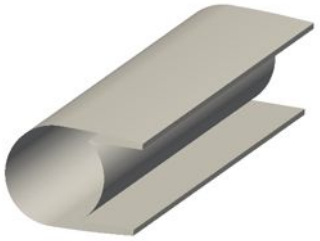

Figure 1: An illustrative sketch of the cylinder with fairings.

2 Numerical methods

Different simulation codes have been used to do the DNS and LES. The code *MGLET* [1] has been used to perform the DNS while the LES were performed with *OpenFOAM* [2, 3]. Both tools are finite volume codes, and in both cases linear central differences and linear interpolation have been used for all spatial terms, hence leading to second order accuracy in space. For the DNS, a third order explicit Runge-Kutta time integration scheme have been used, while

Table 1: Grid and simulation setup. The domain size is $70D \times 40D \times 6D$ for all cases. The 'performance' measure is the wall-time per time step divided by the number of grid points per process, i.e. (time per step)/(gridPts/nProcs). Lower number is indicating better performance.

	DNS	10M LES	20M LES	
Grid design	$2048 \times 800 \times 300$	Unstructured	Unstructured	
Number of cells	491×10^6	10.9×10^6	20.3×10^6	
Time step	0.001	0.001	0.001	D/U_∞
Simulation time	300	600	600	D/U_∞
Cost	140.6×10^3	115.2×10^3	207.9×10^3	CPU-hours
Cost per D/U_∞	468.8	192.0	346.6	CPU-hours
Performance	3.43	63.4	61.8	$\times 10^{-6}$

for the LES a second order semi-implicit Crank-Nicolson scheme [4] was used in the temporal dimension.

The major difference between the codes are in the mesh design and handling of solid boundaries. MGLET uses a regular Cartesian mesh, and introduce the solid geometry through an immersed boundary method. This gives an advantage when it comes to the mesh generation which is very simple, while it poses some challenges especially when it comes to the handling of sharp corners on the geometry. This also inherently leads to unnecessary large number of cells. OpenFOAM on the other hand uses a body-fitted unstructured mesh. This is more flexible, because it is possible to do local refinements around the cylinder and in the wake where high resolution is needed, while keeping the resolution coarse in the far-field regions where the flow is of no interest.

The Smagorinsky eddy viscosity model [5] was used for the LES cases. Both LES and DNS have been performed on the same HPC cluster, hence the CPU hours consumed by the two methods are comparable when it comes to assess the 'cost' of a simulation.

3 Results

Convergence studies have been performed for the DNS with respect to grid resolution. We believe that the simulation presented here is a well resolved simulation which might be considered 'converged' when it comes to mesh resolution. However, for the time-averaged quantities, only 300 D/U_∞ have been simulated after the flow has stabilized, hence there might still be some errors related to the statistical convergence. When it comes to the LES, 600 D/U_∞ have been simulated on each mesh.

The main flow quantities from the simulations are summarized in table 2. An illustration of the instantaneous flow field from the 20M LES is shown in figure 2.

3.1 First and second order statistics

Contours for the time- and spanwise averaged quantities $\langle u \rangle$, $\langle v \rangle$, $\langle u'u' \rangle$ and $\langle u'v' \rangle$ are shown in figure 4. One can observe that some features in the contours from the DNS are not fully symmetric as they should be. This might be due to a too low averaging time. Parnaudeau et al. [6] claimed that over 250 vortex shedding cycles is needed for statistical convergence of the wake behind a circular cylinder at $Re = 3900$. Neither of the simulations presented here are close to that. This can explain some differences, but not all. Please see figure 8 in ref. [6] for an excellent illustration of this issue.

Figure 3 also shows the same significant discrepancies between the LES and DNS in the wake behind the cylinder. LES clearly underpredict both the recirculation length and vortex formation length when compared with DNS. Again this might be due to a too small averaging time for the DNS, however, we do believe that there are other contributions to this deviation as well.

Table 2: Main flow results. C'_L is the RMS of the lift coefficient and C'_D is the RMS of the fluctuating part of the drag coefficient (i.e. after the mean have been subtracted). The overbar indicate a mean quantity. Note that the vortex shedding frequency have been calculated based on a velocity probe in the wake at $x/D = 3$ for the DNS, and based on the time series for lift for the LES.

	DNS	10M LES	20M LES
St	0.227	0.259	0.240
$\overline{C_D}$	0.884	0.813	0.881
C'_L	0.0496	0.0438	0.0503
C'_D	0.0125	0.0140	0.0127
$-\overline{C_{pb}}$	0.767	0.723	0.775

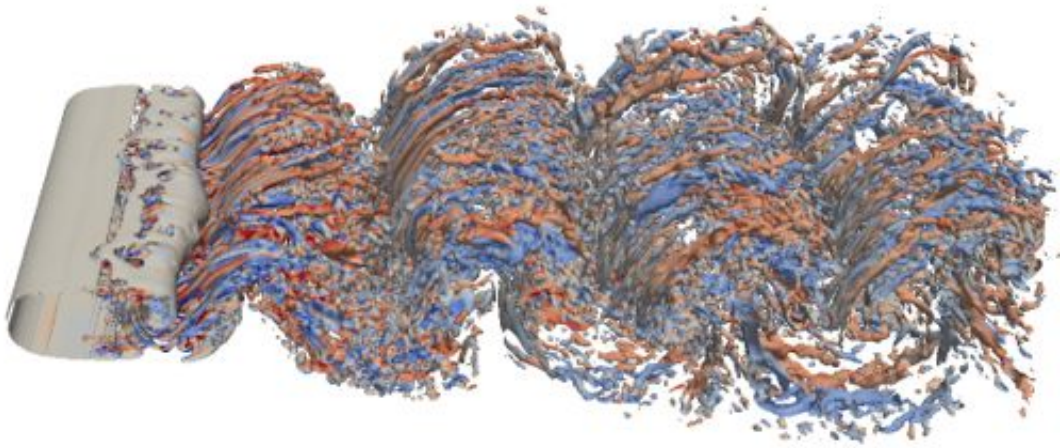

Figure 2: Isosurface of $\lambda_2 = -1$ colored by streamwise vorticity ω_x for the 20M LES case.

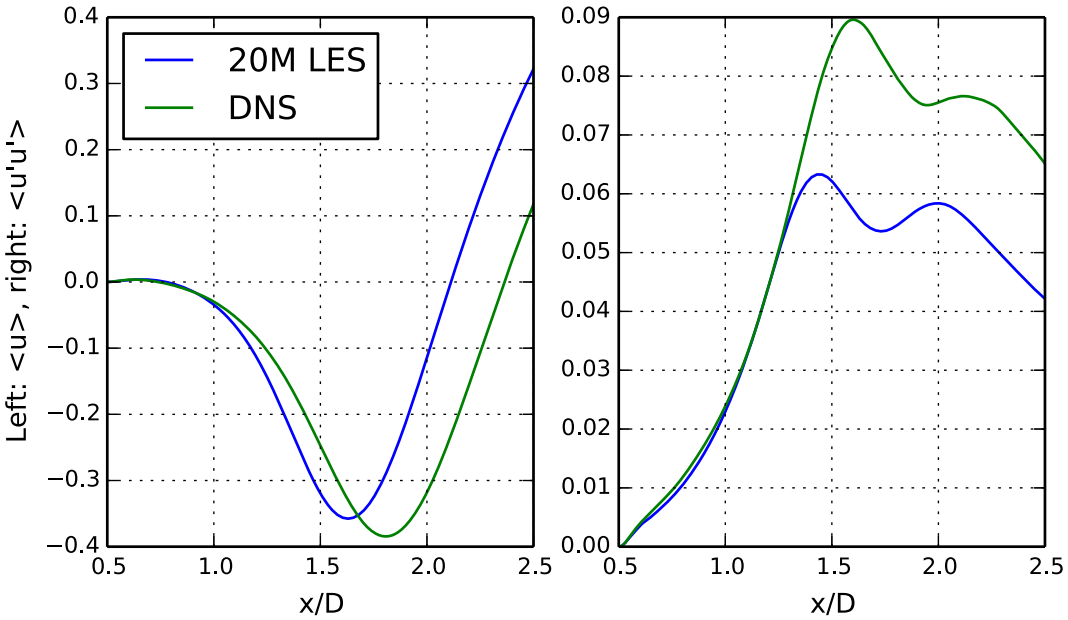

Figure 3: Center-line profiles for $\langle u \rangle$ and $\langle u'u' \rangle$.

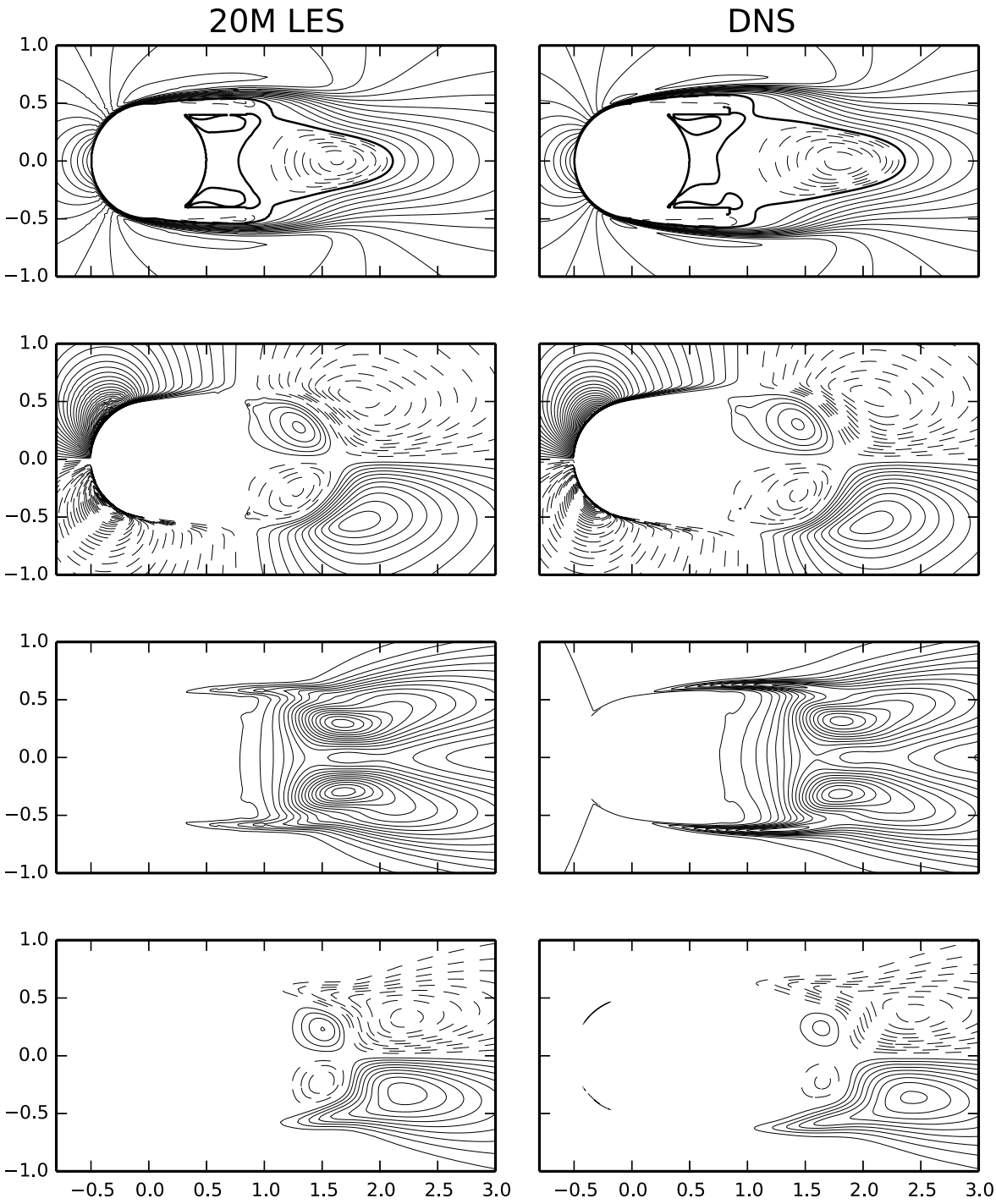

Figure 4: Isocontours of $\langle u \rangle$, $\langle v \rangle$, $\langle u'u' \rangle$ $\langle u'v' \rangle$ (in order from top to bottom) for the 20M LES and DNS respectively. Dashed lines are negative, and a thick line indicate a zero contour (not shown in all plots).

4 Concluding remarks

The DNS and LES presented here do not agree on important statistical flow parameters. Even tough lift and drag forces are captured by the LES simulation, the flow in the wake is not sufficiently accurate to be of any use. *You simply cannot create a mesh, turn on LES and expect the results to be good!*

The difference in computational cost between LES and DNS is not as huge as one might intuitively guess based on the cell counts alone. However, MGLET is a very specialized code and the Cartesian grid facilitates much higher performance than the unstructured grids of OpenFOAM. The internal data structures are very different, and if MGLET can utilize the vector operations available on modern CPUs, while avoid excessive cache misses, that explain much of the higher performance.

In addition to the internal numerics, it is also important to remember that the general concept behind LES is to filter away *isotropic* turbulent scales, while leaving the non-isotropic scales to be resolved. At $Re = 5000$ it is possible that the amount of work saved saved by filtering away these scales are small, because there is little isotropic turbulence present.

5 Further work

This is obviously work in progress. We need to work on the LES and figure out how to get better agreement between LES and DNS. One possible parameter to change is the eddy viscosity model. We believe that a dynamic model in which the Smagorinsky constant C_s is no longer uniform over the domain could be a candidate for a next step in these studies.

We have also access to databases with results from PIV (Particle Image Velocimetry) experiments for the same flow configuration. Comparison of the numerical results with these experiments will be conducted, but problems with statistical convergence will still be an issue in these data.

Additional LES, both with higher and lower mesh resolutions and higher Reynolds numbers are also planned. Due to the computational efficiency of MGLET, it is possible that we will try to do LES with this code as well.

References

[1] M Manhart, F Tremblay, and R Friedrich. MGLET: a parallel code for efficient DNS and LES of complex geometries. In C.B. Jenssen, editor, *Parallel Computational Fluid Dynamics - Trends and Applications*, pages 449–456. Elsevier Science B.V., 2001.

[2] Hrvoje Jasak. *Error analysis and estimation for the finite volume method with applications to fluid flows*. PhD thesis, Imperial College London (University of London), 1996.

[3] Henry G Weller, G Tabor, Hrvoje Jasak, and C Fureby. A tensorial approach to computational continuum mechanics using object-oriented techniques. *Computers in physics*, 12(6):620–631, 1998. URL `http://dx.doi.org/10.1063/1.168744`.

[4] John Crank and Phyllis Nicolson. A practical method for numerical evaluation of solutions of partial differential equations of the heat-conduction type. In *Mathematical Proceedings of the Cambridge Philosophical Society*, volume 43, pages 50–67. Cambridge Univ Press, 1947. URL `http://dx.doi.org/10.1017/S0305004100023197`.

[5] Joseph Smagorinsky. General circulation experiments with the primitive equations: I. The basic experiment. *Monthly weather review*, 91(3):99–164, 1963. URL `http://dx.doi.org/10.1175/1520-0493(1963)091%3C0099:GCEWTP%3E2.3.CO;2`.

[6] Philippe Parnaudeau, Johan Carlier, Dominique Heitz, and Eric Lamballais. Experimental and numerical studies of the flow over a circular cylinder at Reynolds number 3900. *Physics of Fluids*, 20(8):085101, 2008. ISSN 1070-6631. doi: 10.1063/1.2957018. URL `http://dx.doi.org/10.1063/1.2957018`.

Particle Swarm Optimisation

An Alternative in Marine Propeller Optimisation?

Florian Vesting and Rickard E Bensow

Dept. of Shipping and Marine Technology Chalmers University of Technology, 412 96 Gothenburg, Sweden

E-mail: {florian.vesting, rickard.bensow}@chalmers.se

The combination of more available computer resources in personal desktop computers and emerging readily applicable algorithms, inspired from biological phenomena, have made optimisation become feasible in many real-world problems. Especially genetic algorithms (GAs), introduced in the mid-1970s (Holland 1975), are suitable in complex and constrained engineering design problems. Unlike in classical optimisation, GAs are not based on the gradient and continuity of an objective function and most importantly, for multi-objective design tasks, they provide a set of Pareto optimal solutions, from which the final design may be chosen according to the designer's strategy. One of the most popular GAs is the non-dominated sorting genetic algorithm-II, NSGA-II (Deb et al. 2002), which has successfully been applied in marine application (Jung et al. 2007) . However, also GAs have their shortcoming: They are population based and require a large number of evaluations before convergence can be achieved. Hence, we investigate in this paper an alternative optimisation algorithm for the application in propeller design, namely the Particle Swarm Optimisation (PSO) algorithm. Furthermore, the algorithm is extended for multi-objective optimisation through non-dominated sorting procedure and two different perturbation methods are compared to introduce diversity.

The design of a propeller is truly a complex problem. Each design is unique for a certain ship and requires a comprehensive consideration of several constraints such as cavitation, which is in this procedure an omnipresent constraint. It influences the typical objectives, namely propeller efficiency and propeller induced pressure pulses, directly in first order. A common philosophy has been to avoid cavitation within the range of operating condition. Nevertheless, the demand for high efficiency propellers makes this no longer feasible and the presence of cavitation needs to be accepted and considered. Although its development and behaviour is physically profoundly complex and need highly unsteady and computationally costly calculations, it is during the design process with limited time frame, necessary to apply less accurate but faster potential methods. These provide fairly accurate performance predictions (e.g. Lu et al. (2012)) and, with elaborated constraints, have shown to be sophisticated enough to perform optimisation design tasks. Thus we here utilise for the propeller performance, including the prediction of sheet cavitation, the vortex lattice method 'MPUF-3A' (He et al. 2010). The pressure pulses are calculated with a boundary element method, 'HullFPP' (Sun et al. 2007), solving the diffraction potential on a flat hull dummy surface to compute the pressure amplitudes of the first three blade harmonic frequencies. These two tools provide hence the required objectives, namely the propeller efficiency and the pressure pulses.

The PSO emerged in the mid-1990s, introduced by Kennedy et al. (1995) and Eberhart et al. (1995). The concept relies on "flying" a set of prospective solutions, the particles, through the hyperspace and incorporates the idea of a social component controlling the development of the algorithm. Kennedy et al. (1995) developed the algorithm when attempting to simulate the behaviour of swarms. Thus, it is biologically related to motion of e.g. birds and their ability to search the environment to find food sources and avoid predators by information sharing. This motivates a high search efficiency of the PSO. Hassan et al. (2005) found the PSO to arrive at the same high solution quality with less effort for function evaluation than the applied genetic algorithm. However, it appears to be problem dependent, whether the margin in computational efficiency is larger or smaller (Hassan et al. 2005).

Several modifications were proposed to the original algorithm since it was presented by Kennedy et al. (1995), e.g. the inertia weight by Shi et al. (1998) to balance the global and local search. Li (2003) presents a non-dominated sorting PSO which is closely related to the NSGA-II since it uses the same process of non-dominated sorting. We suggest as well a non-dominated sorting PSO which is however slightly different compared to Li (2003) regarding the update of the particle´s personal bests. It begins with an initialisation of particles in the design space, in which each of the N_i particles is assigned with a random position, Eq. (1), and velocity, Eq.(2), in the n-dimensional design space. We omit however the time step length Δt for simplicity in the following equations since it is commonly set to 1.

$$x_{ij} = x_{min} + r(x_{max} - x_{min}), i = 1, \dots, N_i, j = 1, \dots, n \tag{1}$$

$$v_{ij} = \left(-\frac{x_{max} - x_{min}}{2} + r(x_{max} - x_{min}) \right), i = 1, \dots, N_i, j = 1, \dots, n \tag{2}$$

Once the particles are assigned with a position its objectives and constraints can be calculated and the positions of

a particles personal best (x_{ij}^{pb}) and the global best (x_j^{sb}) solutions obtained so far can be determined. These terms can also be referred to as a cognitive component, regarding the personal best, and a social component, regarding the best solution found so far, when updating the particles velocity for the next time step, Eq. (3). The two components determine the degree of a particles self-confidence and its trust in the ability of other members in the swarm to find good solutions.

The particles of the initial swarm are ranked and assigned with the crowding distance, according to the NSGA-II. The following steps are then repeated until the maximum number of time steps is accomplished: A new swarm is introduced equivalent to the child generation in GAs and by mutation of mutation probability p_{mut} modifications are introduced on i) the particles positions (PSO) and ii) the particles velocity (PSOvel). The perturbation is caused by a polynomial mutation operator, as in the NSGA-II, and its impact on the algorithm is compared.

$$v_{ij} = wv_{ij} + c_1 q\left(x_{ij}^{pb} - x_{ij}\right) + c_2 r\left(x_j^{sb} - x_{ij}\right) \tag{3}$$

The mutation is followed by an update of the particles velocities according to Eq. (3), where q and r are random numbers [0, 1] and c_1 and c_2 are constants which are commonly set to 2 to achieve a statistical mean of 1 for the terms $c_1 q$ and $c_2 r$. The inertia weight w is introduced to assign significance to either the cognitive and social component or exploration. When $w > 1$ the particles velocity is assigned with a higher significance and the particle is rather attracted to explore the design space than exploit formerly found best solutions. Since exploration is more important at the early stage of optimisation it is natural to adapt the inertia weight during optimisation advancement towards exploitation. This is achieved by gradually reducing w by a constant factor $\beta \in]0, 1[$. The new velocity is restricted such that $|v_{ij}| < v_{max}$ and eventually the particles position is updated. Figure 1depicts the 2-dimensional interpretation of the velocity update on particle i to time step $k + 1$.

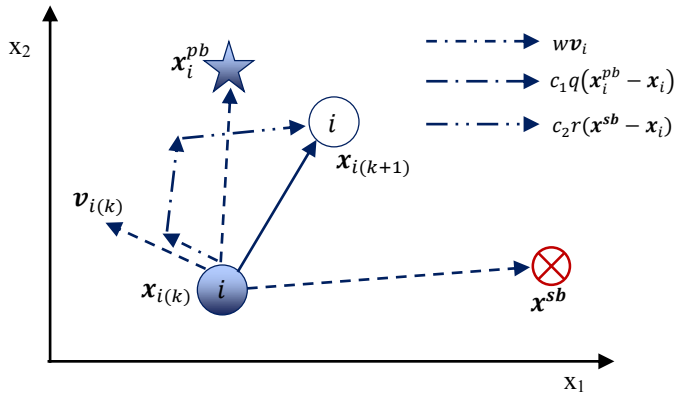

Figure 1 Velocity update on particle i

After evaluation the 2N particles of a combined swarm are ranked and sorted according to their level of non-domination and the swarm is reduced to the new swarm P_i, which is again used to produce the next time step swarm. In PSO the update of x_{ij}^{pb} and x_j^{sb} follows the rather plain approach to substitute the best as soon as one objective is improved compared to the stored value. In PSOvel however, a sum of the objectives is formulated. The best are updated in case the sum is smaller.

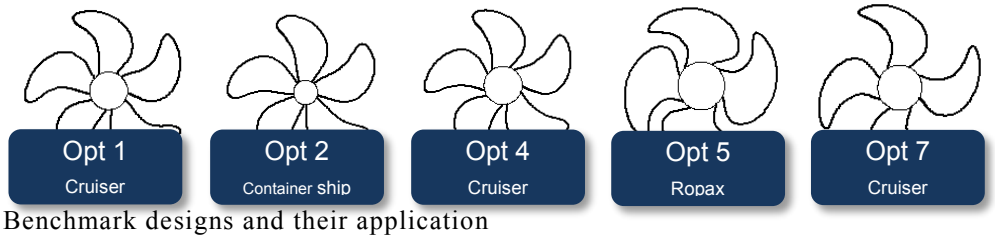

Figure 2 Benchmark designs and their application

In the following we investigate the optimisation behaviour of five benchmark propellers of different design and for different application, Figure 2. The designs are provided by the Rolls-Royce Hydrodynamic Research Centre (RRHRC), Kristinehamn, Sweden, and correspond to a preliminary design, based on early calculations of the project Propeller parameters like the diameter and the operation condition at the design point are already determined. The design task at hand is thus about finding the wake adapted optimal blade geometry. This is, at this point of the design phase, described by standard distribution curves, which are based on experience and design philosophy. Parameters like the blade area ratio or the skew angle at the blade tip are used to modify the

corresponding curves and thereby change the propeller geometry. In total eight parameters as such are applied in the optimisation for the distribution of: Chord, Skew, blade thickness, Rake and Pitch. The latter was only controlled by unloading factors for the root and tip region.

Constraints are selected according to the Rolls-Royce common design procedure. This includes a constraint for a minimum K_T to meet the required thrust and constraints for the dynamic blade stress which is calculated at three different positions on the blade and from which the maximum von Mises stresses are taken at MCR condition. The maximal suction side cavitation volume on the blade, predicted by MPUF-3A is constrained to be reduced compared to the initial design by 5 %. The same holds for the cavitation length. Furthermore, constraints are applied for the corresponding class rules and geometric circumstances like blade collision control (for CPP). The optimisation problem reduces thus to find the best compromise of eight input parameter to $\min\left(f_1(\boldsymbol{x}), f_2(\boldsymbol{x})\right)$ as subject to $g_j(\boldsymbol{x}) \geq \vee \leq limit_j, j = 1, \ldots 6$ inequality constraints.

Optimisations have been fulfilled for the test propellers utilising NSGA-II, PSO and PSOvel on each of the cases. In total 15 optimisations with a target of 40 generations each. For the assessment of the results we restrict ourselves mainly to the median of a population in each generation. The median of a generation is the best indicator in case of a possibly skewed distribution of solutions. The numerical tool produces de facto from time to time nonsense results that mislead the generation mean. To evaluate the performance of the optimisation algorithm we classify the assessment into the categories *performance*, *convergence* and *geometry*, to rate if the optimisation was actually able to improve the design and to rate the confidence of the optimisation to actually find the global optimum. This will be confirmed by a converged geometry, which ideal should be the same regardless of the optimisation algorithm used.

Important in optimisation problems is naturally the validity of the results. For this, we utilise the validity ratio between the number of valid variants and the population size, Figure 3. Form this it is evident that the algorithm aim to produce valid results by improving the number of valid solutions significantly within the first five generations. However, as the optimisation proceeds, validity is sacrificed for exploration. The NSGA-II provides yet the highest ratio of valid results by the end of the optimisation compared to both PSO algorithms. In case of Opt-5 it is the only algorithm that manages to find valid solutions. For Opt-1 and Opt-2, the PSO shows ability to maintain or at least slightly improve the validity after it dropped during the progress. This is different for the PSOvel, as once it starts following a certain trend it cannot recover towards higher validity, Opt-4 and Opt-5.

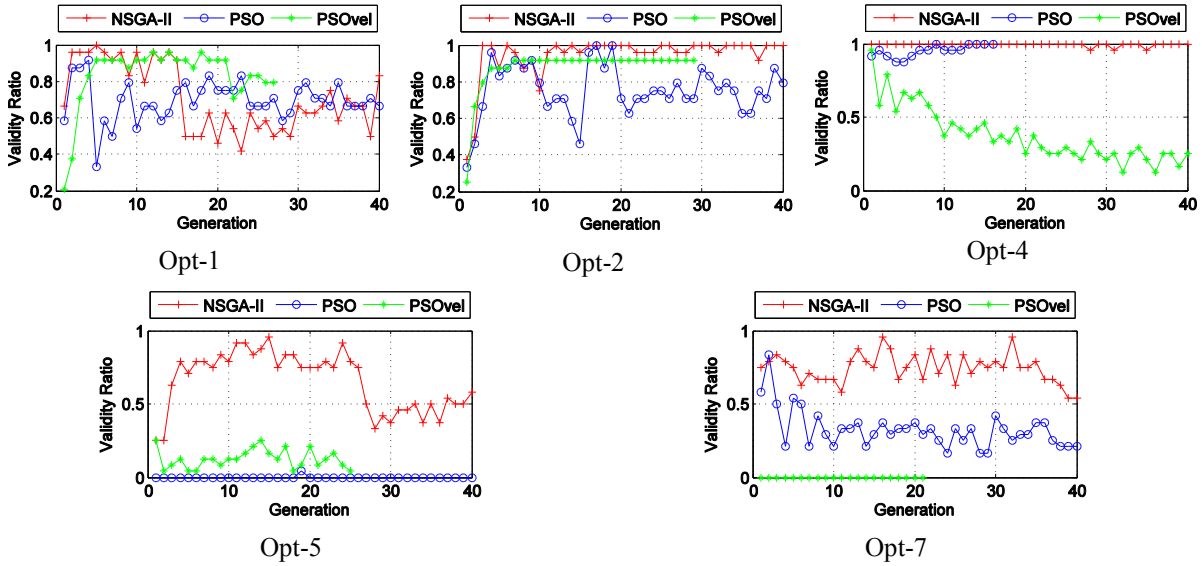

Figure 3 Validity ratio

Figure 4 shows the approximation of the Pareto front. For each propeller the solutions of all three algorithms are included in the plot. A distinct Pareto front determination depends clearly on the formulation of the optimisation problem. The most obvious Pareto front can be seen for the case Opt-2, Opt-4 and Opt-7. It is also evident by the indication of the median of the final generation, in Figure 4, that each algorithm found its own global optimum. Yet the NSGA-II is in all cases closest to a Pareto optimal solution. This is also supported by Figure 9, which shows the progress of the algorithms through the generation median. The NSGA-II provides for all cases the best trade-off between the two objectives. The PSOvel however, can be considered as converged in both objectives for cases Opt-2, Opt-4 and Opt-5.

Figure 5 to Figure 7 presents the final accordance of geometry that develops during the progress of the algorithm.

The most frequent agreement was achieved for the NSGA-II and the PSO algorithms. In case of Opt-1, seven out of eight parameters medians agree after convergence. Figure 5 shows only three parameters, but for all cases it is essential to notice that the NSGA-II also settles early in the progress. An agreement between the geometry of PSO and PSOvel is achieved particularly when the algorithm settles within the first 5 generations towards an extreme parameter value close to or at the boundary, Figure 6. This holds also for the agreement of geometry for all three algorithms as shown in Figure 7.

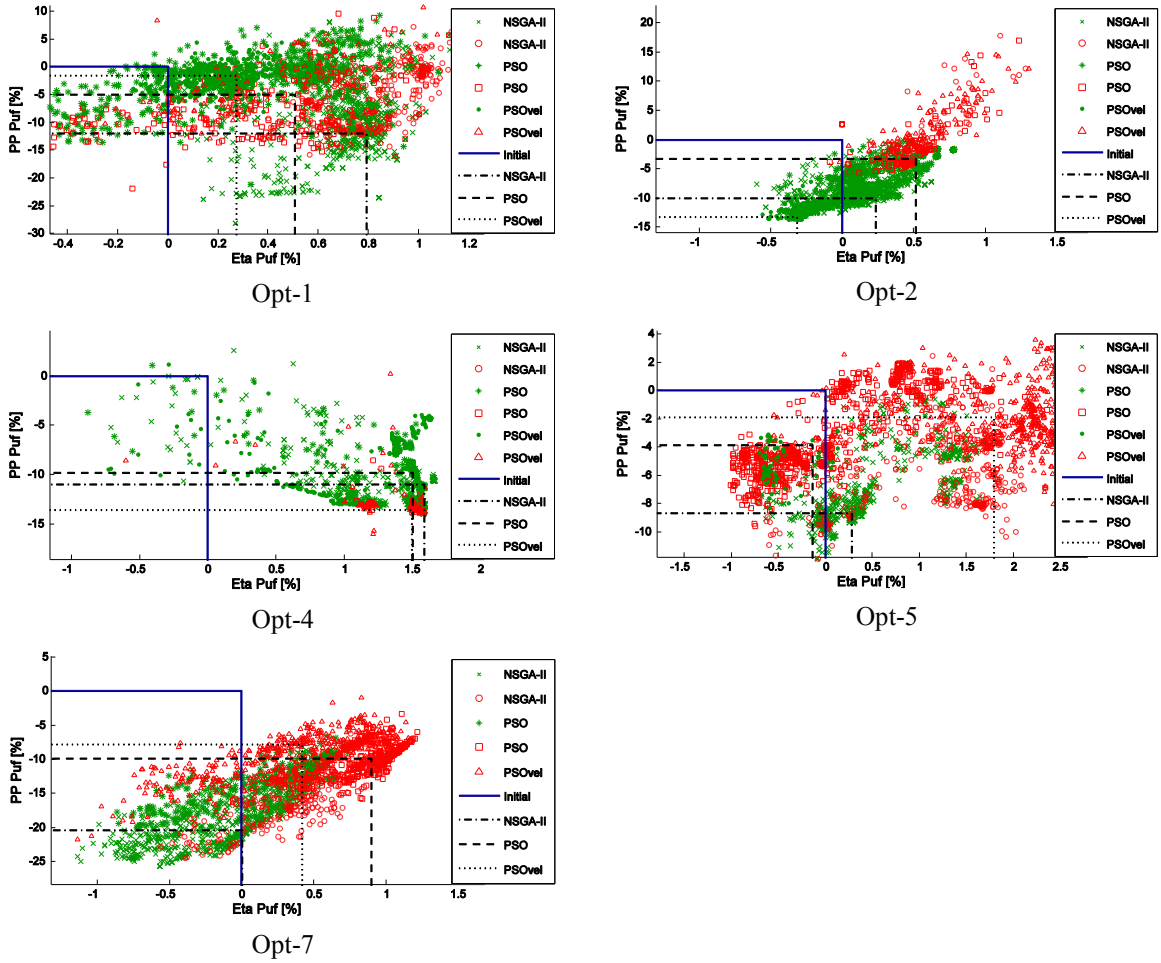

Opt-1 Opt-2

Opt-4 Opt-5

Opt-7

Figure 4 Approximation of Pareto front.

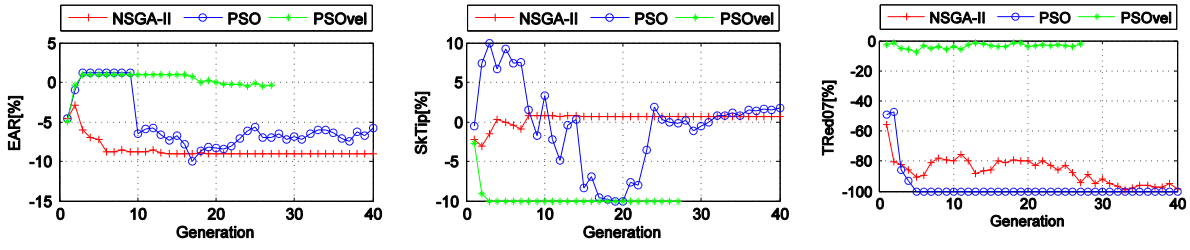

Opt-1 Opt-1 Opt-1

Figure 5 Accordance in final geometry as generation median of PSO and NSGA-II

The development of the algorithms with regard to the two objectives is shown in Figure 9, where we plot again the generation median. These figures show that in almost all cases convergence was achieved by the algorithms. Although for Opt-1 and Opt-5 convergence was either reached for the efficiency or the pressure pulses. Apparently the algorithm still varies input parameters to satisfy the second objective as well, which can be seen from an oscillating second objective. These plots reveal also the preservative behaviour of the PSO algorithms to develop a clear and steep trend towards a certain objective value at the beginning of the progress. This abates rapidly within the first 10 generations and the algorithms converge premature. In Opt-2, Opt-5 and Opt-7, the PSO algorithms offer the highest improvement in one objective sacrificing the other. Although PSOvel includes the sum of objective values to determine and the global best (x_j^{sb}) solutions, this behaviour is particular obvious from the

PSOvel. The NSGA-II however offers the best compromise between the objectives through expanded exploration.

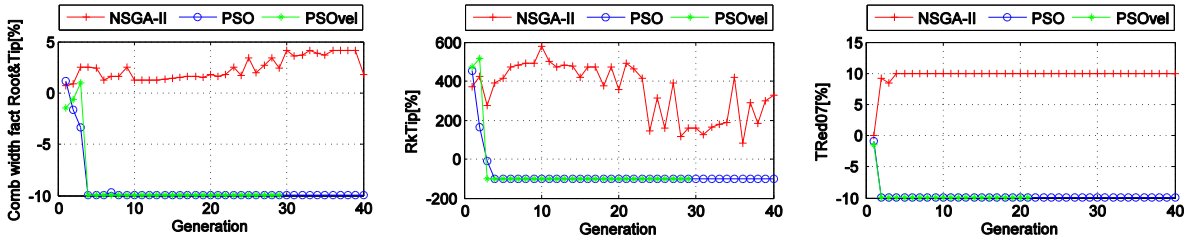

Opt-2 Opt-2 Opt-7

Figure 6 Accordance in final geometry as generation median of PSO and PSOvel

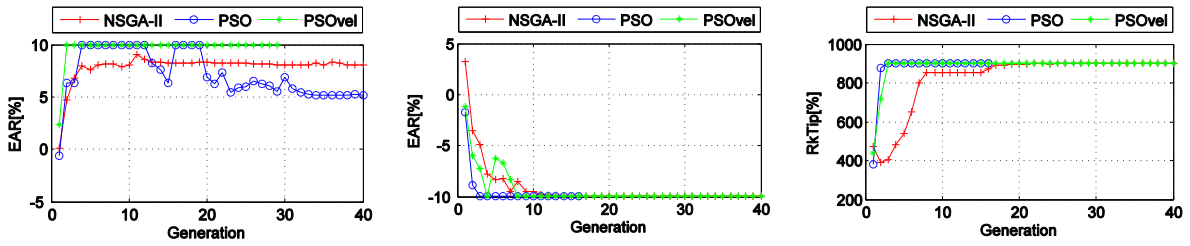

Opt-2 Opt-4 Opt-4

Figure 7 Accordance in final geometry as generation median of all algorithms

The overall performance of the algorithms can be considered as successful. As it is evident from Table 1, each optimisation case could be improved by the algorithms. Table 1 provides the results from selected optimised individuals of each optimisation run, relative to its corresponding initial performance. Naturally, the possible improvement depends on the starting point. Among the present cases, Opt-2 and Opt-4 showed the highest potential for improvement. Figure 9 gives an overview of the performance of the algorithms from a competition in which each algorithm received a score in a range [0, 1] depending on its performance in each category (efficiency, pressure pulse, cavitation volume and von Mises stresses). Hence a high score corresponds to a good performance. The left graph in Figure 9 is based on the individual optimal designs while the right diagram is based on the generation median of the last generation. The NSGA-II is accordingly the designated winner. It outperforms most frequently the improvements of the PSO algorithms. However, not measured in this contest is the convergence rate. Both PSO algorithms converge early to a certain geometry and thus require less evaluations. Most frequently did the PSO algorithms provide extreme solutions for one objective, while the NSGA-II always provide the best trade-off between the objectives. Hence the PSO algorithms offer a semi non-dominated optimisation that focus on one objective. This can be laid to one objective, if the others margin is significantly higher, as e.g. in case of the pressure pulses. On the other hand, the tournament selection process can possibly be employed for the update of the global best solution to ensure the best compromise.

Table 1 Improvements compared to initial design for each algorithm

	Opt-1			Opt-2			Opt-4			Opt-5			Opt-7		
	NSGA-II	PSO	PSOvel	NSGA-II	PSO	PSOvel	NSGA-II	PSO	PSOvel	NSGA-II	PSO	PSOvel	NSGA-II	PSO	PSOvel
ETA	0.45%	0.39%	0.31%	-0.14%	0.05%	-0.32%	1.67%	1.57%	1.63%	1.78%	1.11%	2.32%	0.12%	-0.03%	-0.23%
PP	-12.55%	-7.82%	-2.96%	-9.65%	-5.52%	-13.45%	-10.70%	-11.05%	-4.30%	-6.07%	0.64%	2.13%	-19.08%	-18.94%	-12.36%
CavVol	-20.64%	-5.00%	-19.80%	-11.84%	-6.77%	-14.11%	-100.00%	-100.00%	-100.00%	248.01%	53.77%	125.26%	0.00%	0.00%	0.00%
FEM	-17.60%	-7.13%	-20.96%	-31.70%	-29.24%	-26.35%	-1.04%	-1.82%	-4.91%	-10.57%	9.83%	44.20%	-15.55%	-16.73%	-24.97%

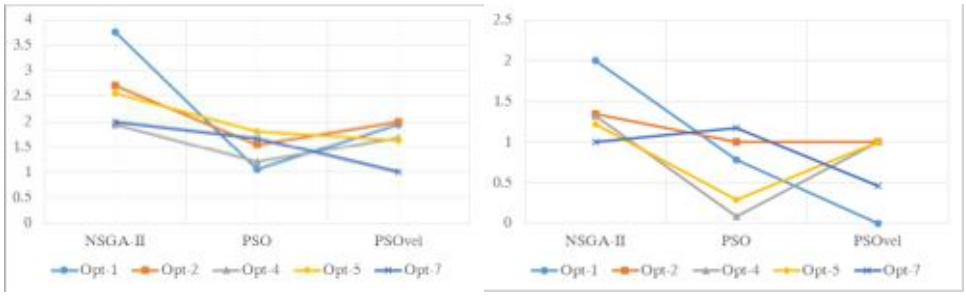

Figure 8 Competition of the algorithms; left by selection of individual optimised solution; right by generation median

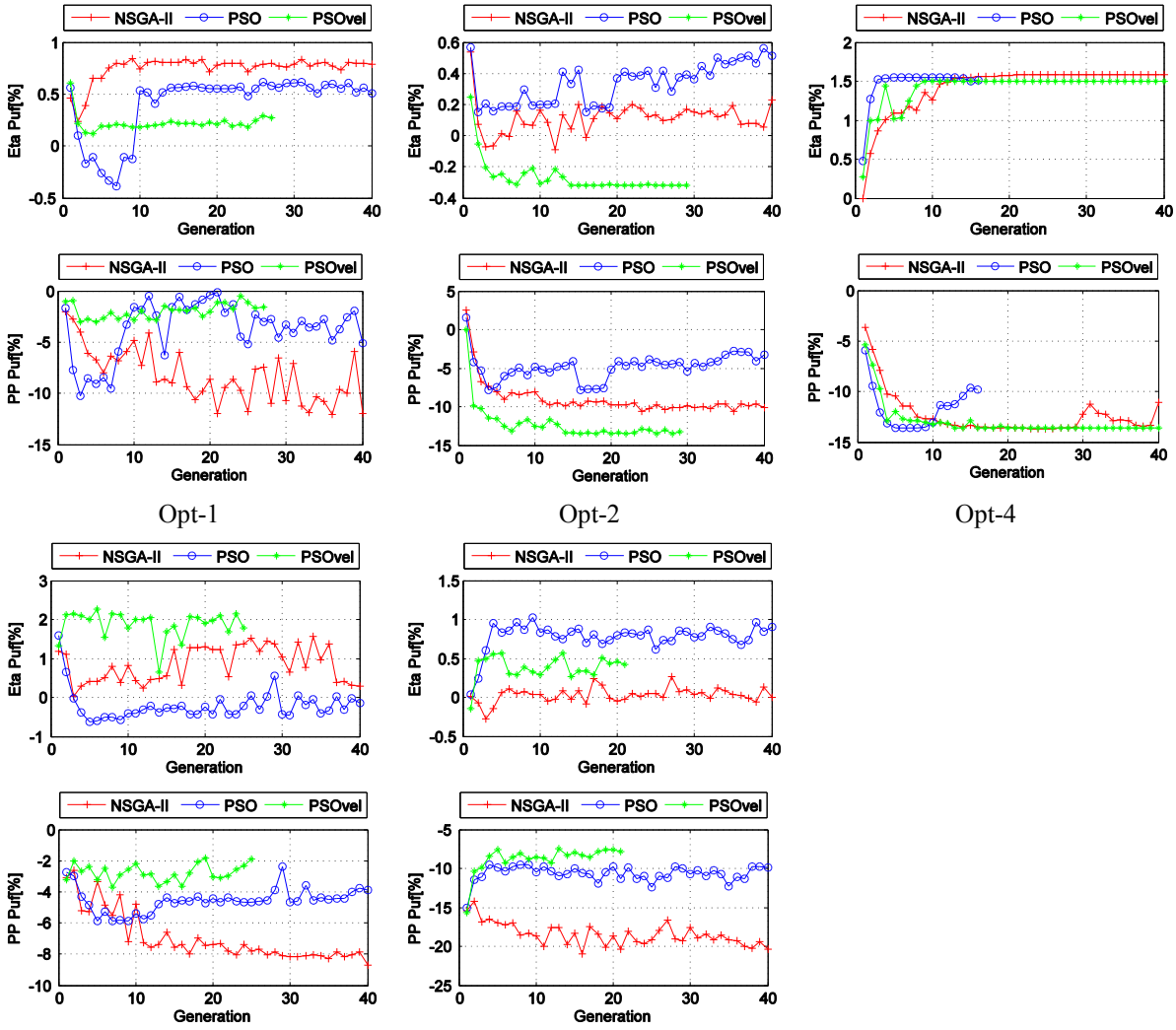

Figure 9 Progress of the algorithms as median of each generation

REFERENCES

Deb, K., Pratap, A., et al. (2002). 'A Fast Elitist Multi-Objective Genetic Algorithm: NSGA-II'. IEEE Transactions on Evolutionary Computation **6**.

Eberhart, R. & Kennedy, J. (1995). 'New optimizer using particle swarm theory'. Sixth International Symposium on Micro Machine and Human Science.

Hassan, R., Cohanim, B., et al. (2005). 'A Comparison of Particle Swarm Optimization and the Genetic Algorithm'. 1 st AIAA Multidisciplinary Design Optimization Specialist Conference, Austin, Texas.

He, L., Chang, S., et al. (2010). MPUF-3A Version 3.0. Austin, University of Texas.

Holland, J. H. (1975). Adaptation in natural and artificial systems : an introductory analysis with applications to biology, control, and artificial intelligence. Ann Arbor, University of Michigan Press.

Jung, J., Han, J. M., et al. (2007). 'Design of marine propellers using genetic algorithm'. 10th International Symposium on Practical Design of Ships and other Floating Structures, PRADS 2007.

Kennedy, J. & Eberhart, R. (1995). 'Particle swarm optimization'. IEEE International Conference on Neural Networks - Conference Proceedings.

Li, X. (2003). A Non-dominated Sorting Particle Swarm Optimizer for Multiobjective Optimization. Genetic and Evolutionary Computation — GECCO 2003. E. Cantú-Paz, J. Foster, K. Debet al, Springer Berlin Heidelberg. **2723**.

Lu, N. X., Svennberg, U., et al. (2012). 'Numerical Simulations of Cavitating FLow on Marine Propeller'. 8th International Symposium on Cavitation, Singapore.

Shi, Y. & Eberhart, R. (1998). 'Modified particle swarm optimizer'. Proceedings of the IEEE Conference on Evolutionary Computation, ICEC.

Sun, H. & Kinnas, S. (2007). HULLFPP, HULL Field Point Potential. Austin, University of Texas.

Application of a homogenous two-phase model to the free surface problem

Ville Viitanen
VTT Technical Research Center of Finland

I. Introduction

This study presents a part of the master's thesis of the author. That work still in progress. The thesis is partly based on the recent development process for the extension of Reynolds-Averaged Navier-Stokes (RANS) solver Finflo to the two-phase methodology (Miettinen et al., 2006), and the intent here is to demonstrate the applicability of this approach to the free surface problem. One should note that the free surface problem is essentially a special case in two phase flows. The problem is solved with a homogeneous mixture model, *i.e.* the continuity equation is conditioned with the void fraction, and the momentum equations are solved for the mixture. This procedure is commonly known as the cavitation model in the literature. It has been implemented to simulate, for instance, cavitating propeller flows. In this paper, the model is in essence used as it is. The convection equation of the void fraction α traditionally used within VOF-solution strategy is used interchangeably with that of the mass fraction x.

The free surface problem is taken as the unidirectional and two-dimensional flow over a submerged ground elevation. The case corresponds to so-called sub-critical situation. The computational case provides interesting comparison since exactly the same problem has been previously computed with the same code, but using the interface tracking approach (Mikkola, 1999). The method is also compared to the results of Bet et al. (1996) and Mikkola (2009).

The governing equations and solution procedure of the code Finflo are presented. In order to avoid unnecessary lengthy reporting, only the main features are described and a more thorough discussion will be given in the thesis. Subsequently, the problem is defined and the solution domain described. Finally, results are provided from the computations.

II. Governing equations

The solution is based on the conservation of mass of each phase and the momentum of the mixture. The former is in differential form for the fluid k

$$\frac{\partial \alpha_k \rho_k}{\partial t} + \nabla \cdot \alpha_k \rho_k \vec{V} = \Gamma_k \tag{1}$$

where α_k is the void fraction for the k:th fluid, and ρ_k its density. The continuity equation can be written with the mass fraction

$$\frac{\partial x_k \rho}{\partial t} + \nabla \cdot x_k \rho \vec{V} = \Gamma_k \tag{2}$$

since the mass and void fractions are linked via $x_k \rho = \alpha_k \rho_k$, and ρ is the mixture density. The void fraction is used in extrapolations of the mass fluxes to the cell faces, and Eq. (2) is used in the implicit stage since the mixture density can be used. The conservation of momentum for the mixture is

$$\frac{\partial \rho \vec{V}}{\partial t} + \nabla \cdot \rho \vec{V} \vec{V} + \nabla p = \nabla \cdot \tau_{ij} + \rho \vec{g} \tag{3}$$

where p is the pressure and τ_{ij} the stress tensor, and $\vec{g}$ the acceleration due to gravity. The effects of turbulence result in the Reynolds-averaged sense into an additional stress tensor that can be combined with τ_{ij}.

The two-phase flow equations are formally the same as in the case of single-phase flow. Note that the averaging required for decreasing the two fluid system into a single field representation is achieved through the conditioning of the conservation of individual phase mass. The approach taken here treats the fluid properties as discontinuous across the interface separating them. These are defined as

$$\phi = \sum_k \alpha_k \phi_k \tag{4}$$

where ϕ is any material property, *e.g.* density. Two fluids accompanying the same computational cell share the same velocity and pressure. The fact that they are treated as a mixture requires the time evolution of the void fraction that is convected with the flow. This follows the solution of the bulk flow equations and is based on the conservation of individual phase mass.

III. Numerical method

The numerical solution of the governing equations is based on the cell centered, multi-block structured finite volume technique. A general form of the governing equations is

$$\mathcal{V}_i \frac{dU_i}{dt} = \sum_j -(\vec{F} - \vec{F}_v)_j \cdot \vec{n}_j S_j + \mathcal{V}_i Q_i \tag{5}$$

where U_i is the unknown variable for cell i, $\mathcal{V}_i$ its volume, $\vec{F}$ the convection flux vector, $\vec{F}_v$ the diffusion flux vector, $\vec{n}_j$ the surface normal of the cell face j and S_j its area. Q_i contains the contribution from the possible source terms. The field equations can be presented in a semi-discretised form

$$\mathcal{V}_i \frac{dx_i \rho_i}{dt} + \sum_j \rho_j \bar{u}_j x_j S_j = \mathcal{V}_i \Gamma_i \tag{6}$$

$$\mathcal{V}_i \frac{d\rho_i \vec{V}_i}{dt} + \sum_j \rho_j \bar{u}_j \vec{V}_j S_j + \sum_j \vec{n}_j p_j S_j = \sum_j \tau_{ij} \cdot \vec{n}_j + \mathcal{V}_i(\rho_i - \rho_\infty)\vec{g} \quad (7)$$

where the sum over j denotes summation over all the faces S_j bounding the control volume i, and $\bar{u} = \vec{V} \cdot \vec{n}$ is the convection velocity. The viscous stress tensor is

$$\tau_{ij} = \mu \left(\frac{\partial u_j}{\partial x_i} + \frac{\partial u_i}{\partial x_j} - \frac{2}{3} \frac{\partial u_k}{\partial x_k} \delta_{ij} \right) - \left(\rho \overline{u_i' u_j'} - \frac{2}{3} \rho k \delta_{ij} \right) \quad (8)$$

where the additional stress tensor appears due to turbulence, and k is the kinetic energy of turbulence. Here, the $k - \omega$ SST model is used as it is.

The source term in the continuity equation denotes the mass transfer. It is driven by the pressure difference compared to the saturation pressure. Now, the mass transfer is set to zero. Additionally the dependencies between the input free stream values of the pressure, temperature and cavitation number have been disabled. However, some of the features of the cavitation model are still active such as the relationship between temperature and density of the gas phase. The energy equation is currently disabled. For details, see the work of Siikonen (2009).

The basic solution algorithm is based on the pressure correction method of the SIMPLE type. It has been developed specifically to handle two-phase flows and the interfaces between them, and is based on the linearisations of the continuity equations (2) for both phases (Miettinen et al., 2006). The Rhie and Chow type damping term is applied in the calculation of the convection velocities. Recently, some novel features have been included in the algorithm. These features resemble those used in traditional density-based methods. The residuals of the unknown variables are calculated simultaneously and only once during an iteration cycle; in traditional pressure correction methods this is done sequentially and in various parts of the procedure. This corresponds to the transformation matrix used in density-based methods to change the residuals of the conservative variables into those of primitive variables. The momentum residuals are transformed through

$$\rho \Delta \vec{V} = \Delta(\rho \vec{V}) - \vec{V} \Delta \rho \quad (9)$$

The same procedure is done for the scalar variables. The error in mass balance from the previous iteration cycle $\Delta\rho$ is eliminated from the residuals (otherwise the equations must be solved coupled to each other). Now the mass imbalance does not contribute to the error made in the calculation of momentum balance. Siikonen (1987) used similar procedure for the solution of the energy equation. In this approach the complexity of the coupled set of equations is avoided by manipulating the explicit residuals.

The implicit stage is based on the standard convection-diffusion equation with first order upwinding for convective fluxes and central differencing for the viscous fluxes. Now the implicit stage is the same for the convection equation of the mass fraction x, Eq. (6), as it is for the momentum equations since the mixture density was used, but without the diffusion term. The discretised equations are integrated in time using the DDADI-factorisation (diagonally dominant alternating direction implicit). The equations are integrated until a steady state is reached.

In the explicit stage for the bulk flow, the inviscid fluxes are evaluated using the Roe's method, and the viscous fluxes with the thin layer approximation. Instead of the mass fractions, the void fractions α are used. This is done for accuracy reasons, since the values need to be interpolated on the cell faces. That is, terms like $x\rho$ are replaced by equivalent expression involving the void fractions, or $x_j \rho_j = \alpha_j \rho_g$. In addition, a constant density can be used. Only one value for the void fraction is needed, for $\alpha_g + \alpha_l = 1$, where g denotes the gas and l the liquid phase. A common choice is $\alpha_g = 1 - \alpha_l = \alpha$.

The convective fluxes are $\alpha \rho_g \bar{u}$, and these require the interpolation of the void fraction to the cell face. It is a well known problem that the interpolation (or extrapolation) of α, that is actually a step profile, may become smeared over multiple cells due to numerical diffusion or to possess unphysical over and under shoots due to numerical dispersion (Darwish and Moukalled, 2006; Leonard, 1991; Queutey and Visonneau, 2007). Such effects are inherent in most robust interpolation schemes, and they can spoil the resolution of the interface if special care is not taken in construction of the method. At present, this interpolation is done using the second order MUSCL formula supplied with a limiter that satisfies the TVD conditions. This is done to suppress the possible formation of new extrema that may form when using higher order schemes. The default choice is the limiter of van Albada. Within this work, the SUPERBEE limiter was implemented since it has favourable features concerning the nature of the problem. SUPERBEE tends to change smooth gradients into a sharp steps as shown by Leonard (1991) which is precisely what is needed here. In fact, it is designed for computations involving contact discontinuities. It may however provide artificial stepping in cases where the flow is not aligned with the computational grid. In addition, the use of flux limiters may produce entropy violating results especially if the scheme is compressive. Results using both limiters, together with non-limited results, are given in Sec. V.

IV. Computational case

The flow of water over a ground elevation submerged to a finite depth is a common test case for flow solvers with free surface resolving capability. The case is computed here with two different grids, and with three different interpolation schemes applied for the convection term. The computations by Mikkola (1999) have been performed with same code that is used in this work but with the free surface tracking method. Mikkola (2009) present the results of the tracking method of his code Yaffa. Bet et al. (1996) used both the tracking method as well as a level-set method to compute the case.

The ground elevation is of Gaussian shape and given by the expression

$$y = y_0 + A\exp(-\beta^2(x - x_0)^2) \qquad (10)$$

where $y_0 = -1$, $A = h - h_b$, $\beta = 1$ and $x_0 = 0$ are chosen to match the other computations. The present case corresponds to a so-called subcritical situation, *i.e.* the depth based Froude number $Fn_h = 0.567 < 1$ (Lowery and Liapis, 1999). The center of the bump located at $(0, -0.9)$. The grid constructed for the computations extends from -30 to $+30$ in x-direction and from -1 to $+5$ in y-direction. The long and high domain ensures senselessness to far-field boundary conditions.

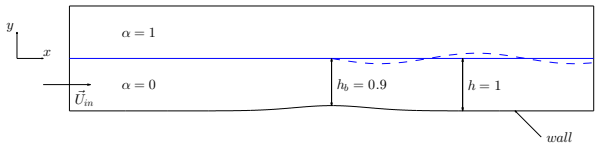

Figure 1: *A schematic view of the submerged ground elevation. The solid blue line depicts the initial free surface level and the dashed gives hint on the formation of the wave downstream of the bump*

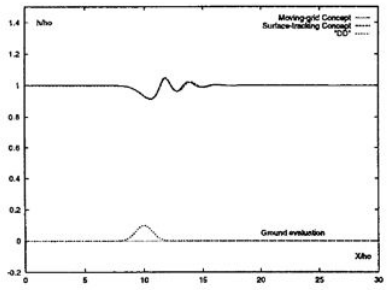

Figure 2: *Computed free surface profile by Bet et al. (1996). h_0 is the height of the undisturbed free surface*

A schematic view of the case is given in Fig. 1 with the initial distribution of the void fraction α. Acceleration due to gravity is in the negative y-direction. The depth based Froude number is set to $Fn_b = |\vec{U}_{in}|/\sqrt{gh_b} = 0.567$. At the lower wall, the no-slip boundary condition is applied, and on the upper wall, the mirror boundary condition is applied.

Finflo is a three-dimensional RANS code, obliging one to use three-dimensional computational grids. The code uses small Reynolds number models, hence the grid needs appropriate resolution in the boundary layer. The first cell height is set to $y = 1 \times 10^{-5}$ m for which $y^+ \approx 1$. A finite and large transverse dimension is used so that the flow would be two-dimensional at least at the centerplane of the domain.

The computed, quasi-steady interface is to resemble that of Fig. 2. The wave length is $\lambda \approx 2\ x/h_0$ with the approximate maximum amplitude $A \approx 0.1\ y/h_0$. In this study, a resolution of consisting at least 30 computational cells for both is assumed to suffice. This sets the limits around the interface to $\Delta x \leq 0.067\ x/h_0$ and $\Delta y \leq 0.0033\ y/h_0$.

Since an intention was to use the recent developments of the VOF method of the code Yaffa (cf. Hänninen and Mikkola (2007)) for reference computations in the master's thesis, two computational grids were constructed. The code Yaffa is run only on a single processor, and for a case to be computed in comprehensible amount of time, the grid resolution must be adjusted accordingly. Finflo uses multiblock structured grids, *i.e.* problems can be run in parallel. Two grids were constructed for the computations with Finflo. Comparison can be facilitated with the use of exactly the same grids (except for the boundary layer), but the parallelisation of Finflo is utilized with a much more dense grid. This comparison however will not be presented here.

The computational grids were constructed based on the considerations above. The coarser grid near the bump is shown in Fig. 3, and the finer in Fig. 4. The coarser grid has the resolution of $\Delta x = 0.05$ m and $\Delta y = 0.0033$ m for the interface and 640 000 cells in total. The finer grid has the resolution of $\Delta x = 0.0095$ m and $\Delta y = 0.0033$ m for the interface and 2.7 million cells in total. Both include numerical damping zones in the far upstream and downstream regions $x < -10$ m and $x > 10$ m.

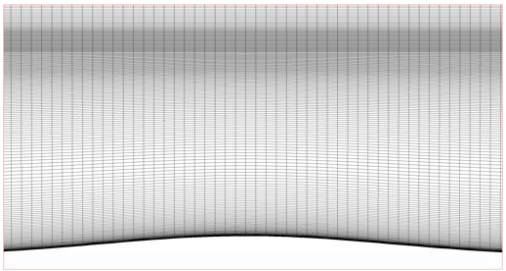

Figure 3: *A close-up view of the coarser grid near the elevation*

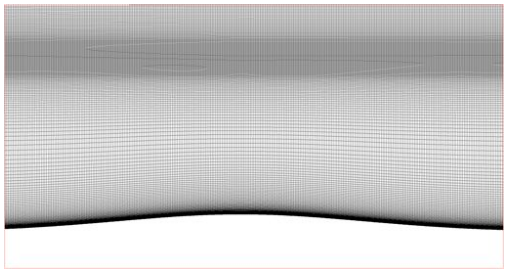

Figure 4: *A close-up view of the finer grid near the elevation*

V. Results

The computations with Finflo are performed on three grid levels for both grids. This is straightforward in structured grids. A converged result is computed on a coarser grid level, and the result used as an initial guess for the finer grid level. This is done for the non-limited and the van Albada limited cases. The SUPERBEE limiter is activated for computations whose initial guess is the van Albada limited computations on the second finest grid level. All results presented here are on the finest grid level. The non-limited results are presented only for the coarser grid (Fig. 3).

An exemplary convergence plot is given for the van Albada limited computations using the coarser grid. Fig. 5 shows the convergence of the explicit residual $\Delta\alpha\rho_g$.

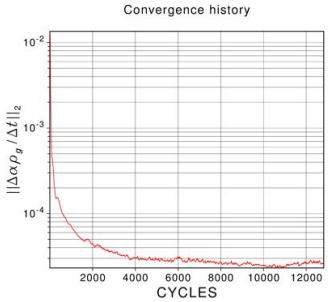

Figure 5: *Convergence of the explicit residual $\Delta\alpha\rho_g$ of the computations with the coarser grid and using the van Albada limiter*

Results using the fine grid are shown in Figs. 6 and 7. They provide an overview of the forming wave field behind the ground elevation as well as a closer view of the interface resolution near the bump. Fig. 8 show the non-limited and the SUPERBEE limited results using the coarser grid. In that case, the van Albada limited results are very close to those obtained with the SUPERBEE limiter and would be undistinguishable in Fig. 8.

The comparison of the present calculations to those of Bet et al. (1996) and Mikkola (1999, 2009) are given in Fig. 9. The computed results are in terms of the contour $\alpha = 0.5$.

VI. Discussion

The free surface problem can be considered as a special case in two-phase flows. Thus it is very interesting to apply the mixture model as it is. In this work, the features of the cavitation model that are related to the cavitating situations per sé have been inactivated. Only the dependency of the material properties of the convection of α (or x) is retained. This convection is driven by the local flow solution via the contravariant velocity $\bar{u}$. Hence, the equation system in principle reduces to that traditionally used in the VOF-type strategy for capturing the free-surface.

As was pointed out, the algorithm itself works for the two separated phases. The hydrostatic pressure is present since the body force due to gravitation is needed in simulations like these, and *seems* to cause no trouble. Thus, the known issue regarding the sharpness of the interface is briefly addressed here with implementation of the compressive SUPERBEE limiter. The results are compared with the van Albada limiter that is currently the default choice for the extrapolation of α to the cell face. For completeness, a calculation is performed without limiting the $\alpha_{i+1/2}$. Upon inspecting the results obtained with the finer grid, Figs. 6 and 7, the updated limiting seems to perform as expected. The interface obtained with the default scheme appears somewhat smoky, whilst the updated scheme seems to compress the interface better. This behaviour is visible also throughout the wave formation. The better performance is not so obvious from the contour of $\alpha = 0.5$ in Fig. 9, which is usually considered as the representation of the free surface. The default scheme approximates the wave troughs either equally as well or better than the new one. The wave crests however support the observations of the former figures. In addition, there seems to be a small phase shift between these two computations. The overall resolution of the finer grid can be considered as good, and it seems to estimate the wave formation more accurately than some of the comparative results.

The computations using the coarser grid predict the first wave equally as well as the finer one, but afterwards the interface becomes more and more smeared. Surprisingly, these computations predict the first wave crest better than the computations using the finer grid, where they overlap with the results of Bet et al. (1996) and Mikkola (1999). This is particularly puzzling since the finer grid is over five times denser in the horizontal direction. The effects of this can then again be seen in the other developing waves, as should have been expected. The consequences of the different cell aspect ratio are not clear on the interface, and testing should be continued. In addition, the use of the compressive scheme on the coarser grid does not result to better resolution. The two computations overlap each other in most parts of the forming wave. The exclusion of the

flux limiter once again proves the need for special attention in the interpolation or extrapolation of the void fraction to the cell faces. Also for some reason, few computations predict distinctly non-symmetric wave profiles around the level of $y = 0$.

Fig. 5 gives an exceptionally favourable convergence history. The downward slope is dominant and a quite steady level is reached relatively soon. This is also due to the good initial guess provided by the readily converged result from the previous grid level (the converged level may not yet be considered as sufficient however). Based on the author's experience on numerical simulations of two-phase flows so far, the convergence histories can come with most exotic shapes, and they may shoot up and back down for several orders of magnitude rather abruptly, even after tens of thousands of cycles. In the solution, these have been seen as oscillatory velocity fields in some parts of the domain, or un-physical 'wandering' of the free surface, for instance. The calculations are mostly converged on some level as these are damped away; sometimes it has been necessary to lower the order of the interpolation scheme of the bulk flow to provide enough of such damping. Additionally, in the damping zones of the finer grid a low order extrapolation was used for this reason. Another, though completely different, problem can follow from the reflective boundary conditions.

The present results were underrelaxed rather heavily. For example, the Courant number was between $0.1 \ldots 0.2$. Also, the drag coefficient continued to decrease steadily but very slowly, especially for the finer grid. The computations have most likely not reached a converged level, and they will be continued. The final results will be presented in the thesis. The calculations have severe stability issues without proper underrelaxation. The relaxation factor for pressure has been as low as $\alpha_p \approx 0.01$ in some cases. This may be a reason for the phase shift still visible. Mikkola (2009) also reports the different grid resolution a possible cause of this.

The testing of the mixture model is far from complete. Some free stream properties are still computed in an untypical way for a traditional VOF model, and it is intriguing to find out the essence of the novel pressure correction strategy with respect to the free surface problem. The smoky behaviour certainly requires attention, and the use of the limiters may be problematic outside the phase boundary. It might not be needed in all index directions either. Useful discretisation practices have been found from the blending or switching strategies, based on the gradient of α and the angle between it and the cell face normal. Despite the deceiving straightforward case, there may be some reflecting waves *upstream* of the bump (Lowery and Liapis, 1999). These however decay as the solution is advanced in time. The present calculation is performed with the pseudo-time marching. Whether this phenomenon has an effect on the solution, it is not clear at present. Some time-accurate simulations done in the past support those observations. The fact that the calculations are most likely not converged can be accredited to many of the observations made above as well.

Despite all the shortcomings, the present application could be considered as a good start. The development process of the code did not concern with the free surface problem, rather one general methodology on two-phase simulations. Some deficiencies of the model with respect to the problem at hand have become clearer along with this study, and future development needs can be formulated better and more accurately. This discussion is resumed in the thesis.

References

F. Bet, D. Hänel, and S.D. Sharma. Simulation of hydrodynamical free-surfece flows. *ECCOMAS'96, John Wiley & Sons Ltd.*, pages 259 – 277, 1996.

M. Darwish and F. Moukalled. Convective schemes for capturing interfaces of free-surface flows on unstructured grids. *Num. Heat Trans. B*, (49):19–42, 2006.

S. Hänninen and T. Mikkola. On the implementation of an interface capturing method. 10th *numerical towing tank symposium*, September 2007.

B.P. Leonard. The ULTIMATE conservative difference scheme applied to unsteady one-dimensional advection. *Comp. Methods Appl. Mech. Engng.*, (88):17–74, 1991.

K. Lowery and S. Liapis. Free-surface flow over a semi-circular obstruction. *Int. J. Numer. Meth. Fluids*, 30:43–63, 1999.

A. Miettinen, E. Salminen, and T. Siikonen. Kaksifaasivirtaussimulointimenetelmien kehitystä ja sovelluksia (in Finnish). Technical report, Finflo Oy, 2006.

T. Mikkola. Testing of two FINFLO -based free-surface codes with Eulerian flow over a Gaussian ground elevation. Report D-56. Helsinki University of Technology, 1999.

T. Mikkola. *Simulation of unsteady free surface flows - code verification and discretisation error*. PhD thesis, Helsinki University of Technology, 2009.

P. Queutey and M. Visonneau. An interface capturing method for free-surface hydrodynamic flows. *Comp. Fluids.*, 36:1481–1510, 2007.

T. Siikonen. Numerical method for one-dimensional two-phase flow. *Num. Heat Trans.*, 12:1–18, 1987.

T. Siikonen. Developments of the cavitation model of the Finflo code. Technical report, Finflo Oy, 2009.

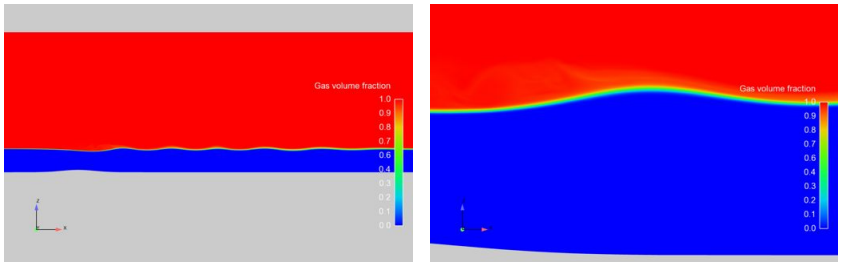

Figure 6: *Computed distribution of α using the van Albada limiter and the finer grid*

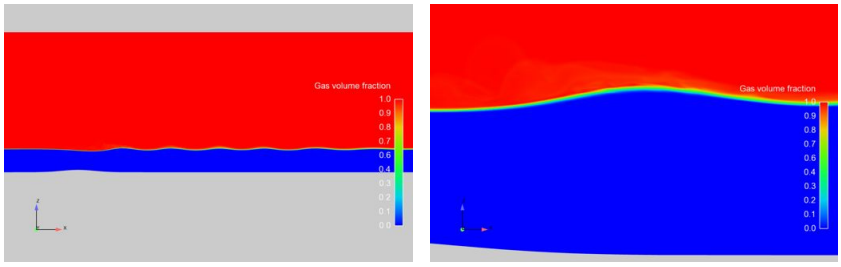

Figure 7: *Computed distribution of α using the SUPERBEE limiter and the finer grid*

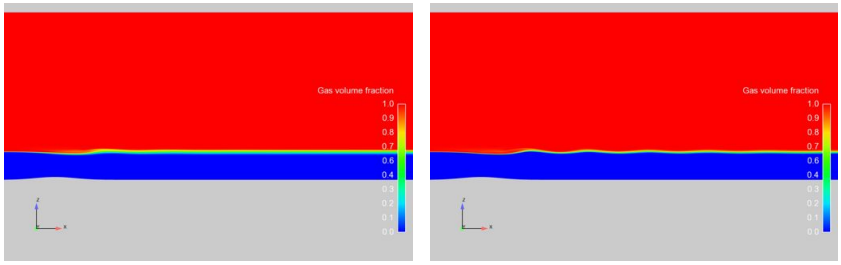

(a) non-limited (b) SUPERBEE limited

Figure 8: *Computed distribution of α on the coarser grid*

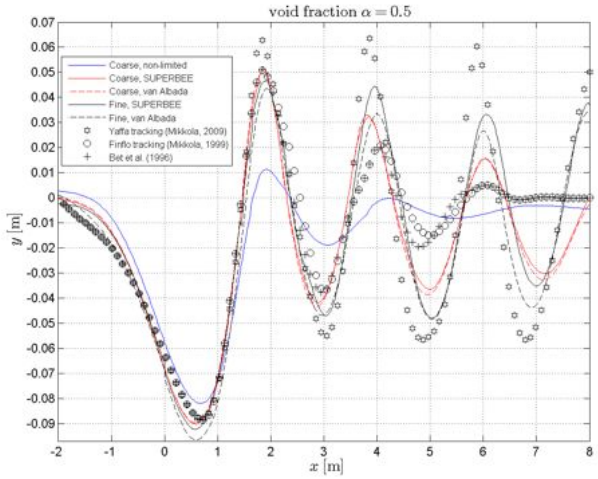

Figure 9: *Comparison of the present computations with the results of Bet et al. (1996) and Mikkola (1999, 2009). The curves present the contour $\alpha = 0.5$*

Hessian-based grid refinement for the simulation of surface-piercing hydrofoils

Jeroen Wackers*, Emmanuel Guilmineau*, Alexandro Palmieri†, and Patrick Queutey*
*LHEEA, Ecole Centrale de Nantes / CNRS-UMR 6598, 1 rue de la Noë, Nantes, France
†CIRI-MAM Tecnopolo della Nautica / UNIBO, Via Sant'Alberto 163 (Ravenna), Italy
Jeroen.Wackers@ec-nantes.fr

1 Introduction

The introduction of foiling catamarans in the 34th America's Cup, held in San Francisco in September 2013, has revolutionised the design of fast sailing boats. Boats flying with their hulls entirely out of the water, supported only by lifting hydrofoils, are no longer exotic and experimental but have become mainstream. Not only will the next edition of the America's Cup feature foiling catamarans again, but foiling has also become essential for the smaller C Class catamarans and production boats capable of full foiling, such as the Flying Phantom, are becoming available at prices affordable by the general sailing public.

As a result, naval architects today need the capacity to accurately simulate surface-piercing, lifting hydrofoils. The flow around such foils is characterised by the interaction of a sharply defined, vorticity-carrying wake with the free surface. Since the foils are strongly curved in an L- or V-shape, the lift distribution and thus the vortex strength in the wake are non-uniform and depend strongly on the immersion height and the sideslip angle. And due to the high velocities at which hydrofoils operate, ventilation and cavitation may occur and must be simulated. Thus, the hydrofoil is a very complete test case, involving most of the physical phenomena occuring in naval hydrodynamics.

It is possible to simplify the computations in the design phase by neglecting certain aspects of the flow. However, this can only be done with a thorough physical knowledge of the flow, in order to know which aspects must be kept and which can be safely removed. Detailed simulation is one of the best ways to obtain such knowledge.

Thus, there is a need for two types of hydrofoil simulation: high-fidelity investigative computations and ship design studies. The latter require large numbers of computations (up to several thousands for the design of an America's Cup yacht), so the simulations must be rapid. Also, automatisation of the workflow is of prime importance: the mesh generation, the computation itself and the post-processing are to be performed by scripts needing no user intervention whatsoever.

For both types of simulation, automatic grid refinement is an ideal tool. Grid refinement is the capacity of adapting the computational mesh to the flow by locally dividing the cells of a coarse original grid into finer cells, there where the flow requires this. It can be used to produce very fine grids around localised flow features, such as trailing wakes, vortices, and the free surface, producing local grid densities which would be prohibitively expensive on uniformly refined grids. Therefore, grid refinement creates physical insight by producing very accurate numerical solutions. It also has a strong potential in the automatisation of computations: since fine grids around the flow features of interest can be created through grid refinement, the generation of the original grid is simplified so it can be more easily performed automatically.

Inversely, the lifting hydrofoil is an ideal test case for grid refinement methods. Since so many physical aspects are present, a refinement technique which can simulate hydrofoils may be expected to be efficient everywhere.

The objective of this paper is to investigate the best way to use the automatic grid refinement procedure included in the RANS solver ISIS-CFD [4, 5] for the simulation of hydrofoils. It concentrates on the choice of the refinement criterion, which determines where exactly the cells will be refined. After a short introduction of the flow solver in section 2, two second-derivative based criteria are described in section 3. These criteria are then tested on a 2D airfoil (section 4) and a 3D hydrofoil (section 5), in order to find the best settings for the refinement criteria. Some physical analysis of the test cases is provided when the adapted-grid solutions make this possible.

2 The ISIS-CFD flow solver

ISIS-CFD, developed at LHEEA and available as a part of the FINE^{TM}/Marine computing suite, is an incompressible unsteady Reynolds-averaged Navier-Stokes (RANS) method [3]. The solver is based on the finite volume method to build the spatial discretisation of the transport equations. Pressure-velocity coupling is obtained through a Rhie & Chow SIMPLE-type method: in each time step, the velocity updates come from the momentum equations and the pressure is given by the mass conservation law, transformed into a pressure equation. The discretisation is face-based. While all unknown state variables are cell-centered, the systems of equations used in the implicit time stepping procedure are constructed face by face. Therefore, cells with an arbitrary number of arbitrarily-shaped faces are accepted. The code is fully parallel using the MPI (Message Passing Interface) protocol.

An automatic adaptive grid refinement technique is included in the solver ISIS-CFD [4, 5]. The method supports the isotropic and anisotropic refinement of unstructured hexahedral meshes. Earlier refinements can be undone in order to adapt the grid to unsteady problems. The refinement criterion, which indicates where the grid must

be refined, is based on metric tensors [4]. And finally, the grid refinement is performed in parallel and includes an automatic dynamic load balancing in order to redistribute the refined grid over the processors when some partitions have been refined more than the others.

3 Hessian-based refinement criteria

The criterion which determines where the grid is refined, is often based on the Hessian matrix of second spatial derivatives. Ideally, grid refinement should reduce the truncation error of the discretisation where this error is the largest, in order to obtain a discretisation which is accurate everywhere. Thus, the refinement criterion should indicate the regions where the truncation error is high. The Hessian is used because the error in finite-volume discretisations comes mainly from the interpolation of the state variables towards the faces. Since this interpolation is linear in general (this is the case in ISIS-CFD) the errors in the interpolation are proportional to the second derivatives of the state variables p and $\mathbf{V}$. Thus, the Hessian is an indicator of the local truncation error.

Initially, we based the criterion on the Hessian of the pressure, because we did not need refinement in the boundary layers. Since the mesh must be as regular as possible in the boundary layers and since their position is known, we perfer to make original grids which are already sufficiently fine there, letting the automatic grid refinement create the fine mesh elsewhere. Thus, the pressure was the logical choice for the refinement criterion.

It was found that the pressure criterion is very suitable for the computation of waves [5], but is unable to track wakes since these are similar to boundary layers. To adapt the mesh to pressure-based flows but also to boundary layers, wakes, and shear layers, we introduce a new criterion based on the Hessians of both the pressure and the velocity. To give equal importance to the different Hessian matrices, they are weighted in the way in which they appear in the flux (the criterion is therefore called "flux-component Hessian criterion").

The pressure Hessian criterion is computed as:

$$\mathbf{C}_p = (\|\mathcal{H}(p)\|)^\alpha, \tag{1}$$

where $\mathcal{H}$ is the Hessian operator and the absolute value of a matrix $\|\cdot\|$ corresponds to a matrix having the same eigenvectors as the original one and the absolute values of its eigenvalues. In the same way, the power α of a matrix is obtained by taking its eigenvalues to the power α while keeping the eigenvectors. In general we take $\alpha = \frac{1}{2}$.

The flux-component Hessian criterion is computed from Hessians of the pressure and velocity components, weighted according to the way they appear in the fluxes. A typical flux is for example $p + \rho u^2$, so the criterion is chosen as:

$$\mathbf{C} = \Big(\max(\,\|\mathcal{H}(p)\|,\, \rho V\|\mathcal{H}(u)\|,\, \rho V\|\mathcal{H}(v)\|,\, \rho V\|\mathcal{H}(w)\|\,)\Big)^\alpha, \tag{2}$$

where the velocity $V = \sqrt{u^2 + v^2 + w^2}$. The maximum of two tensors is computed using the approximative procedure defined by [4].

Numerically, the second derivatives are evaluated as the gradients of the gradients. First, the gradients are computed with a Gaussian evaluation plus misalignment corrections; since the gradients are used in the discretisation of the flow equations they are already known in ISIS-CFD. The pressure gradient is then smoothed [5] but the velocity gradients are not. Finally, the second derivatives are computed by differentiating the gradients using either Gauss's method or a weighted least-squares evaluation. For mixed second derivatives, the derivative computed as $q_{\alpha\beta}$ and the one computed as $q_{\beta\alpha}$ are averaged to get a true symmetrical Hessian matrix.

For law-of-the-wall boundary conditions, the gradient in the first layer of cells on the boundary (and therefore the refinement criterion) depend very strongly on the thickness of this layer. Therefore, we make sure that this layer is never refined parallel to the wall, typically by imposing a minimum cell size that is larger than the thickness of the first layer of cells. This is restrictive, but it is considered that if very fine details of the boundary layer flow are desired, it is necessary to use a low-Reynolds grid anyway, rather than the law of the wall.

4 Nakayama B airfoil

To find the right parameter settings for when these criteria are applied to three-dimensonal flows, the two refinement criteria are tested on the Nakayama B two-dimensional lifting airfoil [2]. This test case is of particular interest since detailed measurements of the velocity and the turbulence intensity (via velocity correlations) have been performed both in the boundary layers and in the wake, up to 2 chord lengths behind the trailing edge. The airfoil is a supercritical profile with chord $c = 61$ cm, placed at $\alpha = 4^\circ$ in the centre of a 137 cm wide test section. The flow is incompressible and $Re = 1.2 \cdot 10^6$. Simulations are performed with the $k - \omega$ SST turbulence model.

Four series of computations have been performed. The first two use the pressure and flux-component criterion respectively with a low-Reynolds (no-slip) boundary condition on the airfoil. The original mesh for these computations has 5755 cells and $y+ \approx 1$ on the walls. A minimum cell size is imposed, below which the cells cannot be refined, but this limit is kept low ($0.0002c$). The other two series use the flux-component criterion with a wall-law boundary condition, for which the original grid has 2623 cells and $y+ \approx 30$. For the first series, the minimum cell

size is $0.001c$, the size of the first layer of boundary cells. For the second series this limit is chosen twice larger ($0.002c$). In all series, the refinement threshold T_r (the parameter giving the global fineness of the grid) is varied.

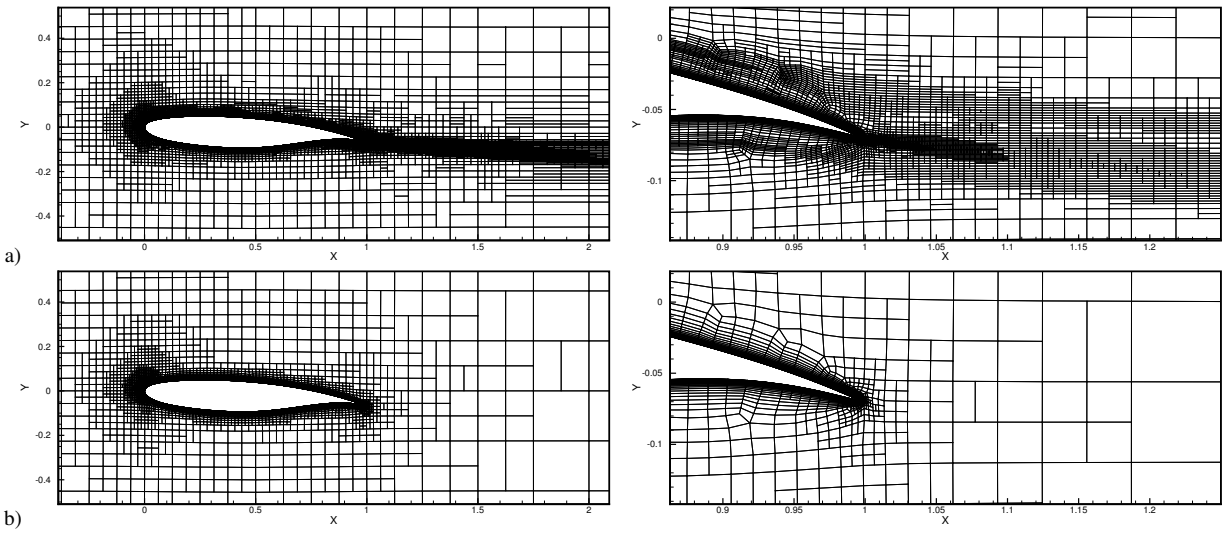

Figure 1: Refined meshes for the Nakayama airfoil, with $T_r = 0.125$. Flux component criterion (a) and pressure criterion (b).

For the first two series, the second finest mesh is shown in figure 1. For the pressure criterion, the refinement is concentrated around the leading edge where the variations in the pressure are the largest. For the flux-component criterion, the boundary layer and the wake are also clearly refined. Surprisingly, the refinement in the boundary layers and in the wake is concentrated near the outside of these phenomena.

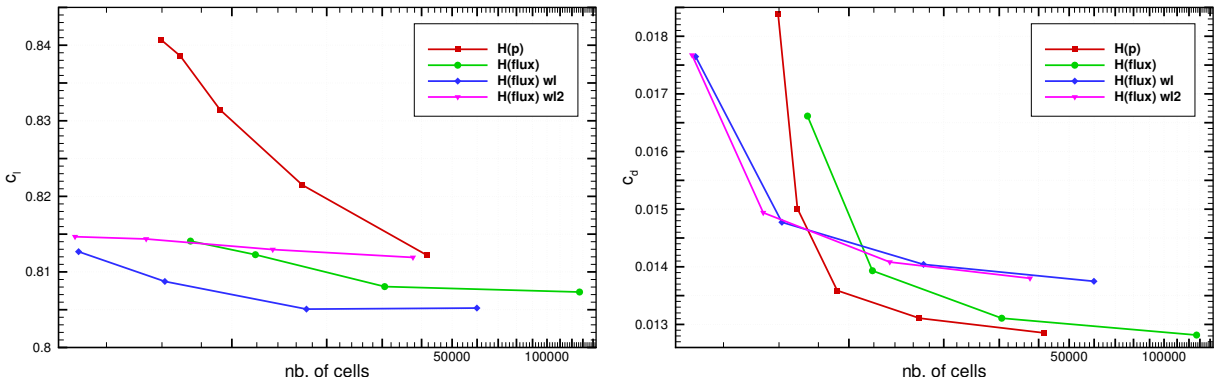

Figure 2: Convergence of lift coefficient c_l (left) and drag coefficient c_d (right) for the Nakayama airfoil.

The convergence of the force coefficients with T_r is shown for the four series in figure 2. For each series, $T_r = 0.5$, 0.25, 0.125, and 0.0625 are shown, plus $T_r = 0.03125$ for the pressure criterion. The lift coefficient seems to converge well, but to different values for each series. Anyway, the difference between the computed values is small, of the order of 1%. For the drag, the low-Reynolds series converge to a value and the wall-law series to another. The differences here are significant, more than 30% between the highest and the lowest value. This is likely due to the insufficient resolution of the leading edge pressure peak on the coarser meshes (it was found that the difference is mostly in the pressure drag).

Figure 3 gives the velocity and one component of the turbulent fluctuation in the near and the far wake, for the flux-component series (with the pressure criterion, the wake is completely diffused). All series converge, though not exactly to the same values for low-Reynolds and wall-law boundary conditions. The most notable effect of the wall law, and the larger minimum cell size even more so, is the attenuation of the turbulence peak at the trailing edge in the near wake. To capture the shape of the far wake, the wall law with $T_r = 0.125$ and minimum cell size $0.002c$ is enough, while the right tendency is already obtained with $T_r = 0.25$.

Compared with the experiments, the shape of the turbulence profiles is well captured but the intensity is too low, so the wake and the boundary layer are too thin. Since the solutions are essentially grid converged due to the automatic refinement, this is a feature of the $k - \omega$ SST model. Also, unlike the experiments, the edges of the wake are very sharp in the numerical solutions. Clearly, this is only observed because of the extra-fine grid around

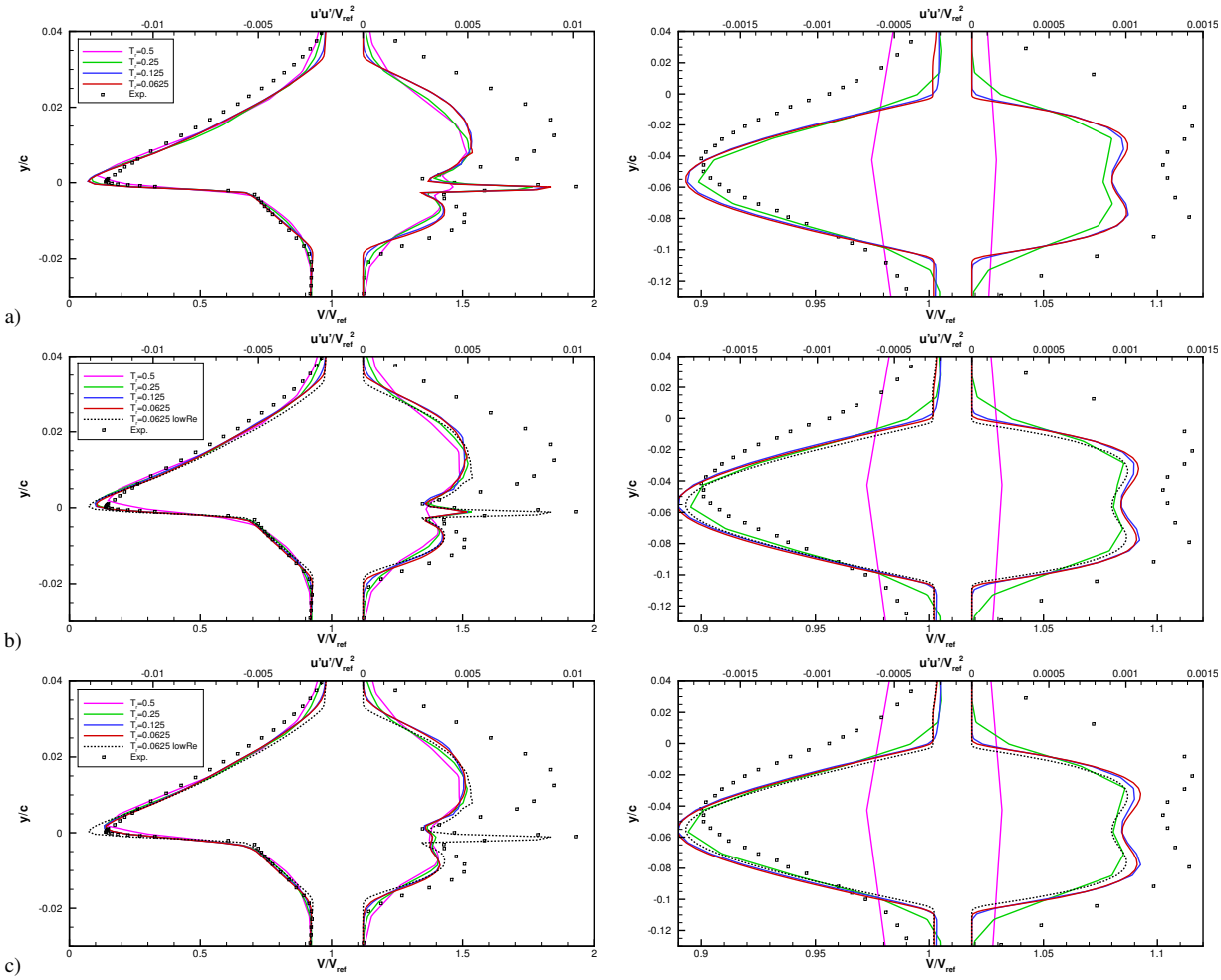

Figure 3: Velocity V (left lines) and fluctuation correlation $\overline{u'u'}$ (right lines) in the wake of the Nakayama airfoil, at $0.01c$ (left) and $2.0c$ (right) behind the trailing edge. Flux-component criterion with low-Reynolds grid (a), wall-law grid and minimum cell size $0.001c$ (b), $0.002c$ (c).

the edge of the wake (figure 1a); on coarser refined grids and therefore on standard boundary layer grids also, the numerical solution is closer to the experiments. Here, numerical diffusion makes you look good! Adaptive grid refinement therefore serves an important role in the separate analysis of numerical and modelling errors.

5 INREC hydrofoil

The second test case concerns a simplified L-shaped hydrofoil of our own design, called the INREC foil. The first objective of this test is to use grid refinement in a production-type context to assess the variation of the forces on the foil with immersion depth and sideslip angle. The second part of the test compares the pressure and flux-component criteria to see if the latter can produce a detailed simulation of the wake.

5.1 Test case

The foil geometry is a 3.5m wing with a 3 to 1 taper set at 15^o with respect to the horizontal, linked by a circular section of $0.5m$ radius to a vertical section with a constant 1m chord. The profile is NACA0012 with its dreadful stall behaviour, the horizontal wing is set at 4^o angle of attack by rotation of the entire hydrofoil. Velocity is $20m/s$, density $\rho = 1026.02kg/m^3$, viscosity $\mu = 0.00122kg/ms$. Computations are performed with different immersions ($0m$ is the upper level of the curved foil section, i.e. the entire wing is in the water at $0m$), and sideslip angles β. Positive sideslip corresponds to hydrofoil motion towards the vertical foil and away from the wing tip.

All computations use 600 time steps of $0.005s$ with acceleration over the first 400 time steps. Wall-law boundary conditions are used. Grid refinement uses the pressure Hessian criterion combined with refinement at the free surface. For the grid refinement, the threshold is $0.02m$ and the Hessian proportion (see [5]) is $c = 0.00052$.

For all immersion depths, the computation was started from the same original grid that is only refined around the hydrofoil, all fine cells needed to capture the free surface are added with automatic refinement. This represents a significant simplification of the workflow. The refined grids have between 2.5M and 4.0M cells.

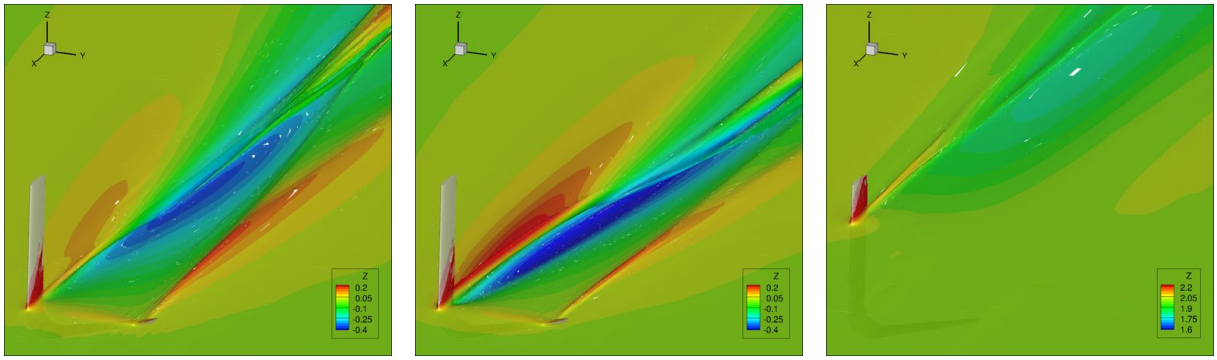

Figure 4: INREC foil, free surface elevation for $0m$ immersion, 0^o and 6^o sideslip, as well as $2m$ immersion, 0^o sideslip (left to right).

5.2 Effects of immersion depth and sideslip

The waves created by the hydrofoil are well captured by the combination of free-surface and pressure-based refinement. Figure 4 shows a trough behind the lifting foil, which is filled by breaking waves coming in from the two sides of the trough. In sideslip condition, the wave behind the vertical foil increases in strength because the sideslip induces a stronger pressure difference over the vertical foil. For greater immersion, the depth of the trough is reduced because the horizontal foil exerces less influence on the surface, being further away.

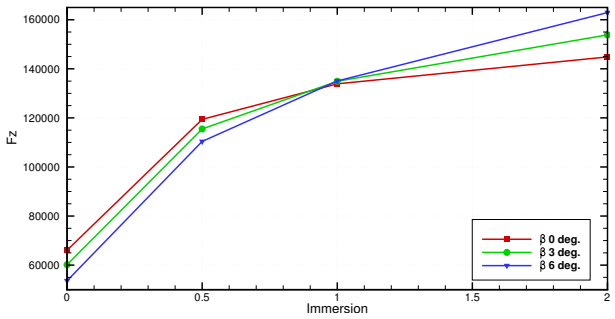

Figure 5: Vertical force on the INREC foil as a function of immersion depth and sideslip.

The dependence of the vertical force on the immersion depth and sideslip is of major importance for the boat which it carries, since the immersion must have a stable equilibrium (ride height stability), otherwise the boat is uncontrollable. Thus, the vertical force must decrease when the immersion decreases. One proposed mechanism for this is a coupling with the sideslip: if the wing goes up, the immersed vertical area decreases, so the drift angle will increase to preserve sideways equilibrium. Thus, if the vertical force decreases with the drift angle, stability is achieved.

For the INREC foil (figure 5), this decrease is observed at low immersion depths but not at $2m$ and in all cases, the variation of vertical force with sideslip is minor. The main ride height stabilisation comes directly from the proximity to the free surface: due to an inverse ground effect, the deformation of the surface reduces the pressure difference over the wing and thus its lift. This effect is present even when the horizontal wing is entirely submerged.

5.3 Computation of the wake

In the previous series of computations, the wake behind the hydrofoil is not resolved well, which was the direct motivation for the recent development of the flux-component criterion. As a first test of this criterion for 3D flow, it is compared with the pressure criterion for a double-body version of the case with 0^o sideslip and $2m$ immersion, where the water surface is replaced by a symmetry plane at $z = 0m$. To make sure that the refinement in the wake is converged, 1000 time steps were computed. The refined grids have 5.1M cells for the flux-component criterion and 2.8M cells for the pressure criterion.

Figure 6 shows the near wake, half a chord length behind the trailing edge. Where the pressure criterion only captures the tip vortex, the flux-component criterion produces a sharp well-defined wake with a jump in the transverse velocities. The solution is detailed enough for the physical analysis of the flow. However, the mesh near the tip is already becoming coarser than at the trailing edge since the wake diffuses and weakens as it travels downstream; for this solution, at about two chord lengths behind the foil most of the grid refinement disappears and the wake is no longer resolved. In future, the settings found with the Nakayama case will be applied to this

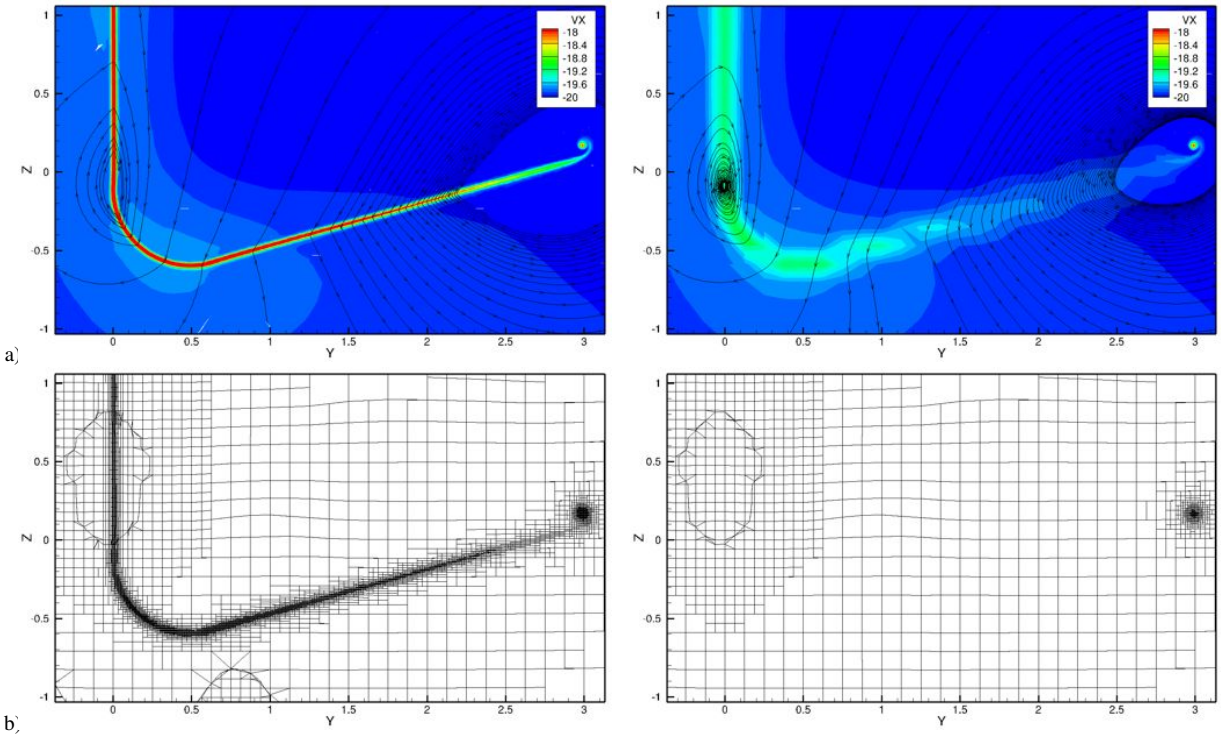

Figure 6: Near wake $0.5m$ behind the trailing edge, axial velocity and transverse streamlines (a) and the meshes (b). The flux-component solution is to the left, the pressure criterion solution to the right.

case in order to further improve the solution. However, the computation of the far wake (10 – 15 chord lengths behind the trailing edge) remains challenging.

6 Conclusion

Automatic grid refinement has a lot of potential for the simulation of lifting, surface-piercing hydrofoils. This paper demonstrates its use to simplify meshing for large series of computations in design studies and to efficiently obtain high-fidelity solutions for physical analysis. The pressure-Hessian based refinement criterion is shown to be useful for the computation of forces, a new refinement criterion based both on the pressure and the velocity is more general and capable of resolving wakes with good detail. Wall-law boundary conditions with moderate values for the refinement threshold are enough to capture the global shape of the wake.

In future work, clear guidelines for refinement parameter settings in arbitrary test cases will be developed. The accurate and efficient computation of drag forces with grid refinement and the simulation of the far wake are interesting open questions.

Acknowledgements

The authors thank students Alban Bazile, Diane Braud and Ambre Rombaut for their help with the computations.

References

[1] A. Loseille, A. Dervieux, and F. Alauzet. Fully anisotropic goal-oriented mesh adaptation for 3D steady Euler equations. *J Comput Phys*, **229**, 2866–2897 (2010).

[2] A. Nakayama. Characteristics of the flow around conventional and supercritical airfoils. *J Fluid Mech*, **160**, 155–179 (1985).

[3] P. Queutey and M. Visonneau. An interface capturing method for free-surface hydrodynamic flows. *Comput Fluids*, **36**(9), 1481–1510 (2007).

[4] J. Wackers, G.B. Deng, A. Leroyer, P. Queutey, and M. Visonneau. Adaptive grid refinement for hydrodynamic flows. *Comput Fluids*, **55**, 85–100 (2012).

[5] J. Wackers, G.B. Deng, E. Guilmineau, A. Leroyer, P. Queutey, and M. Visonneau. Combined refinement criteria for anisotropic grid refinement in free-surface flow simulation. *Comput Fluids*, **92**, 209–222 (2014).

Numerical Simulation of Slamming Problems Based on a CIP Method Using MPI

Peng Wen and Wei Qiu
Faculty of Engineering and Applied Science
Memorial University, Canada

Abstract

This paper presents the numerical solutions of highly non-linear 2-D slamming problems. The slamming problem, governed by the Navier-Stokes (N-S) equations, is treated as a multi-phase problem (solid, water and air), and has been solved by a constrained interpolation profile (CIP) based finite difference method. The interfaces between different phases are captured by density functions. In the computation, the CIP method is employed for the advection phase of the N-S equations and a pressure-based algorithm is applied for the non-advection phase. The bi-conjugate gradient stabilized method (BiCGSTAB) is utilized for solving the linear equation systems. The computational domain is discretized by a set of fixed staggered Cartesian grids. The Massage Passing Interface (MPI) parallel algorithm is implemented in the computations.

Validation studies were carried out for 2-D wedges and a ship section. The computed slamming forces, pressure distributions and water surface elevations were compared with experimental results and numerical results by other methods.

Self propulsion modelling of the KCS container ship using an open source framework

Björn Windén[1*], Stephen Turnock[1] & Dominic Hudson[1]

[1]Fluid-Structure Interactions Group University of Southampton, Southampton, UK. SO17 1BJ

1 Introduction

Recent Numerical Towing Tank Symposia have shown a wide variety of applications of CFD to problems relating to ship performance. More often than not, these depart from the traditional calm water resistance calculation. One reason for this could be the relative confidence established in the ability of Navier-Stokes (NS)-based methods to predict the multiphase flow around a hull in calm water as shown in recent CFD workshops (Larsson et al., 2014). Years of experience with such simulations have also given confidence in supporting methods such as mesh generation etc. More confidence means that the methods are more likely to be used to a larger extent in the ship design process. When looking to build on this confidence to create more comprehensive models, one option is to consider ship resistance and propulsion in a more holistic way.

Experimental measurements on self propelled models is a common method to estimate the powering performance of a ship (Molland et al., 2011, p 151-152). These can be replicated by including the rotating propeller geometry in the NS solution (Carrica et al., 2010; Lübke, 2005). However, in doing so a significant amount of extra computational effort is needed compared to the bare hull case. Using for example an Arbitrary Mesh Interface (AMI) to achieve propeller rotation also complicates the mesh generation process. In order to maintain the attractiveness of NS based methods for use in the ship design process when moving to more holistic simulations, these problems should be addressed.

A NS based solver coupled to a simplified propeller model is a way of simulating self propelled ships without a significant increase in the computational cost (Fu et al., 2010; Phillips et al., 2008; Simonssen and Stern, 2005; Turnock et al., 2010; Windén et al., 2014*a*). Such coupled solvers are usually achieved through body force modelling where the momentum induced into the fluid by the propeller is represented by an extra source term in the momentum equation. However, formulating such a coupling may still require special treatment of the mesh in the stern area to suit the formulation of the chosen propeller model. Furthermore, if considering manoeuvring simulations or simulations in waves, identifying the strength of the body force and the influence of the surrounding velocity field on a propeller behind a moving hull is a challenging task.

Determining how applicable self propelled simulations using body force models are for predicting ship performance is important to establish more experience around the more holistic approach to marine CFD. A framework for coupling a NS based solver with an arbitrary body force model on an arbitrary (dynamic) mesh has been suggested by Windén et al. (2014*b*). This framework would allow the body force approach to be evaluated for simulations of self propelled ships in calm water, manoeuvring, and wave problems. Furthermore, it supports run-time estimation of the nominal wake. The framework allows for propeller models as well as RPM control schemes to be developed by the user using simple templates only requiring the model-specific equations as input. It also allows for more comprehensive sensitivity analyses regarding the discretisation used in the propeller model to be carried out without modifying the overall mesh. The framework is implemented in the open source CFD toolbox OpenFOAM (OpenCFD and The OpenFOAM Foundation, 2010) and so is available to the CFD community.

In this paper, the framework is used to evaluate the applicability of an Unsteady Reynolds Averaged Navier-Stokes (URANS) flow solver coupled with a Blade Element Momentum theory (BEMt) propeller model to study self propulsion in calm water and in waves. This paper is meant as an example of how the framework can be used. More detailed information on the specific implementations is given by Windén (2014*a*) and a detailed description of the framework itself is given by Windén et al. (2014*b*).

2 The numerical towing tank

The flow is modelled using the URANS equations, Eqn. 1

[*] *corresponding author's e-mail*: b.winden@soton.ac.uk

Table 1: Particulars of the KCS model hull.

Scale			1:52.667		
Length Lpp	=	4.3671 m	Beam B	=	0.6114 m
Draught T_m	=	0.2051 m	Displacement ∇	=	0.3562 m^3
Prop. radius R	=	0.0750 m	Hub radius r_H	=	0.0126
Centre of gravity	=	(-0.0647 -0.0668 0) m	Prop. position	=	(2.139 -0.1273 0) m

Table 2: KCS meshes.

	Mesh size	BEMt mesh size	Cells in disk	Time spent on framework
Fine	17.7M	10x10x1	3500	2.4%
Medium	10.8M	10x10x1	2600	1.6%
Coarse	3.1M	10x10x1	400	1%

$$\frac{\partial \overline{u}_i}{\partial t} + \overline{u}_j \frac{\partial \overline{u}_i}{\partial x_j} = \frac{1}{\rho}\left(\mu \frac{\partial^2 \overline{u}_i}{\partial x_j^2} - \frac{\partial \tau_{ij}}{\partial x_i} - \frac{\partial \overline{p}}{\partial x_i} + F_v\right) \tag{1}$$

where F_v is the body force. The free surface is captured using the VOF method and waves are generated using the wave generation toolbox waves2Foam for OpenFOAM. (Jacobsen et al., 2012). The $k-\omega$ SST model (Menter et al., 2003) is used for turbulence closure.

A simplified version of this simulation with a free to surge hull at very low speed was conducted by Windén et al. (2013). In this model, the nominal wake was probed directly at half a diameter forward of the propeller plane. This approach neglects the effects of the propeller induced velocities at this location. The improved model probes the effective wake at the propeller plane and corrects for the propeller induced velocities using the inflow factors known from the BEMt solution as well as a custom correction as suggested by Windén (2014*a*).

The simulation is compared to experimental results available for the self propelled KCS container ship. The particulars of the hull are given in Table 1. The coordinate system Oxyz is right handed with x being the surge, y the sway and z the heave direction respectively.

Three different meshes are created to estimate the grid influence on the results in the following sections. An overview of these are given in Table 2. Here, the size of the Finite Volume (FV) mesh is given as well as the number of radial, circumferential and axial sectors used in the BEMt calculations. Furthermore, the number of FV cells within the propeller disk (0.2 diameters thick) which are given an active body force is also given. Finally, Table 2 presents the overall computational time spent on the framework (including propeller modelling, mapping between FV and BEMt meshes and any other activities relating to the coupling) as a percentage of the total computational time.

Comparison with experimental data is made in terms of the total resistance coefficient C_t as well as the coefficients of thrust K_T and torque K_Q. These are defined as

$$C_t = \frac{F_x}{0.5\rho U^2 S_0} \tag{2}$$

$$K_T = \frac{T}{\rho n^2 (2R)^4} \tag{3}$$

$$K_Q = \frac{Q}{\rho n^2 (2R)^5} \tag{4}$$

where F_x is the surge force, T is the thrust and Q is the torque. n is the rotation frequency of the propeller and S_0 is the wetted surface area which is taken as $S_0 = 0.1803 Lpp^2$. The presented discrepancies in these coefficients are relating to the relative error between the calculated value and the experimental value.

3 Input data to the framework

Apart from the set up of the flow solver which is the same as it would be for a standard bare hull resistance calculation, the following extra input parameters have been used to conduct the simulation. All of these

are provided in two text files (C++ dictionaries) which are read by the framework. The parameters relating to the propeller are given in one dictionary named *propellerDict* which contains

- the name of the propeller model to be used. In this case BEMt. Other options are made selectable when a user creates a new model using the template provided with the framework.
- the name of the RPM control scheme to be used. A set of basic controllers are available, more options are made selectable when a user creates a new model using the template provided with the framework.
- limiters for the controller, e.g. max. permitted RPM increase rate and max. permitted RPM.
- U,g,ρ and other constants.
- the propeller position and orientation in initial state.
- For the BEMt: propeller radius, hub radius, pitch and chord distribution, blade area ratio, number of blades and the number of discretisation steps in the radial and circumferential directions and order of interpolation scheme to map between BEMt and FV meshes.

The parameters relating to the hull are given in another dictionary named *hullDict* which contains

- the centre of rotation, mass, moment of inertia and other parameters relating to the hull.
- the name of boundary patch in the FV mesh which represents the hull.
- definitions of surge and heave directions (the rest are found automatically.)
- for each degree of freedom, definition if this is free, locked or forced (PMM.)

4 Results for the KCS at $Fn = 0.201$ at 840 RPM

Experimental results for the KCS at a fixed RPM of 840 and at $Fn = 0.201$ are available as part of the SIMMAN 2014 workshop on ship manoeuvring (FORCE, 2013). In these simulations, the hull is fixed in heave and pitch in accordance with the experimental set up. The correlation between the experimental results and simulations on the three different meshes are shown in Table 3.

Table 3: Propulsion properties (at 840 RPM) for KCS at $Fn = 0.201$ compared to experimental data.

		EFD	Coarse	Medium	Fine
$1000C_t$	recorded	5.318	5.0898	5.154	5.563
	error	-	-4.296%	-3.083 %	4.608%
K_T	recorded	0.302	0.262	0.2808	0.281
	error	-	-13.245%	-7.020%	-6.954%
K_Q	recorded	0.0429	0.0425	0.460	0.0461
	error	-	-0.932%	7.226 %	7.459%

In these simulations, the dummy propeller controller *fixedRPM* which is available in the framework is used to keep the RPM fixed at all times.

5 Results for the KCS at $Fn = 0.26$ at model self propulsion point

For $Fn = 0.26$, experimental data is available for evaluating the ability of the framework to find the self propulsion point in calm water (Larsson et al., 2010, Test case 2.3b). Here, the $selfPropFinder$ propeller controller is used to control the RPM in order to find the point where $F_x = T$. Contrary to the experimental set up, the model is fixed in heave and pitch in this simulation. In the experiment, a pitch of 0.143° and a sinkage of 0.00833 m was measured.

Table 4: Propulsion properties (at model self propulsion point) for KCS at $Fn = 0.26$ compared to experimental data.

		EFD	Coarse	Medium	Fine
$1000C_t$	recorded	5.222	-	4.885	4.8305
	error	-	-	-6.473%	7.50%
K_T	recorded	0.2530	-	0.2170	0.2215
	error	-	-	-14.22%	-12.45%
K_Q	recorded	0.0408	-	0.0381	0.0381
	error	-	-	-6.62%	-6.62%
n	recorded	14.15	-	-14.91	14.76
	error	-	-	5.418%	4.31%

6 Results for the KCS at $Fn = 0.26$ in waves

After the self propulsion point is found at $Fn = 0.26$, the RPM is fixed and the model is subjected to regular head waves of $\lambda/L_m = 0.85$ and $\zeta_0 = 0.015$ m.

In this section, time histories of relevant quantities are presented both for the time when the hull is subjected to waves but also throughout the self propulsion point finding process. This is done to illustrate the different capabilities of the framework in one continuous time series. Figure 1 shows the development of the surge force where the increases due to switching on the propeller and upon encountering the waves are highlighted. Figure 2 shows the development of the propeller RPM as well as the average (over propeller disk) advance ratio $J = \overline{U_n}/2nR$. Here U_n is the estimated local nominal wake. Finally, Figure 3 shows the development of the thrust and torque coefficients.

Animated images showing the force distribution on the hull and the nature of the unsteady wake for this simulation has been presented by Windén (2014*b*).

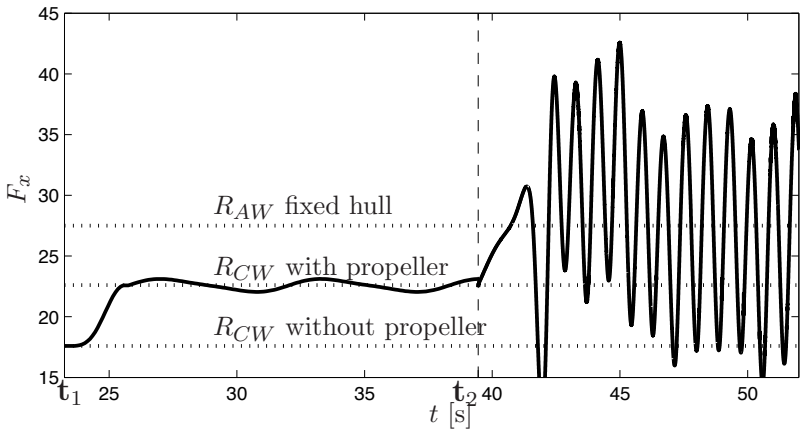

Figure 1: Development of surge force after propeller switch on ($\mathbf{t}_1$) and after wave switch on ($\mathbf{t}_2$).

7 Conclusions

The results shown here indicate how the framework presented by Windén et al. (2014*b*) can be used to study self propulsion of a container ship. A BEMt propeller model is used within the framework together with different propeller controllers. The results for $Fn = 0.26$ where the self propulsion point were found by the framework by varying the RPM show reasonable agreement with experimental data. The errors are comparable to others reported at the Gothenburg 2010 CFD workshop Larsson et al. (2010, p 240-244). They are however relatively high and are mostly comparable to the upper range of these reported values at previous workshops. The difference here is that, using the framework, this is achieved with very little extra computational effort. About 1-2% of the computational time is spent on the framework, this includes all propeller modelling, mapping between meshes, probing of the nominal wake etc. Furthermore, no further attention is paid to the mesh other than what would have been done

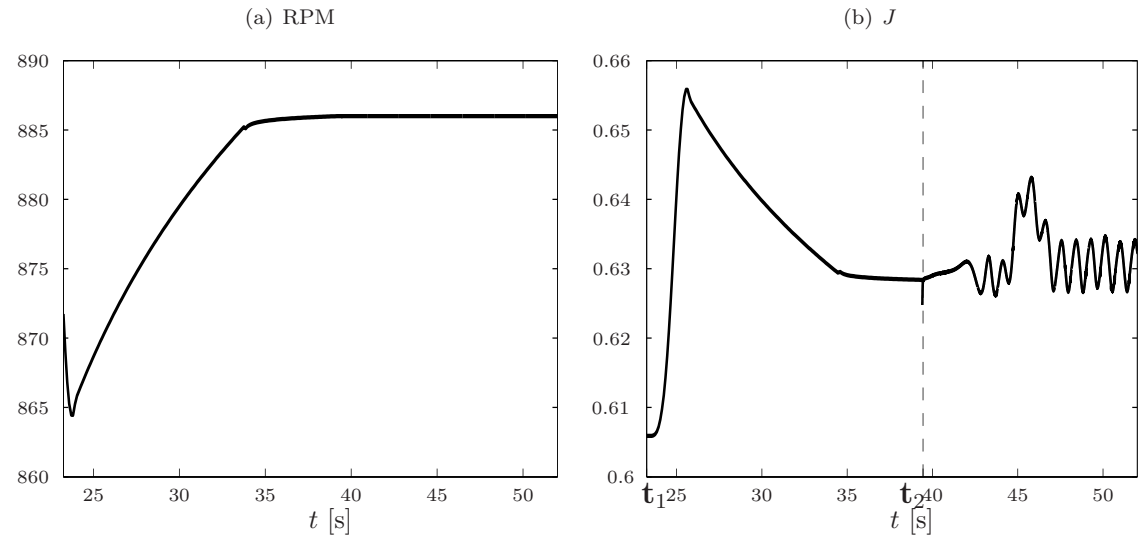

Figure 2: Development of RPM (a) and average J (b) after propeller switch on ($\mathbf{t}_1$) and after wave switch on ($\mathbf{t}_2$).

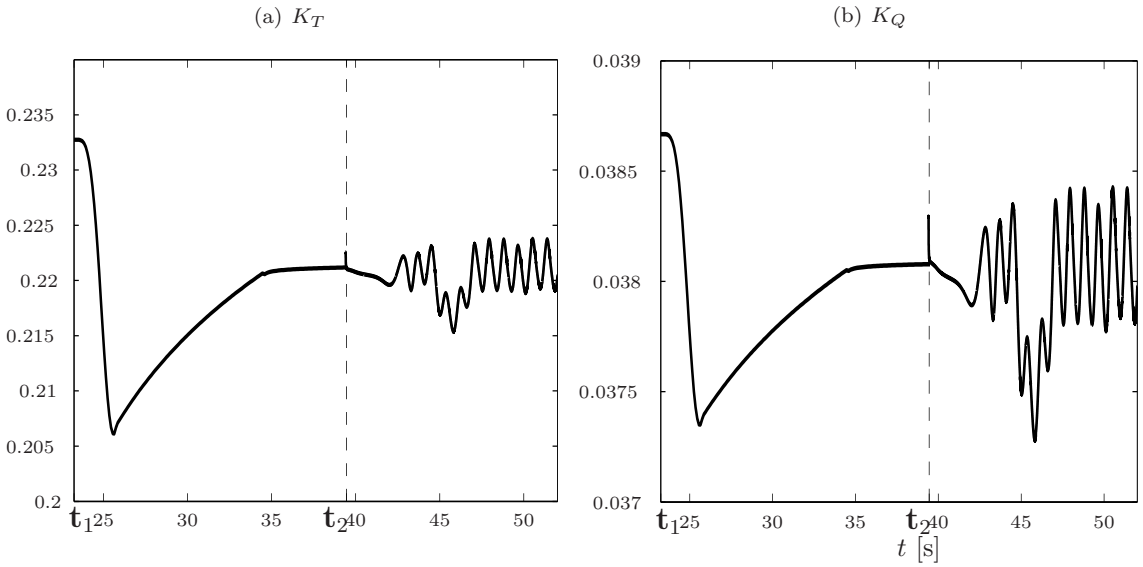

Figure 3: Development of K_T (a) and K_Q (b) after propeller switch on ($\mathbf{t}_1$) and after wave switch on ($\mathbf{t}_2$).

in a standard resistance simulation. This is encouraging for the use of body force modelling as a practical tool in the ship design process. It is likely that, by spending more time on better designing the mesh and by improving the propeller model, the results could be improved. The main purpose of this study is to encourage more similar studies in order to establish further confidence in self propelled simulations.

From the simulation in waves it can be concluded that the variation of thrust and torque is of relatively low amplitude. The mean values of the oscillations in waves correspond roughly to the calm water equivalents. This can be related to previous experiments by Nakamura et al. (1975) suggesting that the open water coefficients remain at the same average value even under waves. This seems to hold true even in this case when the hull is present.

Acknowledgements

This work was carried out within the research project entitled *ship design for enhanced sustainability* which is sponsored by the Lloyd's Register Foundation whose support is gratefully acknowledged.

References

Carrica, P., Castro, A. and Stern, F. (2010), 'Self-propulsion computations using speed controller and discretized propeller with dynamic overset grids', *Journal of Marine Science and Technology* **15**.

FORCE (2013), Experimental data for appended KCS hull in deep water, Technical report, Data gathered by FORCE Technology for the SIMMAN2014 workshop on ship manouvering.
URL: *http://www.simman2014.dk*

Fu, H., Michael, T. and Carrica, P. (2010), A method to perform self-propulsion computations with a simplified body-force propeller model, *in* 'Proceedings of the 2010 CFD Worksop in Gothenburg'.

Jacobsen, N. G., Fuhrman, D. R. and Fredsøe, J. (2012), 'A Wave Generation Toolbox for the Open-Source CFD Library: OpenFoam©', *Int. J. Numerl. Meth. Fluids* **70**(9), 1073–1088.

Larsson, L., Stern, F. and Visonneau, M. (2010), Gothenburg 2010, A Workshop on Numerical Ship Hydrodynamics, Technical report, Chalmers University of Technology.

Larsson, L., Stern, F. and Visonneau, M. (2014), *Numerical Ship Hydrodynamics - An assessment of the Gothenburg 2010 Workshop*, Springer.

Lübke, L. (2005), Numerical simulation of the flow around the propelled KCS, *in* 'Proceedings of the 2005 CFD Worksop in Tokyo'.

Menter, F., Kuntz, M. and Langtry, R. (2003), Ten Years of Industrial Experience with the SST Turbulence Model, *in* 'Proceedings of the 4th International Symposium on Turbulence, Heat and Mass Transfer', pp. 625–632.

Molland, A., Turnock, S. and Hudson, D. (2011), *Ship Resistance and Propulsion: Practical Estimation of Ship Propulsive Power*, Cambridge University Press.

Nakamura, S., Naito, S. and Inoue, R. (1975), 'Open-water characteristics and load fluctuations of a propeller in waves', *Journal of the Kansai Society of Naval Architects* **159**.

OpenCFD and The OpenFOAM Foundation (2010), 'OpenFOAM (Open source Field Operation And Manipulation) Version 1.7.1'.
URL: *www.openfoam.org/archive/1.7.1/download/*

Phillips, A., Turnock, S. and Furlong, M. (2008), Comparisons of CFD Simulations and In-service Data for the Self Propelled Performance of an Autonomous Underwater Vehicle, *in* 'Proceedings of 27th Symposium on Naval Hydrodynamics, Seoul, Korea 5-10 October'.

Simonssen, C. and Stern, F. (2005), 'RANS Maneuvering Simulation of Esso Osaka With Rudder and a Body-Force Propeller', *Journal of Ship Research* **49**(2).

Turnock, S., Lewis, S., Philips, A., Banks, J., Windén, B., Hudson, D. and Molland, A. (2010), Evaluating the self-propulsion of a container ship in a seastate using computational fluid dynamics, *in* 'William Froude Conference: Advances in Theoretical and Applied Hydrodynamics - Past and Future', p. 12.

Windén, B. (2014*a*), Powering Performance of a Self Propelled Ship in Waves, Ph.d. thesis, University of Southampton.

Windén, B. (2014*b*), Visualisation of the flow and force distribution around a self propelled container ship in head waves, Technical report, Dataset and report, University of Southampton.
URL: *http://eprints.soton.ac.uk/id/eprint/365546*

Windén, B., Badoe, C., Turnock, S., Phillips, A. and Hudson, D. (2013), Self propulsion in waves using a coupled RANS-BEMt model and active RPM control, *in* 'Proceedings of the 16th Numerical Towing Tank Symposium, 2-4 September, Duisburg Germany'.

Windén, B., Turnock, S. and Hudson, D. (2014*a*), 'A RANS modelling approach for predicting powering performance of ships in waves', *International Journal of Naval Architecture and Ocean Engineering* **6**(2).

Windén, B., Turnock, S. and Hudson, D. (2014*b*), 'CFD Modelling of a Self Propelled Ship Using Body Force Propeller Models: A Framework for Creating Coupled Solvers', *Journal of Marine Science and Technology* (Pending submission).

CALL FOR PAPERS

18th Numerical Towing Tank Symposium (NuTTS'15)

Cortona, Italy, 28-30th September 2015

Topics:

- Nonlinear flows around marine structures (LES, RANSE, Euler with or w/o free surface)
- Free-surface flows around marine structures (3-d ship seakeeping, free-surface viscous flows)
- Related topics (validation experiments, numerical techniques, grid generation, etc)

Deadlines:

Early feedback (optional):	30 March 2015
Extended Abstracts received:	30 June 2015
Payment received:	30 July 2015

You are invited to participate in the above event. The objective of the event is to provide a forum for informal discussions among experts in the field and to disseminate latest results. Younger workers and Ph.D. students are especially encouraged to participate. The event will be held at the Oasi Neumann Hotel in Cortona. All participants stay and have meals together to maximize interaction and discussion.

The extended abstracts of the proposed talk will be directly reproduced in pdf proceedings. Work in progress, encountered problems, etc. should be discussed in an open, informal atmosphere (no ties!) among colleagues. The first page of the extended abstract should be headed with the title and authors' names, affiliation and email address in a compact form to economize on space. Academic titles and page numbers shall be omitted. The extended abstract shall neither contain an abstract of the abstract, nor keywords, nor further headers. Font size shall not be less than 10pt Times New Roman. Extended abstracts should be limited to 6 pages in A4 format with 2.5 cm margin. An early reply will help us in organizing the event better. For the early feedback, a tentative title or topic will suffice.

Following the tradition of previous NuTTS events, the fees will be kept low to allow a maximum number of scientists to attend. The fees including accommodation (3 nights) and all meals during the symposium will be:

350 Euro PhD candidates and students
400 Euro authors
450 Euro other participants

Contact: Volker Bertram
volker.bertram@dnvgl.com

Sponsors: CNR-Insean, further sponsors to be announced